THÈSE DE DOCTORAT
DE L'UNIVERSITÉ PIERRE ET MARIE CURIE

Spécialité : Physique

École doctorale : "La physique, de la particule à la matière condensée"

réalisée

au laboratoire de Physique et Mécanique des Milieux Hétérogènes

présentée par

Botond TYUKODI

pour obtenir le grade de :

DOCTEUR DE L'UNIVERSITÉ PIERRE ET MARIE CURIE

Sujet de la thèse :

A depinning approach of amorphous plasticity and dewetting

soutenance prévue le 13 juin 2016

devant le jury composé de :

M.	Anaël LEMAÎTRE	Rapporteur
M.	Craig MALONEY	Examinateur
M.	Damien VANDEMBROUCQ	Directeur de thèse
M.	Daniel VIZMAN	Rapporteur
M.	Jérôme CRASSOUS	Rapporteur
M.	Pascal VIOT	Examinateur
M.	Zoltán NÉDA	Directeur de thèse

THÈSE DE DOCTORAT
DE L'UNIVERSITÉ PIERRE ET MARIE CURIE

Spécialité : Physique

École doctorale : "La physique, de la particule à la matière condensée"

réalisée

au laboratoire de Physique et Mécanique des Milieux Hétérogènes

présentée par

Botond TYUKODI

pour obtenir le grade de :

DOCTEUR DE L'UNIVERSITÉ PIERRE ET MARIE CURIE

Sujet de la thèse :

A depinning approach of amorphous plasticity and dewetting

soutenance prévue le 13 juin 2016

devant le jury composé de :

M.	Anaël LEMAÎTRE	Rapporteur
M.	Craig MALONEY	Examinateur
M.	Damien VANDEMBROUCQ	Directeur de thèse
M.	Daniel VIZMAN	Rapporteur
M.	Jérôme CRASSOUS	Rapporteur
M.	Pascal VIOT	Examinateur
M.	Zoltán NÉDA	Directeur de thèse

Contents

Preface

Theoretical foundations of the mechanical properties of crystalline solids are nowadays well established. The ordered structure of these materials allowed for the development of dislocation theories that are by now confirmed by both simulations and experimental methods [32]. A considerable part of the materials, however, does not exhibit such a structural order. Examples include amorphous materials as glasses, but also larger scale amorphous systems such as pastes, foams, colloids or granular material. The mechanical response of amorphous materials, in particular, glasses is less understood, mainly because of the lack of suitable experimental devices: their intrinsic brittleness makes standard macroscopic mechanical tests extremely difficult. Another source of experimental difficulty is that in some of these materials, for instance, structural glasses, plasticity usually manifests at very small scales [147].

Mechanical properties of amorphous materials are more complex on the microscopic scale than their crystalline counterparts due to the lack of long range order. Indeed, in contrast to crystalline solids, disorder eliminates by nature the notion of isolated defects.

In the case of amorphous materials disorder excludes dislocations as an elementary plastic mechanism, moreover, makes extremely difficult to capture the statistics behind these microscopic processes, a difficulty that delayed the proposal on such an elementary mechanism 40 years after the idea of dislocations was introduced [32]. It was not until the late '70s that A. S. Argon came up with the concept of local, slip-like rearrangements of atoms as the elementary process of plasticity in amorphous materials called *shear transformations* [8].

Over the past two decades it has gradually become clearer that many amorphous systems share similar phenomenology at very different scales: model glassy systems [115], metallic glasses [7], bubble rafts [9] and colloids [153, 6]. First, they all flow above a threshold stress. Unlike in fluids however, this flow is not smooth, but is governed by sudden, avalanche-like stress drops and features scaling properties. This complex rheology is believed to be governed by the collective effect of the interacting local rearrangements that have been observed in all these materials. The identification of the elementary processes of plasticity at lower scales has therefore tremendously benefited from larger scale experiments [153, 6, 97, 98, 9].

This common, apparently universal phenomenology as well as the puzzling scaling behavior around yield naturally led to the conjecture that the yielding of amorphous systems is potentially a dynamic phase transition [16, 106].

As such, it shows striking similarities with other dynamic transitions including earth quake phenomena [11] and line depinning [90]. In each of these systems the individual elements follow a stick-slip dynamics and below a critical forcing the system stops, while above the critical forcing it moves indefinitely. A dynamic phase transition then occurs at the critical forcing accompanied by scaling and cascade events. In the introductory chapter 1 we discuss the critical nature of the yielding transition and its similarities with depinning [90], another system exhibiting dynamic transition.

Dynamic phase transitions thus show universal behavior, a phenomenology that is independent of the details of the particular system. Systems at very different scales ranging from charge density waves through dewetting fronts up to earthquakes can manifest in the very same behavior [14, 11]. This universality allows for the construction of simple, almost toy models that reproduce the universal properties, simply because they are insensitive to the very details of the system and thus the model.

Now, if yielding of amorphous materials is indeed a dynamic transition, can simple models reflect its universality? In particular, do the details of these models matter? Many such models have been developed [9, 59, 73, 161, 47] based on the shear transformation picture, considering a mean field interaction between the shear transformations, arguing that as long as we deal with universal properties, the actual form of the interaction is an irrelevant detail. Recently introduced mesomodels based on realistic interactions between the shear transformations started to elucidate that the actual form of the interaction affects the critical behavior [171, 172, 106, 108, 16, 138]. These mesomodels are oversimplified models of amorphous media and most of them are scalar, nevertheless, they are able to reproduce a series of generic properties of amorphous plasticity. We discuss the main idea behind these models in chapter 2.

The elastic interactions associated to the particle rearrangements are highly anisotropic. This anisotropy favors the accumulation of the plastic activity along certain direction leading to shear banding. Persistent shear banding, in turn, leads to fracture nucleation hence the failure of the material. As localization is the main obstacle of improving the strength of amorphous materials [147], its effects cannot be simply neglected by a mean field approach. We address this issue in chapter 3, where we show that the anisotropy of the interaction indeed leads to the localization of the plastic activity which has a dramatic impact on the fluctuations. We show in particular, that the peculiar interaction between the shear transformations allows for deformation modes at no energy costs. These modes can then develop indefinitely and their diffusion governs the dynamics of amorphous systems. In chapter 4 we further explore the way localization affects scaling properties including finite size fluctuations in amorphous systems and relate the scaling to molecular dynamics simulations. Localization and diffusion are features that are completely absent from the standard depinning phenomenology.

In amorphous systems, localization of plastic activity along shear bands is associated to the brittleness and failure of the material [97] and this failure is a serious limitation of the usability of amorphous materials, in particular, the newly developed metallic glasses as structural materials [109, 39, 110]. Recently it has been shown that the nucleation and propagation of shear bands can be controlled by introducing inclusions of a different

composition into the amorphous bulk [4, 82, 72], the potential applications of these composites are thus countless. While several homogenization techniques are available to predict the effective mechanical properties of such composite materials [37, 184, 180], they all focus on the averages properties. Due to the underlying dynamic transition however, close to criticality, the importance of fluctuations is crucial. These fluctuations lead to considerable finite size effects that cannot be captured by standard homogenization methods. On the other hand, the newly developed family of mesomodels [171, 172, 106, 108] has been inherently designed to account for fluctuations, hence they are good candidates in investigating such finite size effects. In chapter 5 we use a mesoscopic model to investigate finite size scaling in an amorphous composite and we show that reinforcement is related to the percolation of shear bands through the inclusions, as well as that hard inclusions may block the propagation of shear bands, reinforcing the material.

From the material science point of view, there is a constant need for newer techniques in tailoring structural materials with imposed mechanical qualities. Understanding localization and the intrinsic universal properties is thus the first step towards the development of structural materials with enhanced mechanical characteristics.

The present thesis has been carried out within the framework of a joint program between ESPCI Paris and UBB Cluj and extensive collaboration with NEU Boston. Accordingly, it consists of two parts. In the first part, we investigate the universal properties of amorphous materials at the yielding transition from the depinning perspective, a phenomenology arising from the competition between elasticity and disorder.

The second part of the thesis introduces a new disordered system. In chapter 6 we investigate the dynamics and roughening of a receding dewetting line on inhomogeneous surfaces. The phenomenology of dewetting on a disordered surface is often related to depinning since the roughening of the contact line is a result of the competition between the pinning of inhomogeneities and the long range elastic forces acting on the line. These elastic forces originate from the surface tension and are usually accounted for in a perturbative treatment [68, 27, 89, 88, 25, 70] under the approximation that the deformations of the contact line are small. While such a framework has been successful in reproducing some features of the contact line morphology, for instance, roughness exponent [26], it does not aim to address the phenomenology associated to large deformations.

Unlike in the standard depinning approach of dewetting [68] where long range elastic interactions are considered along the contact line, here we consider a soft line that allows for large deformations and even the tearing up of the layer. We develop a novel, simplified model of dewetting to investigate the contact line dynamics and morphology when the line can undergo large deformations. Although the method is not a standard depinning model, we find that the system exhibits critical-like properties around a threshold concentration of inhomogeneities.

The work behind this thesis lead to the following publications in peer-reviewed journals: [187, 186, 188].

Part I

Amorphous plasticity

Chapter 1

Introduction

Contents

This introductory chapter aims to present the phenomenon of plastic deformation of amorphous materials through the review of previous scientific results. First, we examine the most relevant phenomenology to our subsequent work regarding the plasticity of amorphous materials, in particular, glasses. We then introduce the main ideas and methodologies behind the multiscale modeling strategy of amorphous plasticity starting from molecular dynamics methods, through coarse grained models up to constitutive models. Finally, we review the scaling properties of amorphous systems underlining in particular the links between the phenomenology of amorphous plasticity and the depinning transition. Emphasizing at every stage of this literature review the questions that are still open, we justify our approach and the methods that will be implemented in this thesis.

1.1 Phenomenology of amorphous plasticity

Glasses have been around for thousands of years and although they are of great industrial importance, their mechanical properties are not well understood to the day. While generally brittle and not meant to deform, especially plastically, at short scales glasses exhibit permanent deformation, which has been evidenced in indentation experiments [177] or under uniaxial load of micropillars (Figure 1.1). Note immediately an original character of glass plasticity: in addition to shear, permanent deformation can involve a volume change. The amount of this densification depends on the structure, more precisely on the available free volume [162]. In amorphous silica (SiO_2) for example a densification of about 20% was reported [91], metallic glasses however are less prone to densify.

Glasses are the textbook example of amorphous materials, meaning that, in contrast to crystalline materials, they do not exhibit long range order in the structure. The constituent particles may show short range organization up to several atomic length scale, but at long range they are disordered and statistically isotropic. The disordered structure can be understood via the glass formation process, wherein the glass is cooled down from its liquid state. From an energetic point of view, the most favorable structure would be a crystalline arrangement, but the dramatic increase in viscosity makes the optimal configuration extremely long to reach. Particles are thus trapped into a metastable configuration. Consequently, the final structure highly depends on the quench rate and slower quench results in a more relaxed configuration. Furthermore, since the glass is a supercooled liquid, it mostly resembles a snapshot of the liquid glass just above the glass transition temperature.

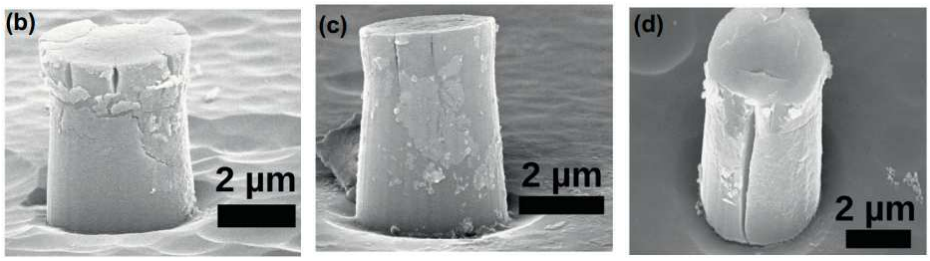

Figure 1.1 – Silica pillars under compressive load, Figure from [96]. While some well defined crack patterns are present, permanent deformation is observed. Initially, the pillars had the shape of a conical frustum. Load was applied from the top. Upon load, the pillars suffered a permanent deformation that is more pronounced on the top of the pillars, where the load was applied.

In mechanical terms, glasses have high hardness and low ductility [147], thus low toughness, meaning that although they are relatively difficult to permanently deform, they are brittle [75]. On the other hand, crystalline materials show exactly opposite mechanical properties: low hardness and high ductility. This striking contrast arises from the structural difference, it is therefore crucial to relate the mechanical properties

to the underlying structure. The aim of present thesis is to take a step towards this direction.

Shear banding

A typical failure scenario of glasses is the nucleation of shear bands. The material then slips along the band where local heating leads to decohesion and hence catastrophic failure [147, 102]. Shear bands are the place where cracks can nucleate, therefore suppressing shear banding and the resulting crack nucleation is of particular technical interest. Due to the reduced amount of free volume in metallic glasses, the excess energy cannot dissipate through permanent volumetric deformations. Excluding densification, the only possible plastic mechanism is the permanent shear deformation which ultimately leads to the formation of thin shear bands (Figure 1.2) [165].

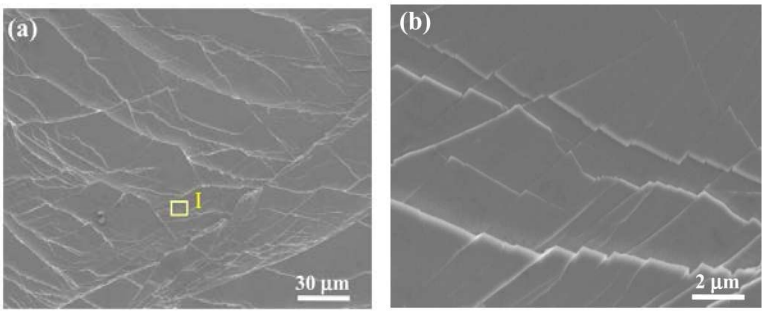

Figure 1.2 – Scanning electron microscopy images of shear bands in a $Zr_{64.13}Cu_{15.75}Ni_{10.12}Al_{10}$ metallic glass at a plastic strain of 40%. (b) is the zoom of the region marked in (a). The patterns were found to have a fractal structure. Figure from [165].

Whether there is one single or multiple shear bands depends on the composition: for instance, in a $Zr_{60+x}Cu_{25-x}Fe_5Al_{10}$ metallic glass it was found that although a larger Zr content (larger x) decreases the hardness of the material, it enhances shear band localization, while at low x shear bands are distributed throughout the whole sample [199]. Controlling shear band formation and the entailing decrease of ductility has been so far the main limitation in the use of glasses as structural materials [147]. As plasticity takes place right before crack nucleation, a deeper understanding of shear banding is the first step in understanding and controlling crack nucleation and propagation.

Interestingly, strain localization, in particular, shear banding before failure does not seem to be a particularity of metallic glasses: on a much larger scale, similar accumulation of deformation along shear bands has been observed in granular materials with glass beads of diameter in the range of a hundred micrometers [97, 98, 6] as shown on Figure 1.3. These bands were found to appear well before failure, and upon failure the deformation is restricted along persistent bands.

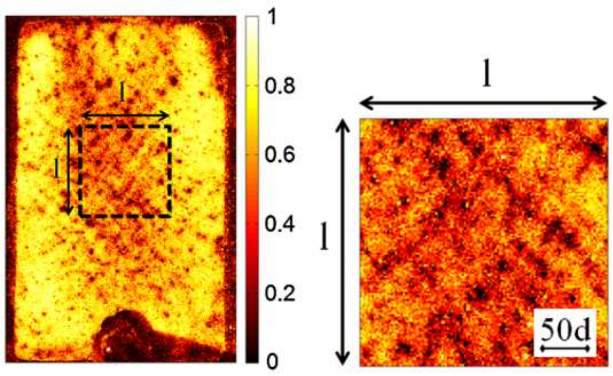

Figure 1.3 – Strain heterogeneities in a sheared granular material captured via image correlation. The image on the right is the zoom of the region marked on the left image. Note the self organization of deformation in shear bands. Figure from [97]

Serrated flow: avalanches and criticality

Although structurally glasses resemble to a supercooled liquid, it has been found that they do not yield smoothly upon load. Instead, beyond their elastic limit and before failure, their flow curve is serrated by sudden stress drops (Figure 1.4). In metallic glasses, this serrated flow has been associated to the accumulation of plasticity along nano-shear bands [166] and the alternating arrest and motion dynamics of the material along these bands.

It was found experimentally that the serrated stress drops resulting from the stick-slip sliding of shear bands show a power-law distribution [7, 94, 166]. The implications of the observed heavy tail distribution are astonishing. Most importantly, in contrast to a light tail distribution (Gaussian, for instance), heavy tail distributions allow for extreme events. Although the probability of extreme events is low, it is still finite and as their consequences are catastrophic, their importance cannot be neglected. As an intuitive comparison between long tail and light tail distributions, let us consider the following example [15, 11]: fluctuations in an ideal gas in thermal equilibrium are Gaussian, thus light tailed, while earthquake distributions are power-law distributed, thus heavy tailed. Although large earthquakes are extremely rare, they do happen and as they have devastating consequences, they cannot be neglected. On the other hand, one would *never* encounter explosion of a reservoir due to thermal fluctuations: the exponential cutoff tail of the Gaussian excludes such extreme events. Since the stress drops show a power-law distribution, we know that glasses allow for extreme events.

Fluctuations generally only become important when considering small sample sizes. At large sample sizes fluctuations tend to average out according to the central limit theorem, when the physical size of the samples is reduced however, sample-to-sample variability is so large that simply using averages for characterization becomes meaningless. With the drive towards the miniaturization of micro electro-mechanical systems

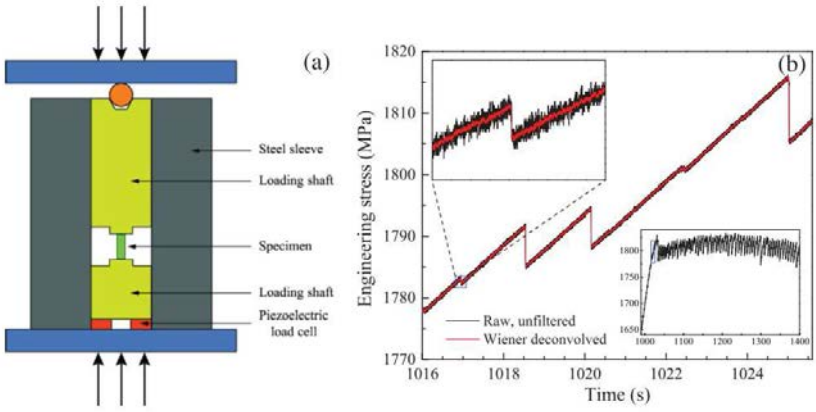

Figure 1.4 – (a) Experimental setup of the avalanche size distribution in a bulk metallic glass under uniaxial load. (b) The measured stress-strain curve is serrated with sudden drops, the material thus exhibits a jerky flow. The power-law distribution of these drops is the footprint of an underlying dynamic transition. Figure from [7]

.

this issue raises practical fabrication problems: a certain quality imposed and reached at larger sizes does not hold at smaller sizes. Fluctuations are so large that averages are no longer representative. As the sample size increases however, equilibrium samples show decreasing relative fluctuations [69]. This is however not the case in systems close to a critical point. In these systems, due to long range correlations, fluctuations do not average out at larger scales. Relative fluctuations are considerable even at the macroscopic scale, allowing for extreme events leading to catastrophic failure. Understanding fluctuations is therefore of crucial interest in detecting and controlling large events responsible for the final failure. Furthermore, fluctuations may serve as an important source of information about the internal state of the material. In particular, studying fluctuation statistics could possibly reveal valuable information about the remaining life of the structure, i.e. the closeness of the system to failure.

Ever since P. Bak introduced the the amazing concept of self organized criticality [14, 12], we know that out of equilibrium systems featuring such intermittent dynamics can show critical behavior over a wide time and length scale, from charge density waves up to earthquakes. In the context of SOC, the observation that the serrated stress drops resulting from the stick-slip sliding of shear bands show a power-law distribution [7] may not be particularly surprising, albeit far from obvious. The implications of this heavy tail distributions are, however, important. In particular, power law crackling is the footprint of criticality [156], thus, in analogy to critical systems, the stress drops are called avalanches. Sometimes avalanches consist of the arrest and motion of a single shear band [110, 200] of width of $\sim 10\ nm$, which is the first hint that the phenomenology of amorphous plasticity may not be that far from the propagation of interfaces in random media, known as depinning [191, 189]. The extent to which these amorphous systems

upon quasistatic load exhibit a dynamic phase transition (critical behavior) is, however, a matter of debate. In the case of the accumulation of multiple shear bands, the avalanche behavior is a result of the cooperative effect of these shear bands. A simple spring-block like model with nearest shear band interactions has successfully supported this observation [166]. Moreover, recent experiments in metallic glasses show a crossover from an uncorrelated nano shear band regime to a regime dominated by the collective activity of nano shear bands [94].

Localized rearrangements: shear transformations

The microscopic mechanism causing the nucleation and propagation of these shear bands is yet to be related to the atomistic structure. In case of crystalline materials, the elementary plastic mechanism is relatively well understood and explained by the motion of dislocations. While crackling may be observed in some cases [51] this can be understood in terms of the stick-slip motion of interacting dislocations pinned on lattice defects [46]. The intermittent dynamics here is given by the alternating pinning (stick) and sudden jump (slip) motion of the dislocations.

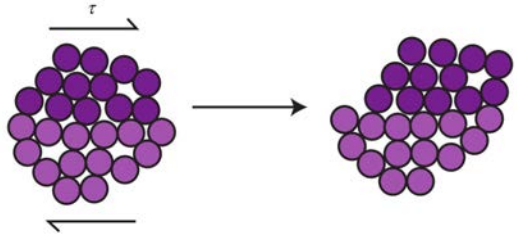

Figure 1.5 – Proposed elementary mechanism of plasticity in amorphous solids: localized rearrangement of a few tens of atoms (Figure from [155]).

In amorphous materials the lack of an underlying lattice structure excludes dislocations as the elementary mechanism of plasticity. Instead, in amorphous materials, one encounters localized atomic rearrangements of a few dozens of atoms as shown on Figure 1.5. These rearrangements are called shear transformations and there is accumulating evidence that this process constitutes the elementary mechanism of plasticity in amorphous solids [8, 52, 155, 59]. The identification of these rearrangements however is extremely difficult both in experiments and simulations, since, in general, the internal structure is statistically unchanged before and after a shear transformation [170, 52]. Clearly, an ongoing shear transformation brings the solid into a more relaxed state (otherwise the shear transformation would not take place), but there is a barrier to cross in the intermediate state, which can be facilitated either by temperature or by external load [8]. Rearrangements follow a stick-slip dynamics at the timescale of the picoseconds [147]. As shear transformations build up, they tend to form shear bands [147, 154]. Shear bands thus can be viewed as the cooperative result of interacting shear transformations.

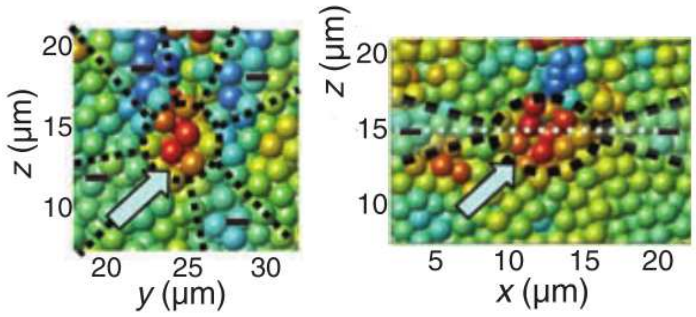

Figure 1.6 – The same localized rearrangement in a colloidal glass under shear viewed from two different planes (Figure from [153, 86]). Color indicates the local shear strain. Note the quadrupolar symmetry in the zy plane and the dipolar symmetry in the zx plane.

Intriguingly, similar rearrangements to shear transformations have been observed at much larger scales in systems composed of bubbles of the size of the millimeters [9], as well as in colloidal glasses, in which the particles are of the size of the micrometers [153, 86, 97, 98, 6] (Figure 1.6) showing that they are a universal characteristic of amorphous systems.

Although shear transformations are localized rearrangements involving a small group of particles only, they are by no means independent [174]. One rearrangement induces a long range elastic stress within the material and may trigger further rearrangements (see, for example the displacement field on Figure 1.7 a). Shear transformations thus interact through the surrounding material and this interaction is at the base of the complexity captured in the behavior of amorphous solids. The elastic interaction between shear transformations is often modeled via the interaction between continuous material inclusions, known as Eshelby inclusions [57]. The macroscopic behavior of the system then can be regarded as the collective effect of interacting Eshelby inclusions. In particular, in an amorphous granular material it has been nicely captured how individual rearrangements collectively build up to form intermittent shear bands which, in turn, self organize into persistent bands leading to failure [98].

1.2 Modeling strategies

In this section we give a brief insight into the methods developed in the past decades intended to investigate the complex plastic behavior that amorphous systems exhibit.

In crystal plasticity experimental methods are available to identify single dislocations. A device that could capture single shear transformations however has not been developed to the day, therefore simulation methods are extensively used in the investigation of amorphous plasticity. Furthermore, their brittleness does not allow for standard mechanical tests [147]. Depending on the scale of interest, there are various methods available to

model the plasticity of amorphous materials [147] (Figure 1.7). On the atomistic scale, the relevant simulation methods are the molecular dynamics methods. On the macroscopic scale one would utilize finite element methods fed with constitutive laws. These are however less common given that at such a large scale glasses fail before experiencing any considerable amount of plasticity. Nevertheless, plasticity can be reached in confined geometries, such as indentation experiments [147, 36, 164]. As an intermediate scale, a coarse grained approach is suitable which should connect microscopic and macroscopic methods.

In what follows, let us briefly review the key concepts behind each of the three approaches.

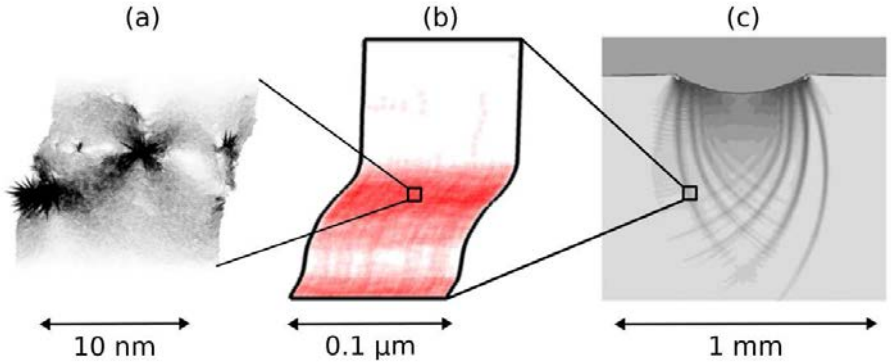

Figure 1.7 – Multiscale modeling of amorphous materials, figure from Ref. [147] At the nanometric scale, atomistic simulations (a), at the micrometric scale mesoscopic models (b) and at the macroscopic scale micromechanical constitutive laws (c) are relevant. The ultimate goal is to connect the three scales.

Molecular dynamics

When it comes to reproducing the properties of amorphous materials with a specific composition on the microscopic scale, one would use advanced molecular dynamics methods involving effective potentials resulting from ab initio calculations. There is significant difference between the mechanical properties of different glasses which is important in real world applications. When interested in obtaining numbers (value of the yield stress, toughness, hardness, etc.) the modeling strategy has to precisely take into account the interatomic potentials. Our purpose here is however to understand generic properties of amorphous plasticity, that is, properties that many different amorphous systems share, regardless to the very details of their composition.

In this spirit, on the atomistic scale, one of the possibilities for a model amorphous system is a bi-disperse mixture of Lennard-Jones particles. The two components are needed in order to inhibit crystallization. The sample is prepared by a quench of the liquid glass mixture and different quench methods are available leading to different structures

in the quenched sample. Usually however measurements are carried out after an initial transient, after which the structural memory resulting from the initial quench protocol is considered erased [114, 101]. Note that a growing interest in the recent years has concerned the encoding of a mechanical memory in the amorphous structure [62].

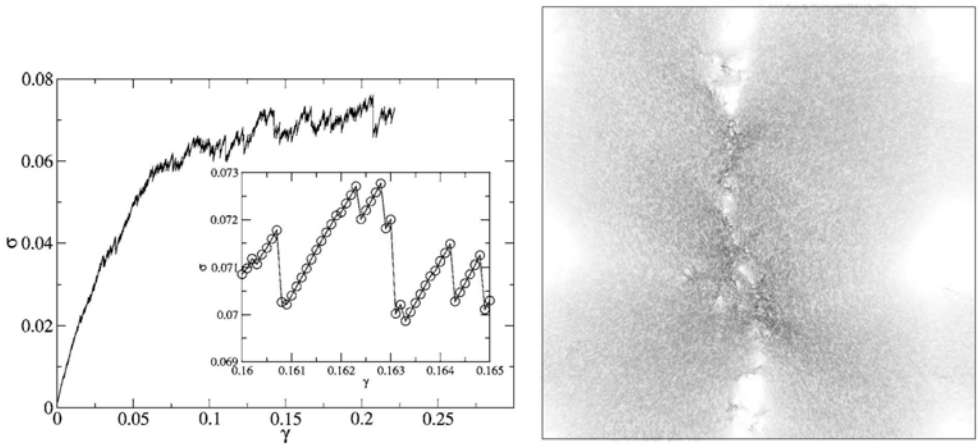

Figure 1.8 – Left: Stress-strain curve from MD simulation of an athermal, bi-disperse Lennard-Jones glass under quasistatic load. After an initial elastic branch yield sets in. Plastic flow is governed by alternating smooth elastic increases and sudden stress drops associated to cascades of plastic events. Right: non-affine displacement field from the same simulation, corresponding to a single avalanche. Note the localization of the slips. Figure from [114]

Although the time limitation due to the computational effort in MD simulations implies extremely large strain rates ($\sim 10^8 s^{-1}$) compared to experiments, a reasonable separation between the internal vibrational time scale and the time scale of the deformation is reached [17]. This separation allows for the sampling of the behavior of deformed amorphous systems. If one is interested in the athermal, quasistatic limit (i.e. $T \to 0$ and $\dot{\gamma} \to 0$), one can impose a dissipative dynamics with frequent energy minimization to compensate for the too high strain rate [112, 111, 114, 115, 183, 174, 100, 52, 59, 60]. Individual plastic rearrangements have been found in these athermal, quasistatic simulations strengthening the idea of the shear transformations [101, 114, 183] (see, for example, Figure 1.7 a). The various tools developed within the molecular dynamics framework have been successful in reproducing a great part of the phenomenology observed in amorphous systems. In particular, one observes the serrated flow curve associated to the plastic events [114], the scaling of the stress drop distributions implying crackling and avalanche behavior [111, 150], as well as anisotropic long-range strain correlation due to localization [116] of plastic events along narrow slip lines (shear bands) [115] (Figure 1.8).

Mesoscopic models

The time limitation of the molecular dynamics simulation methods, as well as the strikingly similar behavior shared by amorphous systems at very different scales (glasses, colloids, granular media, bubble rafts or foams) led to the question whether it is possible to smear out the very details behind the molecular dynamics methods and use a semi-continuous approach.

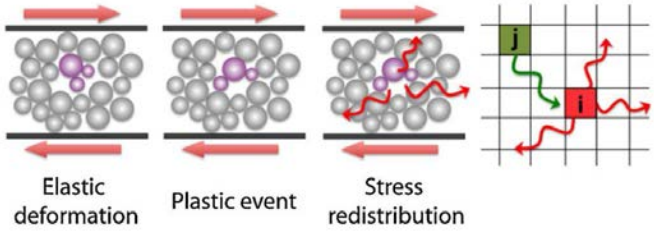

Figure 1.9 – Coarse graining in mesomodels: the material is divided into elastoplastic blocks that account for the elastic consequences of localized plastic events. The mechanical noise associated to plastic events is computed in the continuum limit. Figure from [24]

Starting from the early work of Argon and Bulatov [30, 31], several coarse grained, mesoscopic models have been developed [16, 137, 171, 172, 106, 108, 105, 128, 127, 187, 78, 72] that were proven successful in reproducing various universal properties of the mechanical response of glasses observed in experiments or molecular dynamics simulations. These are minimal ingredient elastoplastic models and the idea behind them is to constitute a bridge between atomistic and finite element simulations. In these models, the material is divided into blocks with an intermediate size. The size of a block has to be large enough for continuum elasticity to hold, but at the same time small enough to isolate plastic events and to account for disorder. As the definition of the size of a shear transformation is unclear, there is no precise definition of this intermediate size either, but ideally it should be larger than the size of a shear transformation (Figure 1.9). A major question then remains: how to transfer microscopic information from molecular dynamics to feed the mesoscale models?

While in MD simulations the simulation units are the particles, in mesomodels the simulation units are the elastoplastic blocks. These models treat the material as continuum, they preserve however the interaction between the shear transformations that enter into the model as continuous material inclusions known as Eshelby inclusions [57]. Local disorder is accounted for either via random thresholds or is introduced into the dynamics. These models have been successful in reproducing the critical-like behavior observed in molecular dynamics and experiments, in particular, avalanche behavior [171], strain localization and shear banding [172] as well as a Herschel-Bulkley type of strain rate dependence [126].

Despite their recent success, the methodology behind these models remains surpris-

ingly fragmented, which makes a systematic comparison of various results extremely difficult. A major question is thus how the different details of the various mesomodels impact the resulting phenomenology? More importantly, how do the results of these models quantitatively compare to experiments or molecular dynamics simulations?

Constitutive laws

The ultimate goal of plasticity would be to provide macroscopic constitutive laws analogous to the Navier-Stokes equations of Newtonian fluids [17] connecting the internal state of the material to macroscopic quantities. Several constitutive models have been attempting to provide such a rheology, but most of them handle the shear transformations as either independent or as interacting via a mean elastic field.

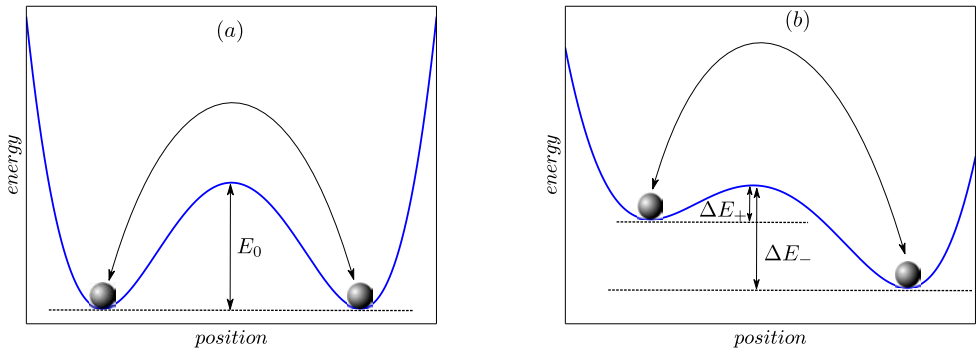

Figure 1.10 – (a) At zero stress, backward and forward energy barriers are symmetric. (b) External stress tilts the potential landscape, hence forward flips produce at a higher rate resulting in a net strain rate.

For instance, Eyring considers single particle flips activated by temperature. The energy barrier to cross for a flip is decreased by the loading stress and the strain rate is given by the difference between forward and backward flip rates [17, 58]. In this picture, only single particles can move into the holes left in their neighborhood. The probability per unit time (rate) for such a move to happen is given by an Arrhenius activation law:

$$R = \frac{1}{\tau} \exp\left[-\frac{\Delta E}{kT}\right] \tag{1.1}$$

where τ is the characteristic lifetime of the given configuration, T is the temperature and ΔE is the energy barrier that has to be crossed to reach the hole. Forward and backward jumps are possible and the associated rates are R_+ and R_-. If the characteristic strain associated to a single flip is ϵ_0, according to Eyring [17, 58] the strain rate is given by the rate difference between forward and backward flips:

$$\dot{\gamma} = \epsilon_0(R_+ - R_-) \tag{1.2}$$

At equilibrium, the back and forth flip rates are equal since the energy barriers of the backward and forward flips are the same. An external stress σ however tilts the energy landscape and induces an asymmetry between the barriers: $\Delta E_{\pm} = E_0 \mp \sigma V$ (see Figure 1.10). Here V is a typical volume of the flip zone. The forward and backward rates are then no longer equal and their difference gives rise to a nonzero strain rate:

$$\dot{\gamma} = \frac{1}{\tau}\epsilon_0 \exp\left[-\frac{E_0}{kT}\right]\left(\exp\left[\frac{\sigma V}{kT}\right] - \exp\left[-\frac{\sigma V}{kT}\right]\right) \tag{1.3}$$

At small stresses the exponentials can be expanded up to the linear term and we recover the rheology of a Newtonian fluid:

$$\sigma = \frac{kT\tau}{2V\epsilon_0}\exp\left[\frac{E_0}{kT}\right]\dot{\gamma} \tag{1.4}$$

At large stresses only the first exponential is kept and we have:

$$\sigma = \frac{kT}{V}\left[\frac{E_0}{kT} + \ln\frac{\dot{\gamma}\tau}{\epsilon_0}\right] \tag{1.5}$$

meaning a slow (logarithmic) dependence on the strain rate. Also, the expression in the brackets is only positive above a threshold strain rate, we recover thus a yield stress fluid behavior.

Argon [9] takes the method one step further considering collective flips of particles, but the subsequent flips are still considered as independent. In STZ theories [59] the heterogeneous density of shear transformation zones is taken into account, and the forward and backward rates weighted accordingly. Dynamical heterogeneities are introduced by Hébraud and Lequeux [73] by considering a probabilistic evolution equation of elastoplastic blocks coupled via mean field. Similarly, in Soft Glass Rheology models elements are considered to interact via a mechanical noise and they can escape their traps by thermal activation [161].

Whereas these models have been proven successful in reproducing some rheology of amorphous systems, in particular, predict jamming and a Herschel-Bulkley rheology above, due to the mean field/mechanical noise type interactions, with a few exceptions [117], they do not allow for localization. While successful in predicting the macroscopic shear band formation when combined with finite element methods [147, 36, 164], they do not seek to connect the underlying structure to the localization behavior on the mesoscale, which, as we will see in the subsequent sections, does have important consequences regarding the plastic response of amorphous systems.

1.3 Scaling properties and the yielding transition

Upon stress, materials exhibit deformation. Up to a stress value they show linear elastic properties. Passed that value, their deformation is still reversible, but nonlinear. Further load leads to irreversible deformation, and, eventually a plastic flow. When driven slowly,

one may encounter sudden stress drops discussed previously. Finally, the material is likely to break (Figure 1.11). While the phenomenon presented here is not particular to amorphous solids as similar behavior is observed for crystalline materials as well, the processes behind the macroscopic behavior are different. While in crystals the stress drops in the flow curve are caused by the pinning of dislocations on defects, in amorphous materials they are related to the particle rearrangements.

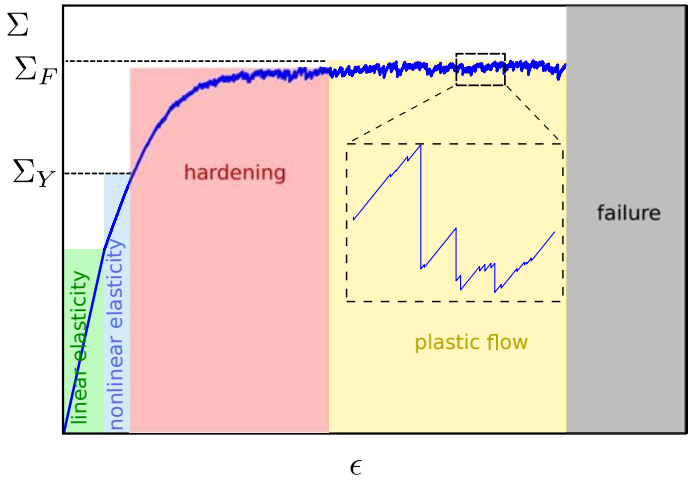

Figure 1.11 – Typical yielding of solids. At small strains the material deforms reversibly, at further load however it yields and eventually fails.

We have already mentioned some evidence that during yield, amorphous systems (in particular, metallic glasses) show critical-like behavior due to the underlying collective stick-slip mechanism that governs their deformation. Upon loading, one observes sudden stress drops obeying a power law distribution, $P(\Delta\Sigma) \propto \Delta\Sigma^{-\tau}$, signaling the cascade-like processes called avalanches. It has been shown experimentally [7, 165] that within these slip avalanches, plastic activity tends to follow a narrowly localized structure.

In addition to the power law distribution, avalanche rates were shown to exhibit finite size scaling in a model Lennard-Jones glass under shear [150]. In particular, the size of the largest event was found to scale as $S_c \propto L^{\alpha}$ with the system size [150]. Both the power law and the finite size scaling seem to hold regardless of whether inertia of the particles is taken into account, however different scaling exponents were obtained depending on the damping showing that although inertia does not destroy criticality, it can place the system into different universality classes [150]. In particular, low damping seems to drive the system into the mean field universality class. As one would not expect considerable localization at low damping, this finding implies that localization plays an important role in the universal behavior.

Displacements in amorphous materials are strongly correlated due to the localized slips along shear bands. Nevertheless, it was found that the mean square displacement increases linearly in time [115]. While this is not a single-particle diffusive process,

an effective diffusion coefficient D can be defined. For this diffusion coefficient finite size scaling was observed [115]: $D \propto L^{\delta_s}$. This scaling could be understood via an independent localized slip line argument. Indeed, as we will see later on, assuming that subsequent avalanches consist of uncorrelated, narrow, percolating slip lines directly leads to the observed finite size scaling.

The dynamics of the plastic yielding is governed by the presence of weak zones that are prone to yield. These zones are characterized by their stress barrier x, i.e. the extra stress necessary for them to deform plastically. The larger their stress barriers, the more stable the zones are. The ones that yield are the weakest ones, that is, the ones that have the smallest barriers. The actual distribution of barriers close to zero thus plays an important role in the yielding process. It was shown [106, 107, 105] that the distribution of these barriers follows scaling with a positive exponent, thus vanishes at zero barrier values: $P(x) \propto x^{\theta}$. Somewhat misleadingly, $P(x)$ is called the density of shear transformations [106, 107, 105], although it represents a probability density and not a spatial density.

Finally, close to the yielding transition, the flow stress shows power law dependence on the strain rate: $|\Sigma - \Sigma^F| \propto \dot{\gamma}^{1/\beta}$. The associated exponent is known as the Herschel-Bulkley exponent [106].

We can thus see that there is accumulating evidence that the yielding process of amorphous solids is indeed a dynamic phase transition. As such, it can be characterized by a set of critical exponents and the associated scaling relations [106]. Moreover, the scenario of the arrest-motion dynamics involving the scaling of avalanches, the Herschel-Bulkley scaling of the flow stress and the underlying critical behavior is strikingly similar to the one observed at the depinning transition that characterizes the advance of an elastic manifold in a random landscape. It is therefore appealing to investigate the yielding transition in the depinning context [106]. As we will see however, key differences arise from the anisotropy of the interactions leading to localization, a phenomenon that is completely absent in classical depinning.

1.4 Analogy between depinning and plasticity mesomodels

We have mentioned that the critical-like behavior of amorphous materials at yield reminds us to the depinning transition. In this section we further develop the similarities amorphous yielding and the depinning transition share.

The depinning problem

The classical depinning problem deals with the motion of an elastic manifold in a disordered landscape [63, 124, 90] under an external forcing and has been used as a model system for wetting front propagation or crack propagation, for instance [134, 89]. In these cases the manifold is a one dimensional line propagating in a two or three dimensional space. Figure 1.12 depicts such a receding dewetting line. As the line advances, the random landscape tends to pin it due to the local energy minima.

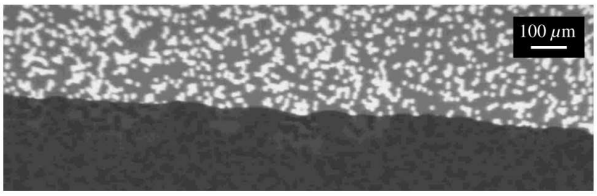

Figure 1.12 – Receding contact line on a disordered surface. Disorders tend to roughen the line, while surface tension tends to smoothen it. Figure from [25].

At large forcing the line does not feel much about the disordered media. As forcing decreases however, the effects of the disordered landscape become more and more prominent and the line becomes rougher. Eventually, below a critical forcing f_c^{ext} the line would stop after a finite distance. There is thus a critical force which separates the moving and the pinned phases. At the boundary of these two phases one encounters a dynamic phase transition with critical properties such as scaling and the divergence of correlation lengths. Since the transition separates the pinned and depinned phases, it is called depinning transition (Figure 1.13). Around the transition, the velocity of the line exhibits a scaling strikingly similar to the Herschel-Bulkley law we see in the yielding transition: $v \propto |f^{ext} - f_c^{ext}|^{\beta}$.

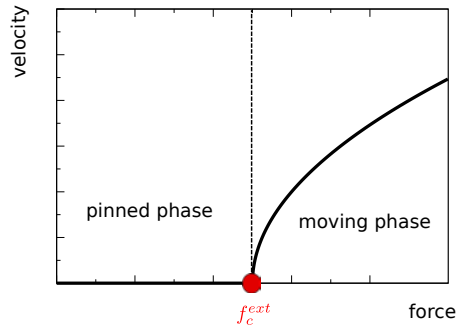

Figure 1.13 – Schematic representation of the depinning transition. Below a critical forcing f_c^{ext} the line stops within a finite distance. Above the critical force it advances indefinitely. Between the two phases one encounters a dynamic transition. Around the transition we have $|f^{ext} - f_c^{ext}| \propto v^{1/\beta}$.

Since in usual applications the inertia of these lines is irrelevant, the motion of a manifold in a random landscape is often described by an overdamped equation of motion. Let us consider a d dimensional elastic manifold propagating in a $d+1$ dimensional space. As an example, a two dimensional ($d = 2$) manifold propagating in a three dimensional space is sketched on Figure 1.15 (c). The overdamped equation of motion of the position $h(\vec{r}, t)$ of such an elastic manifold (described by $z = h(x, y, t)$ on Figure 1.15 (c)) in a

random landscape is given by [63, 90]:

$$\frac{\partial h}{\partial t}(\vec{r},t) = f^{ext}(t) + G * h(\vec{r},t) - \frac{\partial U[\vec{r},h(\vec{r},t)]}{\partial h} \tag{1.6}$$

On the RHS (see Figure 1.14), the first term represents the external forcing which is homogeneous throughout the manifold. The second term describes the elasticity of the line: since we consider linear interactions only, this is given by the convolution of an elastic kernel G and the position of the line. The actual form of the kernel is specific to the system and $G(r,r')$ gives the force response at r due to a localized perturbation at r'. The total force at a given point is then given by the superposition of all the perturbations along the line, hence the convolution. In depinning, this term tends to flatten the manifold since variations of the manifold result in excess elastic energy. The last term describes the effect of the disordered landscape. U is the potential of the landscape and in the depinning picture it generally exhibits many local minima that would pin the interface. The deeper the potential wells in U, the stronger the pinning effect on the line. In particular, if the pinning is strong enough, instead of a smooth propagation, the line will exhibit a motion governed by stick and slip jumps between subsequent minima.

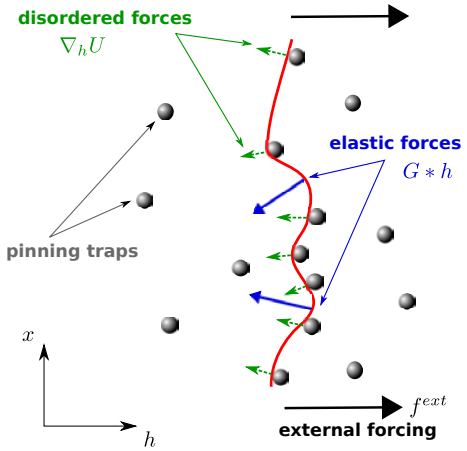

Figure 1.14 – Elastic line advancing in a random potential. Deep local minima pin the line, while the elastic forces tend to flatten it. The dynamics is the result of the competition between the roughening effects of the pinning points and the elastic restoring forces.

Such a system has been known to exhibit a dynamic transition at a critical value f_c^{ext} of the driving force.

In particular, at the critical forcing, the manifold propagates in terms of avalanches, correlations reach the system size and the mean velocity shows a Herschel-Bulkley-like power law dependence on the departure from the critical forcing.

Connection to amorphous plasticity

The stick-slip dynamics associated to the strong pinning of the manifold leads to striking similarities of depinning when compared to plastic yielding. As the phenomenology of depinning has a more solid foundation [63, 90, 124], it is tempting to investigate yielding in the depinning framework.

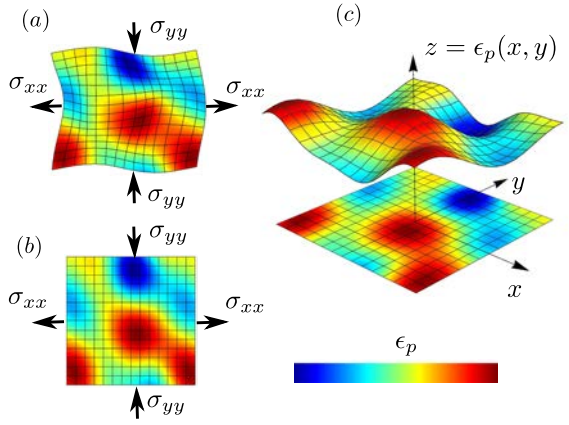

Figure 1.15 – Sketch of a $2d$ amorphous material upon bi-axial loading. (a) The mesh is deformed according to the displacement. The associated strain has a reversible elastic contribution and an irreversible plastic contribution. The latter is represented by the color scale. (b) The same plastic strain field represented on the undeformed reference frame. (c) The plastic strain field represented as a d-dimensional manifold advancing in a $d + 1$ dimensional space.

We have seen that the slip mechanism in amorphous solids is related to the onset of irreversible, localized deformations. One can thus represent the plastic strain field associated to these irreversible deformations as a manifold. In the case of a two dimensional material for example, the local plastic strain can be represented as an extra dimension, as shown on Figure 1.15. One thus obtains a two dimensional manifold propagating in three dimensions, in the direction of the axis given by the plastic strain. The motion of this manifold follows a stick-slip dynamics resulting from the quick atomistic rearrangements, the shear transformations. External loading enforces the onset of such slip events, the loading stress thus can be viewed as an external forcing on the manifold. Between configurations, rearranging particles have to cross a potential barrier to reach a new equilibrium configurations, and this barrier is disordered due to the disordered structure. Finally, the elastic bulk around the shear transformations ensures linear interactions between them, we thus recover all the three elements of the depinning context: external driving, elastic interactions and random landscape. These elements (driving, elastic kernel and disorder) are the key ingredients of mesomodels developed to investigate the yielding transition, the idea is thus to compare the depinning transition to the yielding transition by the means of mesomodels.

While formulating the yielding transition in the depinning framework is appealing, one encounters additional features in the yielding phenomenology. In particular, localization of the plastic activity into shear bands, anisotropic correlations and diffusion [170, 169, 171, 172, 113, 114, 116], as well as the vanishing probability of barriers at zero [106] are all extra features that are not present in classical depinning. As we will show, these phenomena are related to the peculiar form of the interaction between the shear transformations, more precisely, to the anisotropy of this interaction. While in depinning the elastic interactions $G(r, r')$ are isotropic, this is not the case in plasticity which raises several questions. First, how does the anisotropy of the interaction affect localization? Second, how does localization affect the associated critical behavior? To what extent can the depinning framework capture the yielding transition and what other tools do we need beyond? To what extent do mesomodels account for this additional phenomenology?

1.5 Overview of Part I

In order to answer these questions, throughout this thesis:

- We show that the details of the construction of the elastic kernel $G(r, r')$ are crucial to the phenomenology of amorphous plasticity. Therefore, we discuss the very technical details regarding the construction of this interaction kernel.
- We show how the kernel's specificities lead to localization. Specifically, we show that shear bands are soft deformation modes of the kernel and the presence of such modes has a dramatic impact on the resulting phenomenology. Such localization is not present in depinning and cannot be captured by simple mean field approaches and it results in qualitatively different behavior, in particular, divergence of strain fluctuations.
- Due to the long range nature of the elastic interactions, the yielding transition if often handled in the mean field spirit. While mean field interactions allow for avalanches and depinning-like scalings, we show that they are not enough for a proper and complete description of the yielding transition. To that end, we test the modifications of various details of the kernel to see what is crucial and what is not to the physics, focusing in particular to diffusion, scaling properties and stress barriers.
- Equipped with the proper tools, we finally apply the model to amorphous composites and we show that the reinforcement effect of amorphous materials by hard inclusions is closely related to the geometrical percolation of shear bands.

1.6 Conclusions

In this chapter, we introduced the general phenomenology of amorphous plasticity. We have seen that plasticity in amorphous materials takes place under the form of localized

rearrangements of several particles. The large scale dynamics is governed by the collective behavior of the rearrangements. The phenomenology is then the result of the competition between elasticity and disorder. In this context, yielding of amorphous materials is very similar to the depinning transition. In addition to depinning however, amorphous materials show striking localization which ultimately leads to fracture nucleation. Constitutive laws focus on effective properties, disregarding the importance of localization. Molecular dynamics methods on the other hand do not allow for fine-tuning between the nature of disorder and the elastic interactions. The newly developed family of mesomodels was designed to address this issue, by coarse graining the material, yet keeping the elastic interactions. These models thus allow for fluctuations and localization, they are therefore promising in modeling the shear banding behavior and the associated brittleness of amorphous materials. The next chapter is dedicated to presenting the idea and methodology behind these mesomodels.

Chapter 2

Mesoscopic models

Contents

In the previous chapter we have discussed the phenomenology of amorphous plasticity and we concluded that the yielding transition shows critical behavior, similar to the depinning transition. Nevertheless, localization is a key feature in amorphous plasticity that is completely absent in depinning. In the following chapters we investigate the localization of the plastic activity in amorphous systems and the effect of this localization on the universal properties. Since we are interested in generic properties that are independent of the very details of the system, we are going to use mesoscopic models that are expected to reflect such a universal behavior. Nevertheless, as we show, some of the details of these models, in particular the form of the elastic interaction does have a considerable impact on the generic properties. In this chapter thus we review the main ingredients of mesomodels with emphasis on what of these ingredients impacts universal properties.

2.1 A tour of mesomodels

Mesoscale models represent a coarse grained description of amorphous plasticity. In this context, they follow a semi-continuous approach: the material is divided into elastoplastic blocks, and the interaction between these blocks is considered. These blocks may contain several shear transformations, however, since the precise boundaries of shear transformations are still unclear, there is no exact definition of the proper discretization scale. The size of the block has to be large enough for continuum elasticity to hold, but at the same time small enough to account for the local heterogeneities of the plastic behavior related to the structure.

As sketched on Figure 2.1, mesomodels developed so far are built up of several main ingredients, and the combination of these ingredients gives the cooking details of the model. Some of the models involve thermal activation [30, 78], but in the mechanical response we are mainly concerned with athermal models. It can be readily seen, that the zoo of mesomodels has many dimensions and the complexity of this "model space" just keeps increasing over time. The extent to which the particular details of the individual models affect the outcome is a matter of debate and establishing a common framework would be crucial to properly carry out an organized, apples-to-apples comparison.

To give an impression about the various models, here we briefly review some of them. In the subsequent sections of this chapter, we discuss the main ingredients of this models clarifying what aspects are relevant to the generic phenomenology of amorphous plasticity.

It all started with the work of Bulatov and Argon [30, 29, 31] where the plane was tessellated into hexagonal elements forming a hexagonal lattice. One element corresponded to one inclusion prone to undergo an eigenstrain (plastic deformation) and hence inducing a residual stress in the rest of the material. An exact calculation was carried out to account for the stress field due to an eigenstrain and an Arrhenius-like activation mechanism was proposed to overcome the barrier between the two configurations.

To study the inhomogeneous flow in yield stress fluids, Picard et al. [137, 138, 139] developed a model based on the far field interactions of the elastoplastic blocks. Disorder was considered through the rates at which the blocks switched between an elastic and a plastic regime. It was found that at low shear rate, the flow is governed by the cooperative bursts of plastic events.

Similarly to Picard, Nicolas et al. [128, 127, 126] proposed a viscoplastic evolution to model the inhomogeneous flow of soft amorphous solids. The discretization here was performed on a square lattice, but stresses were resolved on a finer mesh. The building tiles could alter between an elastic and a plastic state and the states could be interchanged with predefined rates. The model successfully recovered the rheology of silicon oil droplets in a water-glycerin mixture in a microchannel flow, as well as the Herschel-Bulkley exponent of the flow.

Along the line of Picard et al. and Nicolas et al., Martens et al. [118, 119] showed that diffusion is related to the dynamical heterogeneities. Furthermore, they investigated the shear band formation process for a long range and a short range interaction, both

with quadrupolar anisotropy.

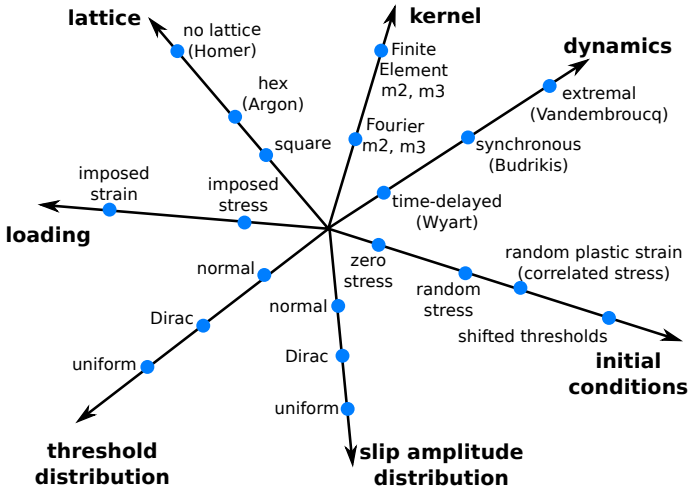

Figure 2.1 – A series of athermal mesomodels. The axis represent orthogonal ingredients, thus, theoretically any combination of these ingredients is possible. The diversity of the models and the lack of a common terminology makes comparison cumbersome. In the upcoming section we discuss which details are relevant to the phenomenology.

In another model, Homer et al. [78, 79] proposed an off-lattice discretization. In this model, the solid was discretized on an irregular triangular mesh and clusters composed of several triangles would correspond to a single shear transformation. A kinetic Monte Carlo method was used to drive the system and the spatial correlation between the activated zones was studied.

Lin et. al proposed a time-delayed activation mechanism in their mesoscopic model [107]. They worked on a square grid, and inclusions could suffer a plastic deformation with a given probability per unit time, thus fixed rate. Unstable zones could be restabilized in case the stress on the unstable site dropped before it yielded. With this model, the Herschel-Bulkley flow was recovered and the density of shear transformation was investigated.

In all the models discussed so far, the disorder from the amorphous structure is represented by disorder in the dynamics. Along another line of mesomodels however, quench disorder is considered, i.e. plasticity is related to threshold instead of rates. Baret et al. [16] proposed a finite difference discretization and, taken from depinning studies, an extremal dynamics for the onset of a plastic event was considered. This method was later on refined [171, 190] where an analytic expression of the kernel was used, for plane loading conditions. A similar approach was used by Budrikis and Zapperi [28], but with strain controlled quasistatic load. In what follows, our methods resemble the most to these latter approaches.

The main idea behind mesomodels is to capture the essential phenomenology of amorphous plasticity. In this view, they are similar to the Ising model used as a model system

for magnetic materials. As of today however, the consensus behind mesomodels are more fragmented: many different methods and implementations are available. In order that they can indeed serve as the Ising model of amorphous plasticity, it has to be clarified first which details of these models are important and which are not to the phenomenology.

2.2 Ingredients

There have been many different attempts to build coarse grained models based on interacting shear transformations. There are however several common concepts these models share. The key ingredients behind any mesomodel are the elastic interactions between individual rearrangements and the disorder associated to the amorphous structure. The dynamics of the amorphous systems is then led by the competition between elasticity and disorder [147]: in the depinning analogy, elasticity tries to smoothen the manifold, while disorder roughens it by repeated pinning. The resulting stationary statistics is thus defined by the interplay between elasticity and disorder [147].

In the mesomodels developed so far, disorder can be of two flavors: it can either enter into the dynamics [130, 83, 84, 126, 107], or into the landscape [171, 16, 28, 105]. Examples of stochastic dynamics include time-delayed models [130, 107] where the yield of unstable zones does not happen instantaneously, but with a given probability per unit time. This time delay is intended to model the coupling between neighboring zones during the rearrangements. The impact of the particular choice of the stochastic dynamics on the universal properties, in particular, avalanche scaling is currently a matter of debate [130, 83] and is beyond the scope of present work. In what follows, in the models we use we are going to introduce disorder through the landscape which would correspond to a quenched disorder.

From now on, we will be only focusing on models with a disorder in the landscape. Across this chapter we therefore review the origins of this static disorder. As the effect of the particular form of the disorder on the phenomenology is not clarified, in later chapters we are testing various forms.

For completeness of the model presentation, we discuss several driving protocols, which are strongly related to the quenched disorder nature of the model. As it was revealed within separate works [171, 28, 105] and confirmed in subsequent chapters however, the use of a particular driving protocol is irrelevant to the universal properties.

On the other hand, the use of the particular elastic interaction can have a dramatic impact on the phenomenology. This issue is going to be addressed in the next chapter, here however we provide a brief overview on the origin of the elastic kernel used in lattice models to capture the elastic interactions.

2.2.1 Threshold dynamics

The onset of plastic events can be understood via a deformation in the potential energy landscape of the amorphous solid [114], as shown schematically on Figure 2.2. Initially, the system is in a stable equilibrium position, i.e. in an energy minimum. External

loading stress however remodels the potential energy landscape. If the loading is small, the solid experiences reversible, elastic deformations. At this stage the depth of the energy minimum changes, but during the process, the minimum remains a minimum. As the loading increases however, the minimum eventually transforms into a saddle. At this point the system is no longer in a stable position, thus irreversible deformations take place in order to reach a new stable configuration. Plastic deformations thus happen at a threshold value of the loading.

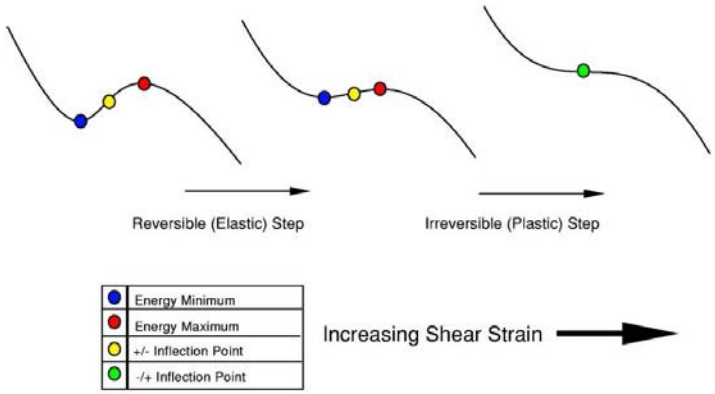

Figure 2.2 – Schematics of an irreversible deformation in amorphous solids. The increasing loading transforms the energy minimum into a saddle. The system is then destabilized and explores a new energy minimum. Figure from [114]

All of the mesomodels use some sort of threshold criterion for the onset of a plastic event. If the stress in a region exceeds a certain threshold value, the zone yields. Here we show that such a criterion is in fact the direct consequence of the multistability of the rearranging zones, that is the possibility of multiple stable equilibrium configurations subject to the same macroscopic conditions. We separate the effects of elasticity and disorder and we argue here that the threshold dynamics is a direct outcome of the competition between elasticity and disorder upon coarse-graining in the direction of propagation.

Disorder leads to multistability

In this section we show the natural emergence of a threshold dynamics and the related stick-slip events from the multistability of the rearranging zones [148, 171]. In order to simplify the picture, let us consider a simple one dimensional problem as an example, early developed in the close context of solid friction [175, 34, 18] and rate independent plasticity [142, 141], namely the motion of a single point in a random potential. The point is connected to an elastic spring and we control the position of the loading end of the spring. Let us denote by x the position of the point and by y the position of the loading end of the spring. Let us further denote by $V(x)$ the random potential, defined

by its correlation, $\langle V'(x)V'(x')\rangle \propto f[(x-x')/b]$ where $f(u) \to 0$ if $|u| \gg 1$, meaning that the potential is correlated up to a distance b.

The total potential energy of the point reads:

$$W(x,y) = \frac{1}{2}k(x-y)^2 + V(x) \tag{2.1}$$

where k is the spring constant. For the point, we consider an overdamped equation of motion:

$$\frac{\partial x}{\partial t} = -\frac{\partial}{\partial x}\left[\frac{1}{2}k(x-y)^2\right] - V'(x) = -\frac{\partial}{\partial x}W(x,y) \tag{2.2}$$

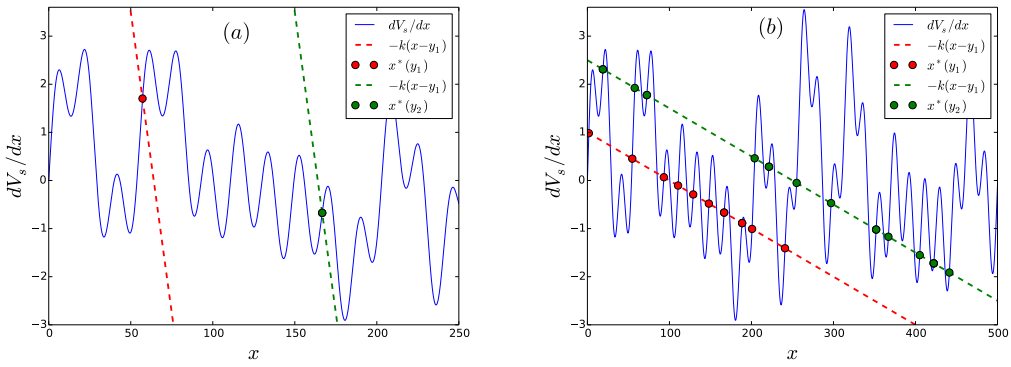

Figure 2.3 – Movement of a point in a random potential. Dots indicate the stable positions. (a) If the driving spring is stiff enough compared to the potential landscape's wells, the dynamics is smooth. This is weak pinning. (b) If the potential traps are deep and narrow enough compared to the spring stiffness, the dynamics is governed by slips between stable positions. As the loading end of the spring y increases, the point eventually reaches instability and jumps to the next stable configuration. This is strong pinning.

Such a system exhibits multistability when disorder overcomes elasticity. Figure 2.3 presents the graphical solution of the equilibrium equation $\partial_t x = 0$. Equilibrium positions for a fixed position y_i of the loading end of the spring are given by the intersections $V'(x) = -k(y - y_i)$. Among these equilibrium positions the ones with $V''(x) > -k$ are stable. It is clear that if the spring is stiff enough, the intersection points follow continuously the shape of $V'(x)$ meaning that for each y^* corresponds one and only one x^* at which the point is in stable equilibrium. The dynamics is thus smooth and this is what we call weak pinning conditions [134] (Figure 2.3 (a)).

On the other hand, if the spring constant k is small with respect to the gradient of the force landscape, there are multiple stable x^* positions for a fixed y^* position of the loading, so the system exhibits multistability (Figure 2.3 (b)). The actual x^* positions that are visited depend on the history of the loading, i.e. the previous positions that have

been visited. This situation is called strong pinning [134]. In this case, as the loading increases, the motion of the point is governed by sudden jumps between subsequent stable positions.

We can thus see that the nature of the dynamics is given by the interplay between the disordered potential and elasticity. If the potential traps are deep and narrow enough compared to the spring stiffness, the system exhibits a stick-slip dynamics. Note that the very same potential could result in a smooth dynamics when loading with a stiffer spring. In strain controlled experiments the stiffness is set by the material's elastic properties, while the random landscape by its inherent disordered structure. The type of dynamics is thus entirely defined by the material properties.

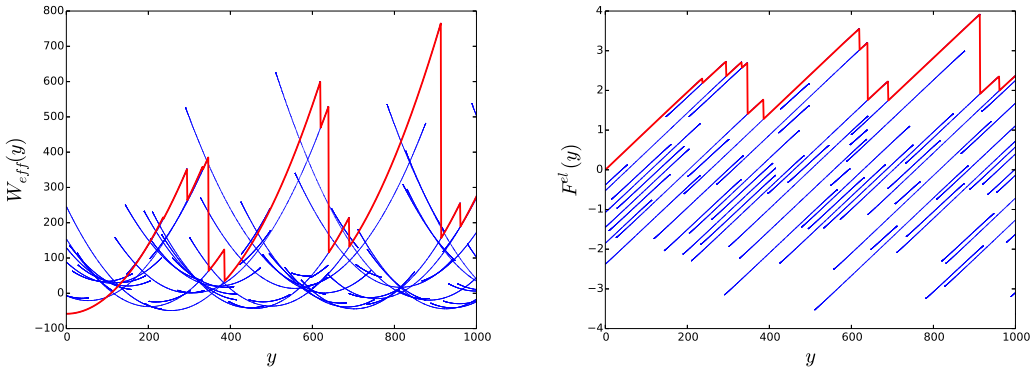

Figure 2.4 – The effective potential and elastic force in the spring for the potential represented on Figure 2.3 (b). The threshold dynamics is a direct consequence of the multistability of the point and the actual path to be followed is history dependent. Blue curves indicate the stable equilibrium positions. The red curves correspond to the positions that are actually visited. The visited positions are history dependent: another starting point would lead to different red curves.

Multistability leads to slips

Although in the strong pinning case multiple stable positions are available, one can define an effective potential $W_{eff}(y) = W[x_i^*, y]$ associated to each stable position (x_i^*, y) for fixed y. As shown on Figure 2.4, the effective potential is composed of a set of truncated parabola-like curves. Upon driving, the system jumps from one local minimum to another one as soon as the elastic force exceeds the threshold value $V'(x)$ of the local maxima of the random force. We recover thus here the phenomenology of the instability inducing local rearrangements at the atomic scale in amorphous materials [114].

We represented on Figure 2.4 such a history-dependent sample trajectory and we see that a threshold dynamics in this simple case of an isolated point is a direct consequence of the multistability of the system. In particular, when coarse-graining at scale b, the

dynamics of jumps between basins of $V'(x)$ is entirely controlled by a series of threshold forces (Figure 2.4).

The phenomenology remains unchanged when dealing with higher dimensional manifolds. In this case however, the disorder has to be compared to the internal elasticity of the manifold (rather than the stiffness of a loading spring)[134]. We see thus in this simple model system that thresholds can be thought of as the effect of the strong pinning potential. When coarse graining in the propagation direction at a scale superior to b, the depinning equation 1.6 can be rewritten as

$$\frac{\partial h}{\partial t}(\vec{r},t) = P\left(f^{ext}(t) + G * h(\vec{r},t) - f^c[\vec{r},h(\vec{r},t)]\right) \tag{2.3}$$

where the $P()$ function accounts for the positive part of its argument, that is $P(x) = x$ if $x > 0$ and $P(x) = 0$ if $x \leq 0$. f^c is the threshold force resulting from the coarse graining. In these depinning-like models thus the disorder of the landscape enters into the model through the threshold forces.

Analogously to depinning, a similar equation of motion can be written for the evolution of the plastic strain in amorphous systems:

$$\frac{\partial \epsilon_p}{\partial t}(\vec{r},t) = P(\Sigma_{load} + G * \epsilon_p(\vec{r},t) - \sigma^c[(\vec{r},\epsilon_p(\vec{r},t))]) \tag{2.4}$$

Recall that the internal stress induced by all the former plastic slips is given by the convolution $G * \epsilon_p(\vec{r},t)$ [57]. The heterogeneity of the yield stress at mesoscopic scale is represented by the quenched random variable σ^c defined by its average $\langle\sigma^c\rangle$ and correlation $\langle\sigma^c(\vec{r},\epsilon_p)\sigma^c(\vec{r}+\delta\vec{r},\epsilon_p+\delta\epsilon_p)\rangle \propto f(\delta\vec{r})g(\delta\epsilon_p)$. Above the mesoscopic scale l at which the coarse graining is performed, we consider short range correlations, that is $f(\delta\vec{r}) \to 0$ if $|\delta\vec{r}| \gg l$. Moreover, thresholds are uncorrelated in between successive events: $g(\delta\epsilon_p) \to 0$ if $\delta\epsilon_p \gg e_0$ where e_0 is the typical plastic strain associated to one elementary event.

Disordered landscape in mesomodels

One way to represent structural disorder in mesomodels is thus through thresholds. As they reflect the underlying disorder, thresholds should be considered random. As any random variable, thresholds are sensitive to their distribution and correlation. While distributed thresholds lead to the statistical hardening of the material [172] by the systematic elimination of the weak zones, constant thresholds do not allow for such a phenomenology. Transient nevertheless is an important aspect of amorphous plasticity, because in many cases materials fail before reaching a stationary plastic flow. An important question to address therefore is: how sensitive mesomodels are to the particular choice of the threshold distribution?

Another aspect of the disordered potential is its correlation along the direction of propagation, or, in the plasticity picture, the correlation over accumulating plastic strain. We have chosen to coarse grain at larger strain amplitudes, i.e. for each of our rearrangements $\delta\epsilon_p \gg e_0$. Still, the strain amplitude of each rearrangement could be random as it comes from a random landscape. The slip amplitude would then correspond to the

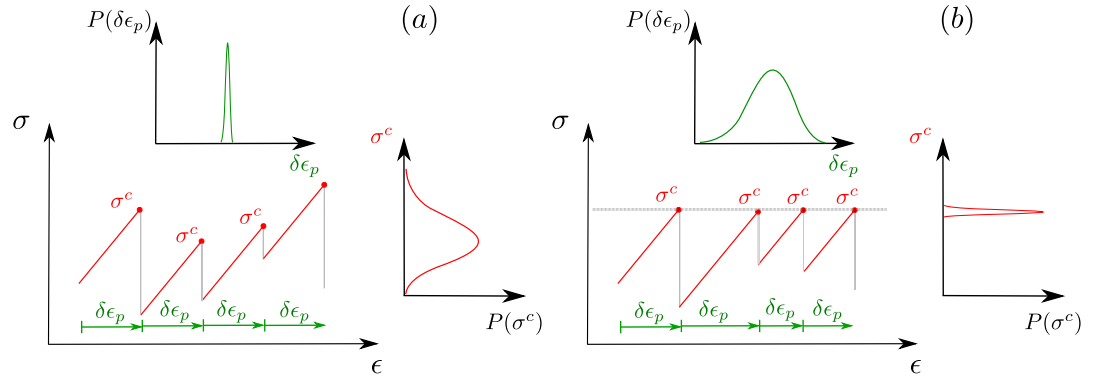

Figure 2.5 – Two extreme possibilities of disorder: (a) spatially correlated potential with distributed height, and (b) spatially uncorrelated potential with constant height. In chapter 4, these two cases are referred to as (a) $Y1$ and (b) $Y0$.

distance between the minima of the asperities on Figure 2.4 and is related to the correlation of thresholds upon plastic deformation. A priori, the actual distribution of these slip amplitudes may be of importance.

Figure 2.5 shows two possible archetypes of the random landscape. In the first one, the potential barriers fluctuate resulting in distributed σ^c thresholds, but at the same time they are highly correlated in space, resulting in a narrow distribution of the slip amplitudes $\delta\epsilon_p$. In the second one, the barriers have a narrow distribution, but they do not show spatial correlation meaning that the slip amplitude distribution is wide. To investigate the impact of the threshold and slip amplitude distribution on the scaling properties, in chapter 4 we test these two extreme cases: one with distributed thresholds and constant slip amplitudes and the other one with constant thresholds and distributed slip amplitudes, but, theoretically, any combination of the two distributions is possible. While there is still debate whether the thresholds and the slip increments are independent or correlated, in the view of a quenched underlying potential the former sets the height of the barrier and the latter the distance between barriers, which, theoretically are two independent features of the potential.

2.2.2 Loading

Similarly to experiments, there are various protocols that come into account when driving the system, but we expect universal properties to be invariant as long as quasistatic loading conditions are fulfilled. Nevertheless, different protocols are appropriate for sampling different properties. For example, avalanches are better defined in strain controlled load [28], while finite size effects may be easier to investigate with extremal dynamics [171]. In the upcoming sections we review some of the possible loading protocols, all of which are quasistatic loading applied to an athermal system. Finite strain rate [28], constant stress [106] and kinetic Monte Carlo methods [78] are available, but we are not

going to use them. Most of the mesomodels consider homogeneous elasticity, loading is then considered homogeneous throughout the system.

Note that all of the methods presented here are intended to integrate eq. 2.4.

Slip criterion

We have seen that the multistability of the rearranging zones in the disordered landscape leads to a threshold dynamics. Let us better define the conditions for a slip to take place. All the strains are measured with respect to the initial configuration. The total strain then has two parts: an elastic part $\epsilon_{el}(\vec{r})$ due to the homogeneous loading and all the previous slips, and a plastic part $\epsilon_p(\vec{r})$ due to the slips:

$$\epsilon_{tot}(\vec{r}) = \epsilon_{el}(\vec{r}) + \epsilon_p(\vec{r}) \tag{2.5}$$

The (total) stress results from the elastic strains:

$$\sigma_{tot}(\vec{r}) = 2\mu\epsilon_{el}(\vec{r}) = 2\mu[\epsilon_{tot}(\vec{r}) - \epsilon_p(\vec{r})] \tag{2.6}$$

The loading stress is then defined as:

$$\Sigma_{load} = \langle\sigma_{tot}\rangle = 2\mu\langle\epsilon_{tot}\rangle - 2\mu\langle\epsilon_p\rangle \tag{2.7}$$

In the simplified picture we are going to use, a site only can bear a pre-defined threshold stress σ^c: if the stress on the site exceeds this value, it yields. The yield criterion reads as:

$$\sigma_{tot}(\vec{r}) > \sigma^c(\vec{r}) \tag{2.8}$$

The inhomogeneous part of the stress only comes from the inhomogeneous part of the residual stresses:

$$\sigma_{tot}(\vec{r}) = \langle\sigma_{tot}\rangle + \sigma^0_{res}(\vec{r}) \tag{2.9}$$

with $\langle\sigma^0_{res}\rangle = 0$, so the local yield criterion becomes:

$$\Sigma_{load} = \langle\sigma_{tot}\rangle > \sigma^c(\vec{r}) - \sigma^0_{res}(\vec{r}) \tag{2.10}$$

The point here is that the local thresholds have to be compared to the total stress experienced by a zone. In eq. 2.4 this criterion is ensured by the $P()$ function.

Extremal dynamics: weakest pruning

Having a long history in the depinning framework [160, 13, 159, 149, 189], the extremal loading protocol assumes that only one site yields at a time and the loading stress is always tuned to the value at which the weakest site just yields, i.e. at any time,

$$\Sigma_{load} = \min_{\vec{r}} \left[\sigma^c(\vec{r}) - \sigma^0_{res}\right] \tag{2.11}$$

This would correspond to a driving with a very floppy spring with vanishing velocity and results in large fluctuations of Σ_{load}. The advantage of such a dynamics is that it produces a series of events from which various other drivings can be reconstructed. Although time is irrelevant, the order of the events matters. Due to the simplicity in the implementation, this is the kind of dynamics that we will be using the most.

Strain driven load: synchronous pruning

A more physical loading assumes that, at any time, all the sites that are unstable yield, that is if

$$\Sigma_{load} > \sigma_Y(\vec{r}) - \sigma^0_{res}(\vec{r}) \tag{2.12}$$

then the site at $\vec{r}$ yields. The loading imposes a fixed total strain that is increased in small steps until one or more events occur. Then the total strain is kept fixed until there are no more events. Slips take place simultaneously, in each round all the unstable sites are pruned up until there are no more unstable sites at that fixed strain. Then the strain is increased again by a small amount, up until the next avalanche is triggered. This driving scheme is more physical in the sense that it captures the possible simultaneity of the events. Moreover, we have a control on the driving since the strain is (externally) imposed, consequently this corresponds to a driving with an infinitely stiff spring, or, in other words, strain controlled experiment.

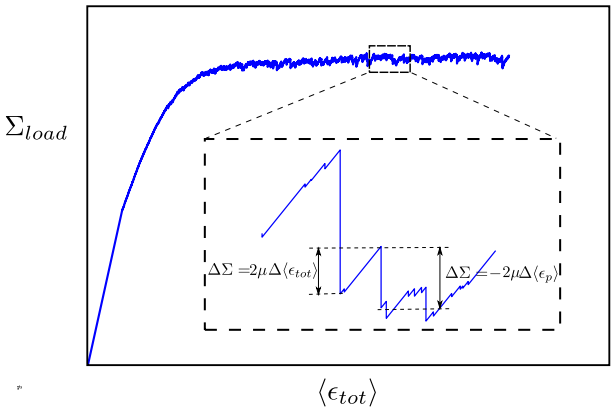

Figure 2.6 – Discharge of an avalanche. During the elastic branches, the strain is increased in small steps until one or more flips are triggered. The strain is kept fixed until the avalanche ends.

The total strain has an elastic part and a plastic part: $\epsilon_{tot} = \epsilon_{el} + \epsilon_p$, and the macroscopic stress is given by the average elastic strain: $\Sigma = 2\mu\langle\epsilon_{el}\rangle$. Recall that here we have a strain controlled driving. Avalanches are assumed to relax at a much faster rate than the typical strain rate, during avalanches therefore we have: $\Delta\langle\epsilon_{tot}\rangle = 0$. No net change in the loading strain implies $\Delta\langle\epsilon_{el}\rangle + \Delta\langle\epsilon_p\rangle = 0$.

For the "discharge" of an avalanche, $\Delta\langle\epsilon_{tot}\rangle = 0$ because $\langle\epsilon_{tot}\rangle$ is fixed (imposed), so the stress drop due to an avalanche is given by:

$$\Delta\Sigma = 2\mu\Delta\langle\epsilon_{el}\rangle = -2\mu\Delta\langle\epsilon_p\rangle \tag{2.13}$$

Similarly, for an elastic loading branch, there are no plastic events so $\Delta\langle\epsilon_p\rangle = 0$ implying $\Delta\langle\epsilon_{el}\rangle = \Delta\langle\epsilon_{tot}\rangle$ so the stress increase due to loading (straining) is:

$$\Delta\Sigma = 2\mu\Delta\langle\epsilon_{el}\rangle = 2\mu\Delta\langle\epsilon_{tot}\rangle \tag{2.14}$$

In the stationary state, when the plastic flow has set in, on average, the stress increases and stress drops have to be the same. On average therefore the total strain, plastic strain and elastic strain are equal. On the loading branches both the total and elastic strains increase, while during avalanches the elastic strain decreases and the plastic strain increases while the total strain is constant.

Quasistatic constant load

By decreasing the loading strain step, one may get arbitrarily close to quasistatic loading conditions. This strategy is however highly ineffective from the numerical point of view. With a finite strain step, each mesoscopic element has to be checked at each time step whether the stress on the given element reached its threshold. If it did, the loading strain is no longer increased until the current avalanche is over. Quasistatic loading would involve a very small strain step to avoid considerable stress overshoot when triggering an avalanche. In the meantime, on the rising elastic loading branches nothing happens, it is therefore a waste of effort to check each block's stability at each time step.

It is rather straightforward to improve the finite strain step protocol in order to get a slow, quasistatic but nevertheless computationally efficient driving. Since there are no flips along the elastic branches, they can be jumped over: instead of increasing the strain in small, predefined steps, the strain increase along each elastic branch is adjusted so that at the end of the branch only the weakest site is triggered. Then, just as previously, the strain is held constant up until the avalanche finishes. Except for the first round (when only the weakest site yields), sites flip synchronously. This loading scheme is then a mixture of extremal dynamics and constant strain load: while synchronous flips are allowed, each avalanche is triggered by the weakest site's flip. This method then allows for true quasistatic, strain controlled loading since it resolves the elastic loading branches with numerical precision, at practically zero computational cost.

The algorithm can be summarized in the following steps:

1. initialize the residual stresses σ_i and thresholds σ_i^c
2. find the weakest site, i.e. the one with the smallest barrier $\min_i[\sigma_i^c - \sigma_i]$
3. increase the total strain up until the weakest site yields
4. yield the weakest site and update the induced elastic stresses
5. check if other sites are unstable.
6. if there are no unstable sites, go to step 2.
7. if there are stable sites yield them all and go to step 5
8. repeat steps 2-7

2.2.3 Stress redistribution: shear transformations as inclusions

We have not told much yet about the way stress is redistributed upon rearrangements in mesomodels. Upon coarse graining, in mesomodels particle rearrangements are handled as material inclusions embedded into the continuous elastic bulk. These inclusions may undergo plastic deformation, but are squeezed by the surrounding elastic material, thus will wind up in a stressed state while inducing stress in the rest of the bulk as well. These inclusions are known as Eshelby inclusions and the stress field induced by them is known for various inclusion shapes [57, 20, 40, 71, 85, 178, 193, 194]. Mesomodels use such inclusions as a continuum counterpart of the shear transformations. When undergoing a plastic deformation, the stress-free reference frame of the Eshelby inclusions changes: a new shape corresponds to the zero stress state. The strain between the initial and new stress-free configurations is called the eigenstrain. Inclusions undergoing an eigenstrain induce a long-range displacement and stress field in the material, which in the far-field limit are strikingly similar to those of a shear transformation [48, 10, 174, 183] (Figure 2.7).

In particular, as shown on Figure 2.7, the elastic fields induced by such an inclusion are highly anisotropic. For instance, for an ellipsoidal inclusion at the origin, undergoing a pure plastic shear deformation with the principal axis oriented along $\pm\pi/4$, the shear stress in the far-field approximation has the form

$$G(r,\theta) \propto -\frac{\cos 4\theta}{r^2} \tag{2.15}$$

Mesomodels then have at their basis a set of interacting Eshelby inclusions via 2.15 (Figure 2.8). Most of these models use a lattice arrangement for the inclusions [30, 29, 31, 128, 127, 126, 171, 190, 16, 28] but there have been several off-lattice attempts put into practice as well [79, 77, 78].

When working on a lattice, similarly to depinning (as we deal with elastic interactions after all), the elastic Eshelby interactions can be defined by an elastic kernel $G_{ij} = G(r_i, r_j)$ which gives the stress on site j when a plastic event happened on site i. The Eshelby kernel in two dimensions decays as $1/r^2$ which makes it a long range interaction. While working with long range interactions has its pitfalls, similar $1/x^2$ interactions occur in crack front propagation or triple contact line propagation ($1+1$ depinning, i.e. line in a plane) and there are available methods to deal with them. In $2+1$ depinning ($2d$ manifold in a $3d$ space) it was found that the $1/r^2$ kernel falls in the mean field universality class. This observation led to the conclusion that, since the Eshelby kernel is long-ranged, it should exhibit mean field universality [47, 73].

The Eshelby kernel however is peculiar in its form. While it indeed decays as $1/r^2$, it is highly anisotropic. In the kernel, there are directions with positive and others with negative stress contributions. Further plastic events are likely to be triggered along the positive stress directions, sites along the negative directions are however stabilized. This anisotropy leads to the preferential localization of the plastic activity along the positive directions of the kernel. This localization, as we will see, does make a major difference. In contrast, in standard depinning with isotropic kernels, whenever a plastic

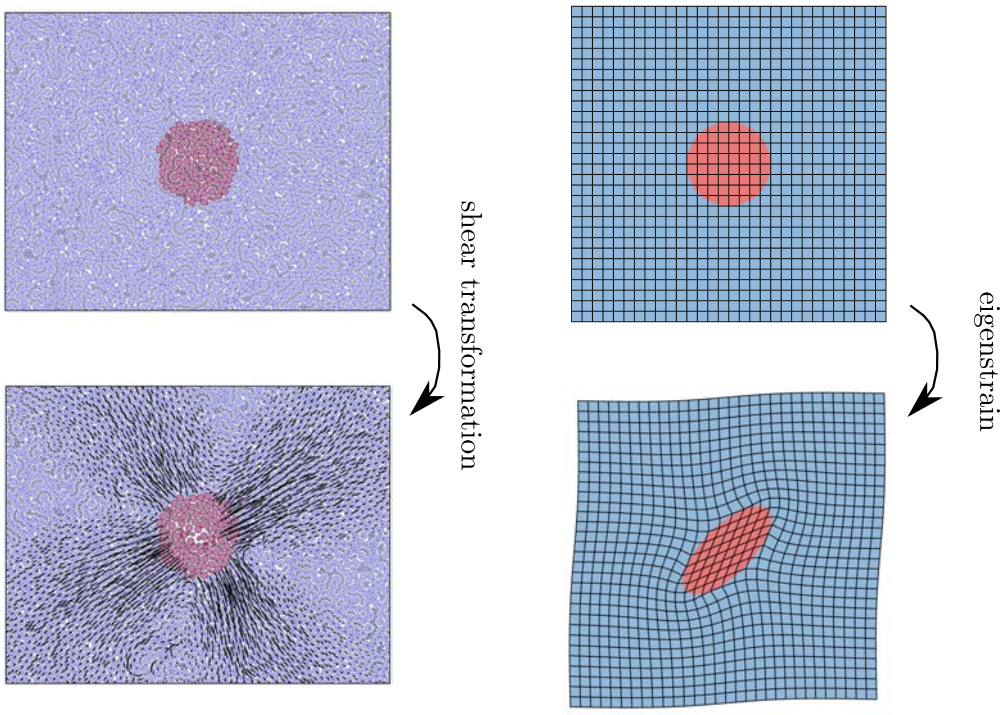

Figure 2.7 – Coarse graining. Left: a shear transformation captured in an atomistic simulation (data provided by S. Patinet). The colored region indicates the scale of coarse graining at which elastic properties are considered homogeneous. Displacements are magnified. As the sharp delimitation of a shear transformation is ambiguous, the coarse grained region may contain one or more plastic events. Note the dipolar symmetry of the displacement field. Right: an inclusion undergoing plastic deformation in a continuous, elastic bulk.

event takes place, all the sites in the system receive a positive excess stress, thus get closer to instability.

We argue thus that the anisotropic nature of the kernel does make it very different from the isotropic long range or the mean field depinning case. In the next chapter we spell out in more details the construction of this kernel, as well as its impact to the universal properties of plasticity.

2.3 Our models

With the concepts of the mesomodels here we summarize the model we are going to use in the upcoming chapters.

The models we use are scalar models, i.e. the tensorial nature of stresses and strains is

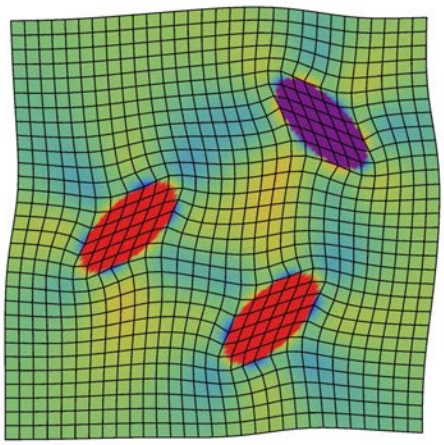

Figure 2.8 – Interacting ellipsoidal Eshelby inclusions. On the figure, the main direction of the eigenstrain is the same for each inclusion. Colors indicate the shear stress. Note the quadrupolar symmetry in this particular arrangement: the induced stress is positive along the 0 and $\pi/2$ directions, but is negative along the $\pm\pi/4$ directions. Moreover, the stress induced by an ellipsoidal inclusion undergoing a homogeneous deformation is homogeneous within the inclusion.

simplified to a scalar description. No densification is considered, the inclusions therefore experience a pure shear eigenstrain. Only the deviatoric part of both the stresses and the strains is considered. The eigenstrain of inclusions is assumed to follow the external symmetry of loading, that is, the principal direction of the inclusion eigenstrain is fixed and is the same as the principal direction of the external loading. Unless stated otherwise, plane strain conditions are considered. The external loading stress is homogeneous.

Disorder enters into the model through the landscape, as such, it is related to thresholds. If the stress on a site is larger than σ^c, it yields some amount $\delta\epsilon_p$. Both σ^c and $\delta\epsilon_p$ are drawn from a uniform distribution or one of them is fixed. Slips and the corresponding stress redistribution are considered instantaneous.

Inclusions live on the sites of a square lattice with periodic boundary conditions and the system is driven under quasistatic loading conditions, either by extremal dynamics or synchronous pruning. To comply with the lattice symmetry, two possible loading geometries are considered, both of them pure shear: the principal directions of the loading stress are either oriented along the 0 and $\pi/2$ directions of the lattice or along the $\pm\pi/4$ directions.

2.4 Conclusions

Throughout this chapter we have seen that an increasing number of mesoscopic approaches have been implemented. These mesomodels intend to model the universal be-

havior of amorphous systems. While some of the implementation details are irrelevant to the phenomenology (loading type, lattice type) other details do matter.

In particular, the key concept behind any of these models is the elastic interaction between the elastoplastic blocks and disorder resulting from the amorphous structure. In the subsequent two chapters we focus on the effect of these two ingredients. The topic of the next chapter is the impact of the elastic kernel on the universal properties of amorphous systems, focusing on fluctuations. We have shown that disorder is related to the distribution and spatial correlations of the underlying potential landscape. The effect of disorder on scaling properties will be investigated in chapter 4.

Chapter 3

Building elastic kernels: all about Eshelby

Contents

In the previous chapter we discussed the two key concepts associated to the mesoscale description of amorphous plasticity: elastic interactions and disorder. The aim of this chapter is to study the first one: we show that the usage of a particular kernel has a dramatic impact on the universal properties. Consequently, the yielding transition does

not fall into the mean field universality class. The reason for this difference lies in the inner properties of the elastic kernel that allows for localization. These properties, namely the possibility of soft deformation modes are particularly sensitive to the construction of the kernel. In this chapter thus we first review the various strategies used to build such a kernel and then test the impact of the actual kernels to the fluctuations. Fluctuations are traditionally downplayed in engineering studies and only effective properties as considered. Recall however that the yielding transition shows critical properties, including correlated, large-scale fluctuations. The importance of these fluctuations cannot be disregarded as these are the ones leading to material failure.

3.1 Building elastic kernels

3.1.1 The Eshelby inclusion

To accomplish coarse graining, shear transformations are considered as material inclusions undergoing an irreversible (plastic) deformation. In mesomodels, the shear transformations are substituted by material inclusions, thus, although the material is regarded as continuous, the interaction between the shear transformations is preserved. These inclusions are known as Eshelby inclusions [57, 20, 40, 71, 85, 178, 193, 194].

Most of the elastoplastic models developed so far use an equivalent coarse graining. In the coarse grained picture thus we end up with a number of Eshelby inclusions embedded into an elastic matrix that interact through the surrounding material (Figure 2.8). This coarse graining allows for a continuum description of elasticity, but it comes at the price that local anisotropies and inhomogeneities in the elastic constants [183] are smeared out.

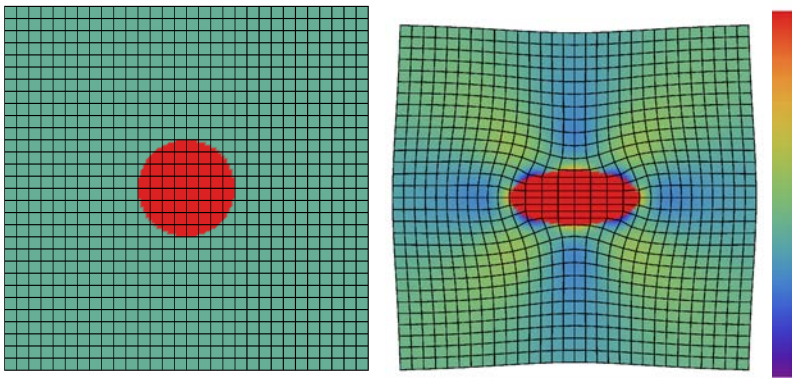

Figure 3.1 – A circular inclusion undergoing a pure shear plastic deformation. The principal axis of the plastic deformation are oriented along 0 and $\pi/2$. The color scale indicates the total strain on the right plot.

Details regarding the computation of the elastic fields induced by an Eshelby inclusion are provided in Appendix A. The most important result for us is that of the far-field shear

stress induced by the plastic deformation of a circular inclusion in two dimensions that is given by [169]:

$$\sigma_{xy} = -\frac{\mu\epsilon_0 a^2}{(1-\nu)}\frac{\cos 4\theta}{r^2} \tag{3.1}$$

where a is the radius of the inclusion, ϵ_0 is its plastic strain, μ is the shear modulus, ν is the Poisson ratio and (r, θ) are the polar coordinates. The plastic strain is considered to have only a deviatoric component and its principal directions along 0 and $\pi/2$, as shown on Figure 3.1. Note that the stress has positive and negative directions, thus it can either stabilize or trigger further plastic events. The long range character of the stress gives rise to a series of issues when it comes to discretization in periodic geometries. In molecular dynamics, these issues are addressed by the use of Lees Edwards boundary conditions [99] and Ewald summation [181], similar techniques in the continuum approach however are less developed.

3.1.2 Discretization of the Eshelby fields

We have discussed that in the coarse grained model, blocks of the material are substituted with Eshelby inclusions containing several shear transformations. The details regarding the calculation of the Eshelby elastic fields are given in the Appendix A. In this rather technical section let us discuss two delicate, but important issues, as follows:

1. How to impose periodic boundary conditions on a finite system?

2. How to discretize the solution so that it can be used as a translation invariant elastic propagator?

In order to perform numerical simulations, the elastic fields have to be discretized somehow. Moreover, in order to avoid unwanted boundary effects, periodic boundary conditions have to be imposed. Since we intend to work on a lattice, our model is particularly sensitive to discretization as various schemes may increase unphysical lattice effects. The main question of this section is thus: how to obtain a stable and physical elastic propagator on a *finite, but periodic square lattice*? The answer is not obvious given that what we have so far is the *continuous* solution of the Eshelby problem in an *infinite* system. Note that the (discretized) elastic propagator is the operator that translates the (discretized) plastic strain field into the internal stress field:

$$|\sigma_{el}\rangle = \hat{G}\,|\epsilon_p\rangle \tag{3.2}$$

In a system with periodic boundary conditions, in the coordinate representation the stress and the plastic strain are related by a simple convolution: $\sigma_{el} = G * \epsilon_p$.

There are various approaches to construct a kernel that satisfies the above conditions (i.e. periodic, discrete and stable).

Image sum

The most straightforward method to construct a periodic and continuous kernel is to sum up the contribution to the stress field of an infinite number of periodic images [169]. Then the discretization can be performed by simply evaluating the values at regularly spaced lattice points.

Such a sum however cannot be computed analytically, therefore one may try to evaluate it numerically by imposing a cutoff beyond which the contributions are neglected. It was shown [169] that a simple truncation of the sum leads to an unstable kernel.

At first it may seem that the problem with this approach is that the stress field decays as $\propto 1/r^2$ in two dimensions. Consequently, approximating the absolute value of the sum with the integral

$$\int_{r_0}^{R} \frac{1}{r^2} 2\pi r \mathrm{dr} \propto \log\left(\frac{R}{r_0}\right) \tag{3.3}$$

does not converge as $R \to \infty$ due to the long range nature of the stress.

The reason why the sum itself nevertheless converges is that there are both positive and negative terms that in turn cancel out, and this is what we call conditional convergence. Conditionally convergent sums however cannot be arbitrary truncated since the final result heavily depends on the actual terms considered up until the truncation. One of the mathematically questionable methods to evaluate the sum was to compute a closed form expression for the sum along the x direction and then only truncate the one fold sum along the y direction [28]. Whereas this seems to give a stable periodic kernel with the proper symmetry and decay, it raises questions about the short-range behavior of the kernel.

An elegant fix to a similar issue in the case of the stress field generated by dislocations in crystals is given in [33, 95]. The dislocation stress field however decreases as $\propto 1/r$, thus have linear spurious field [33, 95]. For our $\propto 1/r^2$ decrease the sum of the first derivatives is already convergent, hence the spurious field is a simple constant which, as we shall see later on is not expected to introduce major differences in the stability. We could therefore conclude that *it is not the truncation of the infinite sum that causes the instability of the kernel*, but the discretization scheme.

Consequently, we need a method that takes care about the periodic images and the discretization at the same time.

3.1.3 Fourier discretization

The method comes from Picard et al. [138] and consists of building a periodic elastic propagator which is the stress response due to a localized shear transformation.

As discussed in the Appendix B, we ultimately want to solve an elastic equation of the form

$$\hat{L}\sigma(\vec{r}) = \epsilon_p(\vec{r}) \tag{3.4}$$

where $\hat{L}$ is a local, linear differential operator, thus it is possible to derive a Green's function for it such that

$$\hat{L}G(\vec{r}) = \delta(\vec{r}) \tag{3.5}$$

and then get the solution for any $\epsilon_p(\vec{r})$:

$$\sigma(\vec{r}) = \int G(\vec{r} - \vec{r'})\epsilon_p(\vec{r'})\mathrm{d}\vec{r'} \tag{3.6}$$

This is true for any linear $\hat{L}$. Since we consider homogeneous elasticity and periodic boundary conditions, in this particular case of an Eshelby inclusion, $\hat{L}$ happens to be translation invariant, which makes it solvable by Fourier methods. We show in Appendix B that its eigenvectors are the Fourier modes, thus it becomes diagonal in that eigenbasis. Whether these Fourier modes are the Fourier transform or the Fourier series, depends on the boundary conditions. With free boundaries, i.e. in the case of a system with infinite size, one has access to the Fourier transform of G (denoted by $\widetilde{G}^{\infty}(\vec{k})$), while in case of a finite system with size L and periodic boundary conditions, one has access to the Fourier series coefficients of G (denoted by $\widetilde{G}^{L}_{pq}$). This is because if $\hat{L}$ is defined with free boundaries, its eigenmodes are the continuous Fourier modes, while if $\hat{L}$ is defined with periodic boundaries, its eigenmodes are the discrete Fourier series. The important remark here is that these two actually have the very same functional form in terms of $\vec{k}$ meaning that:

$$\widetilde{G}^{\infty}(k_x, k_y) = \widetilde{G}^{L}_{pq} \equiv \widetilde{G}(k_x, k_y) \tag{3.7}$$

with $k_x = 2\pi p/L$ and $k_y = 2\pi q/L$. We can then reconstruct both the infinite and the periodic solutions:

$$G^{\infty}(x, y) = \int_{-\infty}^{\infty} \widetilde{G}(k_x, k_y) \exp[i(k_x x + k_y y)] dk_x dk_y \tag{3.8}$$

$$G^{L}(x, y) = \sum_{p,q=-\infty}^{\infty} \widetilde{G}(2\pi p/L, 2\pi q/L) \exp\left[\frac{2\pi i}{L}(xp + yq)\right] \tag{3.9}$$

When working on a lattice, i.e. we are interested in the values of $G^L(x, y)$ on the discrete set of lattice positions $\{x_{ij}, y_{ij}\}$, the Fourier series can be approximated by the Discrete Fourier Transform which we perform numerically. Note however, that this induces a truncation at large wave number, i.e. short distances.

Note that $G^L(x, y)$ gives the stress generated by an infinitely small inclusion, consequently it contains only the far-field component of an inclusion of finite size. For a finite size inclusion with constant plastic strain e_0 within a region Ω, and 0 outside of Ω, the stress is given by:

$$\sigma^L(\vec{r}) = e_0 \int_{\Omega} G^L(\vec{r} - \vec{r'})\mathrm{d}\vec{r'} \tag{3.10}$$

but with this method we will only be dealing with localized events, thus $\sigma^L = G^L$. The computation of $\tilde{G}$ is spelled out in the Appendix A.

In order to give an idea about the quality of the Fourier method, we recall the one dimensional case of a $1/x^2$ decaying kernel. For such a kernel, we know the exact result of the infinite image summation [173]:

$$\sum_{n=-\infty}^{\infty} \frac{1}{(x-nL)^2} = \frac{\pi^2/L^2}{\sin^2(\pi x/L)} \tag{3.11}$$

We have then for the periodic kernel: $G^L_{exact}(x) \propto 1/\sin^2(\pi x/L)$. Similarly, we have for the Fourier transform of $1/x^2$: $\tilde{G}^L_{FT}(k_x) \propto |k_x|$. Figure 3.2 shows a comparison between the two kernels both in the real and the Fourier space. The Fourier discretized kernel shows the proper $1/x^2$ decay at short distances, as well as the roundoff at the box size. The truncation of the high frequency terms in the inverse transform (spectral leakage) however does not allow to resolve the break in the function at the box size in the Fourier space. In the real space, the Fourier kernel thus encounters some unphysical, high frequency oscillations. These oscillations however do not affect the $1/x^2$ decay of the kernel.

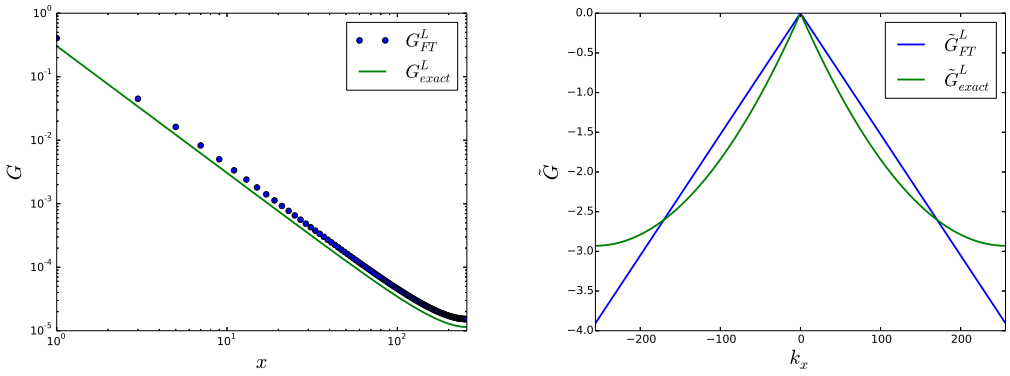

Figure 3.2 – Comparison of the one dimensional exact image sum and Fourier kernels in the real space (left) and the Fourier space (right).

In summary, the main recipe given by this method is: compute the infinite propagator, discretize it in the Fourier space and compute the finite propagator by an inverse discrete Fourier transform. We thus accomplished both discretization and periodic boundary conditions in one step. While this method works in the discretization of the far field component of the Eshelby stress field, it fails to produce a reasonably discretized displacement field because of the sign jump of the components of the displacement field at the edges of the system. In what follows, the kernel discretized with the Fourier method is referred to as the "Fourier quadrupolar" kernel or simply as the "quadrupolar" kernel.

3.1.4 A finite element method

The kernel construction can be refined using finite element methods. This way we gain an easy access to the displacement field, moreover we fully satisfy force balance and compatibility due to the realistic near field. Probably the most intuitive method to discretize the Eshelby inclusions on a square lattice is to discretize the material first and solve the elasticity equations in this discretized picture right away with periodic boundary conditions. A similar approach was used by Nicolas [125] and Homer et al.[77]. In the latter, the two dimensional material was discretized on a triangular mesh with a mesh size smaller than the typical size of an Eshelby inclusion, thus the elastic fields of inclusions of any shape and eigenstrain could be computed. The drawback of such an approach is that the elastic equations have to be solved numerically on the mesh each time a plastic deformation happens. Here we introduce a simpler method that involves the

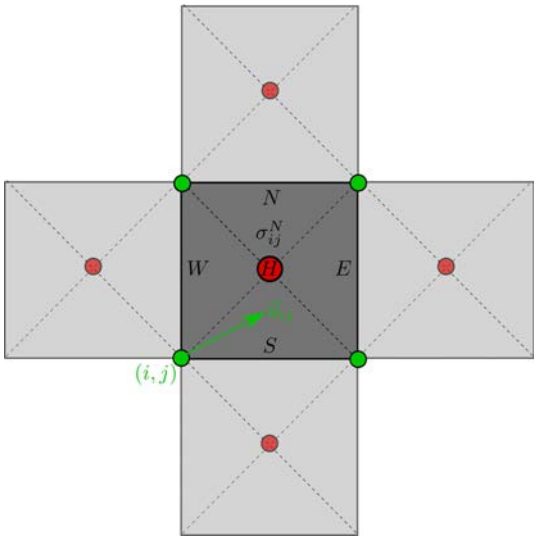

Figure 3.3 – Finite element discretization scheme. Displacements are resolved on the rectangular grid (green nodes), an auxiliary (red) node however has to be added for the stresses in order to avoid floppy checkerboard-like deformation patterns. Stresses are then resolved on each sub-triangle and the average is taken for the plaquette.

computation of the elastic kernel once and for all. In this view, the plane is tiled up with square tiles ("plaquettes") and each tile represents an Eshelby inclusion. Displacements are defined on the corners of the plaquettes ("nodes"), whereas stresses and strains are defined on the plaquettes (Figure 3.3). In order to avoid trivial floppy modes (also termed as "checkerboard instability" in [125]), each plaquette is further divided into 4 triangles, as shown on the figure. These modes result from the linearization of elasticity. Linear elasticity does not penalize deformation modes in which two opposite nodes of the tiles have equal displacements, and the other two opposite nodes have the same magnitude, but reverse displacements. Such modes in linear elasticity can develop at no energy cost

and result in a "checkerboard"-like pattern in the displacement field components. The division of tiles into subtriangles is intended to solve this anomaly.

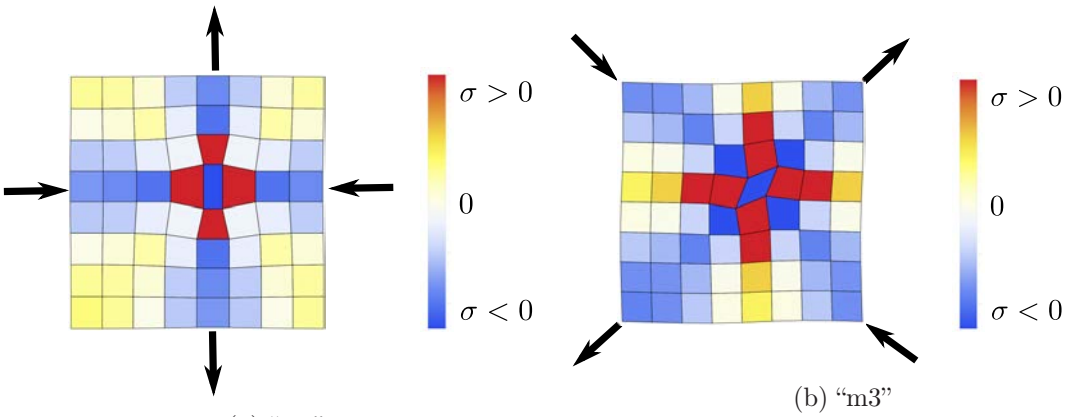

(a) "m2" (b) "m3"

Figure 3.4 – Finite element kernels corresponding to two different loading geometries. "Mode 2" corresponds to a loading direction for which the stress is positive along the $\pm\pi/4$ directions, while "Mode 3" has positive stresses along 0 and $\pi/2$. Both kernels describe plane shear. Colors indicate the stresses on the plaquettes and nodes are represented in the deformed reference frame. Arrows indicate the direction of the external load. The two finite element kernels will be referred to as "m2" and "m3".

The displacement of the middle node H is computed as the average displacement of the 4 nodes. Each triangle has thus a different strain that is defined by the displacements on the corners of the triangles. The stress and strain on a plaquette is then defined as the average strain over the 4 triangles. Such a subdivision allows for the elimination of the unphysical floppy modes. The elasticity equations can be written for the discretized displacement field and be solved analytically, imposing periodic boundary conditions. Detailed calculations are presented in the Appendix D where exact expressions of displacements, stresses and strains are obtained in the discrete Fourier space.

An important result is the average stress drop due to a plastic deformation which, independently of the loading direction is $\Delta\Sigma = \tilde{\sigma}_{00} = -2\mu\langle\epsilon_p\rangle$. While in the Fourier discretization method the $\tilde{\sigma}_{00}$ term is imposed to satisfy boundary conditions, in the finite element method this comes naturally.

The expressions of the stresses depend non trivially on the Poisson ratio which is not surprising: since the tiles touch each other, near field effects become important, in contrast to a far-field approximation. Note that an unexplored question so far is whether considering realistic near field interactions in contrast to the far-field approximation changes the scaling properties or other phenomenology of amorphous plasticity. Figure 3.4 shows two kernels obtained for different loading geometries. Loading geometries are often referred to as "modes", therefore, for the two loading geometries we denote the kernels by "mode 2" and "mode 3". In order to avoid confusion with the soft deformation

modes discussed later on, we abbreviate the two finite element kernels as "m2" and "m3".

While this method produces stable kernels for both loading directions, we will see how this near field amplifies lattice effects: due to the geometrical frustration, one of the loading directions will unrealistically accumulate stress upon deformation. The main advantage of the finite element method is that it gives direct access to the displacement fields in the periodic geometry.

3.2 Are fluctuations kernel-dependent?

When talking about universality, one would expect properties called "universal" to be independent of the details of the particular model used. In this spirit, instead of the Eshelby kernel, mean field approaches were used to model amorphous systems [73, 47]. Mean field approaches very well reproduce properties as avalanche-like behavior or hardening, but it only recently started to become clear that a mean field approach is unable to capture all the generic properties, in particular those related to localization [107, 106, 172]. Here we show that the nature of the kernel and even the details of its building has important effects on the scaling of the fluctuations.

To that end, we focus on the fluctuation of the strain field and compare these fluctuations between the mean field and quadrupolar kernels.

3.2.1 Mean field depinning vs plasticity

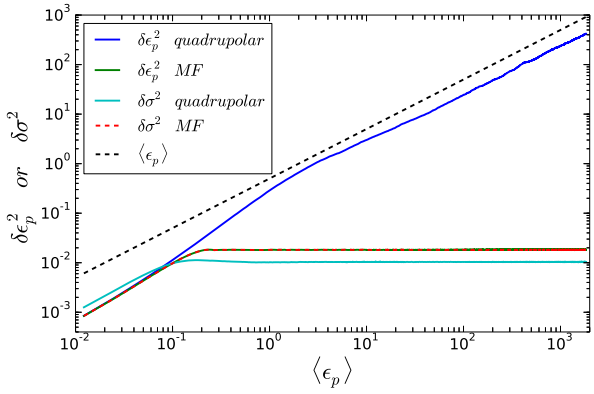

Figure 3.5 – Strain and stress variances for the mean field and the Fourier quadrupolar kernel. Straight dashed black line indicates diffusion. Stress fluctuations saturate for both the mean field and the Fourier quadrupolar kernels, as well as strain fluctuations for the mean field kernel. On the other hand, strain fluctuations converge towards a diffusive regime for the quadrupolar kernel.

Let us first follow the variance of the plastic strain $W = (\delta\epsilon_p)^2$ which would correspond to the interface width in the propagating manifold picture. In the framework of

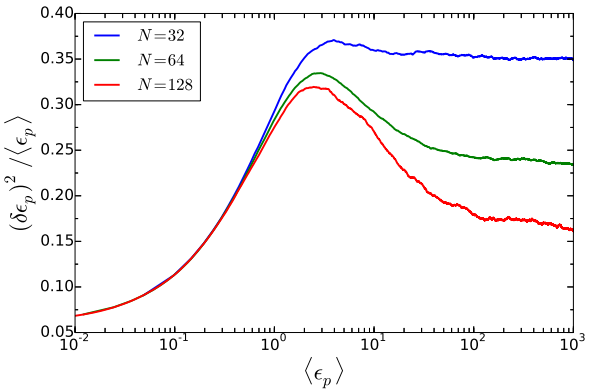

Figure 3.6 – Strain diffusivity for various system sizes for the Fourier quadrupolar kernel. A number of 1000 realizations was used for $N = 32$ and $N = 64$ and 128 realizations for $N = 128$. Fluctuations saturate for the mean field kernel but diffuse for the quadrupolar kernel showing a strong system size dependence: the larger the system, the longer the anomalous subdiffusive behavior.

extremal dynamics used here, the mean plastic strain $\langle\epsilon_p\rangle$ plays the role of a fictive time associated to the total number of iterations (plastic events), therefore it makes sense to put our results in the light of the classical Family-Vicsek scaling for interface growth [124, 173, 123]. The Family-Vicsek model predicts a power law growth of the interface width $W \propto t^{\alpha}$ up to a time scale $\tau \propto L^z$, at which the correlation length ξ has reached the system size: $\xi(\tau) \approx L$. Beyond this timescale, a saturation of the interface fluctuations is observed.

It is not surprising thus that the same Family-Vicsek scaling behavior is observed for the plastic strain fluctuations in the case of the mean field kernel (Figure 3.5).

On the other hand, for the Fourier quadrupolar kernel, although the first power law growth regime is recovered until $\xi \approx L$, the interface width shows no saturation afterwards but a diffusive trend emerges [172](Figure 3.5). Note that the term "diffusion" here simply refers to the $(\delta\epsilon_p)^2 \propto \langle\epsilon_p\rangle$ behavior and not to the actual diffusive behavior of the mean square displacements that will be discussed in a subsequent chapter. Recall that diffusion has been observed in molecular dynamics simulations as well [115, 101], it can be therefore considered as a generic property of amorphous media. On the other hand, such phenomenology is absent in depinning.

While for the quadrupolar kernel the plastic strain fluctuations do not saturate, the stress fluctuations do for both the mean field and the quadrupolar case as they should, otherwise the system would become unstable (Figure 3.5). Recalling that the elastic stress is given by the convolution $\sigma_{el} = G * \epsilon_p$, the fact that $(\delta\sigma_{el})^2$ reaches a plateau while $(\delta\epsilon_p)^2$ does not is a first sign of the presence of soft deformation modes in the kernel, i.e. modes that result in no additional stress.

The diffusivity $D_p = (\delta\epsilon_p)^2/\langle\epsilon_p\rangle$ is expected to be constant for standard diffusion.

On Figure 3.6 we see that the convergence of D_p to a constant value shows a long sub-diffusive transient that increases with the system size. Moreover, D_p shows a strong system size dependence that will be investigated more thoroughly later on.

3.2.2 Strain and displacement fluctuations in the finite element kernels

We saw the emergence of a diffusive regime for the quadrupolar Fourier kernel and we would expect the same diffusive long-time behavior for the finite element kernels. After all, they originate from the similar Eshelby inclusion problem. For the finite element kernels we have access to the displacement fields, therefore we can measure the displacement fluctuations as well. As we can see on Figure 3.7, there is no much difference between the fluctuations at low strains: both strain and displacement start out diffusively, for both of the kernels. On the other hand, the long time behavior is very different: while after an intermediate superdiffusive regime fluctuations for the m3 kernel converge to a second diffusive behavior, fluctuations in the m2 kernel saturate. Despite the fact that both kernels were meant to solve the same problem of the Eshelby inclusion (but in different geometries) and both of them have very similar symmetries, one of them reflects the same diffusive behavior as the Fourier quadrupolar kernel, while fluctuations in the other one saturate just as a mean field kernel would.

Note that although strain fluctuations in the m2 kernel indeed saturate, they do so at a much longer time than the mean field kernel. This observation reflects the extreme sensitivity on the particular discretization, and, at the same time raises the question whether the mean field kernel is sufficient to capture the physics behind amorphous plasticity? If the m2 kernel that exhibits a very similar quadrupolar symmetry to the Fourier kernel or the m3 kernel shows saturation at long times just as the mean field kernel, why would not a mean field approach work? To answer these questions, in the next section we investigate the effect of mean field on the strain fluctuations and correlations by fine-tuning between a mean field kernel and the Fourier quadrupolar kernel.

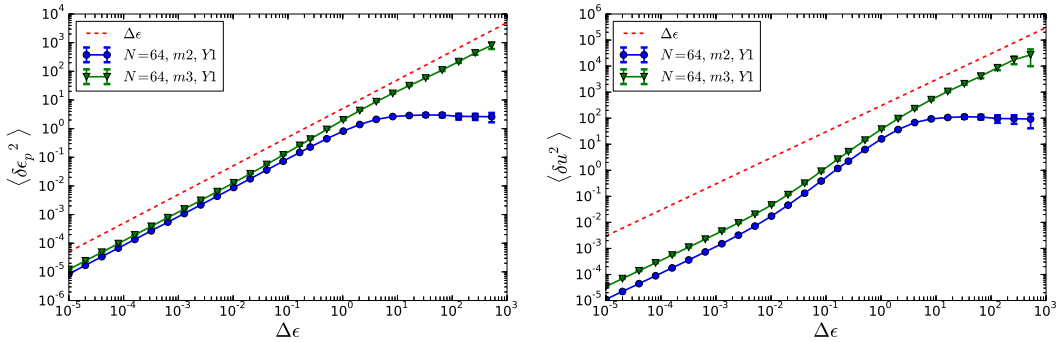

Figure 3.7 – Strain variance (left) and mean square displacement (right) for the finite element kernels. In the long term, both strain and displacement fluctuations saturate for the m2 kernel, but they converge towards a diffusive trend for m3.

3.2.3 Fluctuations of the strain field

Mean field models can reflect some of the behaviors of amorphous systems, for example, avalanche scaling or hardening. They are, however, unable to reproduce features associated to the localization. Here we explore to what extent the particular form of the Eshelby kernel affects localization and the resulting strain fluctuations by fine-tuning between a mean field and the quadrupolar Eshelby kernel. We show that for the Fourier quadrupolar kernel strain tends to accumulate along shear bands and activity is trapped in the bands for long times, but this long time localization is destroyed by the tiniest mean field contribution.

The elastic stress field induced by an Eshelby inclusion is very particular in its form. Since it decays as $1/r^2$ in two dimensions and $1/r^3$ in three dimensions and thus can be considered as long-range, it is often approximated by a simple mean-field interaction [47] disregarding its anisotropic nature. The presence of positive and negative directions in the kernel leads to a considerably different localization mechanism compared to the mean field approximation: new events favor the directions where the kernel is positive, while sites on the negative directions are restabilized.

It is therefore of interest to compare the effects of the mean field approximation on some specific properties of amorphous plasticity, in particular, strain diffusion and the localization of events. In the following, we introduce a weighted kernel which is a hybrid between the quadrupolar Fourier kernel G_Q and the mean field kernel G_{MF} defined as

$$G_a = (1-a)G_Q + aG_{MF} \tag{3.12}$$

Here a gives the weight of the mean field kernel in the weighted kernel G_a. For small a values the quadrupolar symmetry is mainly preserved in the sense that G_a remains negative in the 0 and $\pi/2$ directions. As $a \to 1$, the weighted kernel G_a tends towards a pure mean field kernel. Recall from the previous section that for $a = 0$ we had diffusive strain fluctuations and for $a = 1$ strain fluctuations saturated.

Shear-banding and mechanical history

We have seen that the structure of the elastic interaction strongly affects the evolution of the spatial fluctuations of the plastic strain field and, in particular, the existence of a diffusive regime. In order to get a better grasp on the effects of the mean field and the quadrupolar interactions, we now discuss results obtained for the weighted kernel $G_a = (1-a)G_Q + aG_{MF}$, including other values than $a = 0$ (Fourier quadrupolar) or $a = 1$ (mean field).

In Figure 3.8 we show the evolution of the strain fluctuations (or, interface width in the depinning vocabulary) for different values of the mean field weight a. It is clear that even the smallest mean field contribution breaks down diffusion at long enough times. A transient diffusive regime appears when $a \to 0^+$ and the level of the final plateau increases accordingly. The smaller a, the longer it takes to break down diffusion, but when the interface gets too distorted, the mean field restoring force will eventually stop the divergence of the strain fluctuations.

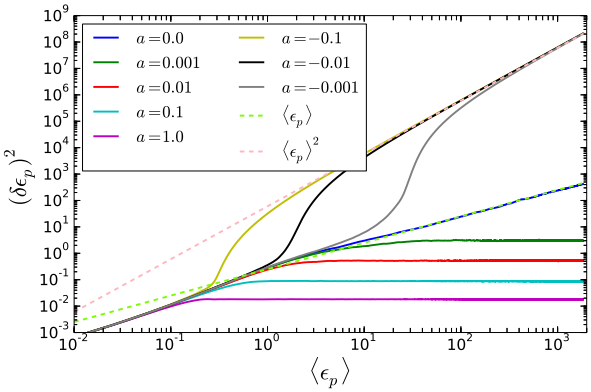

Figure 3.8 – Strain variance for various weights of the weighted kernel. For negative weights the kernel features positive eigenmodes and the dynamics becomes unstable: activity is restricted along a narrow band and strain fluctuations become ballistic. At the same time, even the smallest positive weight leads to the saturation of plastic strain fluctuations. The only situation when a diffusive trend is recovered, is for the pure quadrupolar kernel, i.e. $a = 0$.

The effect of a negative mean field contribution is exactly the opposite: even for the smallest $a \to 0^-$, after the transient, the system results in a fast diverging strain and stress variance. The divergence of the stress (as shown on Figure 3.9) indicates an unstable system. The diffusive regime thus seems to be a specific feature of the quadrupolar kernel which lives at the edge of stability and any mean field contribution tips the system either towards saturation or ballistic evolution $(\delta\epsilon_p)^2 \propto \langle\epsilon_p\rangle^2$ depending on the sign of a.

The dramatic effect of the mean field contribution can be observed in the spatial distribution of the strain field as well (Figure 3.10). For the pure plastic case ($a = 0$) one observes patterns localized along the $\pm 45°$ directions which are the positive directions of the quadrupolar kernel. The patterns are similar for a positive mean field contribution ($a = 0.01$) in that they follow the same orientations, they are however strongly attenuated compared to the pure quadrupolar case; this observation is consistent with the previously introduced results on the saturation of the interface width. A negative mean field contribution ($a = -0.01$) however introduces an extremely strong and persistent localization behavior: as we see, the plastic activity is restrained along a single thin band.

This localization explains the ballistic behavior of the strain variance observed for $a > 0$ as follows. If we assume that the plastic activity is restrained along a single band, and the mean plastic strain experienced by each site on the band is ϵ_0, then the mean squared strain is given by

$$\langle\epsilon_p^2\rangle = \frac{N \times \epsilon_0^2 + 0 \times (N^2 - N)}{N^2} = \frac{1}{N}\epsilon_0^2 \tag{3.13}$$

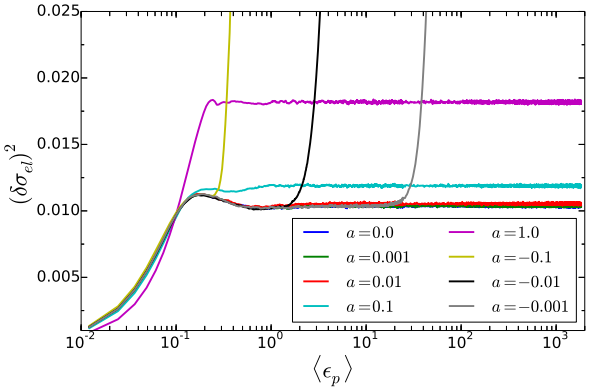

Figure 3.9 – Stress variance for various weights of the mean field kernel. Stress fluctuations saturate even for mean field, however they quickly diverge for any $a > 0$, showing instability.

On the other hand, the mean plastic strain is computed as

$$\langle\epsilon_p\rangle = \frac{N \times \epsilon_0 + (N^2 - N) \times 0}{N^2} = \frac{1}{N}\epsilon_0 \tag{3.14}$$

The plastic strain variance can thus be computed as

$$(\delta\epsilon_p)^2 = \langle\epsilon_p^2\rangle - \langle\epsilon_p\rangle^2 = \epsilon_0^2\left(1 - \frac{1}{N^2}\right) \approx \epsilon_0^2 = N^2\langle\epsilon_p\rangle^2 \tag{3.15}$$

thus we can conclude that the ballistic scaling is a direct consequence of localization.

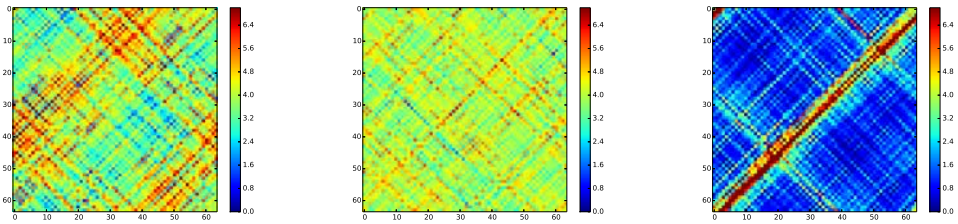

Figure 3.10 – Strain maps for various weights of the mean field kernel at $\langle\epsilon_p\rangle = 4$. From left to right: $a = 0.0$, $a = 0.01$, $a = -0.01$. A positive mean field contribution tends to smear out shear bands, while even the slightest negative contribution leads to persistent localization.

Localization of the strain along bands is called shear banding and it can be regarded as an ergodicity breakdown [179]: plastic deformation only visits a small part of the

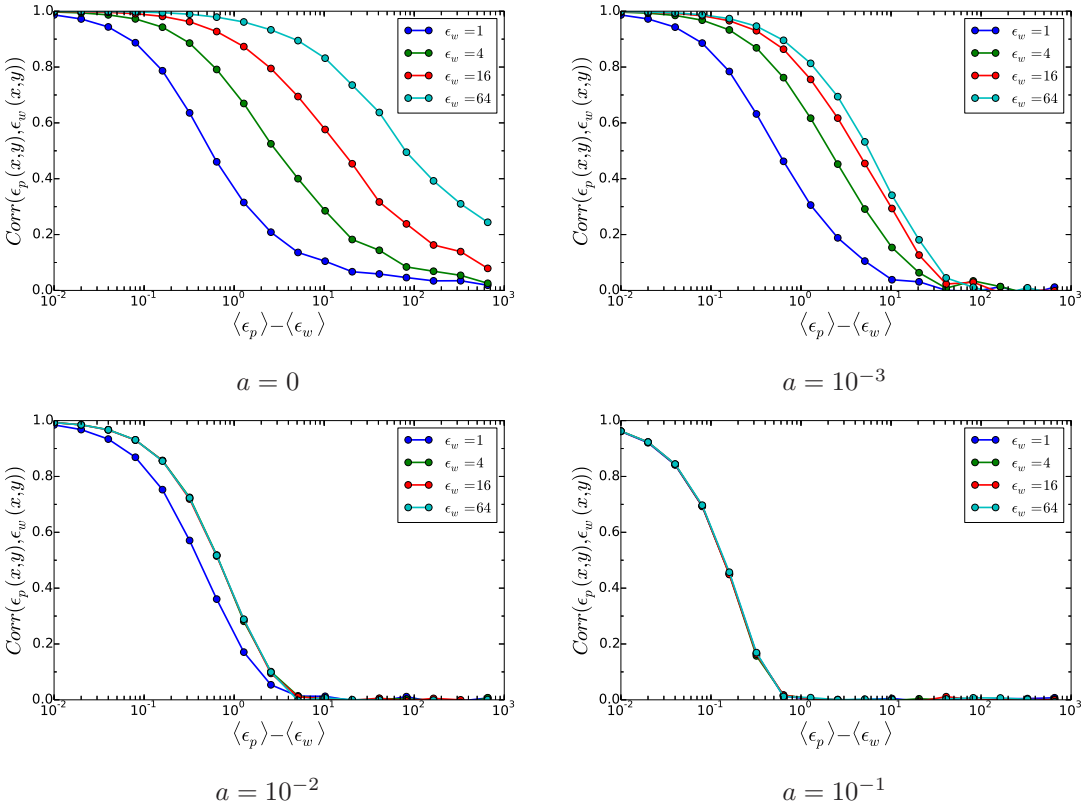

Figure 3.11 – Two point correlations of the plastic strain for various weights of the mean field kernel. The decorrelation time increases with the waiting time for $a = 0$, but eventually converges for any $a > 0$, the larger the weight, the faster.

available phase space. The phase space here is N^2 dimensional and each dimension represents the plastic strain on a given site. If the strain is localized along one band, only an N-dimensional subspace embedded into the N^2 dimensional phase space is visited.

For the bare plastic kernel ($a = 0$) the plastic activity is spread along the whole system, however it is preferentially oriented along the positive directions of the kernel suggesting that activity is trapped within these bands for a considerable amount of time. In fact, one can observe a striking mechanical history effect: the larger the waiting time, the more time the system spends trapped within the restricted subspace defined by a number of shear bands. In Figure 3.11 we plotted the time autocorrelation function of the plastic strain field for increasing waiting times ϵ_w, in the stationary regime. In steady state, one would expect statistical properties to be time independent. In particular, the time necessary to "forget" a given state should be independent of the waiting time in the steady state. In depinning for example, one observes an increase of the decorrelation time, but only in the roughness growing Family-Vicsek scaling regime [80]. As the interface width saturates and the system reaches the steady state, the decorrelation time is

independent of the system's history.

For the quadrupolar kernel however ($a = 0$), we observe a striking mechanical history effect: the decorrelation time increases with the waiting time, although the system is in the steady state. The effect disappears as a positive mean field contribution is added to the kernel ($a > 0$). We have seen that a small mean field contribution leads to the eventual saturation of the interface width. For the quadrupolar kernel, saturation is postponed at infinity, allowing to the above discussed mechanical history effect.

3.3 Soft modes control fluctuations

We have seen that the Fourier quadrupolar kernel leads to a qualitatively different behavior than the mean field kernel. Furthermore, the m2 finite element kernel shows mean field-like saturation of the fluctuations at long times while the m3 kernel reproduces diffusion, in agreement with the Fourier quadrupolar kernel. Moreover, we have seen that the slightest mean field contribution into the kernel leads to the saturation of strain fluctuations. We could therefore conclude, that the inner structure of the kernel has a considerable impact on the properties the system exhibits. Let us therefore take a closer look to the details of the kernel.

In the following, we conduct an analysis based on the eigenvalues and eigenvectors of the elastic kernel showing how these properties affect the localization, in particular, the formation of shear bands. Moreover, we show that shear bands are soft modes of the kernel.

3.3.1 Eigenvalues and eigenmodes of the elastic kernel

Significance of the eigenvalues

The elastic energy of the system corresponding to a particular distribution of plastic strain $|\epsilon_p\rangle$ can be written as

$$E = \frac{1}{4\mu} \langle \sigma | \sigma \rangle \tag{3.16}$$

where $|\sigma\rangle = \hat{G} |\epsilon_p\rangle$ is the elastic stress induced by the plastic strain field. The strain field can be written in the eigenbasis $|e_i\rangle$ of $\hat{G}$ as

$$|\epsilon_p\rangle = \sum_i \langle e_i | \epsilon_p \rangle |e_i\rangle \tag{3.17}$$

Denoting by λ_i the eigenvalue of $\hat{G}$ associated to the eigenvector $|e_i\rangle$ we obtain for the energy:

$$E = \frac{1}{4\mu} \sum_i |\langle e_i | \epsilon_p \rangle|^2 \lambda_i^2 \tag{3.18}$$

meaning that the energy of the i^{th} eigenstate is given by the square of its eigenvalue: $E_i = \lambda_i^2 / 4\mu$. We see thus that the eigenvalues are related to the elastic energy: for the same configuration, a larger eigenvalue means larger energy.

Since $\hat{G}$ is translation invariant, its eigenvalues are given by its Fourier representation (see Appendix B):

$$\lambda_{pq} = \tilde{G}_{pq} \tag{3.19}$$

and its eigenmodes corresponding to the eigenvalue λ_{pq} are plane waves:

$$e_{pq} = \exp\left[-2\pi i \frac{mp + nq}{N}\right] \tag{3.20}$$

meaning that

$$G * e_{pq} = \lambda_{pq} e_{pq} \tag{3.21}$$

This observation immediately enlightens the usefulness of the Fourier discretization scheme since this method gives access to the eigenvalues of the Green's function right away.

Soft modes

In the previous section we have shown that the eigenvalues of the elastic kernel are given by its Fourier representation. For the Fourier quadrupolar kernel, we have access to these eigenvalues right from construction [169]:

$$\lambda_{pq} = \tilde{G}_Q^{pq} = -A(\cos 4\theta_{pq} + 1) = -2A\left[\frac{p^2 - q^2}{p^2 + q^2}\right]^2 \tag{3.22}$$

where θ_{pq} is the polar angle of the (p, q) wavevector in the Fourier space. A is a constant chosen such that the Green's function is normalized, that is $G_{00} = -1$.

Similarly, for the mean field propagator

$$G_{MF}^{mn} = -\delta_m \delta_n + (1 - \delta_m \delta_n)\frac{1}{N^2 - 1} \tag{3.23}$$

we have

$$\lambda_{pq} = \tilde{G}_{MF}^{pq} = -\frac{N^2}{N^2 - 1}(1 - \delta_p \delta_q) \tag{3.24}$$

In both cases, we recognize the translation mode $e_{00} = 1$ of zero eigenvalue $\lambda_{00} = 0$. In the usual depinning case with mean field, laplacian or isotropic kernels this is the only mode characterized by a zero eigenvalue and it reflects the fact that the energy of the interface is a result of the distortion (i.e. variation) of the interface; a constant shift of the interface along the propagation direction should not result in any excess energy.

For the quadrupolar kernel however, we encounter a set of non-trivial eigenmodes that are also characterized by zero eigenvalues. Namely, all the eigenmodes of the form $e_{p,p}(m, n) = \exp[-2\pi i p(m + n)/N]$ and $e_{p,-p}(m, n) = \exp[-2\pi i p(m - n)/N]$ for $p \in [-N/2, N/2)$ are associated to the null eigenvalue. Out of them $2N - 2$ are independent ($e_{p,p} = e_{p,-p}$ for $p = 0$ and $e_{p,p} = -e_{p,-p}$ for $p = -N/2$), the eigenvectors of $\lambda = 0$ thus span a $2N - 2$ dimensional space. We call the modes belonging to the eigenspace

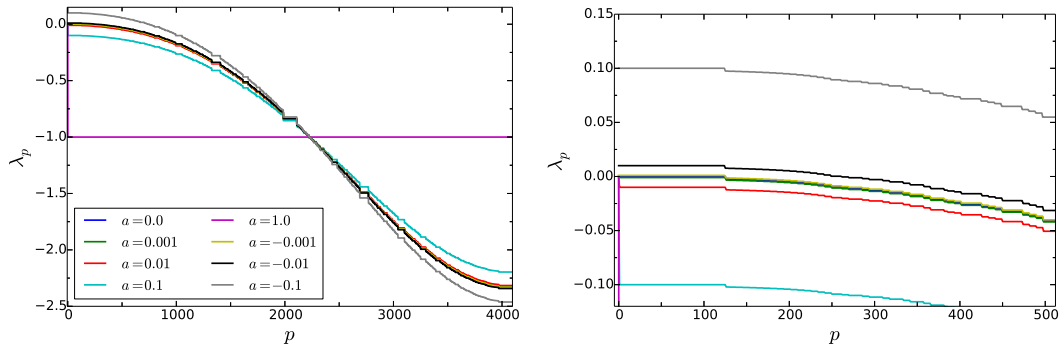

Figure 3.12 – Eigenspectra of kernels with various weights. A nonzero mean field weight opens a gap in the eigenspectrum. $a > 0$ leads to strictly negative eigenvalues, whereas $a < 0$ introduces positive eigenvalues that lead to an unstable propagator. The figure on the right is a zoom-in of the left plot around $\lambda = 0$

spanned by $\lambda = 0$ soft modes as the development of these modes happens at no energy cost.

Let us rewrite the plastic strain field in the Fourier basis:

$$|\epsilon_p\rangle = \sum_{pq} c_{pq} \, |e_{pq}\rangle \tag{3.25}$$

where

$$c_{pq} = \langle e_{pq} | \epsilon_p \rangle = \frac{1}{N^2} \tilde{\epsilon}_{p \; pq} \tag{3.26}$$

Recall that the evolution equation of the plastic strain field can be written as

$$\frac{\partial \epsilon_p(\vec{r}, t)}{\partial t} = P(\Sigma_{load} + G * \epsilon_p(\vec{r}, t) - \sigma^c[(\vec{r}, \epsilon_p(\vec{r}, t))]) \tag{3.27}$$

where the function $P(\cdot)$ accounts for the positive part of its argument. Ignoring for the moment the effect of the function $P(\cdot)$, we can project the above equation onto the Fourier basis. For the RHS we have:

$$\Sigma_{load} \; \delta_p \delta_q + \tilde{G}_{pq} \tilde{\epsilon}_{p \; pq} - \widetilde{\sigma^c}[(\vec{r}, \epsilon_p(\vec{r}, t))])_{pq} \tag{3.28}$$

Since the loading stress is homogeneous in the direct space, it becomes local in the Fourier space. The second term translates the direct space convolution into multiplication in the Fourier space. Using that $\tilde{G}_{pq} = \lambda_{pq}$ and $\tilde{\epsilon}_{p \; pq} = c_{pq}$, the evolution equation for the different modes becomes:

$$\frac{\partial c_{pq}}{\partial t} = \Sigma_{load} \; \delta_p \delta_q + \lambda_{pq} c_{pq} - \widetilde{\sigma^c}[(\vec{r}, \epsilon_p(\vec{r}, t))])_{pq} \tag{3.29}$$

This rewriting thus enables us a better understanding of the diffusive-like behavior observed at long times for the plastic strain. In real space, the spatial coupling is induced

by the non-local elastic interaction kernel, G, while the noise term is local. In the space of eigenmodes, the opposite character is observed, namely the restoring force is local, but noise is not. Since all eigenvalues are null or negative (otherwise the dynamics would be unstable) a competition emerges between the relaxation of the eigenmodes induced by the elastic contribution and a random forcing due to the quenched noise contribution. In particular, at long times, the contribution of the soft modes becomes dominant since they are not submitted to relaxation. The diffusive-like behavior thus directly emerges from a competition between the different soft modes controlled by the quenched disorder.

The strong effect of a small mean field contribution to the Fourier-discretized quadrupolar propagator can now be re-read as the consequence of the opening of a gap in the spectrum of eigenvalues, in other words to the vanishing of the soft modes. In Figure 3.12, the spectra of eigenvalues of the stress redistribution kernel show the gradual gap opening due to the introduction of a mean field contribution to the elastic quadrupolar interaction. The associated restoring elastic force brings back the model to the standard depinning phenomenology.

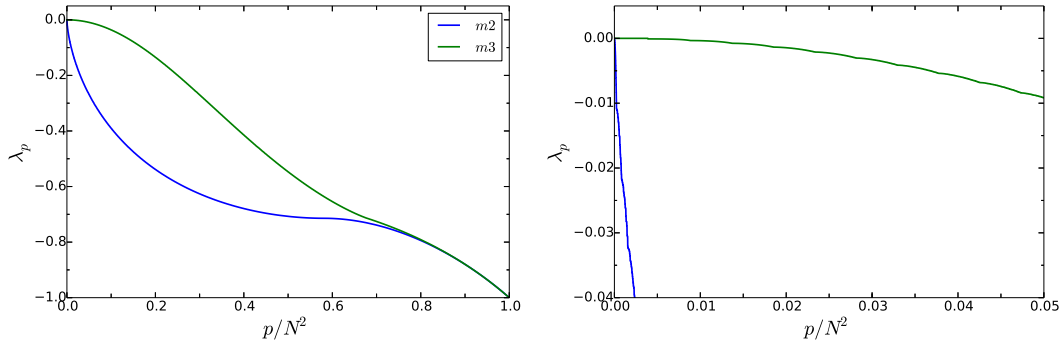

Figure 3.13 – Eigenspectra of the two finite element kernels. While m3 features soft modes, m2 does not. The right plot is a zoom-in of the left eigenspectrum around the null eigenvalue.

The situation is similar for the finite element kernels. Figure 3.13 shows the eigenspectrum of the two finite element kernels, i.e. the eigenvalues in decreasing order. For low eigenvalues the eigenspectra have a very similar form, around $\lambda = 0$ however they are considerably different. While m3 has a zero slope at $\lambda = 0$, thus features soft modes, m2 has a strictly negative slope. The difference at $\lambda = 0$ explains the striking difference in the long time behavior we observe. In this context, the negative slope in the eigenspectrum at the zero eigenvalue has the same effect as an extra mean field component: the finite restoring forces will eventually break down the increase of fluctuations.

Note that this interpretation only holds if we ignore the $P(\cdot)$ function that intervenes in eq. 3.27. When a long integration time in considered, the loading contributes to a positive average that allows for such an interpretation. However, at short time scales, the positive part function unfortunately cannot be simply expressed in Fourier space. A

similar situation appears in classical depinning models. The point is that for the latter ones, a long time integration gives a finite restoring force to any wavelength of manifold fluctuations.

From soft modes to shear bands

We have seen that soft modes control the long term diffusive fluctuations, but we have not said much about their spatial structure.

A more suitable basis can be defined for the eigenspace of $\lambda = 0$ given by the unit shear bands oriented along the $\pm 45°$ directions. Let us define $d_k(m,n) = \delta_{m-n-k}$ and $d'_k(m,n) = \delta_{m+n-k}$ with $k \in [-N/2, N/2)$ the unit shear bands. Since

$$|d_k\rangle = \sum_p \langle e_{p,p}|d_k\rangle \, |e_{p,p}\rangle \tag{3.30}$$

and

$$|d'_k\rangle = \sum_p \langle e_{p,-p}|d_k\rangle \, |e_{p,-p}\rangle \tag{3.31}$$

the shear bands d_k and d'_k belong to the eigenspace spanned by the eigenvectors of $\lambda = 0$. We can thus conclude that pure shear bands appear as soft modes of the Fourier quadrupolar elastic interaction, and, because of the null eigenvalue they do not induce any internal stress. As a counter example, $d_v(m,n) = \delta_{m-v}$ and $d'_v(m,n) = \delta_{n-v}$, i.e. bands oriented along $0°$ and $90°$ are not part of the $\lambda = 0$ subspace, thus they are not soft modes of the Fourier quadrupolar kernel.

The expressions of the Fourier transforms of the finite element kernels is spelled out in the Appendix D and shows that "m3" features non-trivial null eigenvalues while "m2" does not. Since for these two kernels we have the displacement fields, we can visualize their displacements when subject to deformation. Figure 3.14 shows the displacements and the residual stresses for such deformations. We can see that partial shear bands result in nonzero residual stresses for both kernels, but stresses disappear for "m3" when the shear band percolates. On the other hand, a percolating shear band for "m2" still results in a considerable amount of residual stress due to the geometric frustration of the neighboring cells. The major difference observed between the long time behavior of "m2" and "m3" thus can be understood in terms of soft modes. The fact that "m2" does not feature soft modes is the consequence of the discretization, we see therefore that the discretization may have a serious impact on the long time behavior.

Soft modes thus belong to the eigenspace spanned by the eigenvectors belonging to the null eigenvalue and, as we have shown, these modes can be naturally interpreted as shear bands.

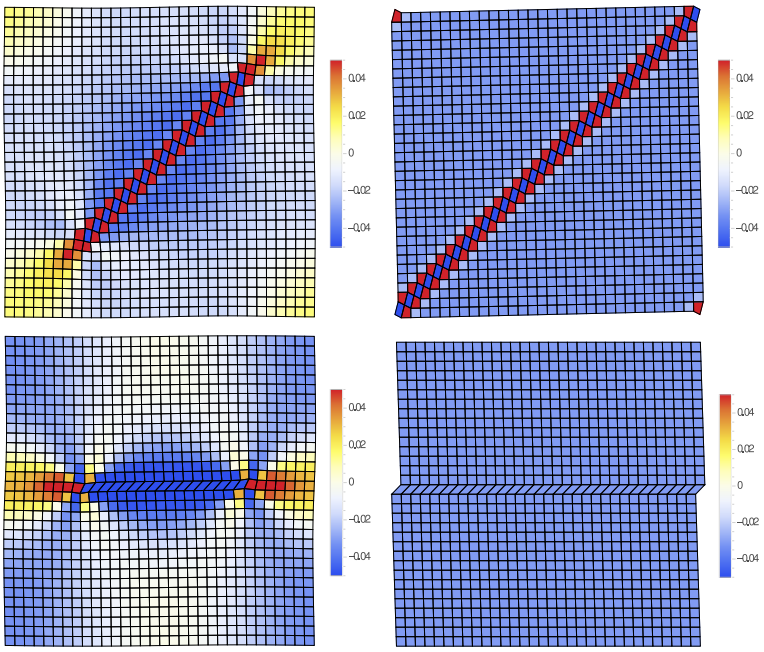

Figure 3.14 – Shear bands for the m2 and m3 finite element kernels. Tiles represent one discretization unit are represented in the deformed reference frame. Color scale indicates the stress in the respective tile. Top row: for the m2 kernel a large residual stress resulting from the geometrical frustration of neighboring tiles is observed even when the band percolates. Bottom row: shear bands are soft modes of the m3 kernel, stresses thus vanish for a homogeneous, percolating shear band.

Evolution of soft modes

To better understand the role of soft modes in the dynamics, we can use the basis of the shear bands and the remaining modes as basis:

$$|e_{pq}\rangle \text{ with } |p| = |q| \tag{3.32}$$
$$|d_k\rangle \text{ with } k \in [-N/2, N/2-1] \tag{3.33}$$
$$\left|d'_l\right\rangle \text{ with } l \in [-N/2, N/2-1] \tag{3.34}$$

The plastic strain can be written in this basis as

$$|\epsilon_p\rangle = \sum_{|p|\neq|q|} c_{pq} |e_{pq}\rangle + \sum_k c_k |d_k\rangle + \sum_k c'_k \left|d'_k\right\rangle \tag{3.35}$$

and, ignoring for the moment the effect of the $P()$ function (which would describe the long-term behavior), projecting the evolution equation 3.27 of the plastic strain field onto

the shear bands and the remaining Fourier modes gives (see Appendix C for details):

$$\partial_t c_{lm} = \lambda_{lm} c_{lm} - [\widetilde{\sigma^c}]_{lm} \text{ for } |l| \neq |m| \tag{3.36}$$

$$\partial_t c_l + 2\frac{1}{N}\sum_k \partial_t c'_k f_{kl} = \sigma^{ext} - \frac{1}{N}\sum_{\vec{r}\in d_k} \sigma^c(\vec{r}) \tag{3.37}$$

$$\partial_t c'_l + 2\frac{1}{N}\sum_k \partial_t c_k f_{kl} = \sigma^{ext} - \frac{1}{N}\sum_{\vec{r}\in d'_k} \sigma^c(\vec{r}) \tag{3.38}$$

with $f_{kl} = |k-l| \pmod 2$. The first equation captures the evolution of the non-soft modes. Since $\lambda \leq 0$, these are the modes associated to $\lambda < 0$, thus we see that all the non-soft modes get attenuated. This is what happens in classical depinning and these strictly negative eigenvalues are responsible for the saturation of the interface width, in this case the plastic strain fluctuations. We observe moreover that, while in the real space the spatial coupling is induced by the non-local elastic kernel and the noise term is local, the exact opposite happens in the Fourier space: the restoring force is local, but the noise is not. We thus observe a competition between the attenuation of the eigenmodes induced by the elastic contribution and a random forcing due to the quenched noise contribution.

The second two equations describe the evolution of soft modes. Although there is a coupling between perpendicular shear bands, these bands do not get attenuated and may survive for long times at no energy costs. The diffusion of these bands thus governs the long term dynamics of the system and leads to a continuously increasing interface width, a phenomenon that is completely absent in classical depinning.

Plane vs antiplane shear

So far our results were restricted to plane shear. Keeping the same two dimensional approach however, it is possible to change the shearing geometry to reproduce anti-plane shearing conditions as shown in Figure 3.15. The latter has been studied in Ref [16] and, from finite difference calculations it has been found that a dipolar kernel with the same $1/r^2$ decay corresponds to rearrangements associated to such a loading:

$$G_D(r,\theta) \propto \frac{\cos(2\theta)}{r^2} \tag{3.39}$$

The same kernel in the Fourier space reads as:

$$\widetilde{G_D}_{pq} = -2A\frac{q^2}{p^2+q^2} \tag{3.40}$$

hence encounters soft modes for $q = 0$ which are shear bands oriented along $\theta = 0$ (Figure 3.16). Analogously to the quadrupolar case, we can decompose the plastic strain field as

$$|\epsilon_p\rangle = \sum_{q\neq 0} c_{pq}\,|e_{pq}\rangle + \sum_k c_k\,|d_k\rangle \tag{3.41}$$

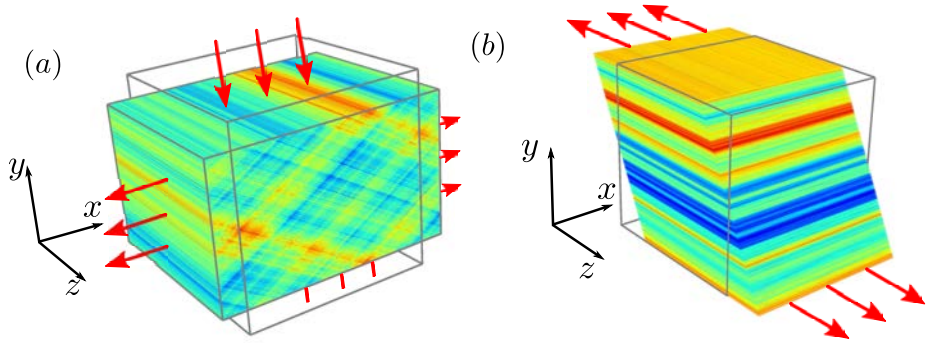

Figure 3.15 – (a) Plane and (b) anti-plane loading. Colors indicate the plastic strain. The kernel associated to plane shear has a quadrupolar symmetry, and the kernel associated to anti-plane loading has a dipolar symmetry which is reflected in the accumulated the shear bands.

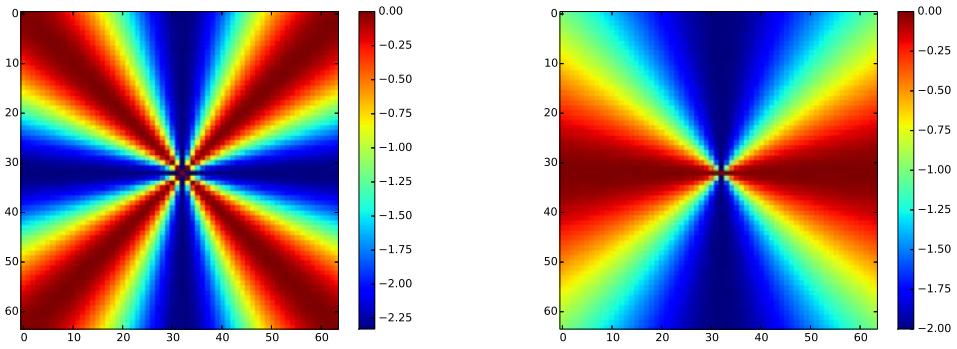

Figure 3.16 – Fourier Transform of the quadrupolar (left) and dipolar (right) kernels. The former exhibits soft modes along the $\pm\pi/4$ direction, while the latter along the 0 direction.

where d_k are the shear bands oriented along the 0° direction.

The depinning like evolution equation for the soft modes and the remaining modes associated to this dipolar kernel read as

$$\partial_t c_{lm} = \lambda_{lm} c_{lm} - [\widetilde{\sigma^c}]_{lm} \text{ for } m = 0 \tag{3.42}$$

$$\partial_t c_l = \sigma^{ext} - \frac{1}{N} \sum_{\vec{r} \in d_k} \sigma^c(\vec{r}) \tag{3.43}$$

$$\tag{3.44}$$

We thus recover the attenuation of the negative modes, and a quasi independent, diffusive

propagation of the soft modes with no elastic coupling among the bands. Some non-trivial coupling is still present through the noise term, this observation may nevertheless constitute the basis of a new approach in which, instead of the interaction between the pointlike shear transformations one considers the set of loosely coupled shear bands as elementary building blocks of an amorphous material.

Fluctuations and age statistics along shear bands

We have shown how the plastic shear bands can be regarded as soft deformation modes of the elastic interaction kernel and how the long time diffusion of the plastic strain fluctuations originates from the competition between these weakly interacting bands. The strength of the coupling defines the intra and inter shear band strain fluctuations, it is therefore straightforward to investigate the contribution of these two quantities to the overall strain fluctuations.

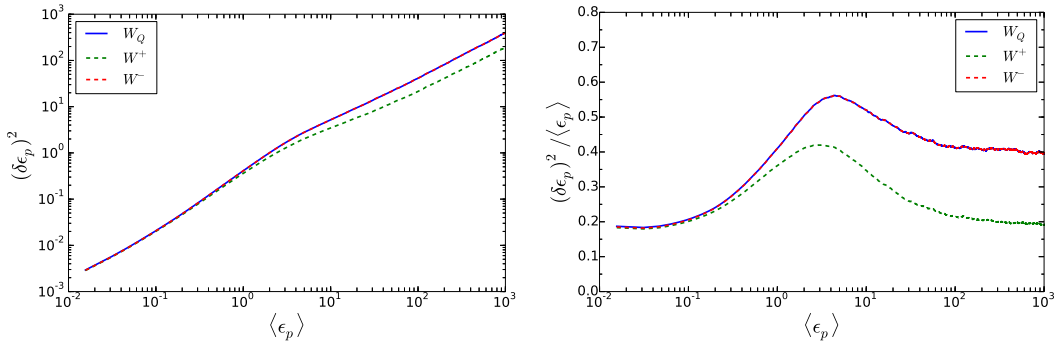

Figure 3.17 – Strain fluctuations along shear bands (W^+) and anti-shear bands (W^-) for plane shear loading. Although fluctuation within shear bands is smaller, it still shows a diffusive increase.

The mean variance of the plastic strain within a shear band is defined as

$$W^+ = \langle W_k \rangle_{\{k\}} \tag{3.45}$$

where

$$W_k = \langle \epsilon_p^2(\vec{r}) \rangle_{\vec{r}\in d_k} - \langle \epsilon_p(\vec{r}) \rangle^2_{\vec{r}\in d_k} \tag{3.46}$$

that is, W_k is the strain variance along the shear band d_k, and W^+ is the mean strain variance along all the shear bands. Recall that for the quadrupolar kernel, shear bands are oriented along the $\pm 45°$ directions. In a similar manner, we can define the strain fluctuations along the $0°$ and $90°$ directions. We have seen that these d_v and d'_v bands are not soft modes of the kernel, moreover, these are the directions which receive a negative stress kick upon a plastic slip, it is therefore of interest to track the W^- mean strain variance along these "anti-shear bands".

In a similar manner, for anti-plane loading, shear bands are oriented along the 0° directions, thus W^+ in this case measures the strain fluctuations along 0° and W^- measures the strain fluctuations along 90°.

Figure 3.17 shows that for the plane shear, the strain fluctuations along the shear bands and anti-shear bands both reach a diffusive regime, the effective diffusivity $D = (\delta\epsilon_p)^2/\langle\epsilon_p\rangle$ is about twice as small within the shear band than the global diffusivity.

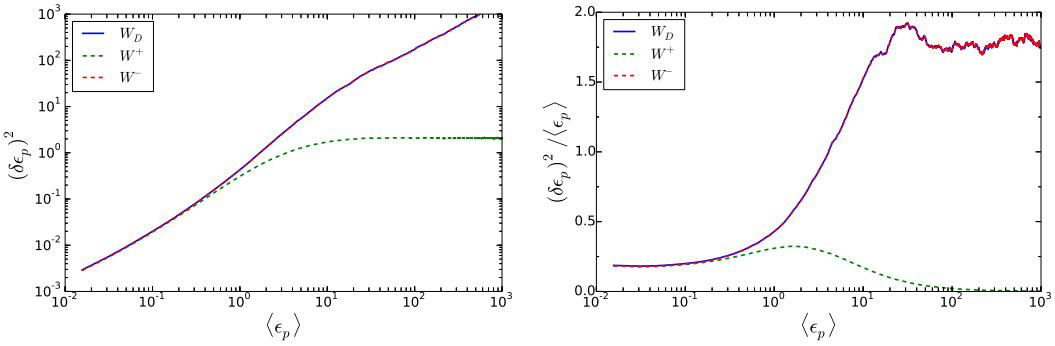

Figure 3.18 – Strain fluctuations along shear bands and anti-shear bands for anti-plane shear loading. Due to the quasi independence of the shear bands in this case, strain fluctuations saturate within the bands, thus the overall diffusive trend can be viewed as the competition between independently diffusing bands.

On the other hand, for the anti-plane loading geometry we observe saturation of the plastic strain variance W^- measured along the shear bands (Figure 3.18). Although the strain fluctuations within the anti-shear bands are almost identical to the overall strain fluctuations, similarly to depinning, the strain variance within the individual shear bands saturates. This result is compatible with our previous reasoning of the soft modes coupling: while for the quadrupolar kernel the intersecting shear bands are coupled, for the dipolar kernel we only have soft modes along a single direction making them quasi independent. This independence allows for the diffusive competition between individual shear bands while still keeping fluctuations along the individual bands low.

In order to get a better grasp on the strain activity localization mechanism, we attempt to characterize the temporal fluctuations as well. To that end, we introduce the age of a site $\epsilon_A(\vec{r})$ which is the average plastic strain $\langle\epsilon_p\rangle$ since the site last yielded. The yielding site's age is then 0 and $\epsilon_A(\vec{r}) = \langle\epsilon_p\rangle$ if the site has never yielded. In the same spirit, we can define $\epsilon_A^+(k)$ the age of shear band k and $\epsilon_A^-(v)$ the age of the anti-shear band v.

We can then follow the distribution $P(\epsilon_A)$ of these age measures. Since the distribution is wide, it is more convenient to track $P(\epsilon_A^*)$ where $\epsilon_A^* = \log(\epsilon_A)$ (Figure 3.19). For both kernels we observe that the age distribution is shifted towards larger values when measured within the shear bands, but this effect is much more pronounced for the dipolar kernel. The upper cutoff in the distributions corresponds to the duration of the

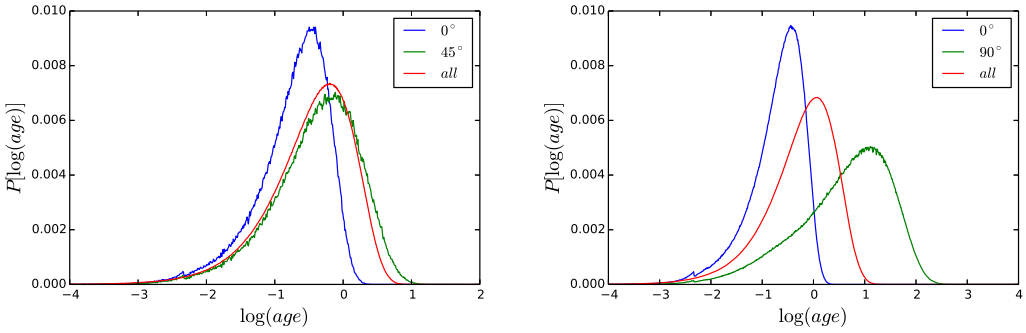

Figure 3.19 – Age distributions along shear bands and anti-shear bands. Left: quadrupolar kernel, right: dipolar kernel. Ages of anti-shear bands have a dramatic increase for the dipolar kernel showing that activity is trapped for long within shear bands. Due to the intersecting perpendicular bands in the quadrupolar kernel, activity can switch bands faster.

subdiffusive regime, indicating that the plastic activity is trapped for long times within a shear band. A potential reason for escaping aging along a shear band for the quadrupolar system stems from the coupling between perpendicular shear bands, thus an event within a shear band may trigger another one along the perpendicular direction. As the dipolar kernel lacks such a coupling, activity is trapped for much longer within the bands, hence the larger shift of the distribution in this case.

3.4 Conclusions

We have shown that the peculiar form of the Eshelby kernel associated to the atomic rearrangements in the mesomodels gives rise to the localization of the plastic activity. At short time scales, localized plastic events rule the dynamics, at longer scales however shear bands develop. The localization along shear bands takes place because these bands can form at no excess energy cost. Deformation can thus be trapped for long times along the bands giving rise to constantly increasing fluctuations. The dynamics is then governed by the loose coupling between the individual bands. It is therefore likely that, one step further from the Eshelby inclusions, amorphous plasticity can be regarded in the new framework of the interplay between disorder and the loose elastic coupling between individual shear bands.

Such a localization is not possible in classical depinning problems with mean field or isotropic interactions. While shear bands are soft modes of the Eshelby kernel, we have seen that their presence may be erroneously suppressed in the kernel by the particular discretization. Soft modes of the elastic kernel allow for strain localization and constantly increasing strain fluctuations which ultimately leads to crack nucleation and material failure. Controlling shear band formation is therefore the first step in suppressing crack

nucleation and reinforcing fragile amorphous materials.

Chapter 4

Scaling properties and finite size effects

Contents

The mesoscale description of amorphous plasticity results from the interplay of elasticity and disorder. In the previous chapter we have played with the elastic interaction and put in evidence the importance of soft modes and we concluded that they have a dramatic effect on strain localization, plastic strain fluctuation and their presence may even affect the universality class in the depinning picture. Here, besides the kernel, we

explore the impact of the disorder on the scaling properties. We focus on the avalanche rate distribution and displacement fluctuations and relate the results to former athermal quasistatic molecular dynamics studies, with special attention to finite size effects.

As the ultimate goal of mesomodels would be to provide a quantitative upscaling, quantitative connection to molecular dynamics is indispensable in the long run. The extent to which the details of the various mesomodels matter is yet unclear and the first step towards the elucidation of the question is to test the way the model details affect universal properties. If the universal properties seen in experiments or molecular dynamics simulations are not reflected in the mesomodels, there is no way they could give quantitative results on non-universal properties, hence mesomodels cannot serve as the Ising model of amorphous plasticity until the effect of various details is well understood.

In this chapter thus we emphasize the impact of disorder on fluctuations and scaling properties. We consider two extreme cases of the disordered landscape: distributed height but fixed width or distributed width but fixed height of the potential barriers. Moreover, we focus on relating critical exponents describing the finite size scaling of avalanche statistics and diffusion coefficient in these mesomodels to their MD counterpart.

4.1 Review of MD results

In this section, we review the most relevant results to our discussion that were obtained from molecular dynamics simulations [150, 115, 111]. The usual molecular dynamics model of a two dimensional model amorphous solid is a packing of two species of particles interacting via a Lennard-Jones potential. The two species are needed to avoid crystallization. There are several protocols to prepare the initial state. The the mechanical behavior depends on the specific protocol, and, in particular the quench rate: slower annealing allows the system to explore lower energy minima in the potential energy landscape and thus results in a more relaxed material [158]. Since so far we have been working with an athermal, quasistatic (AQS) mesoscopic model, we focus on its counterpart in MD as well. In order to ensure AQS, MD models usually use overdamped dynamics and a small, fixed strain step.

4.1.1 Avalanches

We have already mentioned that at vanishing loading rate we encounter a depinning-like transition. Plastic slips thus occur in power-law distributed cascades. The normalized distribution of the avalanches however loses an important information when it comes to size dependence, namely the cumulative number of avalanches over a given strain window. It is therefore of interest to define the avalanche rate $R(S, N)$ as the number of events of size S per unit loading strain [150]:

$$R(S, N) = \frac{n(S, S + \mathrm{d}S, \Delta\epsilon)}{\mathrm{d}S\Delta\epsilon} \tag{4.1}$$

where $n(S, S + \mathrm{d}S, \Delta\epsilon)$ is the number of avalanches of size in between S and $S + \mathrm{d}S$ within a strain window $\Delta\epsilon$. To comply with the notations used so far, we denoted by N

the linear size of the system, thus there are N^2 sites in the mesomodel. In MD the linear size of the system is usually denoted by L, so in the mesomodel we would have $N = L/a$ if a denotes the length of one tile. Normalizing R would give the distribution function of the avalanches.

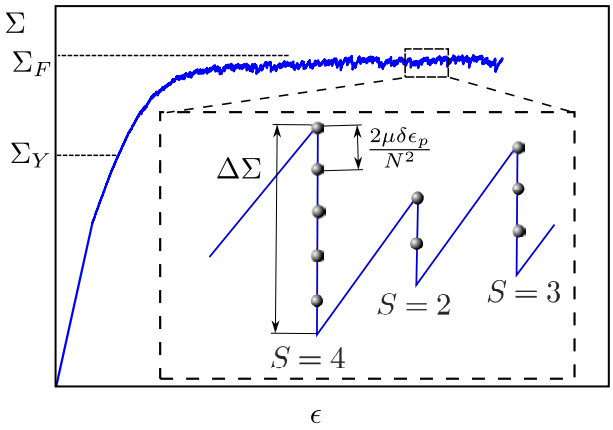

Figure 4.1 – Definition of the avalanche size. The actual flow curve is a result of a mesoscale simulation. Grey dots indicate plastic events. If the slip amplitude $\delta\epsilon_p$ is fixed, the average stress released by one event is $\delta\sigma = 2\mu\delta\epsilon_p/N^2$. The total stress released in the avalanche is $\Delta\Sigma$, $S = \Delta\Sigma/\delta\sigma$ therefore counts the number of events within the avalanche.

Here S is the avalanche size that is defined as

$$S = \frac{\Delta\Sigma}{2\mu}N^2 \tag{4.2}$$

where N is the linear size of the system and $\Delta\Sigma$ is the stress drop during an avalanche. As shown in Figure 4.1, in a corresponding mesomodel, if the slip amplitudes are uniform, this definition of the avalanche size would simply give the number of events within the avalanche.

It has been found that $R(S, N)$ collapses when scaled with N^γ for the small and intermediate S range, with $\gamma = 1.2 > 1$ [150].

As expected for a critical system, $R(S, N) \propto S^{-\tau}$ above a lower and below an upper cutoff, moreover, the avalanche rate obeys the scaling

$$R(S, N) = N^\beta g(S/N^\alpha) \tag{4.3}$$

Note that the notation of the exponent β is taken from MD studies and is by no means the Herschel-Bulkley exponent. For an overdamped system, the value $\beta = -0.2 \pm 0.1$ was found [150].The scaling function $g(y)$ is such that it recovers the power law $g(y) \propto y^{-\tau}$ for $y \ll 1$, thus $R(S, N) \propto N^\beta S^{-\tau}/N^{-\alpha\tau} = N^\gamma S^{-\tau}$ with $\gamma = \beta + \alpha\tau$. Another scaling relation can be derived using the fact that in steady state the average stress increase and

stress drop have to cancel out, giving $\beta + 2\alpha = 2$ in two dimensions. For an overdamped dynamics, $\tau = 1.25$ was found [115] which is considerably smaller than the $\tau = 1.5$ mean field value. In similar conditions, $\alpha = 0.9 \pm 0.05$ has been reported meaning that the largest event size increases somewhat slower than the linear size of the system [115].

4.1.2 Localization and diffusion

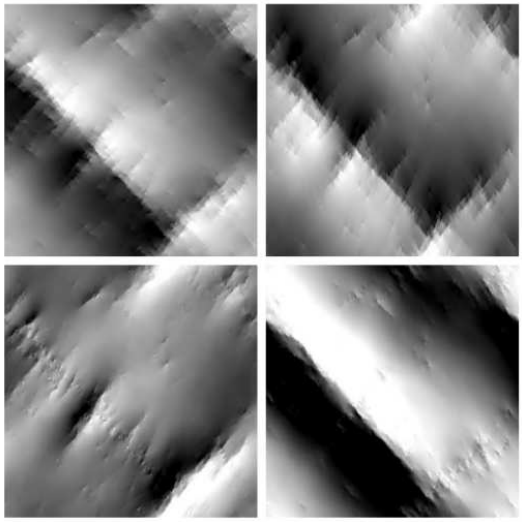

Figure 4.2 – Slip lines in an AQS MD simulation, figure from [115]. Top: projection of the non-affine displacement field onto Δx and Δy. Bottom: projection of the non-affine displacement field onto $\Delta x + \Delta y$ and $\Delta x - \Delta y$.

The localization of plastic events [112] and distribution of displacements [115, 114, 101] have been investigated in similar AQS MD setups. Similarly to mesoscopic models, a preferential orientation of the event clusterization was observed within a narrow line oriented along the Bravais axis of the simulation cell. These so-called slip lines are however not persistent in MD either and upon further shearing the plastic activity moves towards other, apparently uncorrelated slip lines. The typical width of such slip-lines is of the order of the particle diameter, a (Figure 4.2). These slip lines induce long range anisotropic spatial correlations in the system [116, 113]. Nevertheless, it was found that the mean square displacement scales linearly with the applied strain [115], therefore an effective diffusion coefficient can be defined. In order to suppress the effect of convection due to the affine loading, either the non-affine displacement field [115] or the cartesian component perpendicular to the loading direction [183, 101] is considered.

The finite size scaling of the diffusion coefficient supports the idea of the jump of the plastic activity between independent slip lines. It was found [115] that the diffusion coefficient $D = \langle \Delta u^2 \rangle / \Delta\epsilon$ scales linearly with the system size: $D \propto L$. This scaling can be understood via a simple independent slip-line argument [115], as shown on Figure

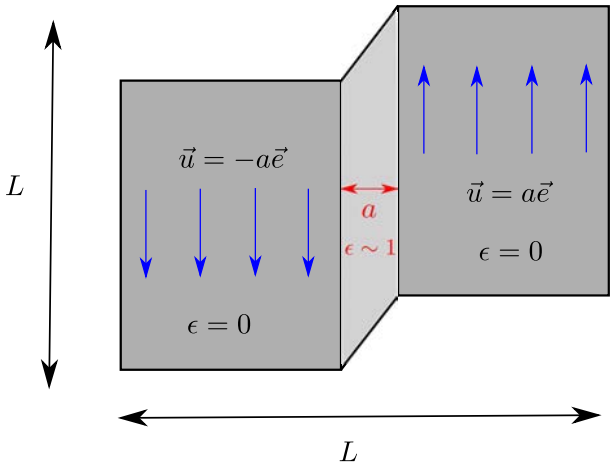

Figure 4.3 – Schematic representation of a slip line. The line has the width of a few particle diameters $\sim a$, and the displacement amplitudes at the edges of the line are also $\sim a$. This gives a strain of the order of unity within the line [115].

4.3. Let us thus assume that plasticity accumulated on a line spanning the system. The width of such a line was found to have one or two particle diameters, a. The displacement amplitudes at the edge of the line are of the order of a as well, meaning that the typical plastic strain within the band is the order of unity. The typical non-affine mean square displacement induced by one slip line is then $\langle \Delta u^2 \rangle = a^2$. Once a slip line has formed, plasticity is assumed to move to another slip line that is uncorrelated with the previous one. The dynamics is then governed by the formation of successive, uncorrelated slip lines. The average plastic strain induced by one line is the weighted average of the plastic strain field throughout the system. The plastic strain within a band is 1 and outside the band is 0, which gives $\langle \epsilon_p \rangle = a/L$. In the steady state, on average, stress cannot increase, nor decrease. Stress increases are given by the loading strain $\Delta\epsilon$ and stress drops by the average plastic strain $\langle \epsilon_p \rangle$. On average, these two have to cancel out, thus $\langle \Delta\epsilon \rangle = \langle \epsilon_p \rangle = a/L$. The diffusion coefficient is then given by $D \propto a^2/(a/L) \propto L$ thus scales linearly with the system size.

While a linear increase of the mean square displacement with the strain was observed starting from rather small strains ($\Delta\epsilon \geq 10^{-3}$), strong spatial correlations are present in the system and displacement distributions have an exponential distribution. As the strain increases, they will eventually converge to a Gaussian [115, 183].

4.1.3 Density of shear transformation zones

Within the material there are zones that yield easier than others, it is therefore of interest to follow the distribution of local stresses close to their thresholds. The measurement of the distance to threshold originates from lattice models [106]. Dividing the material into blocks, each block has a local stress σ_i and a local threshold value at which it yields, σ_i^c,

thus its distance to threshold is defined as $x_i = \sigma_i^c - \sigma_i$, and we are interested in the $P(x)$ distribution. $P(x)$ at low x gives the density of the shear transformation zones, i.e. the zones that are potentially going to yield in the nearest future upon load [106]. Note that $P(x)$ is a probability density function and is not to be confused with the spatial density of shear transformations. $P(x)$ thus contains information about the number of sites that are about to become unstable, it is therefore the low x shape of the $P(x)$ distribution which governs the stability and, in turn the dynamics of the solid. In particular, the shape of $P(x)$ has been related to the Herschel-Bulkley exponent [107]. While in depinning, at low values $P(x)$ goes to a constant, for amorphous plasticity it has been shown that due to the anisotropy of the elastic kernel balance can only hold if $P(0) \to 0$, the distribution thus vanishes at $x \to 0$. Moreover, for small x (close to the threshold) it has been found that $P(x) \propto x^\theta$ with $\theta \approx 0.57$ in two dimensions, thus the value of θ governs the stability of the system and is connected to the avalanche distribution exponent τ and the avalanche size cutoff exponent (fractal dimension) α by [106]:

$$\tau = 2 - \frac{\theta}{\theta + 1}\frac{2}{\alpha} \tag{4.4}$$

While the measurement of $P(x)$ in a lattice model is straightforward, the value of θ seems to depend on the applied stress [108]. The measurement of $P(x)$ in MD is more cumbersome due to the inhomogeneous elasticity. Nevertheless, there has been indirect evidence on a similar scaling in MD [74, 133] and the estimates $0.4 < \theta < 0.6$ were provided for fast quenched glasses, but a strong variation depending on the quench rate and the stationary state have been reported.

4.2 Scaling properties in the lattice model

In order to better comply with the MD conditions, here we will be using the quasistatic dynamics with synchronous flips introduced in chapter 2. While extremal dynamics was suitable to extract universal properties, it cannot be applied to MD, where a constant strain or stress dynamics is the most common. We therefore chose a constant strain load dynamics with vanishing strain rate. This dynamics involves synchronous pruning of all the unstable sites, until no more unstable sites are present, and only then is the loading increased. To ensure quasistatic loading, in between avalanches the strain is always adjusted such that only the weakest site yields. The strain is then held constant until the avalanche triggered by the first event is over. It was found in particular that this dynamics gives more accurate avalanche statistics [106], but it is not expected to affect the universal properties in any way.

Moreover, we will be using the two finite element kernels m2 and m3 depending on the loading geometry. Their Fourier-discretized counterparts will be referred to as m2F and m3F. In the previous chapters m3F was referred to as the Fourier quadrupolar kernel. As discussed previously, we have displacements available only for m2 and m3. Please refer to chapter 3 for details regarding the kernels. Recall that m3, m2F and m3F feature soft modes, however m2 does not.

4.2.1 Distributed thresholds vs distributed slip amplitudes

In chapter 3 we analyzed the way different kernels influence fluctuations in amorphous systems. Here, in addition, we examine the effect of disorder to both fluctuations and scaling properties. To that end, for each kernel, we consider two different protocols that we call $Y0$ and $Y1$. In the $Y1$ protocol the local yield thresholds are drawn from a random distribution, while the slip amplitudes are constant. In the $Y0$ protocol, the yield thresholds are constant whereas the slip amplitudes are drawn from a random distribution. Note that fixing the thresholds results in a first avalanche where all the sites yield a random amount synchronously which corresponds to a random plastic strain field initialization. In other words, we "bake" the Eshelby stresses into the initial configuration. A similar scenario was described in MD by Lemaître [100] thus this is a physical initialization.

The two protocols are meant to account for two different types of disorder associated to the underlying disordered potential landscape. Recalling the depinning analogy, $Y1$ introduces disorder as the fluctuations of the depths of the potential wells, while $Y0$ accounts for disorder as the fluctuations in the widths of the wells, as shown on Figure 2.5.

We have been experimenting with the combination of the two protocols (random initial stresses with constant thresholds and constant slip amplitudes or baked initial stresses with constant thresholds and constant amplitudes), these however resulted in a single narrow and persistent shear band, consistent with [147]. While this persistent behavior deserves a more systematic investigation, here we restrict ourselves to either random thresholds or random slip amplitudes.

This leaves us with the combination of two protocols (random thresholds vs random slips) and four kernels (two Fourier and two finite element), all of which obey a similar quadrupolar symmetry. Simulations for the combination of all the protocols and all the kernels were carried out for four different system sizes ($N = 64, 128, 256, 512$) up to a strain of 2×10^3 and each run has been repeated for 10 different realizations.

4.2.2 Avalanches

We first investigate the distribution of avalanche sizes and the size dependent scaling of the distribution. We compare results obtained for combinations of the two protocols and the four kernels to MD results. Recall that the quasistatic load here keeps the system right at the yielding transition. We therefore expect critical properties, in particular, a power law scaling of the avalanche distributions.

As illustrated in Figures 4.4 and 4.5, we obtain a power-law decay for the avalanche rates $R(S, N)$ for all the kernels and protocols. Note the slight difference on the extension of the power-law regime: the power law regime is longer for the random threshold protocol $Y1$. As expected, the main difference stems from small avalanche sizes S where the avalanches involve a few number of events only. There is no major difference at larger avalanche sizes where the cumulative contribution of a larger number of individual events counts.

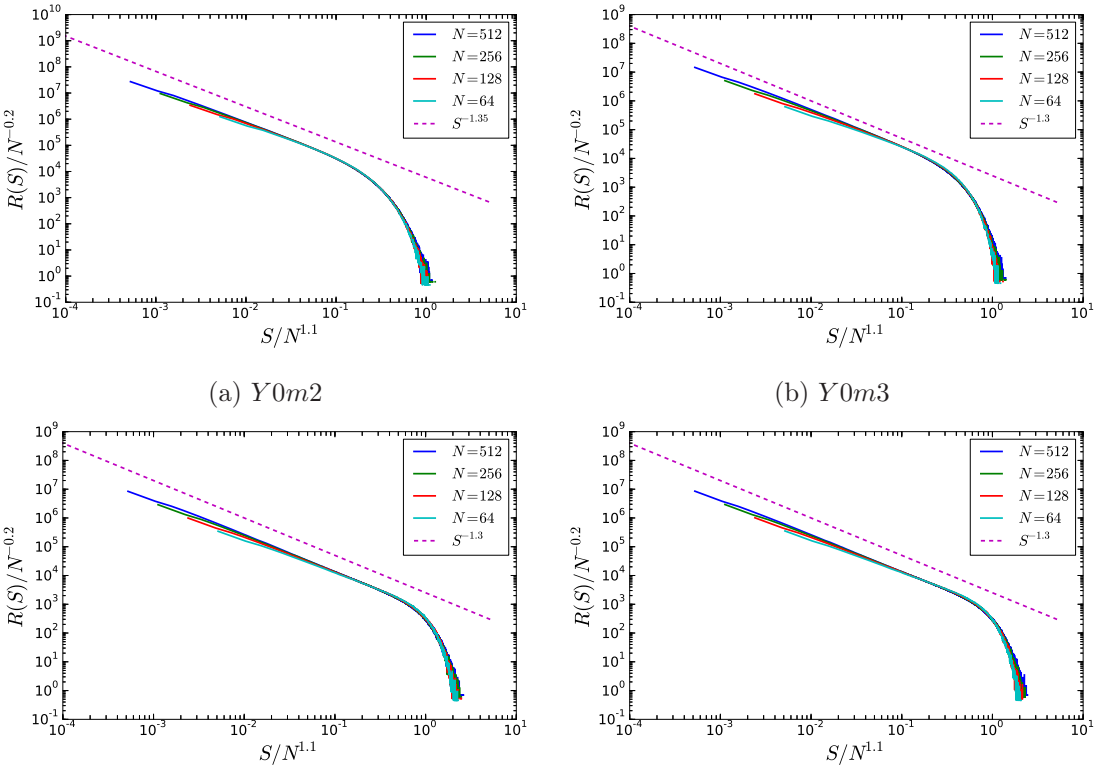

(a) $Y0m2$ (b) $Y0m3$

(c) $Y0m2F$ (d) $Y0m3F$

Figure 4.4 – Avalanche rate $R(S,N)$ finite size scaling for the random slip increment protocol $Y0$.

More importantly, beyond the details of the models, universal features are recovered. Not only the scaling ansatz 4.3 seems to hold, but the same α and β scaling exponents apply for all the protocols and kernels, namely, $\alpha = 1.1$ and $\beta = -0.2$ (Figure 4.4, 4.5). Uncertainty in α and β is approximately 0.05, meaning, for instance, that $\alpha = 1.05$ clearly gives a worse collapse than $\alpha = 1.1$. Since $\alpha > 1$, the size of the largest events increases faster than the system size. Recall that in MD $\alpha = 0.9 < 1$. While $\alpha = 1.1$ is clearly inconsistent with MD, it is consistent with some of the previous lattice model results [106]. On the other hand, in the same lattice model with extremal dynamics protocol, the value $\alpha = 1.0$ was reported [171]. For all the protocols and kernels we find $\gamma = 1.25 \pm 0.05$ which again is close to the $\gamma = 1.3 \pm 0.05$ obtained in MD [115, 151]. Since in previous lattice models the avalanche distribution was measured instead of the avalanche rate, we have no comparison for the exponents β and γ. The scaling relation $2\alpha + \beta = 2$ is valid ($2 \times 1.1 - 0.2 = 2$) thus the considerable difference in β can be viewed as a consequence of the too large α value.

Accurate measurement of scaling exponents is far from being obvious. Fitting either

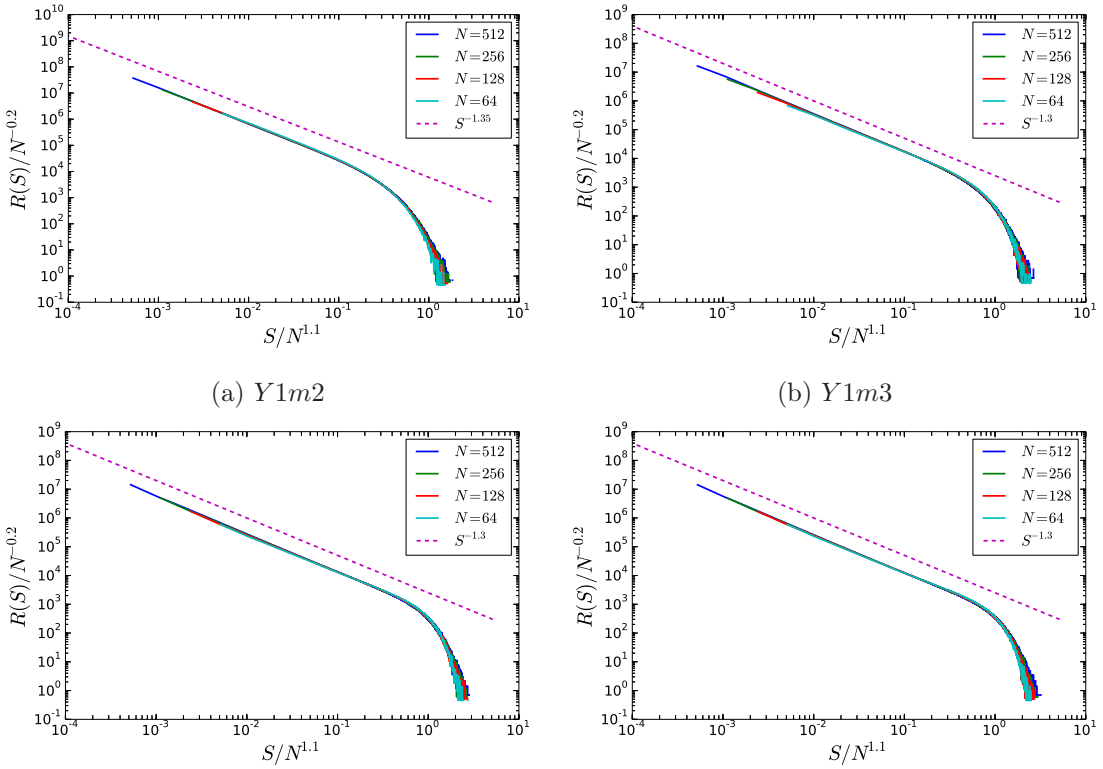

(a) $Y1m2$ (b) $Y1m3$

(c) $Y1m2F$ (d) $Y1m3F$

Figure 4.5 – Avalanche rate $R(S, N)$ finite size scaling for the random threshold protocol $Y1$. Although apparently the same set of finite size scaling exponents (α, β, γ) applies for all the kernels and protocols, the power-law regime is clearer for $Y1$.

on the equally spaced or log-binned histogram is never recommended as the power law nature of the histogram is in contradiction with the assumptions of gaussian distribution in least mean square fitting [41]. For avalanche distributions, for instance, one should use a maximum likelihood estimator with the avalanche exponent as a parameter [41]. In this case however we encounter with a lower and upper cutoff as additional parameters, furthermore, the shape of these cutoffs is unknown. The maximum likelihood method we tried therefore did not seem to perform better than a simple flattening analysis. Avalanche exponents were thus determined by testing several values at a given step (0.05 in this case) and selecting the best one, as shown on Figure 4.6.

For the avalanche rate exponent τ we find $\tau = 1.35 \pm 0.05$ for the m2 kernel and $\tau = 1.3 \pm 0.05$ for all the other protocols and kernels. This latter is consistent with the MD $\tau = 1.25 \pm 0.05$ result, as well as with other lattice model results [106, 171], and is clearly different from the $\tau = 1.5$ value obtained for the mean field kernel [47]. Moreover, the scaling relation $\gamma = \beta + \alpha\tau$ holds: $-0.2 + 1.1 \times 1.3 = 1.23 \approx 1.25$.

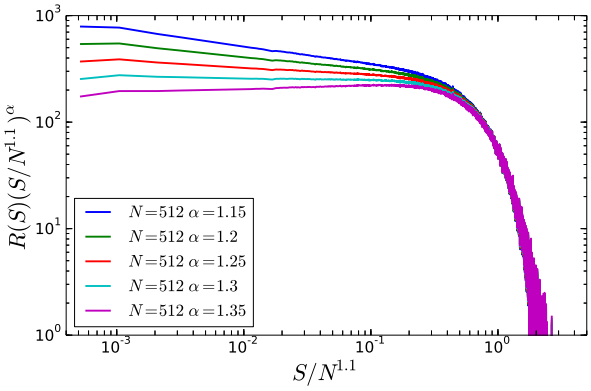

Figure 4.6 – Determination of the avalanche scaling exponent τ. The most horizontal value describes the power law the best. In this case, $\tau = 1.3$

Although in some features (α, β) are considerably different from overdamped MD, in others (τ, γ) the lattice model gives strikingly close results to MD. Moreover, avalanches do not seem to be particularly sensitive to the protocol or the kernel. Based on the avalanche statistics only, one may conclude that they all belong to the same universality class, which, however, is different from the overdamped MD universality class defined by $\alpha = 0.9$, $\beta = 0.2$, $\gamma = 1.3$, $\tau = 1.25$ [115]. The robustness of the avalanche scaling, and, in particular, the avalanche exponent τ is an important result, especially in the light of recent observations that τ may be sensitive to the details of the loading protocol [83].

4.2.3 Density of shear transformation zones

In addition to the two exponents used for describing the depinning transition, Lin et al. proposed a third, additional exponent for the complete description of the yielding transition [106, 107, 108]. The exponent is related to the distribution of stress barriers in the material close to yielding, in other terms, the stress barrier distribution of the weakest spots. These spots are the ones that are the most likely to yield, their $P(x)$ distribution thus governs the dynamics of the yielding transition. In depinning, it was found that for small x, $P(x) \propto x^0$, for the yielding transition however $P(x) \propto x^\theta$ with $\theta > 0$[106, 107, 108]. In this section we examine the $P(x)$ distribution for the two protocols and four kernels.

As shown on Figure 4.7, we observe a power law regime in the $P(x)$ distributions. The scaling however breaks down as $x \to 0$ below a lower cutoff x^* and the distribution plateaus. The appearance of the plateau is inconsistent with [106, 107, 108] where $P(x)$ was found to vanish at $x = 0$, but its cutoff x^* is size dependent, and scales as $x^* \propto N^{-b}$ with $b = 0.9$ thus disappears for an infinite system. Similarly, the level of the plateau diminishes with the system size according to $P(x = 0) \propto N^{-a}$ with $a = 0.6$. The collapse in the power-law regime indicates that $\theta = b/a = 2/3$, thus slightly larger than the 0.57

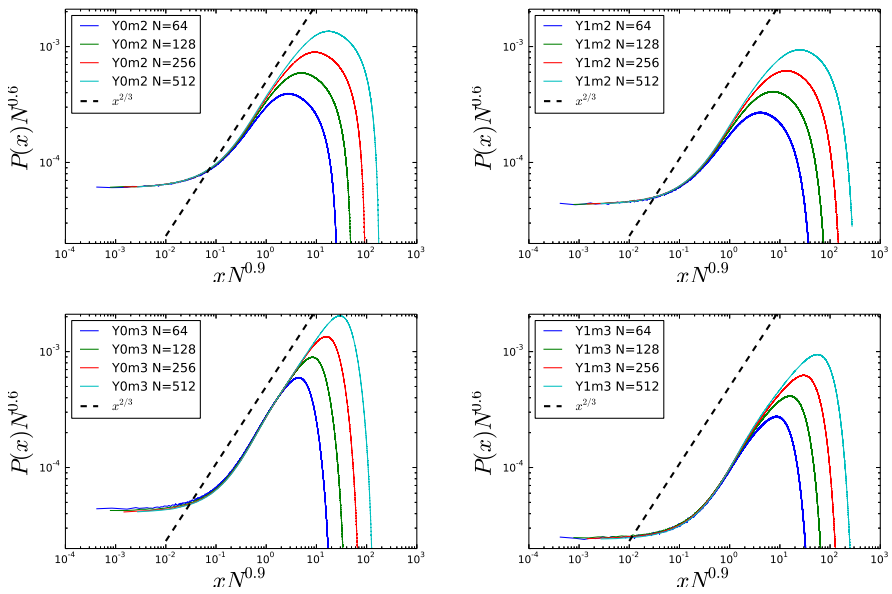

Figure 4.7 – Density of shear transformations. The power law scaling is not clear for m2. The lower plateau seems to reflect finite size scaling and should disappear for an infinitely large system.

value reported for the lattice model [107]. The same (a, b, θ) exponents work for all the kernels (including the two Fourier kernels that are not present on Figure 4.7), but the power-law range is clearer for m3.

The fact that $P(x)$ is not sensitive to the protocol is rather surprising. Distributed thresholds involve a statistical hardening of the material. Due to the systematic yielding of the weakest sites, the actual threshold distribution in the system is different from the uniform distribution we draw the thresholds from. During the transient, the thresholds are shifted towards larger values until they reach a stationary distribution. For the distributed slip increments protocol this is not the case, since there the thresholds are fixed. No statistical hardening is then present for $Y0$. Nevertheless, the $P(x)$ distributions governing the dynamics are robust.

Using these exponents we can infer the value of the avalanche exponent τ using the scaling relation 4.4, which yields $\tau \approx 1.27$ for all the modes and kernels, thus seems to be valid for all the kernels with soft modes (where, recall, we had $\tau \approx 1.3$), but it fails for m2 (for which we obtained $\tau \approx 1.35$).

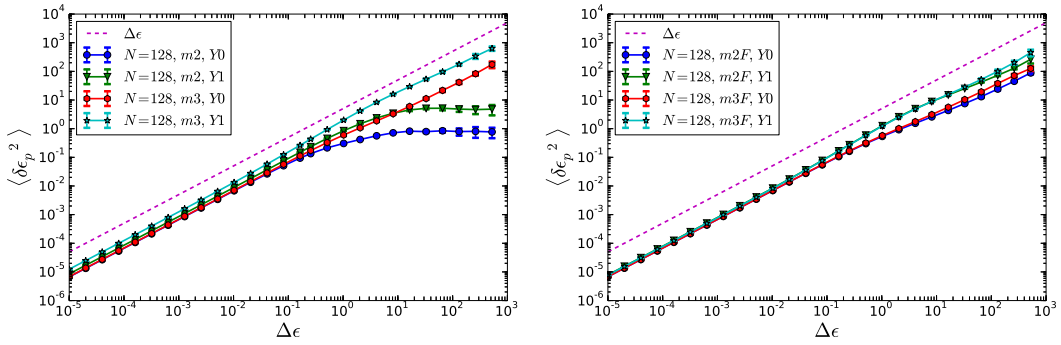

Figure 4.8 – Plastic strain variance for the finite element kernels (left) and for the Fourier kernels (right). Fluctuations saturate for m2 on the long run, but there is no major difference in the short time scaling.

4.3 Diffusion

4.3.1 Fluctuations of the plastic strain field

In chapter 3 we found that the presence of soft modes in the kernel affects the long time strain fluctuations. Indeed, as shown on Figure 4.8, long time plastic strain fluctuations increase for m3, m2F and m3F but saturate for m2 as the latter does not feature any soft modes. All the kernels have a similar quadrupolar symmetry and show diffusive behavior at short times. Short time behavior thus seems unaffected by the lack of soft modes. In the depnning sense, at short times, the deformation of the interface is small enough for the effect of restoring forces to be negligible. For the soft mode kernels, we observe three regimes: a short time diffusive regime, a superdiffusive regime corresponding to the growth regime in the Family-Vicsek picture and a long time diffusive regime. The presence of the three regimes is independent of the protocol. For the m2 kernel, at long times, saturation is observed.

The three regimes can be better identified when looking at the diffusivity $\delta\epsilon_p^2/\Delta\epsilon$ associated to the plastic strain diffusion. Figure 4.9 shows the evolution of the diffusivity for increasing strain windows for various system sizes. As the temporal plastic strain field correlations have not built up, we observe a first plateau that appears for small up to intermediate strain windows. The range of the initial diffusive behavior as well as the value of the diffusivity seem to be independent of the system size, they depend however on the protocol: while for the random slip protocol $Y0$ we observe a persistence of this plateau up to strain values of the order of unity $\Delta\epsilon \approx 1$, in the case of the random threshold protocol $Y1$ we have an earlier departure at $\Delta\epsilon \approx 10^{-2}$ for all the kernels.

After the initial, size independent, constant diffusivity we observe a departure from constant diffusivity. Interestingly, this departure happens almost instantaneously for $Y0$, and the strain variance shows a subdiffusive scaling. For $Y1$ we have a longer regime between $10^{-2} \leq \Delta\epsilon \leq 1$ associated to the "bump" in the diffusivity after which a long

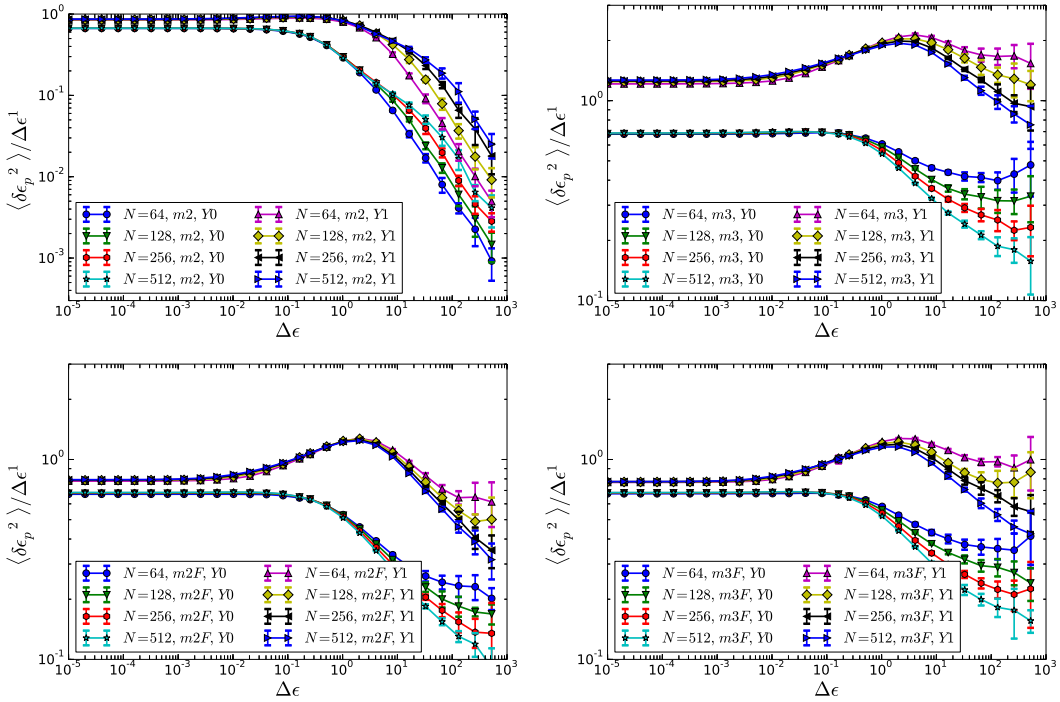

Figure 4.9 – Plastic strain diffusivity for the m2 and m3 (top) and m2F and m3F (bottom) kernels. Three regimes can be identified: an early diffusive regime, a long superdiffusive growth and a late diffusive regime or saturation depending on the kernel. Regardless of the protocol, on the long run, diffusion is observed for m3, m2F and m3F, but saturation of the strain fluctuations for m2 due to the lack of soft modes. Short term diffusion is similar for all the protocols and kernels. The late diffusive regime here is only visible for the smallest system sizes.

subdiffusive scaling sets in. This is valid for all the soft modes kernels, and this is the time where the fluctuations for the m2 kernel saturate. The range of the subdiffusive scaling is size dependent and is smaller for smaller system sizes.

Eventually, at large enough strains, the plastic strain fluctuations reconverge to another diffusive regime, which, however shows considerable size dependence as the diffusivity decreases with the system size. Moreover, the time necessary to reach diffusion increases with the system size. On Figure 4.9 we can observe the second diffusive regime for the two smallest system sizes. The largest ones are still in the subdiffusive scaling as it takes longer for those to reach the second diffusive regime.

4.3.2 Fluctuations of the displacement field

In this section we study the diffusive behavior of the displacement field. The three regimes discussed above can be identified for the displacement fluctuations as well. Figure 4.10

shows the evolution of the mean square displacement for the finite element kernels (recall that we do not have access to the displacements for the Fourier kernels). Initially, both m2 and m3 show a similar diffusive behavior. At large strains the mean square displacement in m2 saturates and in m3 converges to the new diffusive scaling. The crossover in this case however is superdiffusive. Moreover, long term diffusion is reached faster that for the plastic strain fluctuations. The Family-Vicsek growth regime for the displacement fluctuations is thus shorter, but the trend is the same: the $Y0$ protocol reaches diffusion faster than $Y1$.

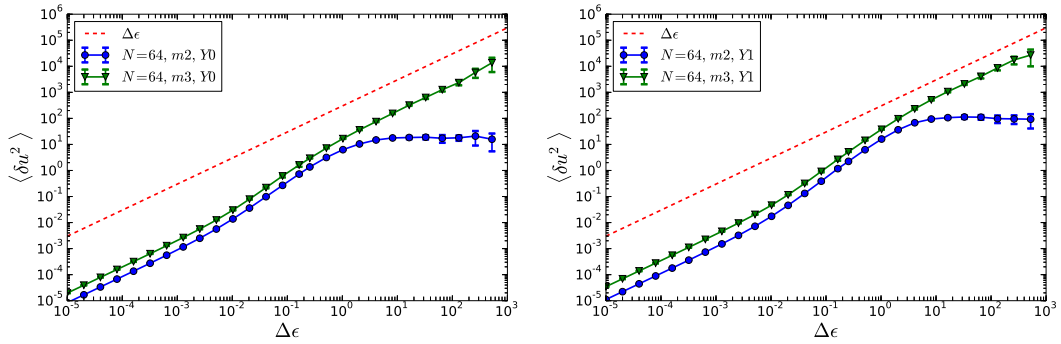

Figure 4.10 – Mean square displacement for the finite element kernels. Left: $Y0$, right: $Y1$.

In what follows, we examine these three regimes (early diffusion, superdiffusive behavior, long term diffusion) from the perspective of the displacements.

Early diffusion and crossover to superdiffusive scaling

Let us first examine the origins of the short term, size and protocol independent diffusive scaling. On Figure 4.11 we show the evolution of the displacement diffusivities for m2 and m3 . We observe an initial diffusive trend for both modes and protocols after which the mean square displacement becomes superdiffusive. The associated diffusion coefficient $D = \delta u^2/\Delta\epsilon$ shows size dependence, and, as shown on Figure 4.11, D scales as $D \propto N^{\delta_s}$ with $\delta_s \approx 1.05$.

The initial diffusion can be understood via a simple balance argument. Assuming that all the avalanches follow the same pattern, the stress-strain curve is a periodic sawtooth function with period $\Delta\epsilon_0$ which is the loading strain between successive avalanches (Figure 4.12). The plastic strain during an avalanche is $\Delta\epsilon_p = \Delta\epsilon_0$ since, on average, the stress cannot increase, nor decrease and the stress released during an avalanche is precisely $\Delta\Sigma = -2\mu\Delta\epsilon_p$, while the stress increase in between avalanches is $\Delta\Sigma = 2\mu\Delta\epsilon_0$. Let us now divide each loading branch into small windows of strain $\Delta\epsilon$. The number of windows within one period is $N_w = \Delta\epsilon_0/\Delta\epsilon$ and, given the loading is homogeneous, there is no increase in the non-affine displacement in the first $N_w - 1$ windows. An avalanche occurs within the N_wth window resulting in a plastic strain field increment

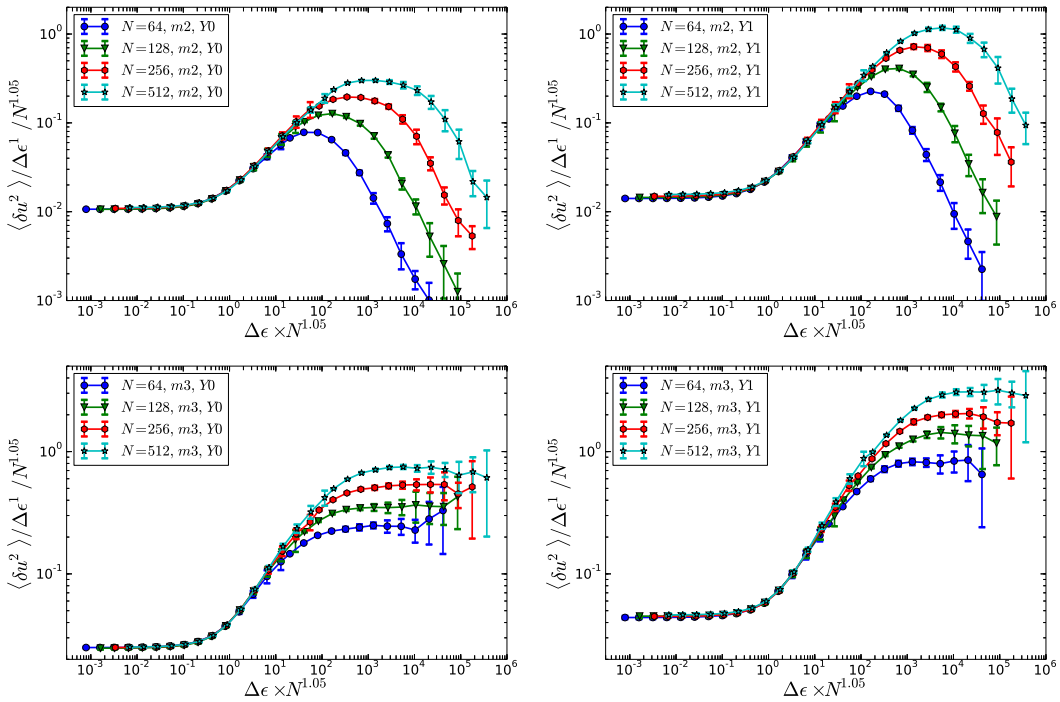

Figure 4.11 – Displacement diffusivities for m2 and m3. Note the scaling of the initial plateau. The associated diffusion coefficient increases slightly faster with the system size than in MD, $D \propto N^{1.05}$

and an associated non-affine displacement field $\vec{u}_0(\vec{r})$. Let us further assume that all the avalanches follow the same pattern. The mean square displacement within one period is thus given by the weighted average of all the zero non-affine displacements on the elastic loading branch and the mean square displacement induced by the avalanche in window number N_w:

$$\langle \delta u^2 \rangle = \frac{0 \times (N_w - 1) + \langle \delta u_0^2 \rangle \times 1}{N_w} \tag{4.5}$$

Inserting $N_w = \Delta\epsilon_0 / \Delta\epsilon$ we readily get the diffusive behavior for small windows:

$$\langle \delta u^2 \rangle = \frac{\langle \delta u_0^2 \rangle}{\Delta\epsilon_0} \Delta\epsilon \propto \Delta\epsilon \tag{4.6}$$

This approximation clearly only works until the window size $\Delta\epsilon$ reaches the size above which the collective occurrence of avalanches starts to impact the localization of plastic activity and, in turn, the cumulated displacement field. The initial diffusive behavior thus can be viewed as the result of independent avalanche shot noise. Note that a similar reasoning can be carried out for the plastic strain field, explaining the initial linear scaling of the plastic strain variance.

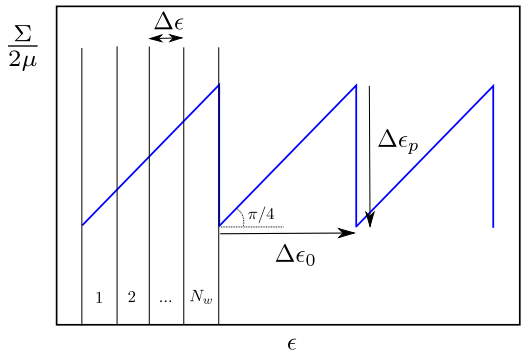

Figure 4.12 – Simplified avalanche dynamics. Stress-strain curve is assumed to follow a sawtooth shape with period $\Delta\epsilon_0$. On the elastic loading branches only affine displacements change.

At this initial stage the mean square displacement and the diffusion coefficient $D = \langle \delta u^2 \rangle / \Delta\epsilon$ show a strong system size dependence. Figure 4.11 shows that a rescaling by $N^{1.05}$ gives an excellent collapse for the initial plateau and parts of the crossover to superdiffusive behavior. This $D \propto N^{1.05}$ scaling is very close to the $D \propto N^{1.0}$ observed in MD simulations [115] and can be understood via the independent slip-line argument discussed previously. We assume that individual avalanches are percolating slip lines of the width of a lattice constant a. The plastic strain in the slip lines is d (which is the typical elementary slip increment). The mean square displacement induced by such a line is $\langle \delta u_0^2 \rangle = d^2 a^2$ and the average strain drop caused by the line-avalanche is $\Delta\epsilon_p = d/N$. Recall that $\Delta\epsilon_p = \Delta\epsilon_0$, therefore we have $\Delta\epsilon_0 = d/N$. This gives the diffusion coefficient:

$$D = \frac{\langle \delta u^2 \rangle}{\Delta\epsilon} = \frac{\langle \delta u_0^2 \rangle}{\Delta\epsilon_0} = da^2 N \propto N \tag{4.7}$$

The same slip-line reasoning explains the size-independence of the plastic strain diffusivity. For a localized shear band, we have a plastic strain fluctuation

$$\delta\epsilon_p^2 = \frac{d^2}{N} - \frac{d^2}{N^2} \approx \frac{d^2}{N} \tag{4.8}$$

giving for the strain diffusivity

$$\frac{\delta\epsilon_p^2}{\Delta\epsilon_0} = d, \tag{4.9}$$

a size independent value.

To further support the idea of the slip-line structure of the individual avalanches, let us examine the crossover strain ϵ^* at which departure from the initial diffusive behavior happens. The crossover strain ϵ^* to superdiffusion seems to obey the same scaling as the diffusion coefficient, $\epsilon^* \propto N^{-1.05}$. As shown on Figure 4.11, a nice collapse for the initial plateau and part of the departure is obtained when rescaling both the diffusion coefficient

and the loading strain by $N^{1.05}$. Since the strain required to form a homogeneous shear band is $\propto 1/N$, we may conclude that departure from the initial diffusive regime occurs after multiple shear bands start forming. In other words, the collective behavior of the developed shear bands causes the subsequent supperdiffusive behavior.

Slip line formation

The departure from the initial diffusive regime is not observed in MD simulations and we can think of two reasons: they are either not carried out to large enough strains to observe the strong localization and the associated collective effect of slip lines or the lattice models are not suitable to capture the collective effect properly. The latter is more probable since at the time displacement distributions already converged to a Gaussian, departure from the linear increase of the mean square displacement was not reported [115]. To get a qualitative idea about the underlying mechanism, on Figures 4.13-4.16 we show the stress field in the stationary state for successive windows of size $\Delta\epsilon = d/N = \epsilon^*$, for the two modes and protocols. On average, this is the window size at which a slip line can form and up to this window we observe diffusion and above it superdiffusion. The individual maps for the two kernels and protocols are similar and we observe that the plastic activity is localized along quasi independent shear bands as predicted. These slip lines tend to percolate throughout the system and they are somewhat more localized for m3 than for m2. The localization of avalanches along slip lines of width in the order of the tens of nanometers in metallic glasses has been observed in many experiments [94, 165, 200, 166, 7].

So far the localization mechanism is similar to MD: individual slip lines form within a window of size ϵ^*. Let us now consider the successive windows. The qualitative difference arises when taking a look at the successive windows: we observe that the plastic activity tends to revisit the same bands multiple times. The bands in successive windows are thus not independent which leads to a superdiffusive mean square displacement above ϵ^*. The strong correlation between successive bands thus leads to a collective behavior that is not observed in MD. As we have shown before, at this stage the collective effect of the bands is rather independent on the kernel, it depends however on the protocol. Examining the stress maps we observe that the bands in the $Y1$ protocol are more persistent than in the $Y0$ protocol which is consistent with the mean square displacement plots, where we see that after ϵ^* the slope is larger for $Y1$. Moreover, it takes about 10 times longer for $Y1$ to reach the second diffusive regime reflecting that persistence is more pronounced and the decorrelation time of the plastic activity in this case is larger.

Long term diffusion

The initial diffusive regime associated to the "kicks" of single shear bands only holds up to a crossover strain $\epsilon^* \propto N^{1.05}$, as shown on Figure 4.11. After ϵ^* a superdiffusive behavior is observed due to the persistence of successive shear bands.

The initial constant diffusivity regime is considerably longer for the plastic strains (Figure 4.9) than for the displacements (Figure 4.17) showing that displacements corre-

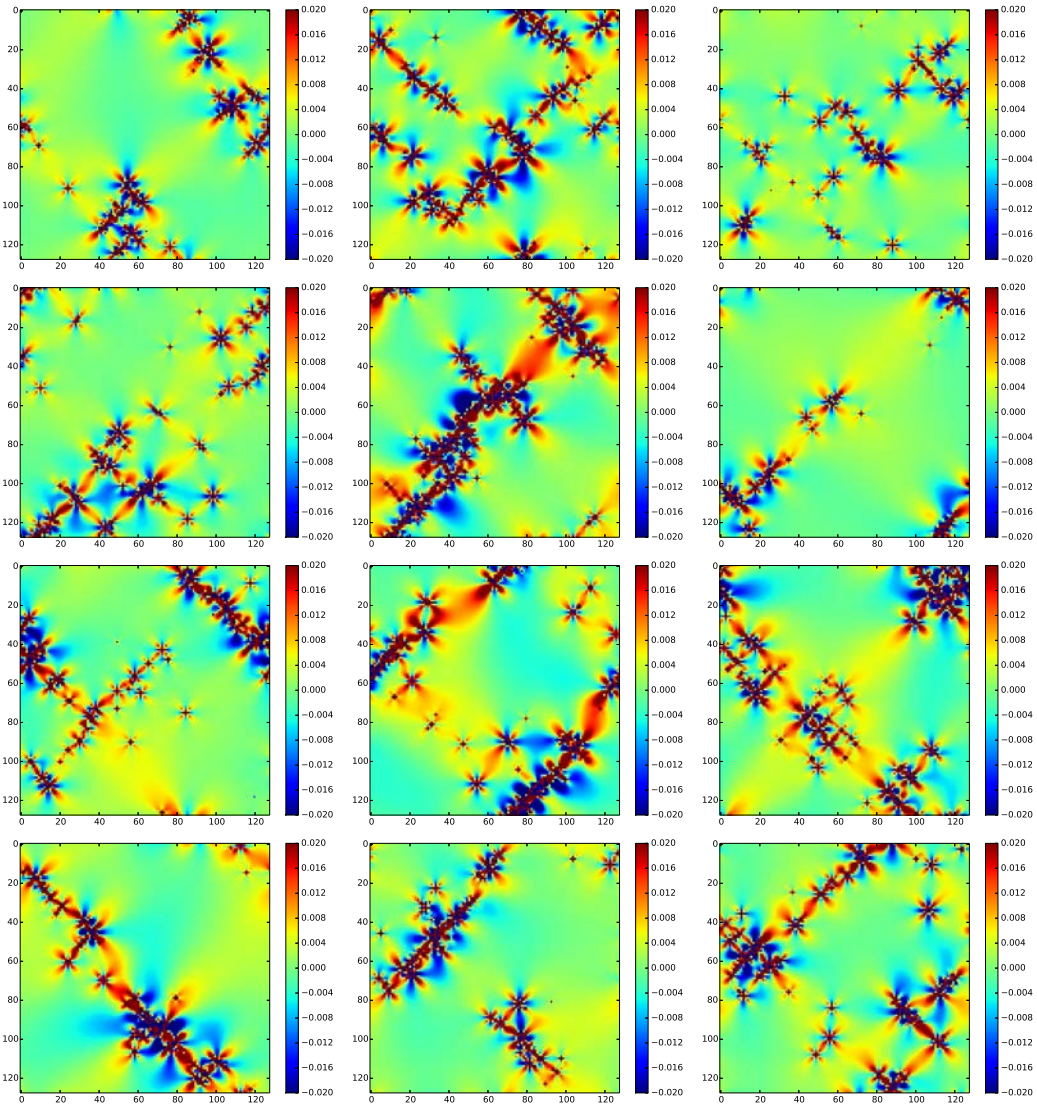

Figure 4.13 – Incremental stress maps for $Y0m2$ over consecutive (non-overlapping) strain windows of size $\Delta\epsilon = d/N$ such that on average, in each window there are N plastic events.

late faster. This is a consequence of the local nature of the plastic strain and the long range of the displacements. The departure to a superdiffusive regime here is peculiar and should not be confused with the initial superdiffusive behavior observed in MD [115, 183]. In the latter, when investigating the mean square displacement, one observes an early quadratic increase with a transition to a linear rise. This quadratic increase is however caused by inhomogeneous elasticity due to the inhomogeneities in the local structure of

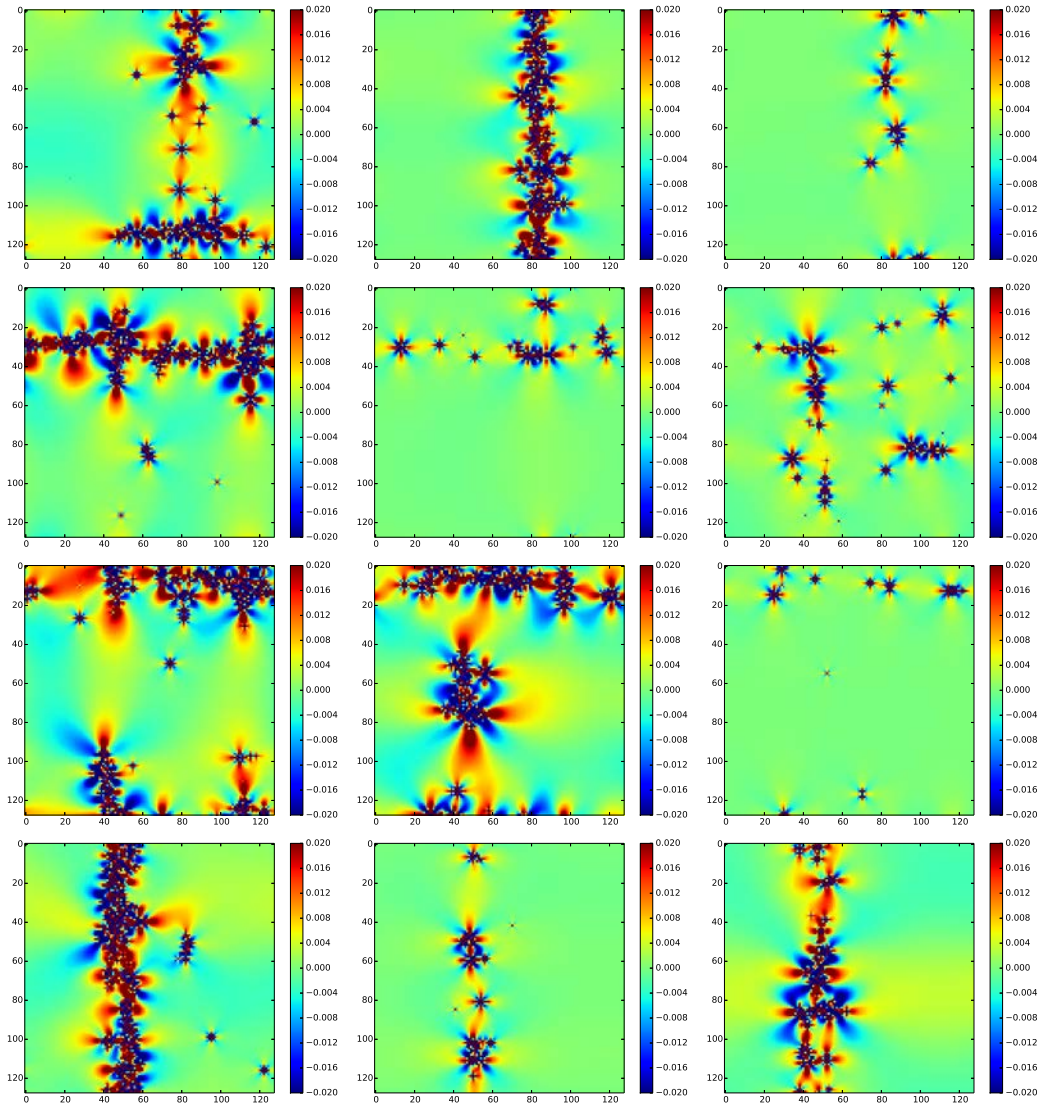

Figure 4.14 – Incremental stress maps for $Y0m3$ over consecutive (non-overlapping) strain windows of size $\Delta\epsilon = d/N$ such that on average, in each window there are N plastic events.

the material it can thus not appear in our coarse grained picture. Based on the mean square displacement and the diffusion coefficient scaling, as well as on the displacement distributions, our initial diffusive behavior would therefore correspond to the long time behavior seen in MD.

Figure 4.17 shows that the crossover strain to the second diffusive regime for m3 is size independent and happens much earlier for $Y0$ ($\Delta\epsilon \approx 1$) than for $Y1$ ($\Delta\epsilon \approx$

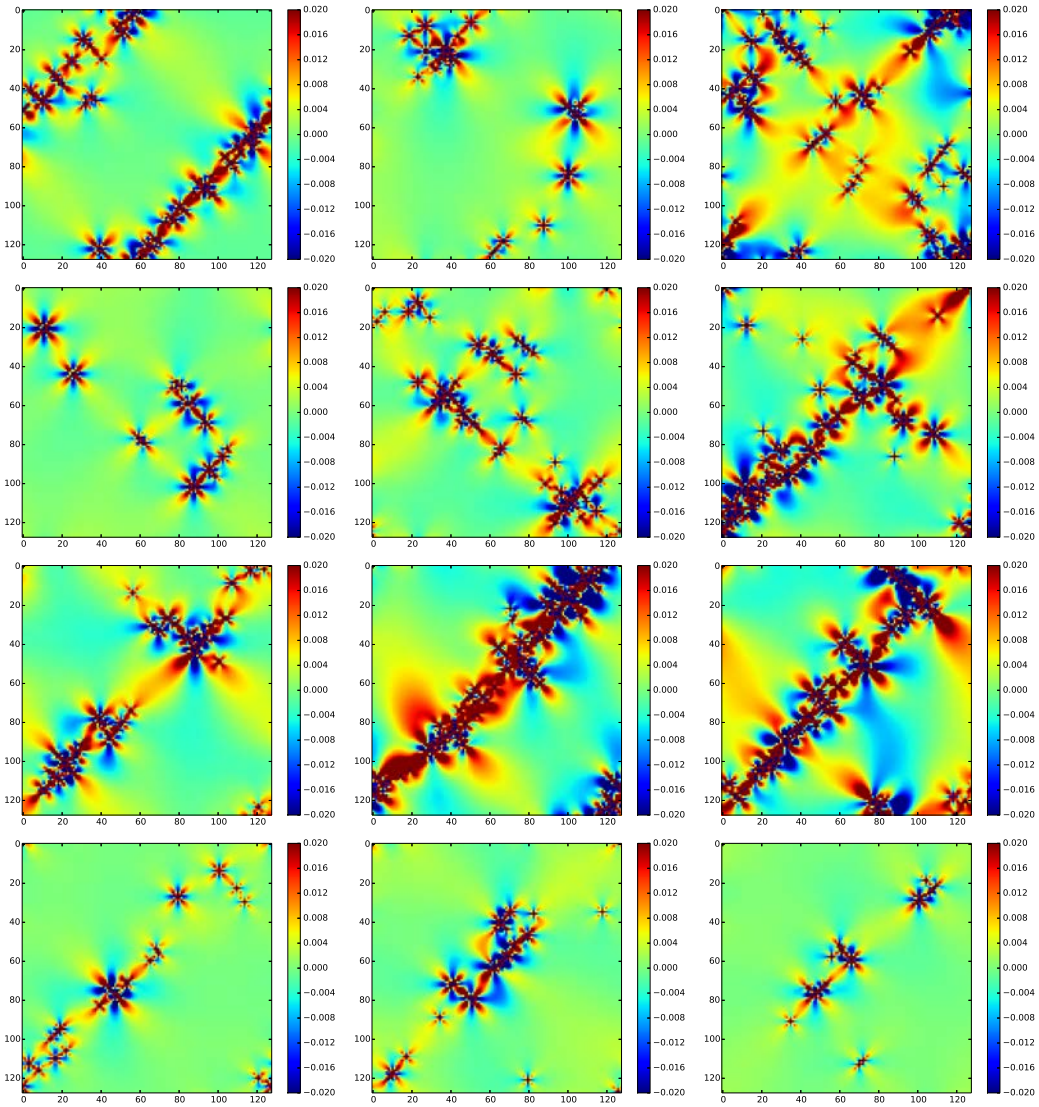

Figure 4.15 – Incremental stress maps for $Y1m2$ over consecutive (non-overlapping) strain windows of size $\Delta\epsilon = d/N$ such that on average, in each window there are N plastic events.

10). The displacement distributions (Figures 4.18, 4.19, 4.20) show that at these strains the cartesian components distribution converged to a normal distribution, whereas the displacement magnitude to a two dimensional Maxwell-Boltzmann.

While at this stage ($\Delta\epsilon \approx 1$ for $Y0$ and $\Delta\epsilon \approx 10$ for $Y1$) the plastic strain fluctuations are still in their long subdiffusive crossover regime (Figure 4.9), the "particle" displacement is already governed by a second diffusive process: the mean square displacement

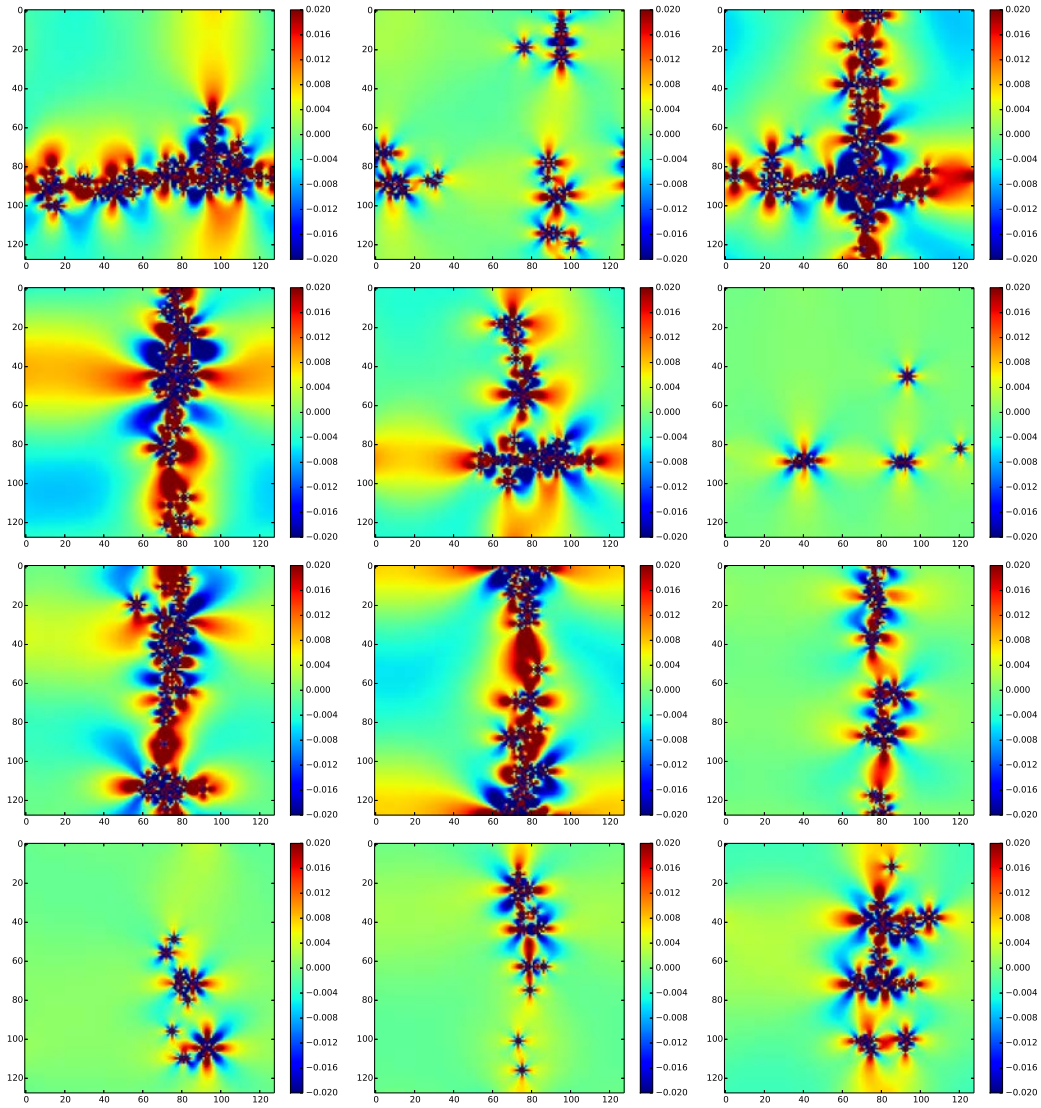

Figure 4.16 – Incremental stress maps for $Y1m3$ over consecutive (non-overlapping) strain windows of size $\Delta\epsilon = d/N$ such that on average, in each window there are N plastic events.

scales linearly with the strain while the displacements have a normal distribution. As shown on Figure 4.17, the diffusion coefficient is system size dependent in this case as well, however this time it scales considerably faster: $D \propto N^{\delta_l}$ with $\delta_l \approx 1.6$. This result is consistent with the $D \propto N^{1.5}$ scaling reported in a similar lattice model [118].

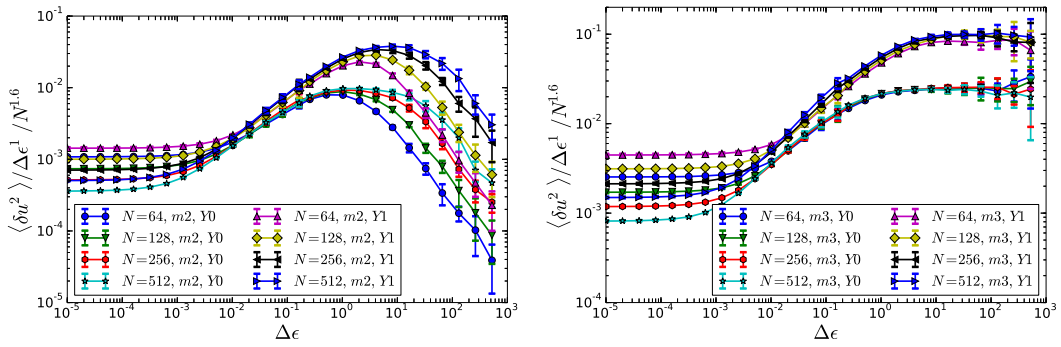

Figure 4.17 – Diffusion coefficients scaled by $N^{1.6}$ for the finite element kernels. Although both kernels show diffusion at very low strains, this is merely a consequence of the Eshelby shot noise. Long term diffusion is the result of the collective effect of slip lines.

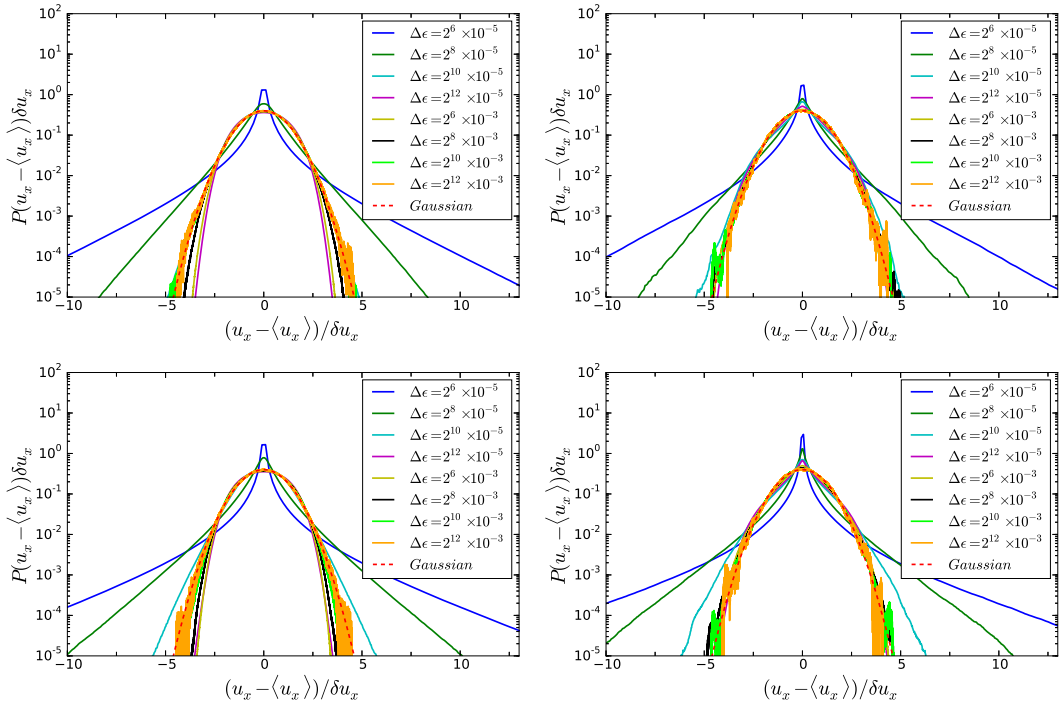

Figure 4.18 – Distribution of the u_x (or, equivalently, u_y) displacements for increasing time windows for a system size of $N = 512$. Top left: $Y0m2$, top right: $Y0m3$, bottom left: $Y1m2$, bottom right: $Y1m3$. Displacement values are rescaled with the standard deviation so that all gaussians collapse into one curve.

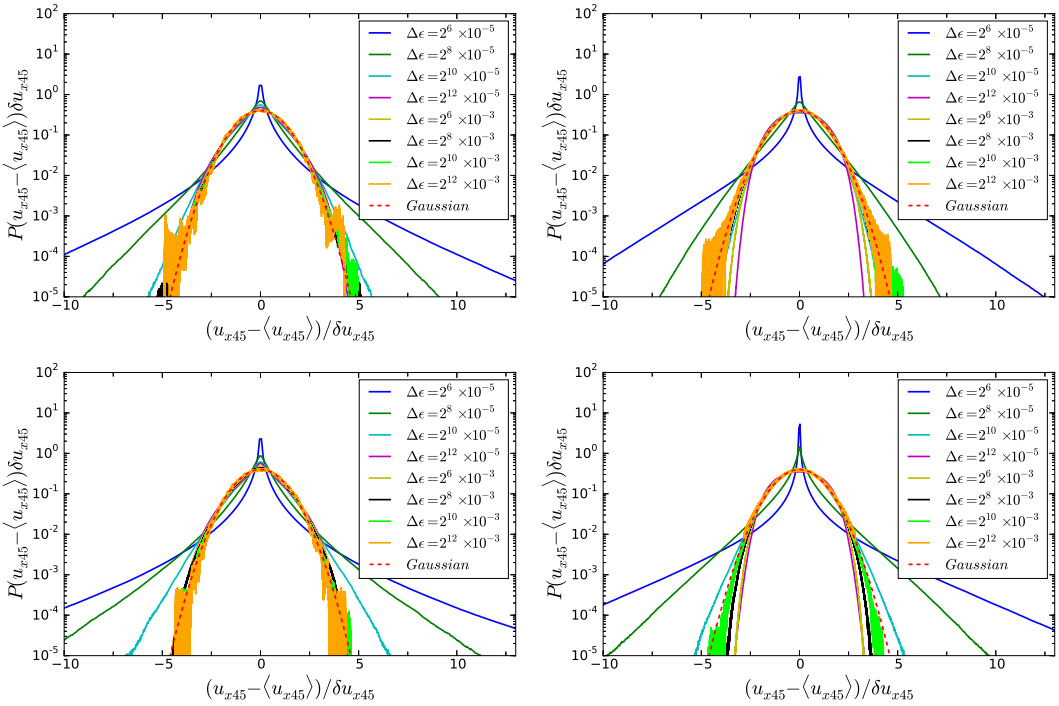

Figure 4.19 – Distribution of the displacements along the 45° (or, equivalently, 135°) direction, for increasing time windows for a system size of $N = 512$. Top left: $Y0m2$, top right: $Y0m3$, bottom left: $Y1m2$, bottom right: $Y1m3$. Displacement values are rescaled with the standard deviation so that all gaussians collapse into one curve.

Evolution of the displacement distribution

Let us now examine the evolution of displacement distributions. At early times the tail of the displacement distributions rather gives information about the distribution of the individual slip amplitudes caused by single slip lines. On Figure 4.18 and 4.19 we represented the evolution of the displacement distribution along the x or y and $x \pm y$ axis, respectively. At early times, the distribution has an exponential tail which is in line with MD results [115, 183] and it has been argued that the exponential tail is associated to the development of shear bands [182]. Indeed, the shape of this early distribution (in particular, the central peak and the exponential tail) is very close to what we get when placing a random number of events at random positions along a single band and compute the corresponding displacement distribution. Similarly, as we show on Figure 4.20, the distribution of the displacement magnitudes at small strain windows has an exponential tail.

Considering the distributions only, it may be tempting to model the evolution of displacements in the system as a random walk with exponentially distributed steps. While such an approach indeed predicts diffusion and complies to the observed distributions

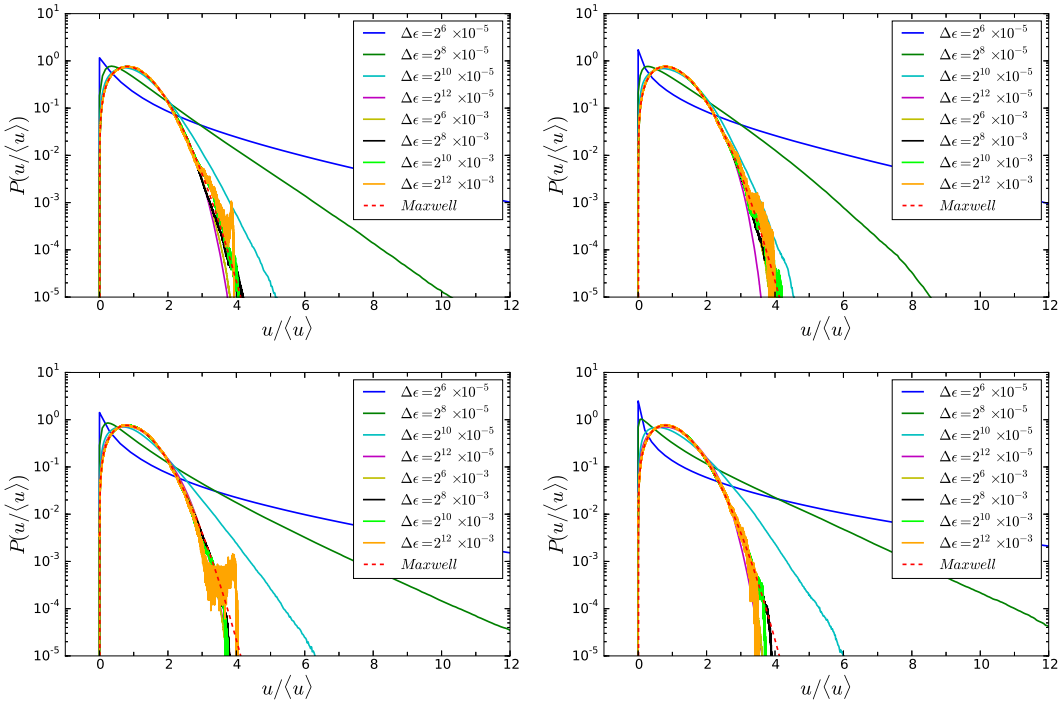

Figure 4.20 – Distribution of the magnitude of displacements u, for increasing time windows for a system size of $N = 512$. Top left: $Y0m2$, top right: $Y0m3$, bottom left: $Y1m2$, bottom right: $Y1m3$. Displacement values are rescaled with the average so that all the two dimensional Maxwell-Boltzmann distributions collapse into one curve.

(exponential tail at short time and normal distribution at long times), it does not account for size effects that are caused by localization. Note that, due to the shear bands, large parts of the system move in a correlated way. As it was stated in [115], therefore, we do not have a one-particle diffusive process.

In a standard diffusive process, at long times the distribution of displacements converges to a normal distribution, according to the central limit theorem. In present case we have a more complex diffusive process than a simple random walk due to the long range anisotropic correlations in the system. Nevertheless, we find that at large times displacement distributions converge to a Gaussian distribution.

Convergence to a Gaussian distribution can be evidenced by following the evolution of the displacement distribution kurtosis $K(\Delta\epsilon)$ which equals 3 for a Gaussian (Figure 4.21). At small strains the kurtosis decreases as $K(\Delta\epsilon) \propto \Delta\epsilon^{-1}$. We have seen that at small strains the mean square displacement is diffusive, $\langle\delta u^2\rangle \propto \Delta\epsilon$. Similarly, following the independent avalanche argument, we have the same dependence for the 4^{th} moment, $\langle\delta u^4\rangle \propto \Delta\epsilon$ which leads to $K(\Delta\epsilon) = \langle\delta u^4\rangle/\langle\delta u^2\rangle^2 \propto \Delta\epsilon^{-1}$. In agreement with the mean square displacements, we observe a size dependent transition that corresponds

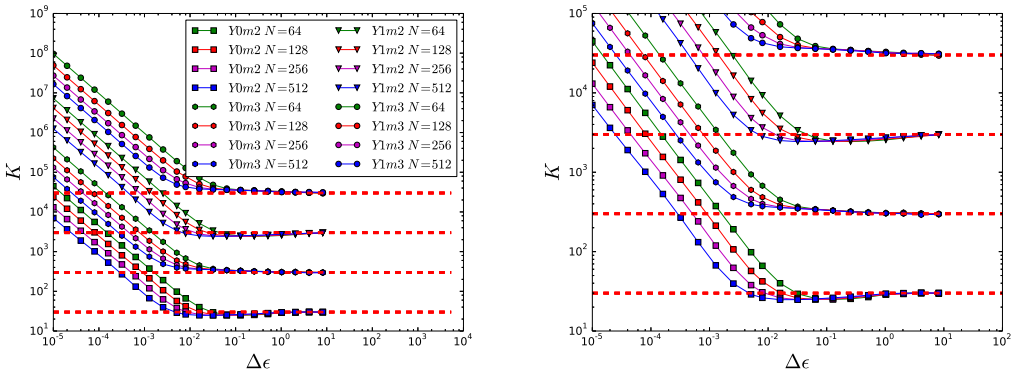

Figure 4.21 – Kurtosis of the $P(u_x)$ distribution. The crossover from the initial scaling is size dependent, but to the second diffusive plateau is size independent. Curves for different modes and protocols are vertically shifted to avoid overlap and red lines indicate the kurtosis value of a corresponding Gaussian. Gaussian distribution is reached at $\Delta\epsilon \approx 1$ for $Y0$ and $\Delta\epsilon \approx 10$ for $Y1$.

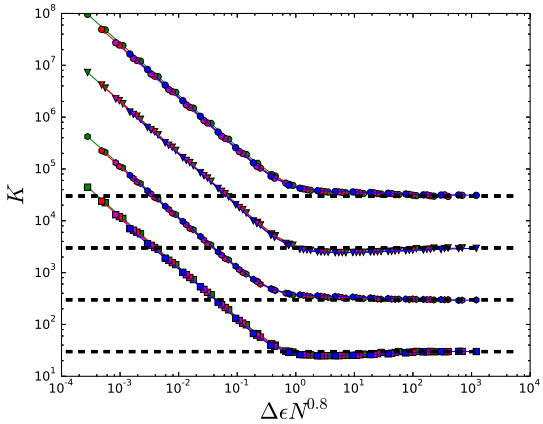

Figure 4.22 – Kurtosis of the $P(u_x)$ distribution. The crossover from the initial diffusive plateau scales as $\epsilon^* \propto N^{0.8}$

to the superdiffusive crossover. For the curtosis however, we have a different scaling for the crossover strain, namely $\epsilon^* \propto N^{-0.8}$ (Figure 4.22). The difference may arise from the similar scaling of the second and the fourth moments which both may contain higher order terms that become important when the first order terms cancel out in the ratio. The crossover to the second diffusive regime is, as expected from the mean square displacements, size independent and happens at the same strain, $\Delta\epsilon = 1$ for the random slip protocol $Y0$ and $\Delta\epsilon = 10$ for the random threshold protocol $Y1$.

We have thus seen that the cartesian components of the displacements reach a normal distribution and the diplacement magnitudes a two dimensional Maxwell-Boltzmann distribution as the mean square displacement reaches the second diffusive regime. At the same time, the diffusion coefficient shows size dependence, therefore this regime is not a one particle diffusive process either. Following the analysis developed in chapter 3, the long time behavior of the system is governed by the presence of soft modes of the elastic interaction, that is, the diffusion of loosely coupled shear bands. Such a shear band diffusion explains the random kicks the sites receive which, as we see, lead to the normal distribution of displacements. These kicks however are correlated since activity tends to accumulate along the bands. We believe therefore that the size dependence of the diffusion coefficient originates from the mean square displacement corresponding to diffusing bands. Note however that the coupling between these bands matters. We tried a simple toy model in which we considered N slip lines. In the model, at each time step, a slip occurs along a randomly selected line. The plastic strain along such a line is homogeneous. Such a model does not predict any size dependence for the strain fluctuations. One step further, we considered a two dimensional system in which strain bands can nucleate in both directions. This model predicts size independent strain diffusivity as well. For the moment therefore it seems that the size dependent diffusivity at long times is the result of the collective behavior of diffusing shear bands.

4.3.3 Trajectories and soft modes

Figure 4.23 depicts sample trajectories of three randomly selected tracers for the two modes and kernels, within a strain window of $\Delta\epsilon = 10$. As we would expect from the localization observed previously, at short times the motion of the particles is strongly correlated in time. The individual increments at short times follow a quasi exponential distribution and, similarly to the trajectory observed in [183], they correspond to the correlated "kicks" of the slip lines. Although the motion is clearly not a single-particle Brownian as strong, anisotropic correlations can be revealed, the mean square displacement nevertheless is diffusive as we have shown, due to the localization mechanism. Once multiple shear bands can form, their collective behavior produces correlated kicks which cause the superdiffusive transition, but at long enough strains they eventually decorrelate and a diffusive trajectory is observed. The direction of the loading can be distinguished between m2 and m3 as the former favors displacements along the $\pm\pi/4$ directions whereas the latter along the 0 and $\pi/2$ axis.

The long term saturation of the displacement fluctuations for m2 is evidenced in the trajectory plots. Recall that for this kernel both the strain and displacement fluctuations saturate, and they did so earlier for $Y0$ therefore the particle positions for this protocol are bounded within a smaller region of the space. For $Y1$ the saturation is observed at the strain of $\Delta\epsilon = 10$ for the depicted $N = 128$ system size meaning that the effect on the trajectories is not as pronounced yet.

We have seen in the soft modes study that the saturation in the plastic strain variance is a result of the lack of null eigenmodes in the elastic propagator. The eigenspace of the zero eigenvalues is spanned by the shear bands and one would intuitively expect that

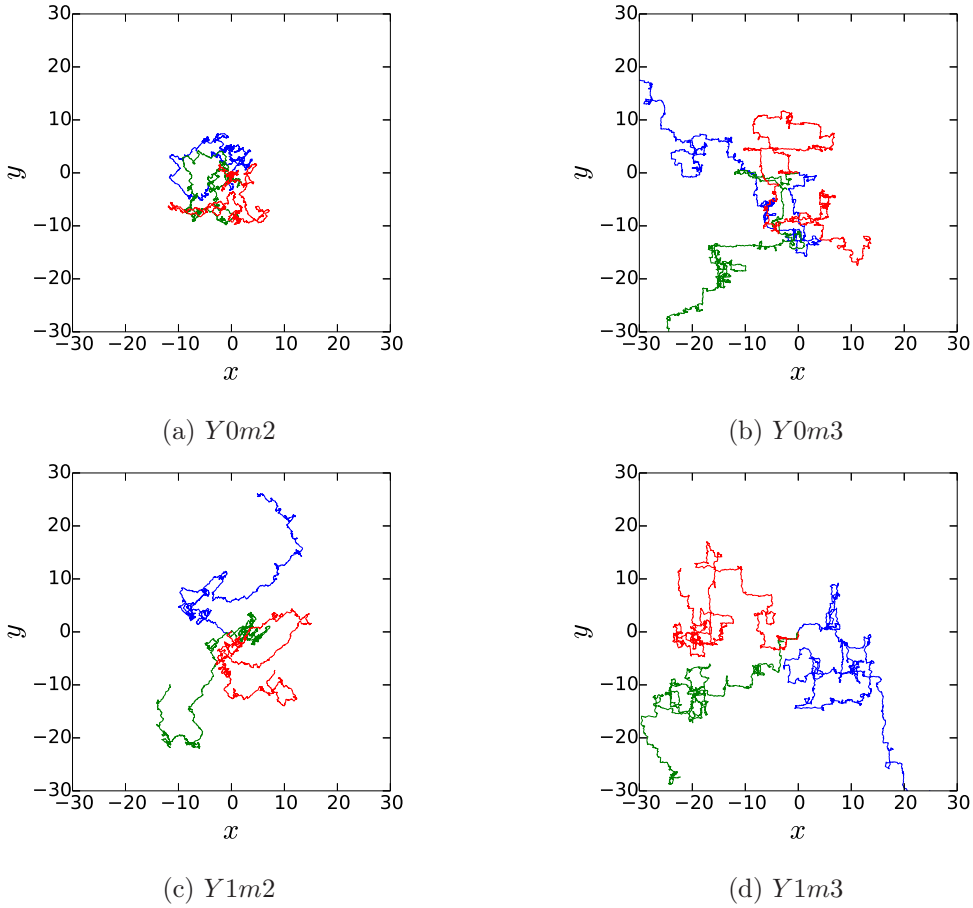

(a) $Y0m2$ (b) $Y0m3$

(c) $Y1m2$ (d) $Y1m3$

Figure 4.23 – Sample path of randomly selected tracers for a maximum strain window of 10. The starting positions of all the tracers was shifted to $(0, 0)$. Note the saturation of the fluctuations for m2. At this stage the $Y1$ protocol is just about to reach the second diffusive regime, hence the confinement effects for $Y1$ are less pronounced.

a homogeneous shear band percolating the entire system does not induce any internal stress. These modes thus could develop at no energy cost, therefore they are favored by the system. Figure 4.24 shows the eigenspectra of the two kernels which show a striking difference at the eigenvalues close to 0. While at low eigenvalues the spectra are alike, at the eigenvalues close to 0 they differ. The m3 kernel's eigenspectra is similar to the Fourier kernel's [171], and soft modes are present in the kernel. On the other hand, there are no soft modes in the m2 kernel since its spectra has a negative slope at $p = 0$. The lack of these modes does not affect the short time behavior as we have shown, it has a dramatic impact however on the long time behavior since enforces the plastic strain, and, accordingly, the displacement fluctuations to saturation. Long term diffusion is therefore excluded for a kernel with no soft deformation modes. Although both kernels were ought

to model the same phenomenon the only difference being in the loading direction, m2 fails to do so reflecting how sensitive these lattice models are to the details of the particular discretization.

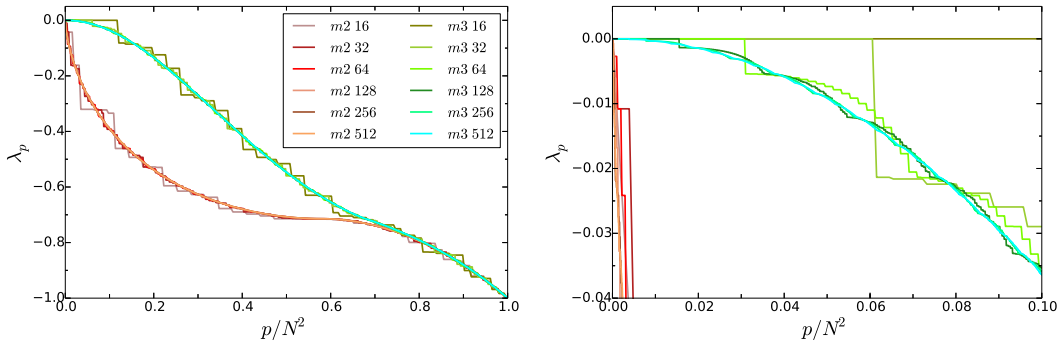

Figure 4.24 – Eigenspectra of the two finite element kernels for various system sizes. While m3 features soft modes, m2 does not.

In this particular case, the discrepancy in the eigenspectra for the m2 kernel is the result of the geometrical frustration in the near field stress. Recall that soft modes are shear bands, and to give an intuitive idea about the reason they induce no stress, we showed the stress generated by a partial and a percolating shear band, respectively, for both kernels on Figure 3.14, in chapter 3. For both kernels, a partial shear band induces an elastic stress within the material and this stress is the largest at the edges of the band, which makes sense since those are the sites which will yield to propagate the band. For m2 however there is a large residual stress along the two sides of the length of the band. While all the residual stresses vanish at the closeup of the band for m3, strong residual stress spots remain at the two sides of the band for m2 due to the geometrical frustration in the neighboring tiles. Our square tile discretization scheme thus does not allow for the healing of the shear bands for m2, in other words, for the development of soft modes which, as we have shown, leads to a pathological long term behavior and breaks down long term diffusion.

4.4 Scaling properties of a minimal kernel

We have seen that soft modes are necessary to recover genuine properties of amorphous plasticity including diffusion and scaling. The question thus naturally arises: are soft modes enough to recover these properties? Is a kernel with reasonable symmetries and soft modes enough? If so, why bother with the rather involved process of building and discretizing long range Eshelby kernels, as well as with the large computation time associated to long range interactions?

Attempts have been made to use a simplified, short range kernel with nearest-neighbor interactions which nevertheless reflects the symmetry of the quadrupolar kernel [119].

The kernel involves nearest neighbor interactions and is defined as shown in Table 4.1. This kernel preserves the quadrupolar symmetry, i.e. it is negative along the $\pm\pi/4$

-1/4	1/2	-1/4
1/2	-1	1/2
-1/4	1/2	-1/4

Table 4.1 – Short ranged quadrupolar kernel.

directions and positive on the vertical and horizontal directions.

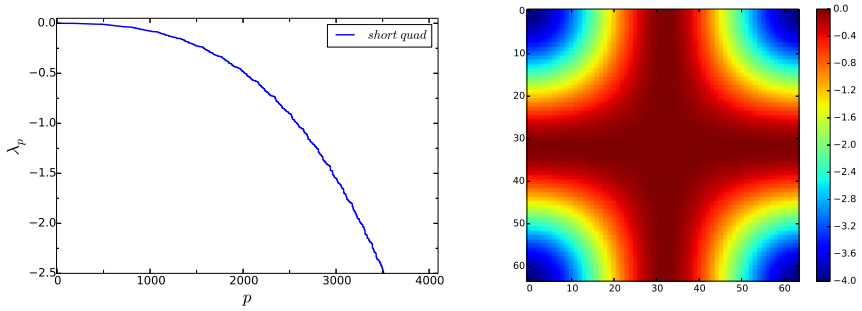

Figure 4.25 – Eigenspectrum and Fourier transform of the short range quadrupolar kernel.

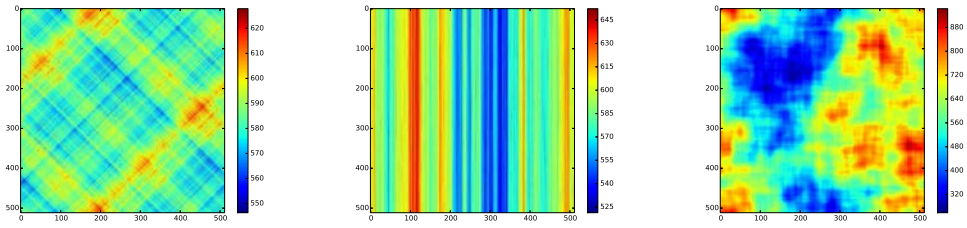

Figure 4.26 – Strain maps belonging to different kernels: quadrupolar, dipolar and short range quadrupolar.

Most importantly, as shown on Figure 4.25, the short range quadrupolar kernel exhibits soft modes along the vertical and horizontal directions. Indeed, the Fourier transform of the kernel is given by $-k_x^2 k_y^2$, therefore we have a series of nontrivial null eigenvalues along the $k_x = 0$ and $k_y = 0$ directions. Alternatively, one can notice that the kernel sums up to zero along any vertical or horizontal profiles. Consequently, a shear band along the 0 or $\pi/2$ direction induces no residual stress.

The kernel shows localization and diffusion, similar to the quadrupolar and the dipolar kernels. On the other hand, avalanche scaling is very different: we obtain $\tau = 1.05$ for the avalanche exponent and $\theta \approx 0.1$ for the stress barrier distribution exponent. Other, finite size related exponents not discussed here are different as well for the short range kernel, hence it definitely falls in another universality class than the long range dipolar or quadrupolar kernels.

As it was revealed in [119] and is shown on Figure 4.26, the short quadrupolar kernel features localization, the emerging shear bands are however short, and by no means they percolate through the system. On the other hand, for the long range kernels shear bands are long. While percolating shear bands are soft modes of the short quadrupolar kernel, the short range nature of the interaction just does not allow for them to develop entirely. This observation helps clarifying the mystery between the similarities of scaling properties, in particular, avalanche distributions between line depinning ($\tau = 1.25$) and plasticity ($\tau = 1.3$): both for the long range quadrupolar and dipolar kernels most of the activity happens along narrow bands. In the depinning pictures this scenario indeed corresponds to the propagation of a one dimensional line in a random landscape. Of course, eventually the activity moves to other bands, thus the collective effect of these loosely coupled bands may be at the origin of the discrepancies. With that in mind, the considerable difference in the scaling properties of the short range quadrupolar kernel arises from the different localization it exhibits. Soft modes are thus necessary, but not enough to reproduce scaling properties of amorphous plasticity: a long range kernel is indeed necessary.

4.5 Summary of scaling relations

kernel	τ	α	β	γ	a	b	θ	δ_s	δ_l
m2	1.35 (1.27)	1.1	-0.2 (-0.2)	1.25 (1.285)	0.6	0.9	2/3	1.05	x
m3	1.3 (1.27)	1.1	-0.2 (-0.2)	1.25 (1.23)	0.6	0.9	2/3	1.05	1.6
m2F	1.3 (1.27)	1.1	-0.2 (-0.2)	1.25 (1.23)	0.6	0.9	2/3	-	-
m3F	1.3 (1.27)	1.1	-0.2 (-0.2)	1.25 (1.23)	0.6	0.9	2/3	-	-
MD	1.25	0.9	0.2	1.3	-	-	[0.4..0.6]	1	-
short quad	1.05	-	-	-	-	-	0.1	-	-

Table 4.2 – Summary of scaling exponents for the four kernels and molecular dynamics [150, 74]. Protocol does not have an impact on scaling. Values in the parentheses are obtained from scaling relations. Values have an accuracy of 0.05.

The scaling exponents of all the quantities we tested are independent on the protocol, we can thus conclude that introducing disorder either through thresholds or slip amplitudes does not affect universality. The choice of the kernel however leads to qualitatively different phenomenology. Our results are summarized in table 4.2. The short term and

long term diffusion coefficient finite size scaling exponents appear in the table as δ_s and δ_l, respectively.

4.6 Conclusions

We found that the hypothesis that avalanches in amorphous media follow slip line (narrow shear band) like patterns is consistent with the observed finite size scaling. Short term diffusive behavior is governed by the rare kicks of individual slip lines, which is confirmed by the finite size scaling of the diffusion coefficient. At long times, diffusion is governed by the collective effect of diffusing shear bands which leads to non-trivial scaling of the diffusion coefficient. The next step would be to carry out a systematic spatial correlation analysis on the strain or displacement patterns in individual avalanches.

Long time behavior is sensitive to the kernel (no soft modes - no diffusion), however the proper symmetry of the kernel and soft modes alone are not enough to reproduce the right universality class. On the other hand, all the universal properties are robust with respect to the protocol. While a realistic disordered landscape (threshold and slip amplitude distribution) has yet to be gathered from MD, we do not expect that it would have considerable impact on the universal properties.

Chapter 5

Application to amorphous composites

Contents

In the previous chapters we showed that the elastic interaction kernel associated to rearrangements in amorphous materials features soft modes that lead to localization and anomalous strain fluctuations. This shear banding and the associated increased fluctuations are at the origin of the brittleness of amorphous materials, for instance, glasses. Recent experiments have shown that shear banding can be controlled by the introduction of a second phase into the amorphous bulk [82]. The role of this second component is to block the development of shear bands. Such composite materials then become reinforced. In this chapter we use the mesomodel with extremal dynamics and the Fourier stress redistribution kernel to model the reinforcement of amorphous materials by hard inclusions. Hard inclusions are modeled as any other lattice site, but with higher yield thresholds. With this simple modification we investigate the flow stress increase with the hard inclusion concentration and explain the observed finite size effects by a simple analytical model based on strain localization, more precisely the percolation of shear bands in between hard inclusions.

5.1 Inclusions in an amorphous bulk

Introducing harder particles into an amorphous material has been used to increase the yield strength of these materials [180]. For example, adding rigid particles or fibers improves the elastic properties of the final composite. From the theoretical point of view, the determination of the effective elastic properties of such a material is a homogenization problem extensively investigated for the case of linear elastic properties [180]. On the other hand, results concerning nonlinear behaviors like fracture [149, 134] or plasticity [35, 50, 185, 167] are less complete. Moreover, standard homogenization techniques fail to capture size effects [35]. Strain-gradient theories [64] have succeeded in reproducing size dependence, however they rely on the introduction of an artificial internal length scale, furthermore, they only predict the average behavior and cannot reflect sample-to-sample fluctuations.

The introduction of hard inclusions into a ductile matrix tends to increase the effective yield stress, the application of composite materials thus are numberless. A good illustration of the practical usage of this reinforcement effect can be found in the development of road pavement materials [38, 198]. The mastic asphalt is composed by relatively large (centimeter scale) stones and a filler material. The filler material consists of smaller (micrometer scale) rigid filler particles and the viscous bitumen. The filler particles make the bitumen viscoplastic and the centimetric scale stones reinforce the mastic asphalt (Figure 5.1).

Mastic asphalt is a soft material, the reinforcement effect of inclusions however applies for hard materials as well. Another illustration of reinforcement is the introduction of soft particles (a second, more ductile phase) in metallic glasses [61, 75] where the ductility of the second phase gives control over the development of shear bands, and, in order over the nucleation of cracks. Interestingly, a reinforcement effect is obtained despite the

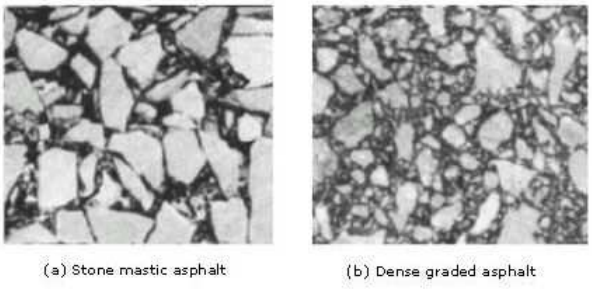

Figure 5.1 – Asphalt is composed of stones and a filler. The filler consists of bitumen and micrometric filler particles in order to increase the filler composites viscosity. The bitumen with filler particles is thus confined between the rougher (a) or finer (b) grained stones [196].

fact that the effective yield stress of the material is decreased due to the soft inclusions (Figure 5.2). In particular, the insertion of crystalline inclusions has been shown to concentrate shear bands in between the inclusions [4] (Figure 5.3).

The understanding of the plastic behavior of amorphous composites is thus crucial in tailoring the mechanical properties of modern materials. Theoretical and numerical modeling methods have been recently deployed to study the effects of microalloying in metallic glasses [49, 67, 4] and of the addition of aggregates in mastic asphalt [1, 3, 2]. These methods however focus on effective properties rather than fluctuations. In chapter 3 however we have shown that due to the presence of soft modes in the elastic kernel fluctuations keep increasing over time, and this fluctuation, as discussed in chapter 4, leads to finite size effects. The critical nature of the yielding transition as well as the localization make simple homogenization descriptions insufficient. Unlike standard analytical calculations or finite element methods, mesomodels were designed to account for fluctuations, in this section therefore we propose an alternative approach to model the plastic behavior of an amorphous matrix reinforced by hard particles.

We use the depinning-like elasto-plastic model introduced previously [172, 171, 190], under the assumption that the elastic properties of the material are homogeneous. This is clearly a strong assumption to make, it allows however for the use of the translation invariant Green's function introduced in chapter 3. In the following, we thus probe the effects of the plastic heterogeneities only. Only the plastic disorder is then considered and local yield thresholds are drawn from a bimodal distribution.

Numerical results show a complex size dependence of the flow stress on the introduction of hard particles. We explain the localization mechanism of the plastic strain and, in turn the flow stress size-dependence by developing a simple analytical, model. Denoting by N the linear size of the system, this model nicely captures the reinforcement size effects in $(\log N/N)^{1/2}$ observed numerically and we show that reinforcement is related to the percolation of shear bands throughout the system in between the hard inclusions. This work has been published in [187].

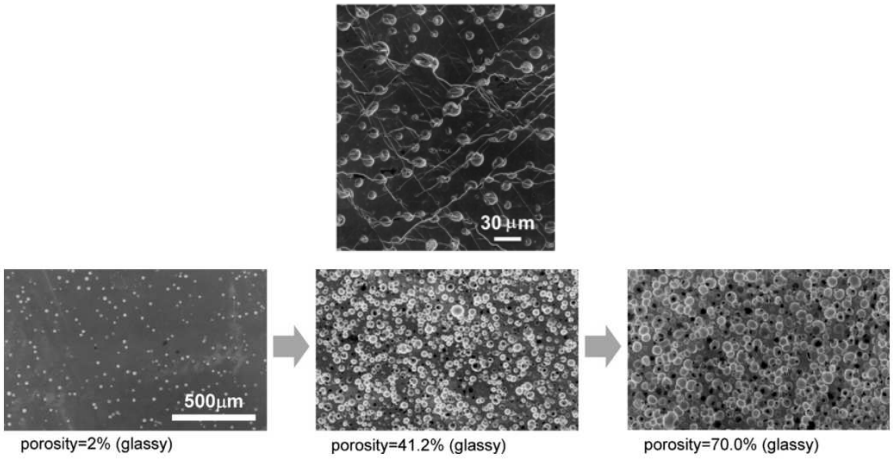

Figure 5.2 – Porous glass alloy. Pores prevent the nucleation of percolating shear bands, thus reinforce the material. Figure from [82].

5.2 Introducing inhomogeneities

The simple depinning like model used so far can be easily extended to model amorphous composite materials. Recall that the stress caused by the plastic slips could be regarded as the superposition of the stress induced by each individual inclusion. So far we have assumed that the elastic properties of the material are homogeneous, thus the stress contribution of the individual inclusions could be computed as the properly centered stress Green's function. In order to use the same method, here we keep this assumption and only the effect of plastic disorder will be considered. For a more accurate method on how to compute the stress field induced by an inclusion in a material with inhomogeneous elastic properties, see [195]. Note however, that taking into account elastic inhomogeneities would involve the use of as many Green's functions as the number of sites in the system. Moreover, the loss of translation invariance causes further problems in imposing periodic boundary conditions. The issue of elastic heterogeneities could be addressed via finite element Green's functions, by building an effective Green's function associated to the inhomogeneous elastic constants. Our purpose here is however to keep the model as simple as possible, therefore we assume homogeneous elasticity within the system.

The amorphous composite is represented by a number of hard inclusions N_{inc} distributed randomly over the system. The linear size of the system is N, hence in our two dimensional model there are a total number of N^2 sites in the system. The fraction of the hard inclusions is defined as $\Phi = N_{inc}/N^2$ and for a fixed concentration Φ always the same number of hard inclusions is inserted into the system. Their position is uncorrelated (except that there can be only one hard inclusion at a given position). Their size is considered the same as the mesh size which is our mesoscopic length scale at which

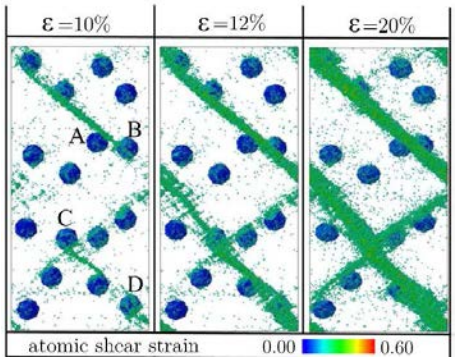

Figure 5.3 – Atomistic simulation of metallic glasses with crystalline inclusions from [4]. Note the persistent shear localization along long, percolating bands in between the inclusions.

we discretize. In metallic glasses [61] or filler particles in bitumen [38] the size of the hard inclusions can be significantly larger than this mesoscopic length scale. This could, in principle, be accomplished in our model by either considering a size distribution of hard inclusions in which a hard inclusion can be of size of several sites or a correlation length of their position causing clusters of hard inclusions. For now however we restrict ourselves to the simpler case of small hard inclusions uniformly distributed along the system as most of the following analysis is generic enough to hold in more complex cases as well.

The plastic thresholds of the amorphous matrix and the hard inclusions are drawn from a bimodal distribution. For the matrix, thresholds are uniformly distributed from $\sigma^c \in [\overline{\sigma^c} + \delta\sigma^c; \overline{\sigma^c} - \delta\sigma^c]$ with $\overline{\sigma^c} = 1$ and $\delta\sigma^c = 1/2$. The inclusions can be either harder or softer (more ductile or less ductile) then the matrix, but as their nature is often crystalline, we expect a narrow distribution of their plastic properties, therefore we consider a constant plastic threshold $\sigma^c = \Sigma^H$ in this case meaning that all the hard inclusions have the same yield stress and, in contrast to the matrix, this does not change after they experience plastic deformation. In the following, we restrict ourselves to the study of hard (less ductile) inclusions ($\Sigma^H > \sigma^c$). Moreover, we consider that the typical plastic strain associated to a plastic deformation is the same for the matrix and the hard inclusions which, for a fixed system size leaves us with two parameters only: the hard site concentration Φ and their yield stress Σ^H.

Simulations were performed with sizes ranging from $N = 16$ up to $N = 256$ and a number of 40 independent realizations of the disorder and hard sites positions. The fraction of hard sites varied between $\Phi \in [2.5 \times 10^{-4}, 0.99]$. Different values of yield strengths were used for the hard inclusions, $\Sigma^H = 4, 10, 40, 10^8$, the latter in order to mimic virtually infinitely hard inclusions. Except for the largest value there is no qualitative difference for the actual value of Σ^H and most of the results will be presented for $\Sigma^H = 10$. Whenever the value of Σ^H plays a role, it will be discussed separately.

5.3 Size dependent flow stress

5.3.1 Amorphous matrix

We first review size effects for an amorphous matrix, in the absence of hard particles. The flow stress Σ^F of the material is defined as the maximum stress experienced by the material along the simulation. It has been shown [171] that the flow stress has a considerable size dependence.

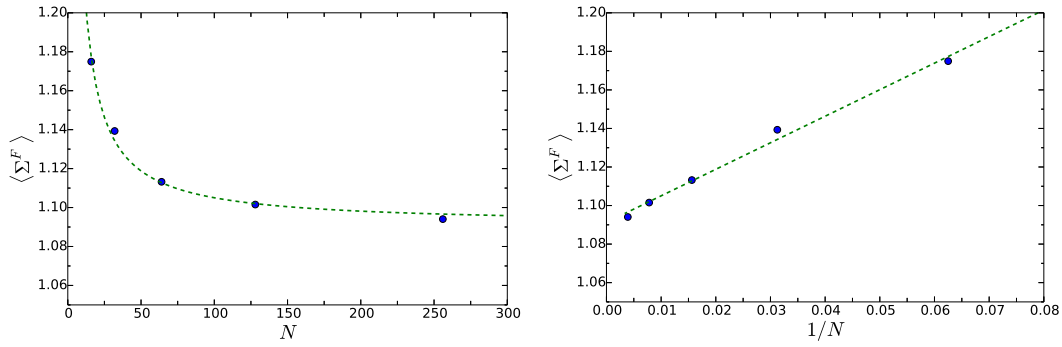

Figure 5.4 – Variation of the average flow stress $\langle \Sigma^F \rangle$ with the linear system size N for an amorphous matrix ($\Phi = 0$) with local thresholds from $\sigma^c \in [0.5; 1.5]$. The dashed line corresponds to $\langle \Sigma^F \rangle = \Sigma^* + A/N$.

Figure 5.4 shows the system size dependence of the flow stress and we see that it obeys a simple power-law:

$$\Sigma^F = \Sigma^* + \frac{A}{N} \tag{5.1}$$

where A is a constant and

$$\Sigma^* = \lim_{N \to \infty} \Sigma^F \tag{5.2}$$

is the flow stress in an infinitely large system. Note that this relationship is not a mere consequence of the central limit theorem as the stresses within the system are strongly correlated: for instance, the values of the effective flow stress are significantly larger than the simple average of the local thresholds $\overline{\sigma^c} = 1$.

Such a power-law dependence is consistent with the critical nature of the model [16, 171, 172]: the flow stress can be considered as the critical driving threshold between a static phase (no plasticity) and a dynamic phase (plastic flow). In the depinning framework, the flow stress would correspond to the critical force, thus its size dependence reflects a divergence of the correlation length: $\xi = N \propto |\Sigma^F - \Sigma^*|^{-\nu}$. With present results, we recover $\nu \approx 1$ [171, 172].

Figure 5.5 shows the same critical behavior: the variation of the standard deviation of the flow stress with the average flow stress shows a linear relationship: $\delta\Sigma^F \propto (\Sigma^F - \Sigma^*)$ and this is consistent with the expected critical behavior [191] $(\Sigma^F - \Sigma^*) \propto \delta\Sigma^F \propto$

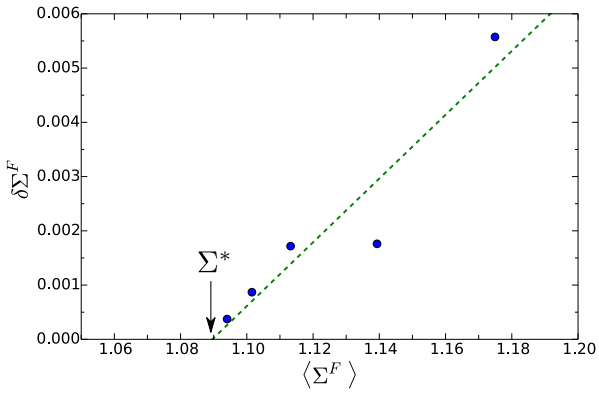

Figure 5.5 – Variation of the standard deviation $\delta\Sigma^F$ of the flow stress with the average flow stress $\langle\Sigma^F\rangle$ for an amorphous matrix with local thresholds from $\sigma^c \in [0.5; 1.5]$ and system sizes $N = 16, 32, 64, 128, 256$. Data is obtained for 40 independent realizations. As expected for a critical transition, a linear dependence is observed. Extrapolating towards zero fluctuations one can estimate the flow stress Σ^* of an infinite system. For the fluctuations then we have $\delta\Sigma^F \propto (\Sigma^F - \Sigma^*)$

$N^{-1/\nu} = N^{-1}$. As expected, as the system size approaches infininty, the flow stress fluctuations vanish and one can use the extrapolated intercept value to estimate the infinite size flow stress Σ^*.

5.3.2 Amorphous composites

In this section, we discuss the dependence of the flow stress on the concentration of the hard sites and its system size dependence, in other words: how does the introduction of hard sites alter the critical finite-size scaling?

Size dependence

As shown on Figure 5.6, for low concentration of hard inclusions there is no much change compared to the pure elastic matrix: a similar decrease and convergence to a well defined value with the system size is observed. The behavior is remarkably different for large concentrations of hard inclusions: a reverse trend is observed and the flow stress actually increases with the system size. For intermediate concentrations there is no clear trend and the flow stress may even be nonmonotonic.

Reinforcement: sub linear size dependent mixing law

Figure 5.7 shows the increase of the flow stress with the concentration of the hard sites Φ, for an inclusion strength $\Sigma^H = 10$ and various system sizes. Error bars show the standard deviation computed for different realizations of the disorder.

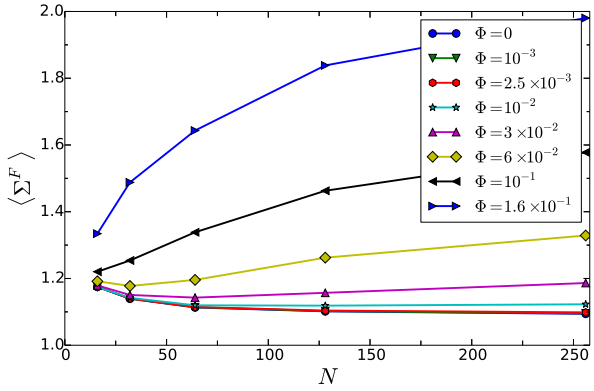

Figure 5.6 – Variation of the average flow stress $\langle \Sigma^F \rangle$ with the linear system size N for an amorphous matrix and for different concentrations of hard sites (Φ). The local thresholds in the matrix are uniformly distributed from $\sigma^c \in [0.5; 1.5]$ and the thresholds of the inclusions is $\Sigma^H = 10$. Depending on the concentration, the yield strength shows either an increasing or a decreasing system size dependence.

The size effects are clear: the larger the system, the larger the reinforcement effect (the associated flow stress) induced by hard inclusions and as the system size increases, the flow stress concentration-dependence converges towards a simple linear mixing law:

$$\Sigma^M(\Phi, N) = (1 - \Phi)\Sigma^A(N) + \Phi\Sigma^H \tag{5.3}$$

where $\Sigma^A(N)$ is the flow stress of a pure amorphous matrix (as plotted on Figure 5.4).

Σ^M obtained from the linear mixing law is known as the Voigt average and usually represents an upper bound [180] for the homogenization of linear properties such as conductivity or elasticity, however it does not necessarily hold for nonlinear properties such as fracture or plasticity, where out-of-equilibrium mechanisms may allow values above the Voigt bound [149, 134]. Despite the lack of precision to model experimental data quantitatively, the Voigt average is widely used to capture the effects of plastic reinforcement [38, 184, 37]

5.4 Hardening and localization

Upon loading, passed a yield stress value, materials yield. If, at some point the material is unloaded, a new, increased elastic limit is obtained: the yield stress thus increases. This behavior is called hardening. The largest possible yield stress that can be achieved is the flow stress. Figure 5.8 shows hardening curves for different values of the hard inclusion yield strength and for different concentrations Φ. Before reaching the stationary state (i.e. before the stress reaches a plateau), two successive hardening behaviors can be observed: the first one is related to the hardening of the pure matrix, whereas the second

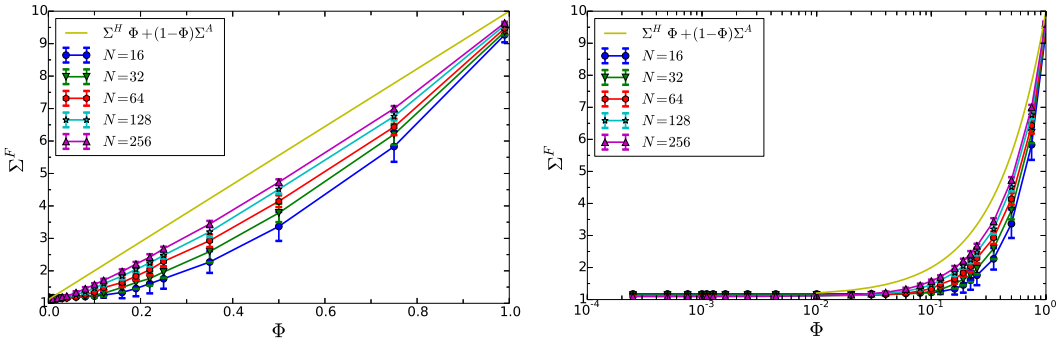

Figure 5.7 – Variation of the average flow stress $\langle \Sigma^F \rangle$ with the concentration of hard sites (Φ) for different system sizes: $N = 16, 32, 64, 128, 256$ for an inclusion yield stress $\Sigma^H = 10$ and matrix thresholds uniformly distributed from $\sigma^c \in [0.5; 1.5]$. For better visualization of low concentration values, the same data is shown on a semi-logarithmic scale.

one appears due to the hard inclusions. Again, if the concentration is low, the hardening curves remain unchanged compared to a pure matrix.

5.4.1 Statistical hardening of the amorphous matrix

In order to better understand the hardening of the composite, we again first review the hardening of a pure matrix, which has been discussed in [171, 172]. In the extremal dynamics used here, always the site that has an elastic stress closest to its threshold yields, and, upon yield, the residual stresses are renewed in the whole system. The hardening in this case is a direct consequence of the systematic pruning of the weak sites, the ones that have the lowest stress barrier, and, consequently, require the least external stress to prune. The systematic exhaustion of the sites with low thresholds leads to a skewed threshold distribution in the stationary state: although the thresholds are always drawn from a uniform distribution, higher threshold values are overrepresented in the system due to the repeated removal of lower threshold values. This is a typical feature of self organized criticality models. For example, the Bak-Sneppen evolutionary model of fitnesses shows a similar convergence to a skewed distribution, predicting that below a critical fitness a site cannot survive [13]. Figure 5.9 shows the evolution of the threshold distribution $P(\sigma^c)$ over increasing plastic strain. Initially, thresholds show a uniform distribution. As the system approaches the stationary state, the distribution becomes more and more skewed towards the larger values until a stationary threshold distribution is reached. This gradual exhaustion clearly leads to statistical hardening: as the external stress is always adjusted to flip the weakest site, a skewed distribution of thresholds means that statistically larger external stress values are more likely to occur.

The same behavior is captured when investigating the stress barrier (effective threshold) distribution $P(\sigma^{eff})$, i.e. the extra stress necessary for the sites to yield (Figure

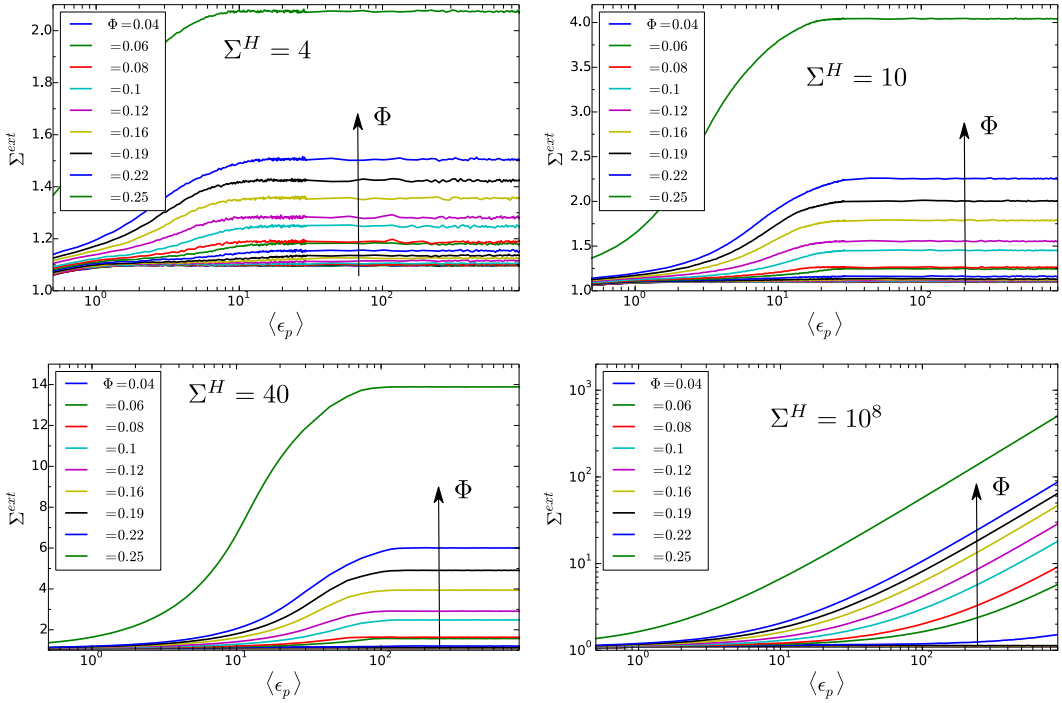

Figure 5.8 – Stress-strain curves for different concentrations of hard sites $0 \leq \Phi \leq 0.25$ and different inclusion strength: $\Sigma^H = 4$, $\Sigma^H = 10$, $\Sigma^H = 40$, $\Sigma^H = 10^8$ for a system size $N = 64$. Concentrations below $\Phi = 0.04$ are not shown in the caption, however they are plotted. For these low concentrations the hardening effect is not visible.

5.10). For each site, the effective threshold is defined as the additional stress required for that site to yield: $\sigma^{eff} = \sigma^c - \sigma^{el}$. An unstable site is characterized by $\sigma^{eff} < 0$, whereas a stable site has $\sigma^{eff} > 0$. In the extremal dynamics used, the global yield stress is given by the lower end of this $P(\sigma^{eff})$ distribution (recall that the external stress is tuned to always prune the weakest site, i.e. the one with the smallest σ^{eff}). The appearance of a sharp front at the lower end of the distribution indicates the emergence of a macroscopic yield stress. Interestingly, the sharp front develops long before reaching the stationary distribution indicating that a macroscopic yield stress can be defined even in the hardening regime.

5.4.2 Inclusion hardening

As seen from the hardening curves and the threshold distributions, for an amorphous matrix a single hardening regime can be observed. However, when hard inclusion are present in a sufficient concentration, an additional hardening regime is captured, characterized by a linear behavior (Figure 5.11). Interestingly, the hardening modulus (the slope of the stress-plastic strain curves) is independent of the hard inclusion yield strength Σ^H

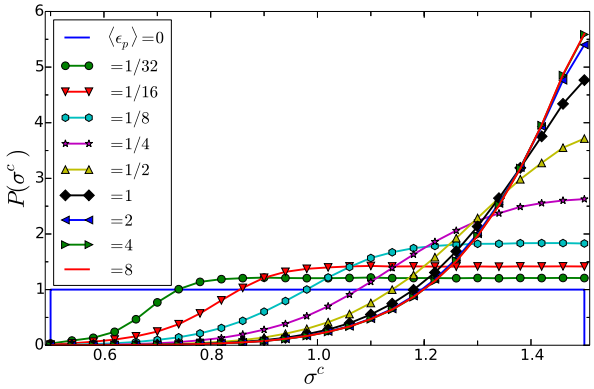

Figure 5.9 – Evolution of the distribution of local plastic thresholds of the amorphous matrix ($\Phi = 0$) upon plastic deformation. A gradual exhaustion of thresholds is observed until a skewed stationary distribution is reached. This is a direct consequence of the threshold dynamics, namely the systematic pruning of the weakest sites.

and it solely depends on the hard sites concentration Φ. Note however, that the harder the inclusions, the longer (larger deformation) it takes to reach the stationary plateau. At small concentrations, the hardening modulus vanishes, indicating that there is no reinforcement of the material, but for larger concentrations, it increases monotonically with the concentration.

Active sites

It is clear that the hardening behavior of the composites is different from that of the amorphous matrix. It would be therefore of interest to capture at which stage of the hardening process the hard sites actually start to deform. To better understand the hardening mechanism, more precisely, the fraction of actively deforming sites until reaching the stationary plateau, we define the normalized average distance between undeformed sites as:

$$Q(\epsilon_p) = \frac{\Phi^{1/2}}{\Phi_u^{1/2}(\epsilon_p)} \tag{5.4}$$

where $\Phi_u(\epsilon_p)$ is the concentration of sites with zero plastic strain when the average plastic strain is ϵ_p. $\Phi^{1/2}$ gives the characteristic distance between the hard sites, and $\Phi_u^{1/2}(\epsilon_p)$ gives the characteristic length between sites with zero strain, i.e. the ones that have not deformed yet. Q is then the ratio between the characteristic distance between hard sites and the characteristic distance between undeformed sites. As sites deform, this latter distance will decrease. Initially, none of the sites have deformed, thus $\Phi_u(0) = 1$ leading to $Q(0) = \Phi^{1/2}$. For large strains, when all the sites have deformed at least once, $\Phi_u(0) = 0$. When $Q(\epsilon_p) = 1$, it is likely that all the matrix sites have deformed at least once, but none of the hard sites deformed yet. $Q(\epsilon_p)$ is a monotonically increasing

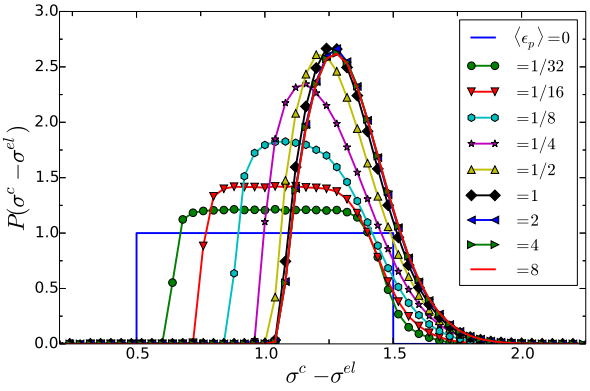

Figure 5.10 – Evolution of the distribution of the effective local thresholds of the amorphous matrix ($\Phi = 0$) upon plastic deformation. The effective thresholds are defined as the stress necessary for a site to yield: $\sigma_c^{eff} = \sigma^c - \sigma^{el}$. The convergence of the sharp lower front is associated to the emergence of a global yield stress since always the sites lying at the lower end of this distribution will yield and the loading stress is adjusted to this lower end value. The yield stress gradually increases upon plastic deformation in the transient hardening regime until it reaches the plateau stress.

function, thus we can conclude that whenever $Q = 1$, that is the point where hard inclusions start to deform. In order to avoid the divergence in Q when all the sites have deformed, we arbitrarily set $Q = N$ when $\Phi_u = 0$, thus

$$Q(\epsilon_p) = \min[(\Phi/\Phi_u)^{1/2}, N] \tag{5.5}$$

In Figure 5.12 we show the evolution of Q alongside with the corresponding stress-strain curve for a small and for a relatively large concentration. At low concentrations, Q reaches a plateau at precisely $Q = 1$ at about the same strain ϵ_p where the stress-strain curve reaches its plateau, we therefore conclude that the stationary state is reached before any of the hard sites deformed. This is compatible with the observation that at low concentrations there is no reinforcement of the composite. Eventually, each hard site will deform ($Q = N$, after the sudden jump), but long after the system reached the stationary state, therefore they do not contribute to the hardening or reinforcement in any way. The situation is very different for larger concentrations: the first hardening regime ends roughly where $Q = 1$, but, as discussed before, there is a second one associated to the hard sites. Indeed, in order to reach the stationary state, some of the hard sites (but not all of them) have to deform. In this case, the hard sites that deform actually contribute to the reinforcement of the material. This mechanism is very different from the low concentration case: while for low concentrations hard sites are deformed by the accumulated internal stresses, here they are deformed by the external loading stress.

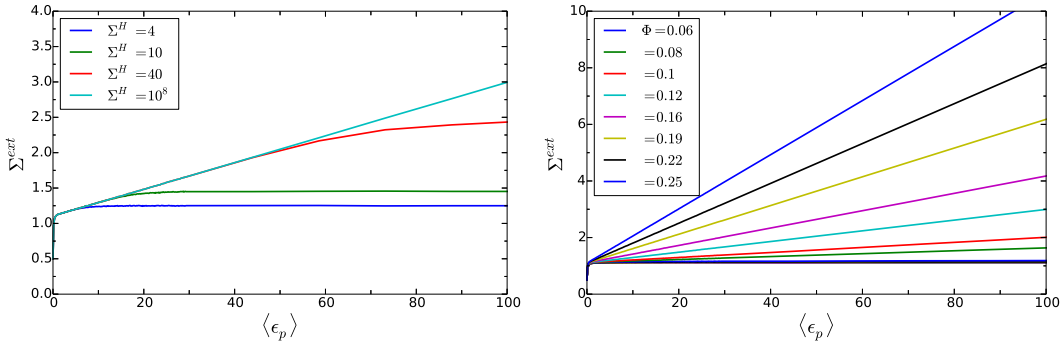

Figure 5.11 – Left: Hardening slopes for various inclusion strengths $\Sigma^H = 4$, $\Sigma^H = 10$, $\Sigma^H = 40$, $\Sigma^H = 10^8$ for a system size of $N = 64$ and a fixed concentration $\Phi = 0.12$. Clearly, the harder the inclusions, the longer the hardening regime, however in the hardening regime, the slope is independent of the inclusion strength Σ^H. Right: Stress-strain curves for (virtually) infinitely hard particles for various inclusion concentrations. The hardening slope increases with the concentration.

An internal skeleton of hard sites

In the initial stage of deformation, only sites of the amorphous matrix can deform. As they experience plastic deformation, an internal stress is accumulated in the system, but hard sites can sustain a much higher level of internal stress then the amorphous matrix, thus they act here as a kind of internal skeleton bearing most of the stress experienced by the structure. This hardening mechanism can be visualized again following the distribution of effective thresholds $P(\sigma^{eff})$ (Figure 5.13). The accumulation of the internal stress on hard inclusions progressively smears out the peak slightly below $\Sigma^H = 10$. Meanwhile, the position of the sharp front corresponding to the macroscopic yield stress keeps increasing. The shift of the lower end of the distribution is thus associated to the first hardening regime (where only the matrix sites deform), while the shrink and disappearance of the peak to the second hardening regime (where hard sites start to deform). Stationarity is reached when the peak has completely disappeared and the lower front settles. For low concentrations, the lower front settles much before the peak disappears, meaning that stationarity is reached long before hard sites start to deform.

A mean field approach of hardening

The reinforcement mechanism can be understood via a simple mean field argument. In the mean field picture, one event of plastic strain ϵ_0 induces an internal elastic stress

$$\sigma^{el} = \begin{cases} -\mu\epsilon_0 & \text{on the deforming site} \\ \mu\epsilon_0/(N^2-1) \approx \mu\epsilon_0/N^2 & \text{everywhere else} \end{cases} \tag{5.6}$$

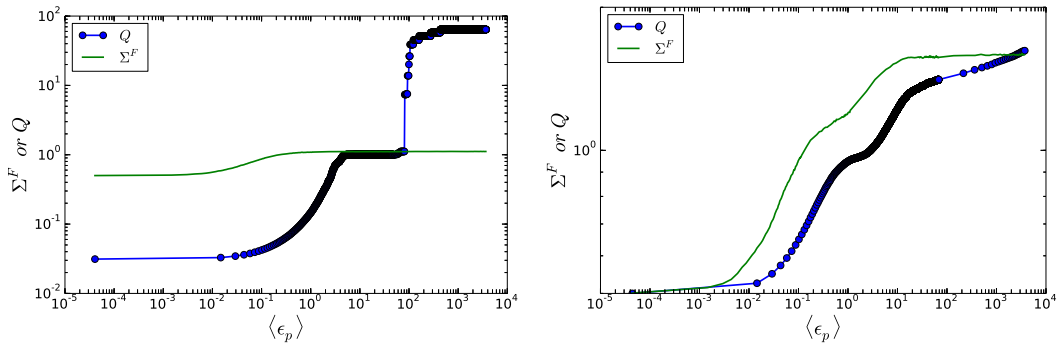

Figure 5.12 – Evolution of the normalized average distance Q for $\Phi = 10^{-3}$(left), $\Phi = 0.25$(right) and $\Sigma^H = 10$, $N = 64$. At low concentration, stationary flow is reached without having to break any hard inclusion, but eventually all the hard sites deform. On the other hand, for large concentrations a second hardening regime is observed and stationary flow is only reached after breaking some of the hard inclusions.

where μ is the shear modulus. We assume that only the (soft) matrix sites deform at this stage, and that their typical deformation is ϵ_s. The plastic deformation ϵ_s of the matrix sites induces an elastic stress in the system. The stress in the soft matrix is given by the local stress drop due to the deformation of the current site plus the stress increase generated by all the other soft sites:

$$\sigma_s = -\mu\epsilon_s + \mu\epsilon_s \frac{1}{N^2} \times (1-\Phi)N^2 = -\mu\epsilon_s\Phi \tag{5.7}$$

where the first term represents the relaxation due to the local deformation, and the second term is the sum of the long-range contributions of all the other sites. The plastic strain in the soft matrix is related to the average plastic strain in the system via

$$\epsilon_s(1-\Phi)N^2 = \langle\epsilon_p\rangle N^2 \Rightarrow \epsilon_s = \langle\epsilon_p\rangle/(1-\Phi) \tag{5.8}$$

since the total number of events is conserved. This leads to

$$\sigma_s = -\mu\frac{\Phi}{1-\Phi}\langle\epsilon_p\rangle \tag{5.9}$$

The global yield stress is given by the minimum stress necessary to prune one site: $\Sigma^F = \min[\sigma^c - \sigma^{el}]$. Since at this stage we assumed that only the matrix sites deform, this minimum will always come from the matrix sites: $\Sigma^F = \min[\sigma^c - \sigma_s]$. Furthermore, assuming $\sigma_c = const$,

$$\Sigma^F = \sigma^c - \sigma_s = \sigma^c + \mu\frac{\Phi}{1-\Phi}\langle\epsilon_p\rangle \tag{5.10}$$

which immediately leads to the hardening slope:

$$M(\Phi) = \frac{\mathrm{d}\Sigma^F}{\mathrm{d}\langle\epsilon_p\rangle} = \mu\frac{\Phi}{1-\Phi} \tag{5.11}$$

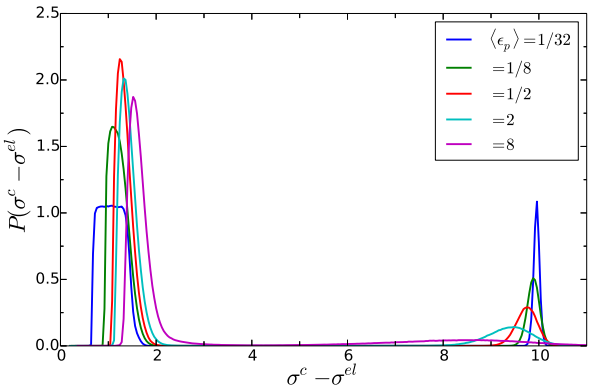

Figure 5.13 – Evolution of the effective threshold $\sigma^{eff} = \sigma^c - \sigma^{el}$ distribution for a composite with $\Phi = 0.16$ and $\Sigma^H = 10$. The accumulation of internal stresses gradually wipes out the peak associated with hard particles. Meanwhile, the sharp front corresponding to the lower end of the distribution increases longer and settles at a higher value than in the case of an amorphous matrix.

We will learn later on that this expression gives only a qualitative dependence of the hardening modulus on the plastic strain, however it readily reflects our observation that the hardening modulus depends only on the shear modulus and the hard inclusion concentration, but not on the system size.

5.4.3 Localization and shear band percolation

The spatial organization of the plastic strain field gives a deeper insight into the hardening process. Figure 5.14 shows the relative plastic strain $\epsilon^p_{ij}/\langle\epsilon^p\rangle$ well in the stationary state for three different concentrations: low ($\Phi = 10^{-3}$), medium ($\Phi = 10^{-2}$) and large ($\Phi = 10^{-1}$), as well as the associated maps of local thresholds σ^c at the end of the simulation, indicating the position of hard inclusions.

Recall that for low concentrations there is no reinforcement. Nevertheless, a tiny number of hard sites (3 in this case) is enough to dramatically retaylor the plastic strain landscape. As expected, the hard inclusions are barely deformed, however they do more than that: they reduce the deformation along the $\pm 45°$ directions that go through them. The $\pm 45°$ directions reflect the symmetry of the elastic kernel and are the natural directions for the plastic activity for a pure amorphous matrix. In the presence of yet a small number of hard inclusions however, plasticity is inhibited along a set of "no-slip" bands that are defined by the positions of the hard inclusions. The hard inclusions lie at the tip of these "no-slip" bands where stress keeps accumulating. This internal stress will eventually prune the hard sites, but is not felt from the outside, hence results in no reinforcement whatsoever.

For medium concentrations, the plastic strain field is more heterogeneous and it is

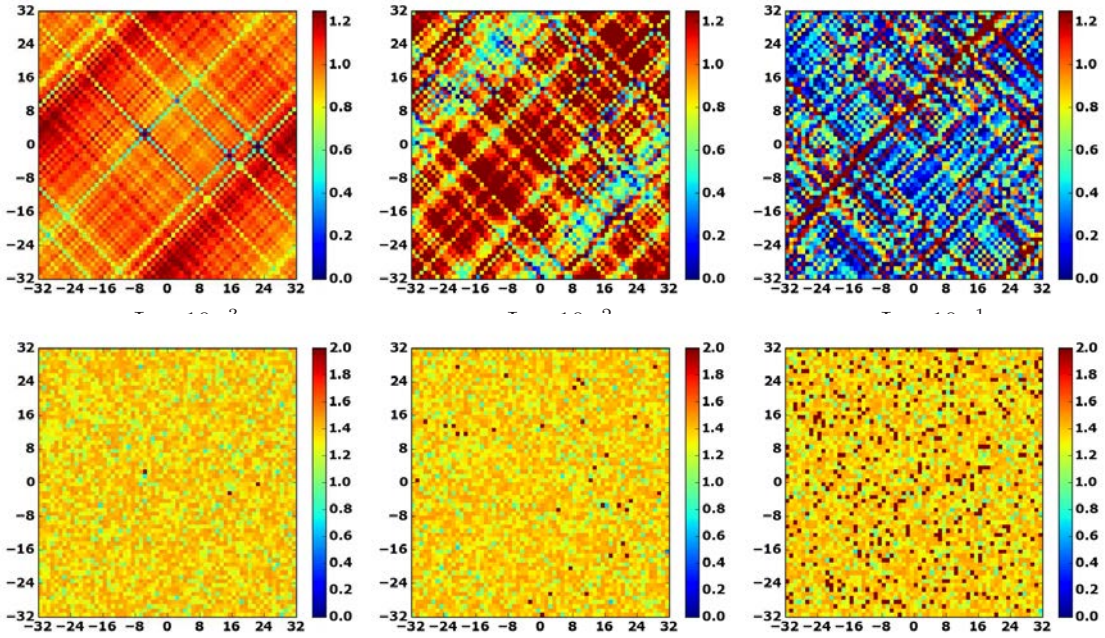

Figure 5.14 – Top row: Maps of the relative plastic strain $\epsilon^{pl}(\vec{r})/\langle\epsilon^{pl}\rangle$ for a system size $N = 64$, inclusion strength $\Sigma^H = 10$, and hard inclusion concentrations $\Phi = 10^{-3}, 10^{-2}, 10^{-1}$. Bottom row: Maps of the associated local plastic thresholds σ^c. The dark dots indicate the position of hard inclusions. At low concentration, no-slip bands form through the hard sites and the accumulated strain is considerably reduced along these no-slip bands. At higher concentrations, no-slip bands cover the whole plane and strain accumulates along a narrow band.

easier to distinguish two kinds of bands, both oriented along the $\pm 45°$ directions: the bands intercepting the hard sites are much less deformed than those with no hard sites.

In the high concentration case, the relative plastic strain field is highly heterogeneous and localized. The vast majority of the plastic deformation is concentrated along a small number of bands. The formation of such a band is represented on Figure 5.15 where the incremental plastic strain over a window of size $\Delta\langle\epsilon^p\rangle = 2$ is represented for increasing starting times. Upon deformation, the plastic activity becomes more and more localized. At this concentration, reinforcing is already visible. The reason of the reinforcement is that the concentration of hard sites is so large, that no shear band can form along the natural slip directions. While at low concentrations shear bands accumulating most of the plastic deformation can form in between the hard sites, at high concentrations this is no longer the case: in order to form even a single shear band, some of the hard sites have to yield. Since the stationary state is reached once at least one shear band is formed, and for high concentrations the formation of any shear bands involve pruning some hard sites, one will experience reinforcement, in contrast to the low concentration situation, where shear bands can form (hence stationarity can be reached) without having to break any

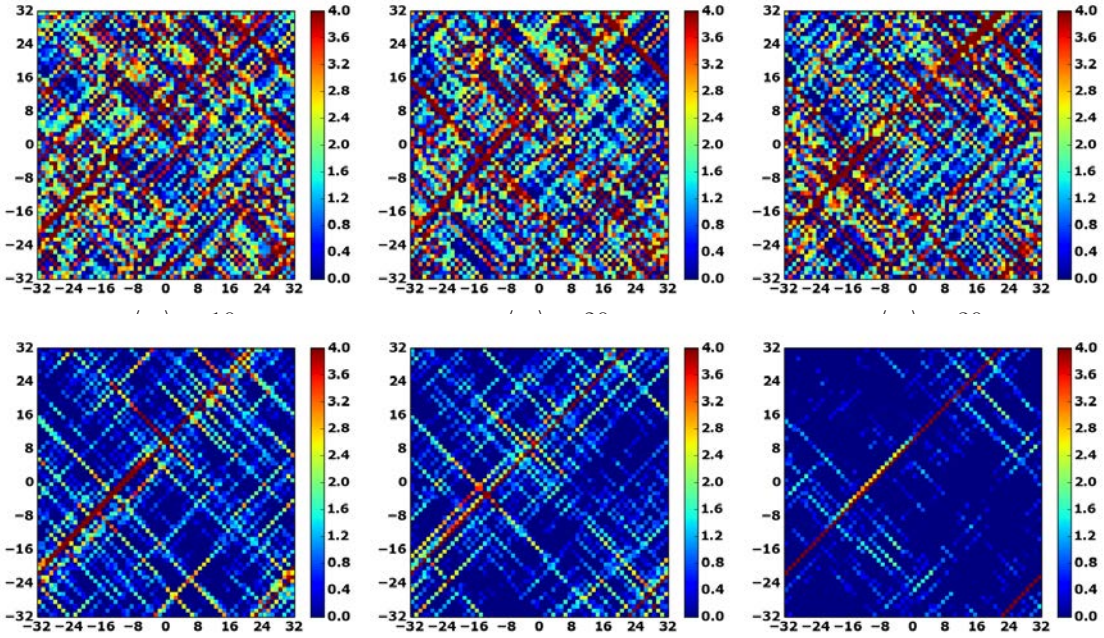

Figure 5.15 – Maps of the incremental plastic strain $\Delta\epsilon^{pl}$ for an inclusion concentration $\Phi = 10^{-1}$, $\Sigma^H = 10$ and $N = 64$, for increasing values of the average plastic strain $\langle\epsilon^{pl}\rangle$. The hard inclusion concentration is relatively high, thus strain accumulates along a single, narrow band over time.

of the hard sites. We can thus conclude, that for low concentrations, hard inclusions are broken by the accumulated internal stress, while at large concentrations by the external stress during the transient period.

5.4.4 The weakest band

To connect the spatial distribution of the plastic activity to the underlying arrangement of the hard inclusions, we consider as elementary units the bands oriented along the $\pm 45°$ directions. We have seen that plastic deformation tends to localize along these bands which reflect the symmetry of the Eshelby quadrupolar stress redistributions. Since hard inclusions are spread in the system randomly, due to statistical fluctuations, each band may contain a different number of hard inclusions. Let us define B_{min} as the weakest band, and B_{max} as the strongest band, having the smallest and respectively the largest average threshold of the sites that lay on the band. If the threshold contrast between the hard sites and the matrix is sufficient, B_{min} and B_{max} are simply the bands containing the smallest and largest number of hard inclusions of all the available $2N$ bands (N bands for each of the 2 possible orientations). Recall that we use periodic boundary conditions, thus all the bands are equivalent. It is then possible to compute the fraction

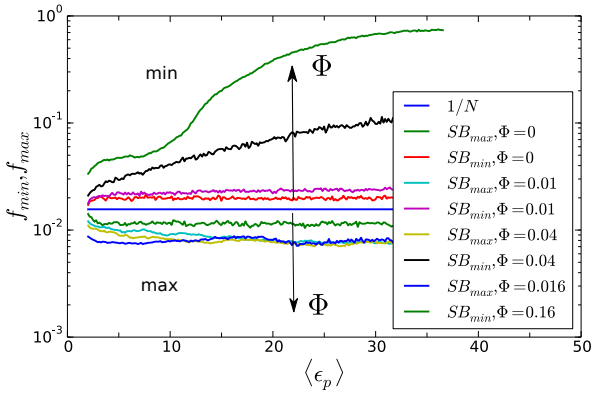

Figure 5.16 – Fractions f_{min} and f_{max} of the incremental plastic strain $\Delta\epsilon^{pl}$ borne by the weakest and strongest slip systems containing the smallest and largest number of hard inclusions. $N = 64$ and $\Sigma^H = 10$. Above a threshold concentration, a dramatic localization is observed along the weakest band.

of the plastic strain accumulated along B_{min} and B_{max} within some strain window (for simplicity, let us take $\Delta\langle\epsilon^p\rangle = 2$, as before):

$$f_{min,\ max} = \frac{\sum_{ij\in B_{\min,\max}} \Delta\epsilon^p_{ij}}{\sum_{ij} \Delta\epsilon^p_{ij}} \tag{5.12}$$

If the strain is uniformly spread, we expect $f_{min} = f_{max} = 1/N$, while if all the strain is localized along B_{min}, for instance, we have $f_{min} = 1$ and $f_{max} = 0$.

For a pure amorphous matrix ($\Phi = 0$ on Figure 5.16), we find $f_{min} \approx 2f_{max}$ meaning that the weakest band deforms about twice as much as the strongest one. For the composites, this effect is somewhat stronger for $\Phi = 10^{-2}$ (which, however still lies below the concentration necessary to block all the bands by hard sites): $f_{min} \approx 4f_{max}$ and no reinforcement is observed at this concentration.

Above a threshold concentration however ($\Phi > 0.01$ on Figure 5.16), all the bands are blocked by one or more hard particles, and this has a dramatic effect on localization: the weakest band bears a larger and larger part of the total strain spread out in the system. Eventually, most of the plastic strain concentrates along the weakest band. We see thus how the underlying structure characterized by the local yield thresholds molds the plastic strain landscape.

5.5 An analytical model

In the previous section we have shown that the plastic strain tends to concentrate along the slip system (band) with the smallest number of hard sites. At low concentrations, there are many bands with no hard sites, above a threhold however all the shear bands

are blocked which leads to the reinforcement of the material. Here we propose a simple analytical model to find the value of this threshold Φ_c and then estimate the value of the flow stress above this threshold.

5.5.1 Percolation

The key idea is that as long as shear bands can percolate through the system, there is no reinforcement, thus the critical threshold Φ_c appears when no shear bands can percolate. In principle, all of the $2N$ bands along the $\pm 45^\circ$ direction have to be blocked, however for the sake of simplicity we only consider one of these directions (since one hard site can block two diagonals, this is not a terribly wrong simplification). Moreover, we assume that the spatial distribution of hard particles is uncorrelated so if we pick a site at random, the probability that the site is a hard inclusion is Φ. We are then interested in the probability that all the diagonals are blocked by hard sites, i.e. the probability that each diagonal contains at least one hard inclusion.

The probability to have *precisely n hard inclusions on a given diagonal* follows a binomial distribution:

$$P(N_d = n) = \binom{N}{n} \Phi^n (1-\Phi)^{N-n} \tag{5.13}$$

where N_d is the random variable counting the number of hard sites on the given diagonal and $N_d = n$ is the event of having precisely n hard sites on that given diagonal.

The probability of having *at least one* hard inclusion on a given diagonal is

$$P(N_d \geq 1) = 1 - P(N_d = 0) = 1 - (1-\Phi)^N \tag{5.14}$$

There are N independent diagonals in the system, thus the probability to have at least one hard inclusion on *each* diagonal is

$$P(B) = [1 - (1-\Phi)^N]^N \tag{5.15}$$

where B stands for "blocked". In other words, $P(B)$ is nothing but the probability that a shear band cannot percolate through the system without hitting a hard site.

The probability $P(B)$ of blocking all the shear bands is shown on Figure 5.17 for various system sizes. Clearly, it increases with the concentration, however it has a considerable system size dependence, and approaches to a vertical jump at $\Phi = 0$ as $N \to \infty$.

We define the percolation threshold as the concentration where $P(B)$ is the steepest, meaning that the threshold is the concentration where the second drivative of $P(B)$ vanishes. Solving

$$\frac{\mathrm{d}^2 P(B)}{\mathrm{d}\Phi^2}\Big|_{\Phi=\Phi_c} = 0 \tag{5.16}$$

for Φ_c leads to

$$\Phi_c(N) = 1 - \frac{1}{(N+1)^{1/N}} \tag{5.17}$$

Figure 5.17 shows the size-dependence of this critical concentration. As $N \to \infty$, $\Phi_c \to 0$. The reinforcement curves on Figure 5.7 show a trend which is consistent with our newly

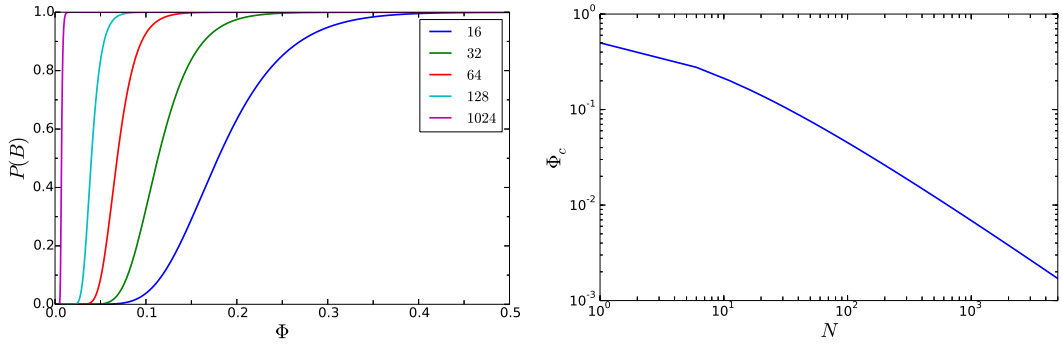

Figure 5.17 – Left: Probability $P(B)$ of having at least one hard inclusion on **each** diagonal, for various system sizes $N = 16, 32, 64, 128, 1024$. The critical fraction Φ_c is given by the inflexion point of $P(B)$ and its system size dependence is plotted on the right.

derived $\Phi_c(N)$ dependence: the larger the system, the smaller the critical concentration Φ_c above which reinforcement is observed.

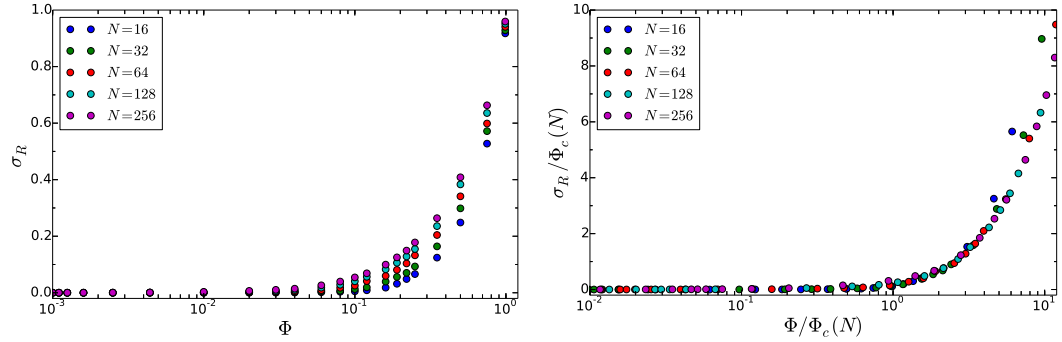

Figure 5.18 – Increase of the rescaled flow stress. The existence of a threshold concentration is put into evidence by the collapse of the reinforcement curves when scaled with the threshold concentration.

We can define the rescaled flow stress $\sigma_R(\Phi, N)$ as the reinforcement factor with respect to the flow stress of the pure amorphous matrix:

$$\sigma_R(\Phi, N) = \frac{\Sigma^F(\Phi, N) - \Sigma^A(N)}{\Sigma^H - \Sigma^A(N)} \tag{5.18}$$

where $\Sigma^A(N) = \Sigma^F(\Phi = 0, N)$. Figure 5.18 shows that by rescaling both σ_R and Φ with the critical concentration, the curves corresponding to different system sizes collapse into a single master curve.

5.5.2 Effective plastic behavior is defined by the weakest band

The weakest band follows weak elastic line depinning

Equipped with the idea that most of the plastic strain is concentrated along the weakest band, we can take one step further and estimate the size and concentration dependence of the flow stress $\Sigma^F(\Phi, N)$. Under the assumption thus that all the plasticity happens along one single (the weakest) band, our two dimensional problem has reduced to a one dimensional problem. This problem is well known from elastic line or crack front depinning studies [65] with an elastic kernel that decays as $1/x^2$ with the distance. Such a kernel is simply a slice of the Eshelby kernel along a diagonal. The homogenization procedure in this context has been studied in [134] and it was found that depending on the disordered landscape one may either recover an effective toughness that is simply the average of the thresholds along the line, or a significantly larger effective toughness. If the threshold landscape in the direction of propagation is smooth enough, the fracture line can follow it smoothly and the effective toughness is indeed the average of the thresholds along the line. This condition is referred to as "weak pinning". On the other hand, if the landscape is rough, the line will jump between subsequent potential minima and the effective toughness in this case is given by the positions actually visited. This situation is called "strong pinning".

For the weakest diagonal, weak pinning conditions hold since the threshold of the hard sites is fixed (does not change upon deformation) and is sufficiently larger than the thresholds in the matrix. For a pure line with no hard sites "weak pinning" conditions would not hold because the threshold landscape fluctuations are too sharp. If the line however contains some hard sites, its flow stress can be computed simply as the weighted average of the flow stress of the pure line and the yield stress of hard sites. The linear mixing law on Figure 5.19 shows that this is a good approximation.

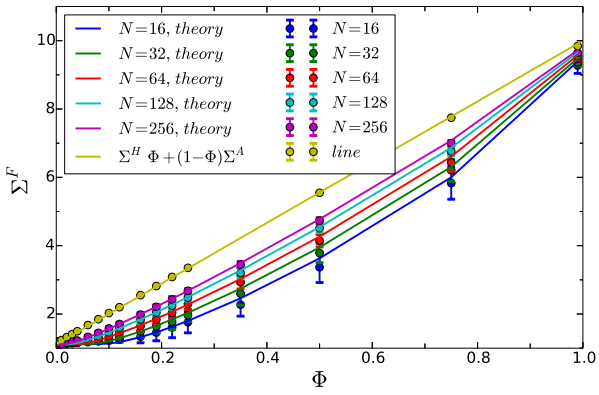

Figure 5.19 – Exact analytical predictions of the flow stress concentration dependence based on the weakest band model (eq. 5.26). The linear mixing law describes the reinforcement of a one dimensional depinning line.

Weakest band yield stress

We have thus seen that although a linear mixing law does not work for the composite, it works very well for a one dimensional elastic line. We have seen as well that most of the plastic strain is borne by the weakest diagonal, thus the flow stress of the system is close to the flow stress of that one diagonal. We can therefore approximate the flow stress of the composite as the weighted average of the flow stress of the amorphous material Σ^A and the hard inclusion yield stress Σ^H *on the weakest band*. Denoting by m the number of hard inclusions on the weakest band, this reads as:

$$\Sigma^F = \frac{N - \langle m \rangle}{N}\Sigma^A + \frac{\langle m \rangle}{N}\Sigma^H \tag{5.19}$$

where $\langle m \rangle$ is the average number of hard sites on the weakest band which remains to be computed.

An exact formula for $\langle m \rangle$ can be obtained starting from the definition of the average:

$$\langle m \rangle \ = \sum_{n=0}^{N} nP(m=n) = \sum_{n=1}^{N} nP(m=n) \tag{5.20}$$

where $P(m=n)$ is the probability of *having precisely n hard inclusions on the weakest diagonal*. The variable n can be trivially rewritten as

$$n = \sum_{k=0}^{n-1} 1 \tag{5.21}$$

so

$$\langle m \rangle \ = \sum_{n=1}^{N}\sum_{k=0}^{n-1} P(m=n) = \sum_{k=0}^{N-1}\sum_{n=k+1}^{N} P(m=n) \tag{5.22}$$

where the second equality is a result of an equivalent reindexing of terms. The sum over n gives the complementary cumulative distribution function, therefore

$$\langle m \rangle = \sum_{k=0}^{N-1} P(m \geq k+1) = \sum_{n=1}^{N} P(m \geq n) \tag{5.23}$$

where we recover the classical result: the expected value of a random variable is given by the sum of 1 minus the cumulative distribution function.

Obviously we still have to find $P(m \geq n)$, the probability that the weakest band contains at least n hard sites. Let us denote by $P(N_d \geq n)$ that a randomly selected diagonal contains at least n hard sites. The event that *the weakest band contains at least n hard sites* is then the same as the event that *all the bands contain at least n hard sites*. Since we assumed the position of the hard sites is independent:

$$P(m \geq n) = P(N_d \geq n)^N \tag{5.24}$$

We have also seen that the distribution of the number hard sites on a diagonal $P(N_d = n)$ is a binomial distribution, thus $P(N_d \geq n)$ is the complementary cummulative distribution of that binomial distribution and it can be expressed with the aid of the regularized incomplete β function I_Φ as

$$P(N_d \geq n) = I_\Phi(n, N - n + 1) \tag{5.25}$$

which gives a closed form expression of the average number of hard inclusions on the diagonal with the minimum number of hard inclusions:

$$\langle m \rangle = \sum_{n=1}^{N} [I_\Phi(n, N - n + 1)]^N \tag{5.26}$$

The flow stress computed using the above formula for various concentrations and system sizes is plotted on Figure 5.19 along with the simulation data and they show a good agreement.

Weakest band yield stress fluctuations

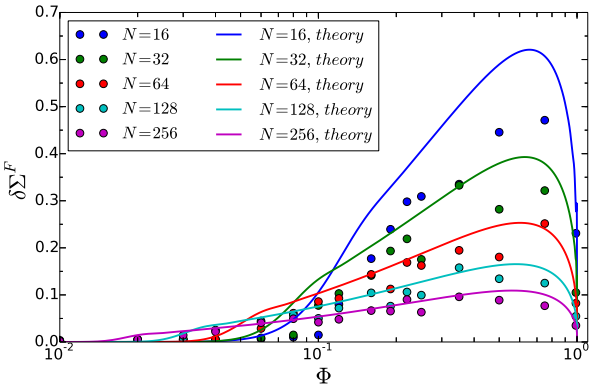

Figure 5.20 – Analytical predictions of the flow stress fluctuations. Since our approach assumes that the positions of the inclusions are independent, it tends to overestimate fluctuations. As the system size (and thus, at constant concentrations, the number of hard sites) increases, the hypergeometric distribution of dependent draws converges towards our assumed binomial distribution of independent draws, consequently the estimation works better for larger systems.

One may try to push the method presented above even further and estimate the fluctuations in the flow stress (i.e. its standard deviation $\delta\Sigma^F$) which is related to the fluctuations of m via

$$\delta\Sigma^F = [\langle \Sigma^{F2} \rangle - \langle \Sigma^F \rangle^2]^{1/2} = \frac{\Sigma^H - \Sigma^A}{N} [\langle m^2 \rangle - \langle m \rangle^2]^{1/2} \tag{5.27}$$

The mean square of m is defined as

$$\langle m^2 \rangle = \sum_{n=1}^{N} n^2 P(m=n) \tag{5.28}$$

Again, n^2 can be replaced by

$$n^2 = \sum_{k=1}^{n} (2k-1) \tag{5.29}$$

and reindexing gives

$$\langle m^2 \rangle = \sum_{n=1}^{N} \sum_{k=1}^{n} (2k-1) P(m=n) = \sum_{k=1}^{N} (2k-1) \sum_{n=k}^{N} P(m=n) \tag{5.30}$$

where the inner sum can be evaluated finally giving

$$\langle m^2 \rangle = \sum_{n=1}^{N} (2n-1) P(m \geq n) = \sum_{n=1}^{N} (2n-1) [I_{\Phi}(n, N-n+1)]^N \tag{5.31}$$

Flow stress fluctuations estimated with the above formula are shown on Figure 5.20 and we see that the prediction follows the right trend. In contrast to the average flow stress estimation however, the prediction of fluctuations is less accurate and systematically tends to overestimate fluctuations. As the system size increases however, the predicted values are closer and closer to the simulation values. We conclude therefore, that this bias is a side effect of our assumption that the position of hard sites is independent. However, at a fixed concentration, always a fixed number of hard sites is spread out in the system, so the number of the hard sites within the different realizations does not fluctuate. This leads to a reduced fluctuation compared to our assumption of placing a hard inclusion on a lattice site with probability Φ where the actual number of hard inclusions in the system could differ in each realization. More precisely, the number of hard sites on a diagonal rather follows a hypergeometric distribution which, however, at large N converges to our assumed binomial, and this is why our prediction works the best for large N.

A manageable approximation

Although we obtained an analytical expression both for $\Sigma^F(\Phi, N)$ and $\delta\Sigma^F(\Phi, N)$, the computation of $\langle m \rangle$ involves a large sum of the regularized incomplete β function evaluated at various points, which, in turn, involves the computation of factorials and that is computationally expensive. In what follows, we derive an approximate but much simpler to handle expression for $\langle m \rangle$.

To that end, we use a result from extreme value theory on the minimum of N independent, identically distributed random variables for the probability to have an outcome N_d less or equal to the average minimum over a block of N draws:

$$P(N_d \leq \langle m \rangle) = \frac{1}{N} \quad \text{as } N \to \infty \tag{5.32}$$

Denoting by

$$f(\Phi, N) = \frac{\langle m \rangle}{N} \tag{5.33}$$

the average fraction of hard inclusions on the weakest band:

$$P(N_d \leq fN) = \frac{1}{N} \quad \text{as } N \to \infty \tag{5.34}$$

It turns out that for random variables coming from a binomial distribution (and in our case, we saw that N_d is binomially distributed), we can utilize a result from cryptography studies [22, 23]:

$$P(N_d \leq fN) = \frac{\Phi(1-f)^{1/2}}{(\Phi - f)(2\pi N f)^{1/2}} \exp[-ND(f||\Phi)] \quad \text{as } N \to \infty \tag{5.35}$$

where $D(f||\Phi)$ denotes the Kullback-Leibler divergence given by

$$D(f||\Phi) = f \ln \frac{f}{\Phi} + (1-f) \ln \frac{1-f}{1-\Phi} \tag{5.36}$$

Denoting by $\epsilon = \Phi - f$, $\epsilon \to 0$ as $N \to \infty$ and we can use of another property of the Kullback-Liebler divergence [22, 23]:

$$D(f||\Phi) = \frac{\epsilon^2}{2\Phi(1-\Phi)} + \mathcal{O}(\epsilon^3) \tag{5.37}$$

so we have

$$\frac{1}{N} = \frac{\Phi}{\epsilon} \left[\frac{1 - \Phi + \epsilon}{2\pi N(\Phi - \epsilon)} \right]^{1/2} \exp\left[-\frac{N\epsilon^2}{2\Phi(1-\Phi)} \right] \tag{5.38}$$

which, to the first order in ϵ becomes

$$\frac{1}{N} = \frac{1}{\sqrt{2\pi}} \frac{\sqrt{\Phi(1-\Phi)/N}}{\epsilon} \exp\left[-\frac{N\epsilon^2}{2\Phi(1-\Phi)} \right] \tag{5.39}$$

Let us define $\epsilon' = \epsilon / \sqrt{\Phi(1-\Phi)/N}$ so the above equation can be rewritten as

$$\epsilon'^2 = 2 \ln \frac{N}{\sqrt{2\pi}\epsilon'} \tag{5.40}$$

This is a transcendental equation in ϵ' and only an approximate solution can be obtained.

To obtain an approximate solution, we define the variable r such that:

$$\epsilon' = \sqrt{2h_N}(1 + r) \, , \tag{5.41}$$

where $h_N = \ln \frac{N}{\sqrt{2\pi}}$. The variable r tends to 0 in the limit of large N. We also have:

$$\epsilon'^2 = 2h_N(1+r)^2 = 2h_N(1+2r) + \mathcal{O}(r^2) \, , \tag{5.42}$$

to first order in r. Using the transcendental equation 5.40 and iterating once in ϵ, we get:

$$\epsilon'^2 = 2\ln\frac{N}{\sqrt{2\pi}\sqrt{2h_N}(1+r)} \ . \tag{5.43}$$

Equating the right hand sides of equations 5.42 and 5.43 leads to:

$$2h_N(1+2r) = 2\ln\frac{N}{\sqrt{2\pi}\sqrt{2h_N}(1+r)} \ , \tag{5.44}$$

$$= \ln\frac{N}{\sqrt{2\pi}\sqrt{2h_N}} - 2\ln(1+r) \ , \tag{5.45}$$

$$= \ln\frac{N}{\sqrt{2\pi}\sqrt{2h_N}} - 2r \ . \tag{5.46}$$

to first order in r. Eq. 5.46 is a linear equation in r, its solution reads:

$$r = \frac{\ln\frac{N}{\sqrt{2\pi}\sqrt{2h_N}} - h_N}{2h_N+1} \ . \tag{5.47}$$

Finally, we obtain for the average fraction of hard sites on the weakest diagonal:

$$f(\Phi,N) = \Phi - \left[\frac{2\Phi(1-\Phi)}{N}h_N\right]^{1/2}(1+r_N) \tag{5.48}$$

where

$$r_N = -\frac{1}{2}\frac{\ln(2h_N)}{2h_N+1} \tag{5.49}$$

$$h_N = \ln\frac{N}{\sqrt{2\pi}} \tag{5.50}$$

Size scaling of the flow stress

The rescaled flow stress $\sigma_R(\Phi,N)$ in this approximation is equal to $f(\Phi,N)$:

$$\sigma_R(\Phi,N) = \frac{\Sigma^F(\Phi,N) - \Sigma^A(N)}{\Sigma^H - \Sigma^A(N)} = f(\Phi,N) \tag{5.51}$$

meaning that $\Phi - \sigma_R(\Phi,N) \propto (\ln N/N)^{1/2}$. As shown on Figure 5.21, the scaling is obeyed for low Φ and large N because that is where the analytical approximation holds.

Figure 5.22 shows the estimates of the rescaled flow stress $\sigma_R(\Phi,N)$ based on the analytical computation of $f(\Phi,N)$. Again, the approximation works the best for low concentrations and large system sizes. The bias is considerable at low N compared to Figure 5.19, which gave a better approximation with an exact expression. We can therefore conclude that the bias is due to the approximations made during the computation of $f(\Phi,N)$. Finally, the distance of the flow stress to the linear mixing law can be computed as

$$\delta = \Sigma^L - \Sigma^F = (\Phi - f)(\Sigma^H - \Sigma^A) \propto (\ln N/N)^{1/2} \tag{5.52}$$

and we see that it obeys the same $(\ln N/N)^{1/2}$ scaling.

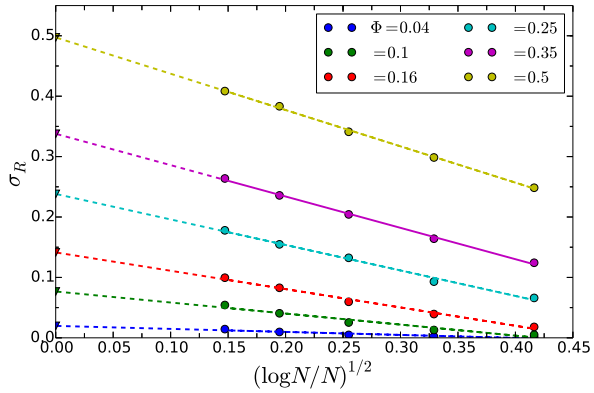

Figure 5.21 – Size scaling of the rescaled flow stress $\sigma_R(\Phi, N)$. Dots indicate simulation data and lines the analytical $(\log N/N)^{1/2}$ prediction. Interception on the vertical axis indicates the $N \to \infty$ limit, i.e. the stress value obtained from the linear mixing law.

Scaling behavior of the hardening regime

Finally, we show how the above analysis along with a modified mean field argument can elucidate the hardening behavior. Figure 5.23 shows that the expression obtained from the simple mean field reasoning for the hardening modulus $M(\Phi, N) = \mu\Phi/(1-\Phi)$ strongly overshoots the simulation data. In order to derive a better approximation, we use our previous knowledge on the localization of the plastic activity along the weakest band. We propose therefore a simplified elastic kernel that obeys the same quadrupolar symmetry as the Fourier kernel used so far, it is however mean field in the sense that we do not account for any decay with the distance from the plastic event. The kernel we used for a system of size N is defined as

$$G_{ij} = \begin{cases} -1 & i = j = 0 \\ \frac{1}{N-1} \approx \frac{1}{N} & i = j \text{ or } i = -j \\ -\frac{1}{N-1} \approx -\frac{1}{N} & i = 0 \text{ or } j = 0 \\ \frac{1}{N^2-4(N-1)} \approx \frac{1}{N^2} & \text{elsewhere} \end{cases} \tag{5.53}$$

As usual, we have stress relaxation at the center, and along the bands oriented towards the 0° (x) and the 90° (y) directions, a positive "kick" along the bands at ±45° and a mean-field stress in the rest of the system. Note that the sum along any band in the ±45° directions is approximately zero:

$$\frac{1}{N^2} \times N + \frac{1}{N} \times 1 - \frac{1}{N} \times 2 = 0 \tag{5.54}$$

meaning that a homogeneous deformation along such a band results in a vanishing internal stress, hence deformations along these directions are soft modes of the kernel. This

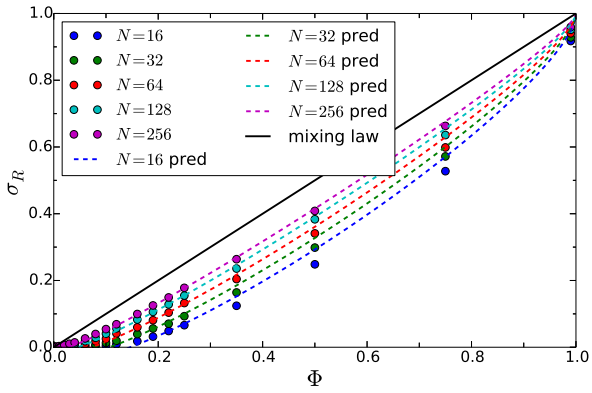

Figure 5.22 – Analytical predictions of the rescaled flow stress concentration dependence. Clearly, our approximation is based on the large N assumption, hence it works the best for large system sizes.

property allows us to consider these bands non-interacting if we neglect the inhomogeneity of the plastic strain along the individual bands. Moreover, along the central band we recover a one dimensional mean field interaction: unit stress drop on the deforming site and a constant stress increase $1/N^2$ everywhere else on the band. We consider thus a set of N non-interacting bands, each of them having a mean plastic strain ϵ_i, so that the mean plastic strain in the system $\langle \epsilon_p \rangle = \langle \epsilon_i \rangle$. During the hardening stage, all the plastic strain is borne by the soft matrix sites since the hard inclusions do not deform. Note that we fixed the average value of the plastic strain in each band, meaning that the typical strain ϵ_{si} borne by each soft site may differ from band to band and is given by

$$\epsilon_{si} = \frac{\epsilon_i}{1 - f_i} \tag{5.55}$$

where f_i is the fraction of hard inclusions on band i.

Since the bands are independent, the internal stress on the soft matrix sites induced by the plastic strain field can be separately written for each band as

$$\sigma_{si} = -\mu\epsilon_{si} + \mu\epsilon_{si}\frac{1}{N} \times (1 - f_i)N \tag{5.56}$$

which can be further written as

$$\sigma_{si} = -\frac{1}{1 - f_i}\mu\epsilon_i + \mu\epsilon_i = -\frac{f_i}{1 - f_i}\mu\epsilon_i \tag{5.57}$$

Here the first term comes from the local relaxation on the deforming site, while the second one is the stress increase due to the deformation of all the other sites on the same band. The effect of deformations along other bands is not counted since the bands are considered independent due to the soft modes.

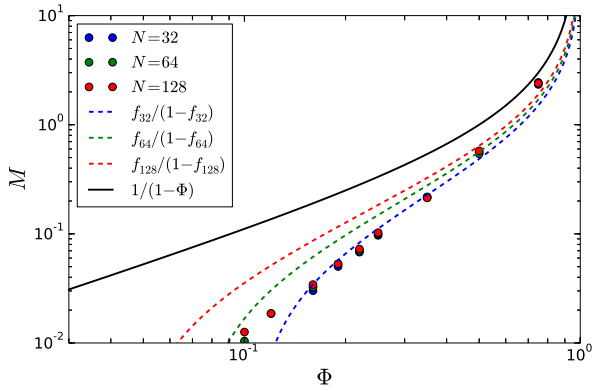

Figure 5.23 – Mean field estimate of the hardening modulus. Although the estimate recovers the right trend, it shows system size dependence which was not observed in simulations.

Again, the external stress is given by $\Sigma^F = \langle \min(\sigma^c - \sigma_{si}) \rangle$ which can be approximated as

$$\Sigma^F \approx \sigma^c + \min\left[\frac{f_i}{1-f_i}\right] \mu\langle\epsilon_i\rangle = \sigma^c + \frac{f}{1-f}\mu\langle\epsilon_p\rangle \tag{5.58}$$

where the second equality holds since $f_i/(1-f_i)$ is monotonically increasing. Recall that f denotes the fraction of hard inclusions on the weakest band. We then finally reached to an expression of the hardening modulus:

$$M(\Phi, N) = \frac{\mathrm{d}\Sigma^F}{\mathrm{d}\langle\epsilon_p\rangle} = \mu\frac{f(\Phi, N)}{1 - f(\Phi, N)} \tag{5.59}$$

The hardening modulus in the linear regime is solely controlled by the fraction of the hard sites on the weakest band. Figure 5.23 shows that the estimate performs much better than the simple mean field approximation $\mu\Phi/(1-\Phi)$, interestingly however we encounter size effects that are not reflected by the simulation data.

We can give an estimate to the strain accumulated during the second hardening (reinforcement) regime ϵ_H:

$$\Sigma^F - \Sigma^H \approx M(\Phi, N)\epsilon_H \tag{5.60}$$

On the other hand, by definition $\Sigma^F - \Sigma^H = \sigma_R[\Sigma^H - \Sigma^A]$ and we saw that $\sigma_R = f$. Putting it all together:

$$\epsilon_H = (1-f)[\Sigma^H - \Sigma^A]/\mu \tag{5.61}$$

leading to the scaling

$$\frac{\mu\epsilon^H}{\Sigma^H - \Sigma^A} - (1-\Phi) \propto (\ln N/N)^{1/2} \tag{5.62}$$

in the limit of large N where $r_N \to 0$.

5.6 Conclusions

The plastic behavior in amorphous composites shows two types of system size dependence: one associated to the amorphous matrix as described in [172] and another one associated to the hard inclusions. While the former results in an $1/N$ dependence of the flow stress with the system size, the latter predicts a size dependent threshold concentration below which no reinforcement is observed. The threshold concentrations corresponds to the percolation of shear bands through the system within the hard inclusions. Above the threshold concentration, the distance of the flow stress to a linear mixing law scales as $(\log N/N)^{1/2}$ and the flow stress increases with the system size. The linear mixing law then gives an upper bound to the flow stress. We have shown that the increase in the flow stress is associated to the breakthrough of the weakest shear band over hard sites and the flow stress value is governed by the accumulation of plastic activity along the weakest band. Finally, we developed a simple model based on the weakest shear band hypothesis that turned out to predict well the flow stress value, its size dependence and even the flow stress fluctuations.

Appendix A

Eshelby inclusions

There are various methods available to compute the elastic fields associated to plastic inclusions and they deliver the solution in various forms [57, 20, 40, 71, 85, 178, 193, 194]. Depending on the quantity of interest, the shape of the inclusion and the boundary conditions, one or the other may be more convenient. Although, theoretically it is possible to connect the results of different methods since, at the end of the day they solve the same problem, in practice this can be cumbersome. For instance, when interested in the closed form solution of the displacement field induced by an ellipsoidal inclusion in an infinite bulk, one may consider Eshelby's solution [10, 57, 193]. For an approximate far-field solution of a two dimensional circular inclusion embedded in an infinite matrix, the complex potential method is more appropriate because it readily delivers the solution grouped by expansion terms. When a circular inclusion is enclosed in a periodic matrix, Picard's method is the most convenient one since the solution in this case comes in the Fourier space [138].

To get an idea about how to attack the inclusion problem, in this section we briefly review the basic idea behind some of the available methods and also present their results for future reference. Let us thus consider a two-dimensional, infinite, linear, isotropic elastic material with a circular inclusion with the very same elastic properties as the bulk. Let us denote by a the radius of the inclusion, by μ and ν the shear modulus and Poisson ratio of the material. Let us further assume that the inclusion suffers a homogeneous pure shear plastic deformation, such that $\epsilon^{inc}_{p\ xy} \equiv \epsilon_0$ and $\epsilon^{inc}_{p\ xx} = \epsilon^{inc}_{p\ yy} = 0$. In other words, the stress-free reference frame of the inclusion has changed: it is now in a stress-free state when his strain compared to the initial reference frame of the undeformed inclusion is ϵ_0. The inclusion is however sorrounded by the elastic bulk, hence it is squeezed into the material. Consequently, the inclusion is unable to reach its stress-free configuration, but at the same time, it "pushes" on the bulk inducing a stress into the whole material.

The problem to solve therefore is: given the size of the inclusion a and its eigenstrain (plastic deformation) ϵ_0, what is the displacement field $\vec{u}(\vec{r})$, and the associated stress $\sigma_{\alpha\beta}(\vec{r})$ within the inclusion and outside the inclusion?

Note that nothing has been stated about why the inclusion suffers a plastic deformation. There are various reasons this could happen including thermal activation or mechanical load, but the activation mechanism is irrelevant in the computation of the above mentioned quantities.

Eshelby's method

Ehelby's original method consists of a 4-step thought experiment [10, 57, 193] (Figure A.1):

1. The inclusion that undergoes a plastic deformation is removed from the matrix. Since they do not interact, the stress is zero both within the inclusion and the matrix.

2. A traction force $\vec{T}$ is applied to the surface of the inclusion to deform it back to its original shape. The stress in the matrix is still zero, but the stress in the inclusion is not. Assuming the deformation is homogeneous (as it will be later on proven), the

stress in the inclusion is proportional to its eigenstrain since that is the necessary elastic strain that deforms it back to its original shape.

3. The inclusion is placed back into the matrix. There is no change in any of the elastic fields compared to the previous step.

4. A force with equal magnitude with the previously applied surface traction, but opposite direction $\vec{F} = -\vec{T}$ is applied along the surface of the inclusion. This force thus cancels the traction and leads us back to the original problem. What is to be noted is that *an inclusion undergoing an eigenstrain has the same effect as applying a body force $\vec{F}$ on the boundaries of the inclusion with no eigenstrain.*

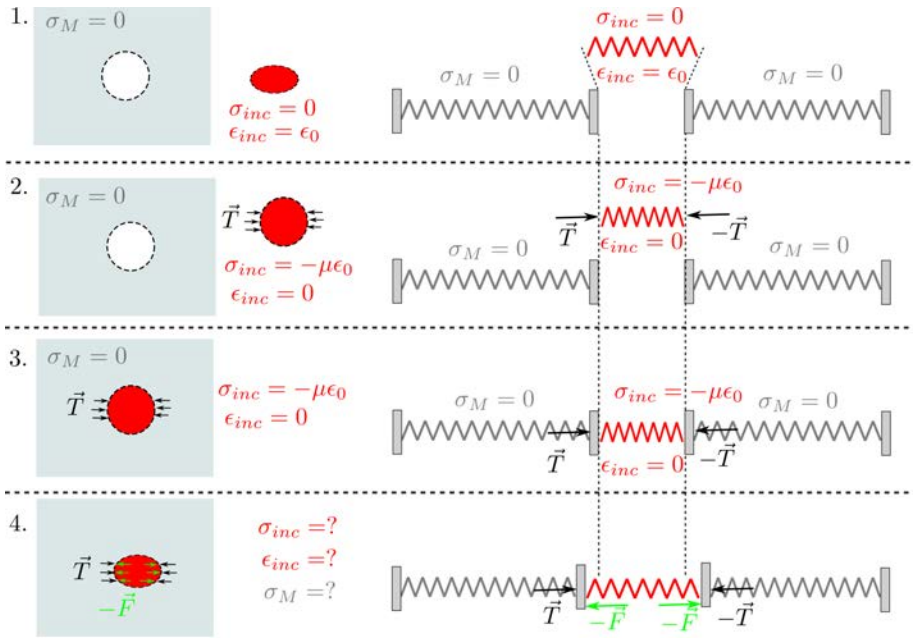

Figure A.1 – Eshelby's thought experiment. Since it is always easier to think in 1D, I included the analogous 1D inclusion as well.

The elastic problem thus has reduced to:

1. finding the surface force $\vec{T}(\vec{r})$ and the corresponding $\vec{F}(\vec{r}) = -\vec{T}(\vec{r})$ that deforms the distorted inclusion back to its original shape and

2. solve the elastic problem of applying that force along the boundaries of the imaginary inclusion in a matrix with no inclusions.

The solution first involves the computation of the Eshelby tensor that relates the strain within the inclusion to its eigenstrain. Then the Lamé-Navier equations are solved for the displacements in the matrix. Details regarding the solution are spelled out in

[10, 57, 193] and here I only provide the final result. Note that plain strain conditions were considered and zero displacement at infinity was imposed. It turns out that, within a circular inclusion with a homogeneous eigenstrain, the Eshelby tensor is constant all along the inclusion, consequently the stress and strain are homogeneous as well. Within the inclusion, one finds that $\sigma^I_{xx} = \sigma^I_{yy} = 0$, similarly $\epsilon^I_{xx} = \epsilon^I_{yy} = 0$ and:

$$\begin{aligned} u^I_x &= \frac{3-4\nu}{4(1-\nu)} y\ \epsilon_0 \\ u^I_y &= \frac{3-4\nu}{4(1-\nu)} x\ \epsilon_0 \\ \epsilon^I_{xy} &= \frac{3-4\nu}{4(1-\nu)} \epsilon_0 \\ \sigma^I_{xy} &= -\frac{2\mu}{4(1-\nu)} \epsilon_0 \end{aligned} \tag{A.1}$$

whereas outside the inclusion:

$$\begin{aligned} u_x(x,y) &= \frac{\epsilon_0}{2(1-\nu)} \frac{a^2}{r^2} y \left(1 - 2\nu + \frac{a^2+4x^2}{2r^2} - \frac{2a^2x^2}{r^4}\right) \\ u_y(x,y) &= \frac{\epsilon_0}{2(1-\nu)} \frac{a^2}{r^2} x \left(1 - 2\nu + \frac{a^2+4y^2}{2r^2} - \frac{2a^2y^2}{r^4}\right) \end{aligned} \tag{A.2}$$

with $r = (x^2+y^2)^{1/2}$.

From the displacement fields it is easy to compute the strain fields:

$$\epsilon_{xx} + \epsilon_{yy} = \frac{\partial u_x}{\partial x} + \frac{\partial u_y}{\partial y} = -a^2\epsilon_0 \frac{1-2\nu}{1-\nu} \frac{\sin 2\theta}{r^2} \tag{A.3}$$

$$\epsilon_{xx} - \epsilon_{yy} = \frac{\partial u_x}{\partial x} - \frac{\partial u_y}{\partial y} = -a^2\epsilon_0 \frac{1}{2(1-\nu)} \sin 4\theta \left(\frac{2}{r^2} - \frac{3a^2}{r^4}\right) \tag{A.4}$$

$$\epsilon_{xy} = \frac{1}{2}\left(\frac{\partial u_x}{\partial y} + \frac{\partial u_y}{\partial x}\right) = a^2\epsilon_0 \frac{1}{4(1-\nu)} \cos 4\theta \left(\frac{2}{r^2} - \frac{3a^2}{r^4}\right) \tag{A.5}$$

and, using Hooke's law, the stress fields:

$$\sigma_{xx} + \sigma_{yy} = (\lambda + 2\mu)(\epsilon_{xx} + \epsilon_{yy}) = -a^2\epsilon_0 \frac{2\mu}{1-\nu} \frac{\sin 2\theta}{r^2} \tag{A.6}$$

$$\sigma_{xx} - \sigma_{yy} = 2\mu(\epsilon_{xx} - \epsilon_{yy}) = -\frac{a^2\epsilon_0\mu}{1-\nu} \sin 4\theta \left(\frac{2}{r^2} - \frac{3a^2}{r^4}\right) \tag{A.7}$$

$$\sigma_{xy} = 2\mu\epsilon_{xy} = a^2\epsilon_0 \frac{\mu}{2(1-\nu)} \cos 4\theta \left(\frac{2}{r^2} - \frac{3a^2}{r^4}\right) \tag{A.8}$$

Note the quadrupolar symmetries of the shear components. Moreover, interestingly, although there is no volumetric deformation of the inclusion, there is a pressure component in the induced elastic field which obeys a dipolar symmetry.

Complex potentials

In two dimensions, it is possible to solve the inclusion problem with a complex potential formalism [169, 122]. First, the spatial coordinates are represented by the complex number $z = x + iy = r\exp(i\theta)$. We further introduce the following complex functions for the displacements, stresses and body forces:

$$\begin{aligned} \mathbf{U} &= U_x + iU_y \\ S_0 &= \sigma_{xx} + \sigma_{yy} \\ \mathbf{S} &= \sigma_{yy} - \sigma_{xx} + 2i\sigma_{xy} \\ \mathbf{F} &= F_x + iF_y \end{aligned} \tag{A.9}$$

In terms of these complex functions, the balance equations and compatibility equations in terms of stresses (also known as Beltrami-Michell equations):

$$\boldsymbol{\nabla} \cdot \sigma + \vec{F} = 0 \tag{A.10}$$

$$(1-\nu)\left[\frac{\partial^2\sigma_{xx}}{\partial y^2} + \frac{\partial^2\sigma_{yy}}{\partial x^2}\right] - \nu\left[\frac{\partial^2\sigma_{xx}}{\partial x^2} + \frac{\partial^2\sigma_{yy}}{\partial x^2}\right] - 2\frac{\partial^2\sigma_{xy}}{\partial x\partial y} = 0 \tag{A.11}$$

can be rewritten as:

$$\frac{\partial S_0}{\partial z} - \frac{\partial \mathbf{S}}{\partial \bar{z}} + \bar{\mathbf{F}} = 0 \tag{A.12}$$

$$\frac{\partial^2 S_0}{\partial z \partial \bar{z}} + \frac{1}{4(1-\nu)}\left(\frac{\partial \mathbf{F}}{\partial z} + \frac{\partial \mathbf{F}}{\partial \bar{z}}\right) = 0 \tag{A.13}$$

This can be easily verified by noting that for a function $f(z)$:

$$\frac{\partial f}{\partial z} = \frac{1}{2}\left[\frac{\partial f}{\partial x} - i\frac{\partial f}{\partial y}\right] \tag{A.14}$$

$$\frac{\partial f}{\partial \bar{z}} = \frac{1}{2}\left[\frac{\partial f}{\partial x} + i\frac{\partial f}{\partial y}\right] \tag{A.15}$$

Note that for the second equation both the compatibility and the balance equations were used, that is the reason why it contains no σ_{xy}, it involves, however the force $\mathbf{F}$.

The reason for rewriting the elasticity equations in the complex plane is that the general solution of these equations is known and can be written in terms of two holomorphic functions φ and ψ called the Kolossov - Muskhelishvili potentials. Assuming zero body force ($\mathbf{F} = 0$), the general solution has the form [cite again]:

$$2\mu\mathbf{U} = (3-4\nu)\varphi(z) - z\overline{\varphi'(z)} - \overline{\psi(z)} \tag{A.16}$$

$$S_0 = 2\left[\varphi'(z) + \overline{\varphi'(z)}\right] \tag{A.17}$$

$$\mathbf{S} = 2\left[\bar{z}\varphi''(z) + \psi'(z)\right] \tag{A.18}$$

We introduce one more auxiliary function:

$$\mathbf{K} = 2\left[\varphi(z) + z\overline{\varphi'(z)} + \overline{\psi(z)}\right] \tag{A.19}$$

which is useful for computing the force per unit area acting on an arbitrary surface (in 2D actually curve) in the material. Let us assume that such a curve is described by $z = z(s)$ and has a normal vector $\vec{n} = \vec{n}(s)$. The force per unit area (length in 2D) acting on the curve is then given by $\vec{f} = \boldsymbol{\sigma} \cdot \vec{n}$ and its complex counterpart can be computed as

$$f_x + i f_y = -\frac{i}{2}\frac{\partial \mathbf{K}}{\partial s} \tag{A.20}$$

Note that so far nothing has been assumed about the specific elasticity problem other that is two dimensional and there are no body forces therefore the equations and functions introduced up to now are very general.

Now we have to apply the general method to the inclusion problem. Solving the elasticity problem is practically equivalent to determining the functions $\varphi(z)$ and $\psi(z)$ inside and outside the inclusion. The inclusion undergoes a homogeneous plastic deformation. The complex displacement field that describes the unconstrained deformation is $\boldsymbol{U_p} = i\epsilon_0 \bar{z}$.

The potentials within the inclusion can be written in form of Laurent series. Since the functions are supposed to go to a finite value as $z \to 0$, no negative powers can appear:

$$\varphi^{in}(z) = \sum_{n=1}^{\infty} \alpha_n^{in} z^n \tag{A.21}$$

$$\psi^{in}(z) = \sum_{n=1}^{\infty} \beta_n^{in} z^n \tag{A.22}$$

Similarly, the potentials should vanish as $|z| \to \infty$, therefore no positive powers can appear in the expansion of the potentials outside the inclusion:

$$\varphi^{out}(z) = \sum_{n=1}^{\infty} \alpha_n^{out} z^{-n} \tag{A.23}$$

$$\psi^{out}(z) = \sum_{n=1}^{\infty} \beta_n^{out} z^{-n} \tag{A.24}$$

The continuity of displacements at the boundary of the inclusion implies:

$$\mathbf{U}_{el}^{in}(z = ae^{i\theta}) + \mathbf{U}_p(ae^{i\theta}) = \mathbf{U}^{out}(ae^{i\theta}) \tag{A.25}$$

whereas the continuity of forces on the boundary (ie. the equilibrium of the boundary) implies:

$$\frac{\partial \mathbf{K}^{in}}{\partial s}(ae^{i\theta}) = \frac{\partial \mathbf{K}^{out}}{\partial s}(ae^{i\theta}) \tag{A.26}$$

with $s = a\theta$.

Plugging in the potential expansions into the continuity conditions, and matching the coefficients one obtains:

$$\alpha_n^{in} = 0,\ \beta_1^{in} = -i\frac{\mu\epsilon_0}{2(1-\nu)},\ \beta_{n\neq 1}^{in} = 0 \tag{A.27}$$

$$\alpha_1^{out} = \frac{\mu\epsilon_0}{2(1-\nu)}ia^2,\ \alpha_{n\neq 1}^{out} = 0,\ \beta_3^{out} = a^2\alpha_1^{out},\ \beta_{n\neq 3}^{out} = 0 \tag{A.28}$$

Within the inclusion thus we have:

$$\varphi^{in}(z) = 0,\ \psi^{in}(z) = -i\frac{\mu\epsilon_0}{2(1-\nu)}z \tag{A.29}$$

which leads to:

$$\mathbf{U}^{in} = \mathbf{U}_{el}^{in} + \mathbf{U}_{p}^{in} = i\epsilon_0\frac{3-4\nu}{4(1-\nu)}\bar{z} \tag{A.30}$$

$$S_0^{in} = 0 \tag{A.31}$$

$$\mathbf{S}^{in} = -i\frac{\mu}{1-\nu}\epsilon_0 \tag{A.32}$$

Similarly, outside the inclusion:

$$\varphi^{out}(z) = \frac{\mu\epsilon_0 ia^2}{2(1-\nu)}\frac{1}{z},\quad \psi^{out}(z) = \frac{\mu\epsilon_0 ia^4}{2(1-\nu)}\frac{1}{z^3} \tag{A.33}$$

which leads to:

$$\mathbf{U}^{out} = \frac{i\epsilon_0 a^2}{4(1-\nu)}\left[(3-4\nu)\frac{1}{z} - \frac{z}{\bar{z}^2} + \frac{a^2}{\bar{z}^3}\right] \tag{A.34}$$

$$S_0^{out} = -\frac{\mu\epsilon_0}{1-\nu}i\left[\frac{1}{z^2} - \frac{1}{\bar{z}^2}\right] \tag{A.35}$$

$$\mathbf{S}^{out} = \frac{\mu\epsilon_0 ia^2}{1-\nu}\frac{1}{z^3}\left[2\bar{z} + 3\frac{a^2}{z}\right] \tag{A.36}$$

Extracting then the displacements and stresses from the complex displacements and complex stresses gives back the same results as in the previous section (plugging in $z = r\exp(i\theta)$ gives the result right away in polar coordinates).

The advantage of this method is that it elegantly simplifies the solution of tensorial differential equations. Its main disadvantage however is that it only works in two dimensions.

Picard's method

This solution uses the linearity of the elastic equations and assumes the material is incompressible [138]. Therefore, first we compute the displacement field caused by a point-force at the origin in a two-dimensional, isotropic, incompressible, translation-invariant elastic medium. Translation invariance essentially means that the medium is either infinitely large or finite, but its edges are periodically folded up.

Incompressibility and equilibrium equations read as:

$$\boldsymbol{\nabla} \cdot \vec{u}(\vec{r}) = 0 \tag{A.37}$$

$$\boldsymbol{\nabla} \cdot \boldsymbol{\sigma}(\vec{r}) + \vec{f}\delta(\vec{r}) = 0 \tag{A.38}$$

The stress tensor can be decomposed into an isotropic and a deviatoric part. Since we assume incompressibility, we can only apply Hooke's law on the deviatoric part and leave the pressure in the isotropic part:

$$\boldsymbol{\sigma}(\vec{r}) = -p(\vec{r})\mathbf{I}_2 + 2\mu\boldsymbol{\epsilon}(\vec{r}) \tag{A.39}$$

with $\boldsymbol{\epsilon} = (\boldsymbol{\nabla}\vec{u} + \boldsymbol{\nabla}\vec{u}^T)/2$. Substituting into the stress, and then the stress into the balance equation, we end up solving for $\vec{u}(\vec{r})$:

$$\boldsymbol{\nabla} \cdot \vec{u} = 0 \tag{A.40}$$

$$\mu\boldsymbol{\nabla} \cdot \left(\nabla\vec{u} + \boldsymbol{\nabla}\vec{u}^T\right) - \boldsymbol{\nabla} \cdot (p\mathbf{I}_2) + \vec{f}\delta(\vec{r}) = 0 \tag{A.41}$$

Since the system is translation invariant, we use Fourier methods to solve the above equations. Whether we Fourier transform the equations or expand them in Fourier series, is a matter of boundary conditions: the former is appropriate for an infinite system, while the latter for a finite but periodic system. Note that the closed form expression of the displacements is the same regardless whether we Fourier transform or expand in Fourier series.

Transforming the first equation and the second one (by cartesian components) and eliminating the pressure one arrives to:

$$k_y\tilde{u}_x - k_x\tilde{u}_y = \frac{1}{\mu k^2}(f_x k_y - f_y k_x) \tag{A.42}$$

$$k_x\tilde{u}_x + k_y\tilde{u}_y = 0 \tag{A.43}$$

The solution can be written as:

$$\widetilde{\vec{u}} = \widetilde{\boldsymbol{O}} \cdot \widetilde{\vec{f}} \tag{A.44}$$

where

$$\widetilde{\boldsymbol{O}} = \frac{1}{\mu k^4}\begin{bmatrix} k_y^2 & -k_x k_y \\ -k_x k_y & k_x^2 \end{bmatrix} \tag{A.45}$$

is known as (the Fourier transform of) the "Oseen"-tensor.

Now that we have the displacement field due to a point-force, let us compute the displacement field due to an arbitrary shear eigenstrain (plastic strain) distribution $\boldsymbol{\epsilon}^p$ such that $\boldsymbol{\epsilon}^p_{xx} = \boldsymbol{\epsilon}^p_{yy} = 0$. The total strain then is composed by an elastic and a plastic part: $\boldsymbol{\epsilon} = (\boldsymbol{\nabla}\vec{u} + \boldsymbol{\nabla}\vec{u}^T)/2 = \boldsymbol{\epsilon}^p + \boldsymbol{\epsilon}^{el}$ but is only the elastic part that results in stress, Hooke's law thus changes to:

$$\boldsymbol{\sigma} = -p\mathbf{I}_2 + 2\mu(\boldsymbol{\epsilon} - \boldsymbol{\epsilon}^p) \tag{A.46}$$

thus the equilibrium equation modifies to:

$$\mu\boldsymbol{\nabla}\cdot\left(\nabla\vec{u}+\boldsymbol{\nabla}\vec{u}^T\right)-\boldsymbol{\nabla}\cdot(p\mathbf{I}_2)-2\mu\boldsymbol{\nabla}\cdot\boldsymbol{\epsilon}^p=0 \tag{A.47}$$

Due to linearity, the solution to the above equation can be written as [138]:

$$\vec{u}(\vec{r})=\int\boldsymbol{O}(\vec{r}-\vec{r}')[-2\mu\boldsymbol{\nabla}\cdot\boldsymbol{\epsilon}^p(\vec{r}')] \tag{A.48}$$

or, in the Fourier space:

$$\widetilde{\vec{u}}(\vec{k})=\widetilde{\boldsymbol{O}}\cdot(2\mu i\vec{k}\cdot\widetilde{\boldsymbol{\epsilon}^p}) \tag{A.49}$$

Remembering that $\boldsymbol{\epsilon}^p_{xx}=\boldsymbol{\epsilon}^p_{yy}=0$, this reduces to

$$\tilde{u}_x = 2\mu i\tilde{\epsilon}^p_{xy}(\tilde{O}_{xx}k_y+\tilde{O}_{xy}k_x) \tag{A.50}$$

$$\tilde{u}_y = 2\mu i\tilde{\epsilon}^p_{xy}(\tilde{O}_{xy}k_y+\tilde{O}_{yy}k_x) \tag{A.51}$$

For a localized, point-like inclusion $\epsilon^p_{xy}=\alpha\delta(\vec{r}')$ where α is a constant related to the inclusion. In order to connect it to physical parameters, we impose that the average plastic strain around the inclusion within an (imaginary) volume πa^2 be ϵ_0, thus:

$$\epsilon_0=\frac{1}{\pi a^2}\int\epsilon^p_{xy}d\vec{r}=\frac{\alpha}{\pi a^2} \tag{A.52}$$

thus $\alpha=\pi a^2\epsilon_0=\tilde{\epsilon}^p_{xy}$ which leaves us with

$$\tilde{u}_x = 2\mu i\pi a^2\epsilon_0(\tilde{O}_{xx}k_y+\tilde{O}_{xy}k_x) \tag{A.53}$$

$$\tilde{u}_y = 2\mu i\pi a^2\epsilon_0(\tilde{O}_{xy}k_y+\tilde{O}_{yy}k_x) \tag{A.54}$$

It is possible to show that the above displacement field is equivalent to that of a force quadrupole as $a\to 0$, but $a^2\epsilon_0$ kept constant. The quadrupolar force field can be written as:

$$\frac{\vec{f}}{f_0}=\begin{bmatrix}0\\1\end{bmatrix}\delta(x-a,y)+\begin{bmatrix}0\\-1\end{bmatrix}\delta(x+a,y)+\begin{bmatrix}1\\0\end{bmatrix}\delta(x,y-a)+\begin{bmatrix}-1\\0\end{bmatrix}\delta(x,y+a) \tag{A.55}$$

while its Fourier transform (using the shift property):

$$\widetilde{\vec{f}}=2if_0\begin{bmatrix}\sin ak_y\\ \sin ak_x\end{bmatrix}\approx 2if_0a\begin{bmatrix}k_y\\k_x\end{bmatrix} \tag{A.56}$$

Comparing the displacement field generated by this force quadrupole gives $f_0=\mu\epsilon_0\pi a$. The shear stress can then be computed using:

$$\tilde{\sigma}_{xy} = 2\mu(\tilde{\epsilon}_{xy}-\tilde{\epsilon}^p_{xy}) \tag{A.57}$$

$$\tilde{\epsilon}_{xy} = -\frac{i}{2}(k_y\tilde{u}_x+k_x\tilde{u}_y) \tag{A.58}$$

which gives

$$\tilde{\sigma}_{xy} = -8\mu\pi a^2\epsilon_0\frac{k_x^2k_y^2}{k^4} \tag{A.59}$$

Appendix B

Eigenvalues and eigenvectors of translation invariant operators

Here we show that that the eigenvectors of a translation invariant linear operator are the Fourier modes, and its eigenvalues are the Fourier transform. This result is known under various forms, and the most common form is the Block theorem [176, 81]. Here we spell out the main idea behind it, in a light that meets our needs.

First, let us consider the translation operator $\hat{T}$ defined as

$$\hat{T}_{\vec{a}} \left|\varphi(\vec{r})\right\rangle = \left|\varphi(\vec{r}+\vec{a})\right\rangle \tag{B.1}$$

for a field $|\varphi(\vec{r})\rangle$.

Let us say that an operator $\hat{L}$ acts on $|\varphi\rangle$ such that

$$\hat{L}\left|\varphi\right\rangle = \left|\psi\right\rangle \tag{B.2}$$

Then the operator $\hat{L}$ is translation invariant if

$$\hat{L}(\hat{T}\left|\varphi\right\rangle) = \hat{T}\left|\psi\right\rangle \tag{B.3}$$

The right hand side of the above equation can be written as $\hat{T}\left|\psi\right\rangle = \hat{T}\hat{L}\left|\varphi\right\rangle$, thus we can conclude that if an operator is translation invariant, it commutes with the translation operator, that is

$$[\hat{L}, \hat{T}] = 0 \tag{B.4}$$

An important consequence of the above commuting relation is that since $\hat{T}$ and $\hat{L}$ commute, they have a common eigenbasis. It is therefore enough to find the eigenvectors of $\hat{T}$ and construct the eigenbasis of $\hat{L}$ starting from there.

The task is therefore to find the $|u\rangle$ eigenvectors and $\lambda(\vec{a})$ of the operator $\hat{T}_{\vec{a}}$:

$$\hat{T}_{\vec{a}}\left|u\right\rangle = \lambda(\vec{a})\left|u\right\rangle \tag{B.5}$$

Applying a translation of $\vec{a}$ and then a translation of $\vec{b}$ to any vector is equivalent to applying one translation $\vec{a}+\vec{b}$. Also, translation operators commute among themselves, therefore they have a common set of eigenfunctions. Moreover, all the translation operators commute with $\hat{L}$, thus this is precisely the set of eigenvectors we are interested in.

$$\hat{T}_{\vec{a}}\hat{T}_{\vec{b}}\left|u\right\rangle = \lambda(\vec{a})\lambda(\vec{b})\left|u\right\rangle \tag{B.6}$$

$$\hat{T}_{\vec{a}+\vec{b}}\left|u\right\rangle = \lambda(\vec{a}+\vec{b})\left|u\right\rangle \tag{B.7}$$

and since $\hat{T}_{\vec{a}}\hat{T}_{\vec{b}}\left|u\right\rangle = \hat{T}_{\vec{a}+\vec{b}}\left|u\right\rangle$ we have

$$\lambda(\vec{a})\lambda(\vec{b}) = \lambda(\vec{a}+\vec{b}) \tag{B.8}$$

which directly leads to the eigenvalues of the translation operator:

$$\lambda(\vec{a}) \equiv \lambda_{\vec{k}}(\vec{a}) = \exp\Big(i\vec{k}\vec{a}\Big) \tag{B.9}$$

Note that the base of the exponential function is irrelevant and is simply pinned by the definition of $\vec{k}$. Furthermore, the argument of the exponential has to be purely imaginary as we expect bounded eigenvalues in the infinite space.

Projecting the eigenvalue equation to the coordinate basis, we get:

$$\langle \vec{r}| \hat{T}_{\vec{a}} |u\rangle = \exp\Big(i\vec{k}\vec{a}\Big) \langle \vec{r}|u\rangle \tag{B.10}$$

or

$$\langle \vec{r} - \vec{a}|u\rangle = \exp\Big(i\vec{k}\vec{a}\Big) \langle \vec{r}|u\rangle \tag{B.11}$$

Recall that we are looking for the common eigenvector system of all the translation operators, so we expect the above expression to be valid for any $\vec{a}$ which leads to the eigenvectors

$$\langle \vec{r}|u\rangle \equiv \langle \vec{r}|u_{\vec{k}}\rangle = \exp\Big(i\vec{k}\vec{r}\Big) \tag{B.12}$$

We have thus found the common eigenfunctions of all the translation operators and this will be the eigensystem of the $\hat{L}$ operator as well and we see that they are precisely the Fourier modes.

This is the basis in which $\hat{L}$ is diagonal, and the eigenvalues of $\hat{L}$ are given by

$$\begin{aligned} \lambda &= \langle u_{\vec{k}}| \hat{L} |u_{\vec{k}}\rangle & \text{(B.13)} \\ &= \iint \langle u|\vec{r}\rangle \langle \vec{r}| \hat{L} |\vec{r}'\rangle \langle \vec{r}'|u\rangle \, \mathrm{d}\vec{r}\mathrm{d}\vec{r}' & \text{(B.14)} \end{aligned}$$

Since $\hat{L}$ is translation invariant, $\langle \vec{r}| \hat{L} |\vec{r}'\rangle = L(\vec{r} - \vec{r}')$ and the eigenvector projections are given by

$$\begin{aligned} \langle u|\vec{r}\rangle &= \langle \vec{r}|u\rangle^* = \exp\Big(-i\vec{k}\vec{r}\Big) & \text{(B.15)} \\ \langle \vec{r}'|u\rangle &= \exp\Big(i\vec{k}\vec{r}'\Big) & \text{(B.16)} \end{aligned}$$

which leads to

$$\begin{aligned} \lambda &= \iint L(\vec{r} - \vec{r}') \exp\Big[-i\vec{k}(\vec{r} - \vec{r}')\Big] \mathrm{d}\vec{r}\mathrm{d}\vec{r}' & \text{(B.17)} \\ &\propto \int L(\vec{r}) \exp\Big[-i\vec{k}\vec{r}\Big] \mathrm{d}\vec{r} & \text{(B.18)} \end{aligned}$$

showing that *the eigenvalues of $\hat{L}$ are given by its Fourier transform.* The very same reasoning applies in a discretized space, however in that case the eigenvalues are given by the discrete Fourier transform, whereas in a continuous, but finite space by the Fourier series.

Appendix C

Evolution equation of soft modes

Quadrupolar kernel

With the notations in the main script, the following projections are valid for the Fourier quadrupolar kernel (with positive directions along the $\pm 45^\circ$ directions):

$$\langle d_k | e_{pq} \rangle = N \exp\left[-\frac{2\pi i}{N} pk\right] \delta_{p+q} \tag{C.1}$$

$$\langle d'_k | e_{pq} \rangle = N \exp\left[-\frac{2\pi i}{N} pk\right] \delta_{q-p} \tag{C.2}$$

$$\langle d_k | d_l \rangle = \langle d'_k | d'_l \rangle = N\delta_{kl} \tag{C.3}$$

$$\langle d_k | d'_l \rangle = 2(1 - \delta_{|k-l|\%2}) \tag{C.4}$$

Here % denotes the modulo (remainder) operation. The last projection results form the fact that the d_k and d'_l bands intersect in two points due to the periodic boundary conditions, but each d_k band intersects only every other d'_l band. This is a discretization issue and, for a quadrupolar kernel with positive directions along 0° and 90° this scalar product would always be 1.

Recall that we use the basis

$$|e_{pq}\rangle \text{ with } |p| = |q| \tag{C.5}$$

$$|d_k\rangle \text{ with } k \in [-N/2, N/2 - 1] \tag{C.6}$$

$$|d'_l\rangle \text{ with } l \in [-N/2, N/2 - 1] \tag{C.7}$$

Note however, that not all of the above are independent and orthogonal, nor normalized.

The plastic strain can be written in this basis as

$$|\epsilon_p\rangle = \sum_{|p|\neq|q|} c_{pq} |e_{pq}\rangle + \sum_k c_k |d_k\rangle + \sum_k c'_k |d'_k\rangle \tag{C.8}$$

and the following projections hold:

$$\langle e_{lm} | \epsilon_p \rangle = c_{lm} \text{ for } |l| \neq |m| \tag{C.9}$$

$$\langle e_{lm} | \epsilon_p \rangle = N\delta_{l+m} \sum_k c_k \exp\left[-\frac{2\pi i}{N} lk\right] \tag{C.10}$$

$$+ \; N\delta_{l-m} \sum_k c'_k \exp\left[-\frac{2\pi i}{N} lk\right] \text{ for } |l| = |m| \tag{C.11}$$

$$\tag{C.12}$$

but we do not care about the latter. Projecting onto the shear bands gives:

$$\langle d_l | \epsilon_p \rangle = Nc_l + 2 \sum_k c'_k [1 - \delta_{|k-l|\%2}] \tag{C.13}$$

$$\langle d'_l | \epsilon_p \rangle = Nc'_l + 2 \sum_k c_k [1 - \delta_{|k-l|\%2}] \tag{C.14}$$

Again, this expression would be simpler for the rotated quadrupolar kernel where each perpendicular shear band cross.

Since we are interested in the evolution of the various modes, let us then take the evolution equation

$$\partial_t \left|\epsilon_p\right\rangle = \left|\sigma^{ext}\right\rangle + \hat{G}\left|\epsilon_p\right\rangle - \left|\sigma^c\right\rangle \tag{C.15}$$

and project it to our basis. First, onto the basis associated to the zero eigenvalues:

$$\partial_t \left\langle e_{lm}|\epsilon_p\right\rangle = \left\langle e_{lm}\middle|\sigma^{ext}\right\rangle + \left\langle e_{lm}\right|\hat{G}\left|\epsilon_p\right\rangle - \left\langle e_{lm}|\sigma^c\right\rangle \ , \ |l| \neq |m| \tag{C.16}$$

In the above equation, we use:

$$\begin{aligned}
\left\langle e_{lm}\middle|\sigma^{ext}\right\rangle &= [\widetilde{\sigma^{ext}}]_{lm} = \sigma^{ext}\delta_l\delta_m = 0 \text{ for } |l| \neq |m| && \text{(C.17)}\\
\left\langle e_{lm}\right|\hat{G}\left|\epsilon_p\right\rangle &= \lambda_{lm}\left\langle e_{lm}|\epsilon_p\right\rangle = \lambda_{lm}c_{lm} && \text{(C.18)}\\
\left\langle e_{lm}|\sigma^c\right\rangle &= [\widetilde{\sigma^c}]_{lm} && \text{(C.19)}
\end{aligned}$$

so we get an attenuation of the non-soft modes:

$$\partial_t c_{lm} = \lambda_{lm}c_{lm} - [\widetilde{\sigma^c}]_{lm} \tag{C.20}$$

We may now project to the shear bands:

$$\partial_t \left\langle d_k|\epsilon_p\right\rangle = \left\langle d_k\middle|\sigma^{ext}\right\rangle + \left\langle d_k\right|\hat{G}\left|\epsilon_p\right\rangle - \left\langle d_k|\sigma^c\right\rangle \tag{C.21}$$

Here the following hold:

$$\begin{aligned}
\left\langle d_k\middle|\sigma^{ext}\right\rangle &= N\sigma^{ext} && \text{(C.22)}\\
\left\langle d_k\right|\hat{G}\left|\epsilon_p\right\rangle &= 0 \text{ since } \left\langle d_k\right|\hat{G} = \langle 0| && \text{(C.23)}\\
\left\langle d_k|\sigma^c\right\rangle &= \sum_{\vec{r}\in d_k}\sigma^c(\vec{r}) && \text{(C.24)}
\end{aligned}$$

which gives the evolution equation of the shear bands:

$$\begin{aligned}
\partial_t c_l + 2\frac{1}{N}\sum_k \partial_t c'_k[1-\delta_{|k-l|\%2}] &= \sigma^{ext} - \frac{1}{N}\sum_{\vec{r}\in d_k}\sigma^c(\vec{r}) && \text{(C.25)}\\
\partial_t c'_l + 2\frac{1}{N}\sum_k \partial_t c_k[1-\delta_{|k-l|\%2}] &= \sigma^{ext} - \frac{1}{N}\sum_{\vec{r}\in d'_k}\sigma^c(\vec{r}) && \text{(C.26)}
\end{aligned}$$

Rotated quadrupolar kernel

Let us consider the rotated Fourier quadrupolar kernel. Here we have positive stress directions along the 0 and 90 directions, thus $\lambda_{pq} = 0$ for $p = 0$ or $q = 0$. This would

correspond for the "m3" loading in the finite element kernels. This will give $\langle d_k | d'_l \rangle = 1$ and simplify the evolution equations to:

$$\partial_t c_{lm} = \lambda_{lm} c_{lm} - [\widetilde{\sigma^c}]_{lm} \tag{C.27}$$

$$\partial_t c_l + \frac{1}{N} \sum_k \partial_t c'_k = \sigma^{ext} - \frac{1}{N} \sum_{\vec{r} \in d_k} \sigma^c(\vec{r}) \tag{C.28}$$

$$\partial_t c'_l + \frac{1}{N} \sum_k \partial_t c_k = \sigma^{ext} - \frac{1}{N} \sum_{\vec{r} \in d'_k} \sigma^c(\vec{r}) \tag{C.29}$$

Dipolar kernel

For the dipolar kernel, $\lambda_{pq} = 0$ for $q = 0$ leaving us with a single direction of soft modes, d_k. These modes however are decoupled since $\langle d_k | d_l \rangle = N \delta_{kl}$:

$$\partial_t c_{lm} = \lambda_{lm} c_{lm} - [\widetilde{\sigma^c}]_{lm} \tag{C.30}$$

$$\partial_t c_l = \sigma^{ext} - \frac{1}{N} \sum_{\vec{r} \in d_k} \sigma^c(\vec{r}) \tag{C.31}$$

$$\tag{C.32}$$

It is then clear that the soft modes receive random, uncorrelated (for large N, gaussian distributed) kicks hence we encounter diffusion.

Appendix D

Finite element calculations

One possible overcome of the discretization issues is to solve the inclusion problem readily in a discretized and periodic geometry. The exact calculations are not particularly difficult, they are however prone to error due to the many indices involved, therefore we spell out these calculations for easier reusability in the future. The calculation details may be skipped by the reader without any setback regarding the understanding of the manuscript.

D.1 Discretization of the displacement field and strains

As shown on Figure 3.3, displacements are discretized on a square lattice. In order to avoid unphysical floppy modes that result from inhomogeneous deformations of the plaquettes, each plaquette is further divided into 4 triangles labeled by: N, W, S, E. The strain within a plaquette is defined then as the average of the strains of the 4 triangles. The strain within one triangle is considered homogeneous. For the W triangle of plaquette (i, j), for instance:

$$u^\alpha_{Hij} - u^\alpha_{ij} = \frac{\partial u^\alpha_{ij}}{\partial x}\frac{a}{2} + \frac{\partial u^\alpha_{ij}}{\partial y}\frac{a}{2} = \epsilon^{\alpha xW}_{ij}\frac{a}{2} + \epsilon^{\alpha yW}_{ij}\frac{a}{2} \tag{D.1}$$

For the other edge of the same triangle:

$$u^\alpha_{Hij} - u^\alpha_{ij+1} = \frac{\partial u^\alpha_{ij}}{\partial x}\frac{a}{2} - \frac{\partial u^\alpha_{ij}}{\partial y}\frac{a}{2} = \epsilon^{\alpha xW}_{ij}\frac{a}{2} - \epsilon^{\alpha yW}_{ij}\frac{a}{2} \tag{D.2}$$

Solving for the strains:

$$\epsilon^{\alpha xW}_{ij} = \frac{1}{a}[2u^\alpha_{Hij} - u^\alpha_{ij} - u^\alpha_{ij+1}] \tag{D.3}$$

$$\epsilon^{\alpha yW}_{ij} = \frac{1}{a}[u^\alpha_{ij+1} - u^\alpha_{ij}] \tag{D.4}$$

Here H labels the center of the plaquette, such that:

$$u^\alpha_{Hij} = \frac{1}{4}[u^\alpha_{ij} + u^\alpha_{i+1j} + u^\alpha_{i+1j+1} + u^\alpha_{ij+1}] \tag{D.5}$$

The same reasoning applies for the other three triangles:

$$\epsilon^{\alpha xN}_{ij} = \frac{1}{a}[u^\alpha_{i+1j+1} - u^\alpha_{ij+1}] \tag{D.6}$$

$$\epsilon^{\alpha yN}_{ij} = \frac{1}{a}[-2u^\alpha_{Hij} + u^\alpha_{ij+1} + u^\alpha_{i+1j+1}] \tag{D.7}$$

$$\epsilon^{\alpha xE}_{ij} = \frac{1}{a}[-2u^\alpha_{Hij} + u^\alpha_{i+1j+1} + u^\alpha_{i+1j}] \tag{D.8}$$

$$\epsilon^{\alpha yE}_{ij} = \frac{1}{a}[-u^\alpha_{i+1j} + u^\alpha_{i+1j+1}] \tag{D.9}$$

$$\epsilon^{\alpha xS}_{ij} = \frac{1}{a}[-u^\alpha_{ij} + u^\alpha_{i+1j}] \tag{D.10}$$

$$\epsilon^{\alpha yS}_{ij} = \frac{1}{a}[2u^\alpha_{Hij} - u^\alpha_{i+1j} - u^\alpha_{ij}] \tag{D.11}$$

The strain within plaquette (i,j) is then given by the average over the 4 triangles:

$$\epsilon_{ij}^{\alpha\beta} = \frac{1}{4}[\epsilon_{ij}^{\alpha\beta N} + \epsilon_{ij}^{\alpha\beta E} + \epsilon_{ij}^{\alpha\beta S} + \epsilon_{ij}^{\alpha\beta W}] \tag{D.12}$$

D.2 Solving the equilibrium equations

The energy of one plaquette is quadratic in the strains:

$$\Phi_{ij} = \frac{K}{2}e_{1ij}^2 + \frac{G}{2}e_{2ij}^2 + \frac{G}{2}e_{3ij}^2 \tag{D.13}$$

where

$$\begin{aligned} e_{1ij} &= \epsilon_{ij}^{xx} + \epsilon_{ij}^{yy} && \text{(D.14)}\\ e_{2ij} &= \epsilon_{ij}^{xx} - \epsilon_{ij}^{yy} && \text{(D.15)}\\ e_{3ij} &= \epsilon_{ij}^{xy} + \epsilon_{ij}^{yx}\,, && \text{(D.16)} \end{aligned}$$

while the total energy of the system is:

$$\Phi = \sum_{ij} \Phi_{ij} \tag{D.17}$$

The elastic force acting on node (i,j) is given by the first derivative of the energy:

$$F_{ij}^{\alpha} = -\frac{\partial \Phi}{\partial u_{ij}^{\alpha}} = -\left(\frac{\partial \Phi_{i-1j-1}}{\partial u_{ij}^{\alpha}} + \frac{\partial \Phi_{ij-1}}{\partial u_{ij}^{\alpha}} + \frac{\partial \Phi_{i-1j}}{\partial u_{ij}^{\alpha}} + \frac{\partial \Phi_{ij}}{\partial u_{ij}^{\alpha}}\right) \tag{D.18}$$

All the other derivatives are zero since the energy of a plaquette only depends on the displacements on its nodes. In the presence on external forces, the equilibrium equations are:

$$F_{ij}^{\alpha} + F_{ext\ ij}^{\alpha} = 0 \tag{D.19}$$

which are the discrete form of the Lame-Navier equation. Since the elastic forces are linear in displacements:

$$F_{ij}^{\alpha} = \sum_{pq\beta} \frac{\partial F_{ij}^{\alpha}}{\partial u_{pq}^{\beta}} u_{pq}^{\beta} = -\sum_{pq\beta} \frac{\partial^2 \Phi}{\partial u_{ij}^{\alpha} \partial u_{pq}^{\beta}} u_{pq}^{\beta} = -\sum_{pq\beta} H_{ijpq}^{\alpha\beta} u_{pq}^{\beta} \tag{D.20}$$

and the equilibrium equations can be rewritten as:

$$\sum_{pq\beta} H_{ijpq}^{\alpha\beta} u_{pq}^{\beta} = F_{ext\ ij}^{\alpha} \tag{D.21}$$

When imposing periodic boundary conditions, the Hessian H is translation invariant and it is possible to define h such that:

$$h_{\Delta i\ \Delta j}^{\alpha\beta} = h_{p-i\ q-j}^{\alpha\beta} = H_{ijpq}^{\alpha\beta} \tag{D.22}$$

and rewrite the equilibrium eq:

$$\sum_{\beta\Delta i\Delta j} h^{\alpha\beta}_{\Delta i\ \Delta j} u^{\beta}_{i+\Delta i\ j+\Delta j} = F^{\alpha}_{ext\ ij} \tag{D.23}$$

Evaluating the energy derivatives, one obtains:

$$\begin{aligned}
h^{xx}_{-1,-1} &= h^{xx}_{-1,1} = h^{xx}_{1,-1} = h^{xx}_{1,1} = \frac{1}{a^2}(-G - K/2) && \text{(D.24)}\\
h^{xx}_{-1,0} &= h^{xx}_{1,0} = \frac{1}{a^2}(-2G - 3K) && \text{(D.25)}\\
h^{xx}_{0,-1} &= h^{xx}_{0,1} = \frac{1}{a^2}(-2G + K) && \text{(D.26)}\\
h^{xx}_{0,0} &= \frac{1}{a^2}(12G + 6K) && \text{(D.27)}
\end{aligned}$$

$$\begin{aligned}
h^{xy}_{-1,-1} &= h^{xy}_{1,1} = \frac{1}{a^2}(-K) && \text{(D.28)}\\
h^{xy}_{-1,1} &= h^{xy}_{1,-1} = \frac{1}{a^2}(K) && \text{(D.29)}
\end{aligned}$$

$$\begin{aligned}
h^{yy}_{-1,-1} &= h^{yy}_{-1,1} = h^{yy}_{1,-1} = h^{yy}_{1,1} = \frac{1}{a^2}(-G - K/2) && \text{(D.30)}\\
h^{yy}_{-1,0} &= h^{yy}_{1,0} = \frac{1}{a^2}(-2G + K) && \text{(D.31)}\\
h^{yy}_{0,-1} &= h^{yy}_{0,1} = \frac{1}{a^2}(-2G - 3K) && \text{(D.32)}\\
h^{yy}_{0,0} &= \frac{1}{a^2}(12G + 6K) && \text{(D.33)}
\end{aligned}$$

Note that $h^{xy}_{ij} = h^{yx}_{ij}$ and $h^{\alpha\beta}_{ij} = 0$ everywhere else.

$\hat{H}$ is a linear operator that, when feeded with the displacement field, returns the elastic force field:

$$\hat{H}\,|u\rangle = |F_{ext}\rangle \tag{D.34}$$

We are, however, interested in its inverse in order to compute the displacement field for a given force field. Denoting by λ_i the i-th eigenvalue and $\left|v^i\right\rangle = \{v^{i\alpha}_{mn}\}$ the i-th eigenvector of $\hat{H}$:

$$\begin{aligned}
\hat{H}\,|v_i\rangle &= \lambda_i\,|v_i\rangle && \text{(D.35)}\\
\langle v_i|\,\hat{H}\,|u\rangle &= |F_{ext}\rangle && \text{(D.36)}\\
\lambda_i\,\langle v_i|u\rangle &= \langle v_i|F_{ext}\rangle \Rightarrow \langle v_i|u\rangle = \frac{1}{\lambda_i}\,\langle v_i|F_{ext}\rangle && \text{(D.37)}
\end{aligned}$$

The problem thus reduces to finding the eigenvalues and eigenvectors of $\hat{H}$.

Introducing the coordinate basis $\left|n^{lm\alpha}\right\rangle = \{\delta_{li}\delta_{mj}\delta_{\alpha\beta}\}$, for any vector $|u\rangle$ we have:

$$\left\langle n^{lm\alpha}\middle|u\right\rangle = u^{\alpha}_{lm} \tag{D.38}$$

and the $\hat{H}$ matrix elements are simply:

$$\left\langle n^{rs\beta}\middle|\,\hat{H}\,\middle|n^{lm\alpha}\right\rangle = \sum_{ijpq\delta\gamma} H^{\gamma\delta}_{ijpq}\delta_{pl}\delta_{qm}\delta_{\alpha\gamma}\delta_{ir}\delta_{js}\delta_{\delta\beta} = H^{\alpha\beta}_{rslm} = h^{\alpha\beta}_{r-l,s-m} \tag{D.39}$$

Projecting eq. D.35 to $\left\langle n^{lm\alpha}\right|$:

$$\begin{aligned}
\left\langle n^{lm\alpha}\middle|\,\hat{H}\,|v^i\right\rangle &= \left\langle n^{lm\alpha}\middle|\,\hat{H}\sum_{rs\beta}\left|n^{rs\beta}\right\rangle\left\langle n^{rs\beta}\middle|v^i\right\rangle && \text{(D.40)}\\
&= \sum_{rs\beta}\left\langle n^{lm\alpha}\middle|\,\hat{H}\,\middle|n^{rs\beta}\right\rangle\left\langle n^{rs\beta}\middle|v^i\right\rangle && \text{(D.41)}\\
&= \sum_{rs\beta} H^{\alpha\beta}_{lmrs}\left\langle n^{rs\beta}\middle|v^i\right\rangle = \sum_{rs\beta} h^{\alpha\beta}_{r-l,s-m}\left\langle n^{rs\beta}\middle|v^i\right\rangle && \text{(D.42)}\\
&= \lambda_i\left\langle n^{lm\alpha}\middle|v^i\right\rangle && \text{(D.43)}
\end{aligned}$$

Since $\hat{H}$ is translation invariant, it commutes with the translation operator $\hat{T}$ which means they must have a common eigenvector system. In $2D$, the eigenvectors of $\hat{T}$ have the form:

$$\left\langle n^{lm\alpha}\middle|v^i\right\rangle = \frac{1}{NM}P^{pq}_{\alpha}\exp\left[2\pi i\left(\frac{lp}{N}+\frac{mq}{M}\right)\right] \tag{D.44}$$

therefore it is reasonable to check the same form for the eigenvectors of $\hat{H}$. Plugging in D.44 in the last equation of D.43:

$$\sum_{rs\beta} h^{\alpha\beta}_{r-l,s-m}P^{pq}_{\beta}\exp\left[2\pi i\left(\frac{rp}{N}+\frac{sq}{M}\right)\right] = \lambda_i P^{pq}_{\alpha}\exp\left[2\pi i\left(\frac{lp}{N}+\frac{mq}{M}\right)\right] \tag{D.45}$$

which leads to:

$$\sum_{\beta}\widetilde{h}^{\alpha\beta}_{pq}P^{pq}_{\beta} = \lambda_i P^{pq}_{\alpha} \tag{D.46}$$

with $\alpha,\beta\in\{x,y\}$. Since $h^{\alpha\beta}_{lm}$ is sparse, its Fourier transform is easily computable:

$$\begin{aligned}
\widetilde{h}^{xx}_{pq} &= \frac{2}{a^2}\left[-(2G+3K)C_p+(-2G+K)C_q-(2G+K)(C_pC_q-3)\right] && \text{(D.47)}\\
\widetilde{h}^{xy}_{pq} &= \frac{4}{a^2}KS_pS_q && \text{(D.48)}\\
\widetilde{h}^{yy}_{pq} &= \frac{2}{a^2}\left[(-2G+K)C_p+(2G+3K)C_q-(2G+K)(C_pC_q-3)\right] && \text{(D.49)}\\
& && \text{(D.50)}
\end{aligned}$$

with $C_p = \cos(2\pi p/N)$, $C_q = \cos(2\pi q/M)$, $S_p = \sin(2\pi p/N)$, $S_q = \sin(2\pi q/M)$. At this stage thus our problem has been reduced to finding the eigenvalues and eigenvectors of the 2×2 matrix $\widetilde{h}^{\alpha\beta}_{pq}$. The resulting eigenvalues can be labeled as $\lambda_i \equiv \lambda^{\delta}_{pq}$ and their expression is:

$$\lambda^{x}_{pq} = \frac{2}{a^2}[(6G+5K) - (2G+K)(C_p + C_q) - (2G+3K)C_pC_q] \tag{D.51}$$

$$\lambda^{y}_{pq} = \frac{2}{a^2}[(6G+K) - (2G+K)(C_p + C_q) - (2G-K)C_pC_q] \tag{D.52}$$

while the corresponding eigenvectors $P^{pq}_{\alpha} \equiv P^{pq\delta}_{\alpha}$:

$$(P^{pqx}_{x}, P^{pqx}_{y}) = \frac{1}{\sqrt{1 + \tan^2\frac{\pi p}{N}\cot^2\frac{\pi q}{M}}}\left(\tan\frac{\pi p}{N}\cot\frac{\pi q}{M},\ 1\right) \tag{D.53}$$

$$(P^{pqy}_{x}, P^{pqy}_{y}) = \frac{1}{\sqrt{1 + \cot^2\frac{\pi p}{N}\tan^2\frac{\pi q}{M}}}\left(-\cot\frac{\pi p}{N}\tan\frac{\pi q}{M},\ 1\right) \tag{D.54}$$

The eigenvectors of $\hat{H}$ are then labeled as $\left|v^i\right\rangle \equiv \left|v^{pq\delta}\right\rangle$ and given by eq. D.44.

D.3 Point force

In the coordinate basis, a point force acting on node (i, j) along direction β has the coordinates:

$$\left\langle n^{lm\alpha}\middle|F\right\rangle = f_0\ \delta_{li}\delta_{mj}\delta_{\alpha\beta} \tag{D.55}$$

The same force in the eigenbasis has the form:

$$\left\langle v^{pq\delta}\middle|F\right\rangle = \sum_{lm\alpha}\left\langle v^{pq\delta}\middle|n^{lm\alpha}\right\rangle\left\langle n^{lm\alpha}\middle|F\right\rangle \tag{D.56}$$

$$= f_0\sum_{lm\alpha}\left\langle v^{pq\delta}\middle|n^{lm\alpha}\right\rangle\delta_{li}\delta_{mj}\delta_{\alpha\beta} \tag{D.57}$$

$$= f_0\left\langle v^{pq\delta}\middle|n^{ij\beta}\right\rangle = f_0\left\langle n^{ij\beta}\middle|v^{pq\delta}\right\rangle^{*} \tag{D.58}$$

$$= f_0 P^{pq\delta}_{\beta}\exp\left[-2\pi i\left(\frac{ip}{N} + \frac{jq}{M}\right)\right] \tag{D.59}$$

which immediately gives the solution for the displacement in the eigenbasis:

$$\left\langle v^{pq\delta}\middle|u\right\rangle = \frac{1}{\lambda^{\delta}_{pq}}\left\langle v^{pq\delta}\middle|F\right\rangle = \frac{1}{\lambda^{\delta}_{pq}} f_0 P^{pq\delta}_{\beta}\exp\left[-2\pi i\left(\frac{ip}{N} + \frac{jq}{M}\right)\right] \tag{D.60}$$

Switching back to the coordinate basis:

$$u^{\alpha}_{lm} = \left\langle n^{lm\alpha} \middle| u \right\rangle = \sum_{pq\delta} \left\langle n^{lm\alpha} \middle| v^{pq\delta} \right\rangle \left\langle v^{pq\delta} \middle| u \right\rangle \tag{D.61}$$

$$= f_0 \sum_{pq\delta} \frac{P^{pq\delta}_{\alpha} P^{pq\delta}_{\beta}}{\lambda^{\delta}_{pq}} \exp\left[2\pi i \left(\frac{(l-i)p}{N} + \frac{(m-j)q}{M}\right)\right] \tag{D.62}$$

$$= f_0 \sum_{pq} B^{\alpha\beta}_{pq} \exp\left[2\pi i \left(\frac{(l-i)p}{N} + \frac{(m-j)q}{M}\right)\right] \tag{D.63}$$

where

$$B^{\alpha\beta}_{pq} = \sum_{\delta} \frac{P^{pq\delta}_{\alpha} P^{pq\delta}_{\beta}}{\lambda^{\delta}_{pq}} \tag{D.64}$$

For a point force at the origin $(i, j) = (0, 0)$ the displacement is given by a simple inverse discrete Fourier transform of the respective $B^{\alpha\beta}_{pq}$ components:

$$u^{\alpha}_{lm} = f_0 \sum_{pq} B^{\alpha\beta}_{pq} \exp\left[2\pi i \left(\frac{lp}{N} + \frac{mq}{M}\right)\right] \tag{D.65}$$

$$\widetilde{u}^{\alpha}_{pq} = f_0 B^{\alpha\beta}_{pq} \tag{D.66}$$

D.4 Stresses

Stresses are defined on the sub-triangles of each plaquette as:

$$\sigma^{\alpha\beta N}_{ij} = \frac{\partial \Phi}{\partial \epsilon^{\alpha\beta N}_{ij}} \tag{D.67}$$

and similarly for the other three E, W, S triangles. The stress on a plaquette is then the average over the triangles:

$$\sigma^{xx}_{ij} = \frac{1}{4} K (e^{N}_{1ij} + e^{E}_{1ij} + e^{W}_{1ij} + e^{S}_{1ij}) + \frac{1}{4} G (e^{N}_{2ij} + e^{E}_{2ij} + e^{W}_{2ij} + e^{S}_{2ij}) \tag{D.68}$$

$$\sigma^{yy}_{ij} = \frac{1}{4} K (e^{N}_{1ij} + e^{E}_{1ij} + e^{W}_{1ij} + e^{S}_{1ij}) - \frac{1}{4} G (e^{N}_{2ij} + e^{E}_{2ij} + e^{W}_{2ij} + e^{S}_{2ij}) \tag{D.69}$$

$$\sigma^{xy}_{ij} = \sigma^{yx}_{ij} = \frac{1}{4} G (e^{N}_{3ij} + e^{E}_{2ij} + e^{W}_{3ij} + e^{S}_{3ij}) \tag{D.70}$$

Along with equations D.6 and D.14 thus the stresses are defined in terms of displacements:

$$\begin{aligned}
\sigma_{ij}^{xx} &= \frac{1}{2a}[(G+K)(-u_{ij}^x - u_{i,j+1}^x + u_{i+1,j}^x + u_{i+1,j+1}^x) && \text{(D.71)}\\
&+ (G-K)(u_{ij}^y - u_{i,j+1}^y + u_{i+1,j}^y - u_{i+1,j+1}^y)] && \text{(D.72)}\\
\sigma_{ij}^{yy} &= \frac{1}{2a}[(G-K)(u_{ij}^x + u_{i,j+1}^x - u_{i+1,j}^x - u_{i+1,j+1}^x) && \text{(D.73)}\\
&+ (G+K)(-u_{ij}^y + u_{i,j+1}^y - u_{i+1,j}^y + u_{i+1,j+1}^y)] && \text{(D.74)}\\
\sigma_{ij}^{xy} &= \frac{1}{2a}G(-u_{ij}^x + u_{i,j+1}^x - u_{i+1,j}^x + u_{i+1,j+1}^x && \text{(D.75)}\\
&- u_{ij}^y - u_{i,j+1}^y + u_{i+1,j}^y + u_{i+1,j+1}^y) && \text{(D.76)}
\end{aligned}$$

and:

$$\begin{aligned}
\sigma_{ij}^{(1)} = \sigma_{ij}^{yy} + \sigma_{ij}^{xx} &= \frac{1}{a}K(-u_{ij}^x - u_{i,j+1}^x + u_{i+1,j}^x + u_{i+1,j+1}^x && \text{(D.77)}\\
&- u_{ij}^y + u_{i,j+1}^y - u_{i+1,j}^y + u_{i+1,j+1}^y) && \text{(D.78)}\\
\sigma_{ij}^{(2)} = \sigma_{ij}^{yy} - \sigma_{ij}^{xx} &= \frac{1}{a}G(u_{ij}^x + u_{i,j+1}^x - u_{i+1,j}^x - u_{i+1,j+1}^x && \text{(D.79)}\\
&- u_{ij}^y + u_{i,j+1}^y - u_{i+1,j}^y + u_{i+1,j+1}^y) && \text{(D.80)}\\
\sigma_{ij}^{(3)} = \sigma_{ij}^{xy} && && \text{(D.81)}
\end{aligned}$$

D.5 Eigenstrain on a plaquette - mode 2

Here we show that applying an eigenstrain to one of the plaquettes is equivalent to applying a quadrupole of forces at the vertices of that plaquette. Let us suppose that plaquette (l,m) undergoes an eigenstrain along mode e_2, so its energy becomes:

$$\Phi_{ij} = \frac{K}{2}e_{1ij}^2 + \frac{G}{2}(e_{2ij} + e_0\delta_{il}\delta_{lm})^2 + \frac{G}{2}e_{3ij}^2 \tag{D.82}$$

The energy of all the other plaquettes is the same as before. In this case, eq. D.20 is not valid any more since there will be inhomogeneous terms in the first derivative that are linear in e_0, and the second derivative makes them vanish. Instead, it modifies to:

$$\begin{aligned}
F_{ij}^{\alpha} &= \sum_{pq\beta}\frac{\partial F_{ij}^{\alpha}}{\partial u_{pq}^{\beta}}u_{pq}^{\beta} + \sum_{pq}\frac{\partial F_{ij}^{\alpha}}{\partial e_{0pq}}e_{0pq} && \text{(D.83)}\\
&= -\sum_{pq\beta}\frac{\partial^2\Phi}{\partial u_{ij}^{\alpha}\partial u_{pq}^{\beta}}u_{pq}^{\beta} - \sum_{pq}\frac{\partial^2\Phi}{\partial u_{ij}^{\alpha}\partial e_{0pq}}e_{0pq} && \text{(D.84)}\\
&= -\sum_{pq\beta}H_{ijpq}^{\alpha\beta}u_{pq}^{\beta} - F_{0ij}^{\alpha} && \text{(D.85)}
\end{aligned}$$

so the equilibrium equations modify to:

$$\sum_{pq\beta}H_{ijpq}^{\alpha\beta}u_{pq}^{\beta} = F_{ext\ ij}^{\alpha} - F_{0ij}^{\alpha} \tag{D.86}$$

meaning that eigenstrains have the same effect as an extra external force field. With an eigenstrain of the form $e_{0pq} = e_0 \delta_{lp} \delta_{mq}$:

$$F^{\alpha}_{0ij} = \frac{\partial^2 \Phi}{\partial u^{\alpha}_{ij} \partial e_0} e_0 = e_0 \frac{\partial}{\partial e_0} \left[\frac{\partial \Phi_{i-1j-1}}{\partial u^{\alpha}_{ij}} + \frac{\partial \Phi_{ij-1}}{\partial u^{\alpha}_{ij}} + \frac{\partial \Phi_{i-1j}}{\partial u^{\alpha}_{ij}} + \frac{\partial \Phi_{ij}}{\partial u^{\alpha}_{ij}} \right] \quad \text{(D.87)}$$

From the brackets, only the derivative of one term can be non-zero at a time, when $(l,m) = (i-1, j-1), (i-1, j), (i, j-1), (i, j)$, or, which is the same, $(i,j) = (l+1, m+1), (l+1, m), (l, m+1), (l, m)$. Those are 4 force terms with 2 components each:

$$F^{\alpha}_{0\ l+1,m+1} = e_0 \frac{\partial}{\partial e_0} \frac{\partial \Phi_{lm}}{\partial u^{\alpha}_{l+1,m+1}} \quad \text{(D.88)}$$

$$F^{\alpha}_{0\ l+1,m} = e_0 \frac{\partial}{\partial e_0} \frac{\partial \Phi_{lm}}{\partial u^{\alpha}_{l+1,m}} \quad \text{(D.89)}$$

$$F^{\alpha}_{0\ l,m+1} = e_0 \frac{\partial}{\partial e_0} \frac{\partial \Phi_{lm}}{\partial u^{\alpha}_{l,m+1}} \quad \text{(D.90)}$$

$$F^{\alpha}_{0\ l,m} = e_0 \frac{\partial}{\partial e_0} \frac{\partial \Phi_{lm}}{\partial u^{\alpha}_{l,m}} \quad \text{(D.91)}$$

$$\text{(D.92)}$$

Evaluating the derivatives:

$$F^{x}_{0\ l+1,m+1} = F^{x}_{0\ l+1,m} = F^{y}_{0\ l+1,m} = F^{y}_{0\ l,m} = \frac{2G}{a} e_0 \quad \text{(D.93)}$$

$$F^{x}_{0\ l,m+1} = F^{x}_{0\ l,m} = F^{y}_{0\ l+1,m+1} = F^{y}_{0\ l,m+1} = -\frac{2G}{a} e_0 \quad \text{(D.94)}$$

which proves that as far as the displacements are concerned, if plaquette (l,m) undergoes an eigenstrain of magnitude e_0 along the e_2 mode, this is equivalent to applying a suitable quadrupole of forces to the vertices of that plaquette. Without any loss of generality, to simplify notation, further on we consider $(l,m) = (0,0)$. Also, there are no external forces. The equation to be solved thus can be reduced to solving the initial, eigenstrain-free system subject to 8 point forces with magnitude $f_0 = 2G/a$ each. Adding up the displacements for all the point forces, one obtains:

$$u^{\alpha}_{lm} = f_0 \sum_{pq} (B^{x\alpha}_{pq} A^{x}_{pq} + B^{y\alpha}_{pq} A^{y}_{pq}) \exp\left[2\pi i \left(\frac{lp}{N} + \frac{mq}{M} \right) \right] \quad \text{(D.95)}$$

or

$$\widetilde{u}^{\alpha}_{pq} = f_0 (B^{x\alpha}_{pq} A^{x}_{pq} + B^{y\alpha}_{pq} A^{y}_{pq}) \quad \text{(D.96)}$$

with

$$A^{x}_{pq} = 1 - \exp\left[-2\pi i \frac{p}{N} \right] - \exp\left[-2\pi i \left(\frac{p}{N} + \frac{q}{M} \right) \right] + \exp\left[-2\pi i \frac{q}{M} \right] \quad \text{(D.97)}$$

$$A^{y}_{pq} = -1 - \exp\left[-2\pi i \frac{p}{N} \right] + \exp\left[-2\pi i \left(\frac{p}{N} + \frac{q}{M} \right) \right] + \exp\left[-2\pi i \frac{q}{M} \right] \quad \text{(D.98)}$$

For the stresses, equations D.71 are valid if the respective plaquettes have no eigenstrains, however one has to take into account the eigenstrain on plaquette $(0,0)$. Once computing all the stresses like if there was no eigenstrain on any plaquettes, the following adjustment has to be made (according to eq. D.67):

$$\sigma_{00}^{xx} \rightarrow \sigma_{00}^{xx} + e_0 G \tag{D.99}$$
$$\sigma_{00}^{yy} \rightarrow \sigma_{00}^{yy} - e_0 G \tag{D.100}$$

Fourier-transforming equations D.71, the mode-2 stress $\sigma^{(2)} = \sigma_{yy} - \sigma_{xx}$ can be obtained from:

$$\widetilde{\sigma}_{pq}^{(2)} = \frac{G}{a}\widetilde{u}_{pq}^{+}\left(\exp\left[\frac{2\pi i q}{M}\right] - \exp\left[\frac{2\pi i p}{N}\right]\right) \tag{D.101}$$
$$+ \frac{G}{a}\widetilde{u}_{pq}^{-}\left(1 - \exp\left[2\pi i\left(\frac{q}{M} + \frac{p}{N}\right)\right]\right) - 2Ge_0 \tag{D.102}$$

where:

$$\widetilde{u}_{pq}^{+} = \widetilde{u}_{pq}^{x} + \widetilde{u}_{pq}^{y} \tag{D.103}$$
$$\widetilde{u}_{pq}^{-} = \widetilde{u}_{pq}^{x} - \widetilde{u}_{pq}^{y} \tag{D.104}$$

The last term comes from the stress drop at plaquette $(0,0)$ which appears as a constant in the Fourier space. Putting it all together and after ages of calculations one obtains:

$$\widetilde{\sigma}_{pq}^{(2)} = 2Ge_0[\frac{4G}{1 - C_p C_q} \tag{D.105}$$
$$(\frac{(C_p - C_q)^2}{(6G+5K) - (2G+K)(C_p + C_q) - (2G+3K)C_p C_q}$$
$$+ \frac{S_p^2 S_q^2}{(6G+K) - (2G+K)(C_p + C_q) - (2G-K)C_p C_q}) - 1]$$

where $C_p = \cos(2\pi p/N)$, $C_q = \cos(2\pi q/M)$, $S_p = \sin(2\pi p/N)$, $S_q = \sin(2\pi q/M)$. Far from the inclusion, i.e. $p \ll N$ and $q \ll M$ the sines and cosines can be developed up to the second order and one recovers the classical far-field result:

$$\widetilde{\sigma}_{pq}^{(2)} \approx -\frac{2GK}{G+K}\left(\frac{P^2 - Q^2}{P^2 + Q^2}\right)^2 e_0 \tag{D.106}$$
$$\lim_{p\to 0}\lim_{q\to 0}\widetilde{\sigma}_{pq}^{(2)} = \lim_{q\to 0}\lim_{p\to 0}\widetilde{\sigma}_{pq}^{(2)} = -\frac{2GK}{G+K}e_0 \tag{D.107}$$

where $P = 2\pi p/N$ and $Q = 2\pi q/M$.

With the same approach, for the mode-1 stress:

$$\widetilde{\sigma}_{pq}^{(1)} = \frac{K}{a}\widetilde{u}_{pq}^{+}\left(-1 + \exp[i(P+Q)]\right) \tag{D.108}$$
$$+ \frac{K}{a}\widetilde{u}_{pq}^{-}\left(\exp[iP] - \exp[iQ]\right) \tag{D.109}$$

which, after the math gives:

$$\widetilde{\sigma}^{(1)}_{pq} = -8KGe_0 \frac{C_q - C_p}{(6G+5K) - (2G+K)(C_p+C_q) - (2G+3K)C_pC_q} \tag{D.110}$$

which in the limit $p \ll N$ and $q \ll M$ gives:

$$\widetilde{\sigma}^{(1)}_{pq} \approx -\frac{2GK}{G+K}\left(\frac{P^2-Q^2}{P^2+Q^2}\right)e_0 \tag{D.111}$$

$$\lim_{p\to 0}\lim_{q\to 0}\widetilde{\sigma}^{(1)}_{pq} = -\frac{2GK}{G+K}e_0 \tag{D.112}$$

$$\lim_{q\to 0}\lim_{p\to 0}\widetilde{\sigma}^{(1)}_{pq} = \frac{2GK}{G+K}e_0 \tag{D.113}$$

For mode-3 stress we have:

$$\widetilde{\sigma}^{(3)}_{pq} = \widetilde{\sigma}^{xy}_{pq} = \frac{G}{2a}\widetilde{u}^{+}_{pq}\left(-1+\exp[i(P+Q)]\right) \tag{D.114}$$

$$- \frac{G}{2a}\widetilde{u}^{-}_{pq}\left(\exp[iP]-\exp[iQ]\right) \tag{D.115}$$

which leads to:

$$\widetilde{\sigma}^{(3)}_{pq} = \frac{8G^2}{a^2}e_0\frac{S_pS_q(C_p-C_q)}{1-C_pC_q}\left(\frac{1}{\lambda^x_{pq}}-\frac{1}{\lambda^y_{pq}}\right) \tag{D.116}$$

Plugging in the eigenvalues gives the final expression:

$$\widetilde{\sigma}^{(3)}_{pq} = 4G^2e_0\frac{S_pS_q(C_p-C_q)}{1-C_pC_q}\Big[\frac{1}{(6G+5K)-(2G+K)(C_p+C_q)-(2G+3K)C_pC_q}$$

$$- \frac{1}{(6G+K)-(2G+K)(C_p+C_q)-(2G-K)C_pC_q}\Big] \tag{D.117}$$

In the far-field limit, mode-3 stress has the form:

$$\widetilde{\sigma}^{(3)}_{pq} \approx 2G\frac{G-K}{G+K}e_0\frac{PQ(Q^2-P^2)}{(P^2+Q^2)^2} \tag{D.118}$$

$$\lim_{p\to 0}\lim_{q\to 0}\widetilde{\sigma}^{(3)}_{pq} = \lim_{q\to 0}\lim_{p\to 0}\widetilde{\sigma}^{(3)}_{pq} = 0 \tag{D.119}$$

D.6 Eigenstrain on a plaquette - mode 3

This time the energy of the plaquette with the eigenstrain is given by:

$$\Phi_{00} = \frac{K}{2}e^2_{1\ 00} + \frac{G}{2}e^2_{2\ 00} + \frac{G}{2}(e_{3\ 00}-e_0)^2 \tag{D.120}$$

With the same reasoning as above, this is equivalent to a quadrupole of forces acting on the corners of plaquette $(0,0)$:

$$F^x_{0\ 11} = F^x_{0\ 01} = F^y_{0\ 11} = F^y_{0\ 10} = -\frac{2G}{a}e_0 \tag{D.121}$$

$$F^x_{0\ 10} = F^x_{0\ 00} = F^y_{0\ 01} = F^y_{0\ 00} = \frac{2G}{a}e_0 \tag{D.122}$$

$$\tag{D.123}$$

For this configuration, we have:

$$A^x_{pq} = -1 - \exp\Big[-2\pi i\frac{p}{N}\Big] + \exp\Big[-2\pi i\left(\frac{p}{N}+\frac{q}{M}\right)\Big] + \exp\Big[-2\pi i\frac{q}{M}\Big] \tag{D.124}$$

$$A^y_{pq} = -1 + \exp\Big[-2\pi i\frac{p}{N}\Big] + \exp\Big[-2\pi i\left(\frac{p}{N}+\frac{q}{M}\right)\Big] - \exp\Big[-2\pi i\frac{q}{M}\Big] \tag{D.125}$$

whereas, for the stresses:

$$\sigma^{xy}_{00} \rightarrow \sigma^{xy}_{00} - e_0 G \tag{D.126}$$

$$\sigma^{yx}_{00} \rightarrow \sigma^{yx}_{00} - e_0 G \tag{D.127}$$

The mode-3 stress $\sigma^{(3)} = \sigma_{xy}$ can be obtained from:

$$\widetilde{\sigma}^{(3)}_{pq} = \frac{G}{2a}\widetilde{u}^{+}_{pq}\left(-1+\exp\Big[2\pi i\left(\frac{q}{M}+\frac{p}{N}\right)\Big]\right) \tag{D.128}$$

$$+ \frac{G}{2a}\widetilde{u}^{-}_{pq}\left(\exp\left[\frac{2\pi iq}{M}\right] - \exp\left[\frac{2\pi ip}{N}\right]\right) - Ge_0 \tag{D.129}$$

which leads to:

$$\widetilde{\sigma}^{(3)}_{pq} = Ge_0[\frac{4G}{1-C_pC_q} \tag{D.130}$$

$$(\frac{S_p^2S_q^2}{(6G+5K)-(2G+K)(C_p+C_q)-(2G+3K)C_pC_q}$$

$$+ \frac{(C_p-C_q)^2}{(6G+K)-(2G+K)(C_p+C_q)-(2G-K)C_pC_q}) - 1]$$

The mode-2 stress in this case has exactly the same expression as the mode-3 in the previous case (checked independently):

$$\widetilde{\sigma}^{(2)}_{pq} = 4G^2e_0\frac{S_pS_q(C_p-C_q)}{1-C_pC_q}[\frac{1}{(6G+5K)-(2G+K)(C_p+C_q)-(2G+3K)C_pC_q}$$

$$- \frac{1}{(6G+K)-(2G+K)(C_p+C_q)-(2G-K)C_pC_q}] \tag{D.131}$$

Finally, for the mode-1 stress we obtain the following expression:

$$\widetilde{\sigma}^{(1)}_{pq} = 8KGe_0\frac{S_pS_q}{(6G+5K)-(2G+K)(C_p+C_q)-(2G+3K)C_pC_q} \tag{D.132}$$

Part II

Dewetting of thin liquid layers

Chapter 6

Soft line in quenched disorder

Contents

In the first part in the thesis we have shown that the yielding transition of amorphous materials has many features in common with the depinning transition of elastic lines. Both phenomena are a result of the competition between disorder and long range elastic interactions. In that sense, many systems can be modeled in the depinning framework. For example, the roughening of a moving dewetting contact line on inhomogeneous surfaces is governed by the competition of the surface tension forces and the pinning-like

interactions with the inhomogeneities of the surface. This roughening process has been intensively studied in the depinning framework. As we have seen however, the depinning framework is limited to linear interactions, thus small deformations only. Moreover, standard depinning methods do not allow for the eventual tearing up of the layer due to large deformations.

In this chapter, we precisely address these two issues. We develop a depinning-like model which aims to capture large deformations and eventual tearing up of the liquid layer. We show that there exist a critical concentration of inhomogeneities below which the line stops within a finite distance, and above this concentration it moves indefinitely. Right at the critical concentration however large deformations of the line occur with long correlations which may be the footprint of a peculiar depinning-like transition.

6.1 Introduction and motivation

Contraction of thin liquid layers on solid surfaces due to dewetting or drying is a common phenomenon. It is observable for instance, on plants' leafs as the water breaks up into small droplets, in non-sticking pans as the oil layer shrinks or on an outdoor oil-polluted surface after rain. Another well-know example is the contraction of the liquid layer covering the eyeball, the characteristic time scale of a complete contraction being the time elapsed between two successive blinks [76, 157]. Dewetting plays an important role in the tire industry as well: when the contraction of the wetting layer on the tire's groove is too slow, aquaplaning is more likely to occur [120, 135, 136]. Dewetting is also important in the lubricant manufacturing, however in this case exactly the opposite effect is desired: the more a lubrifient remains on the surface of sliding pieces, i. e. the larger its contraction time, the better.

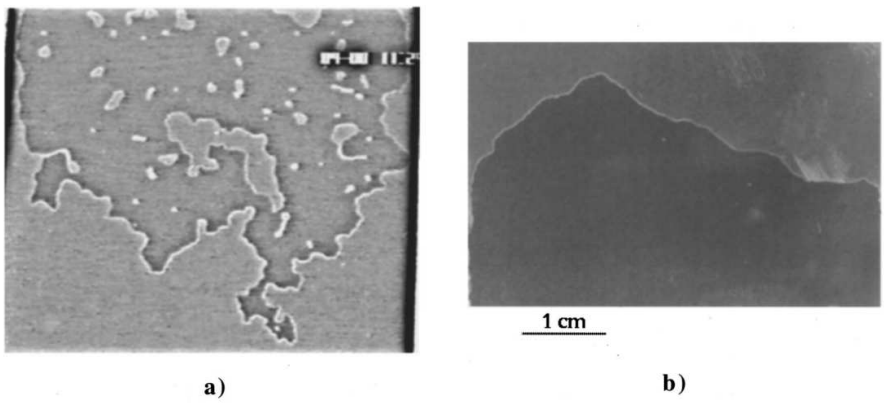

Figure 6.1 – Roughening of a moving fluid interface in a Hele-Shaw cell in presence of inhomogeneities following a (a) strongly disordered pattern and (b) weakly disordered pattern. Figure from [131]

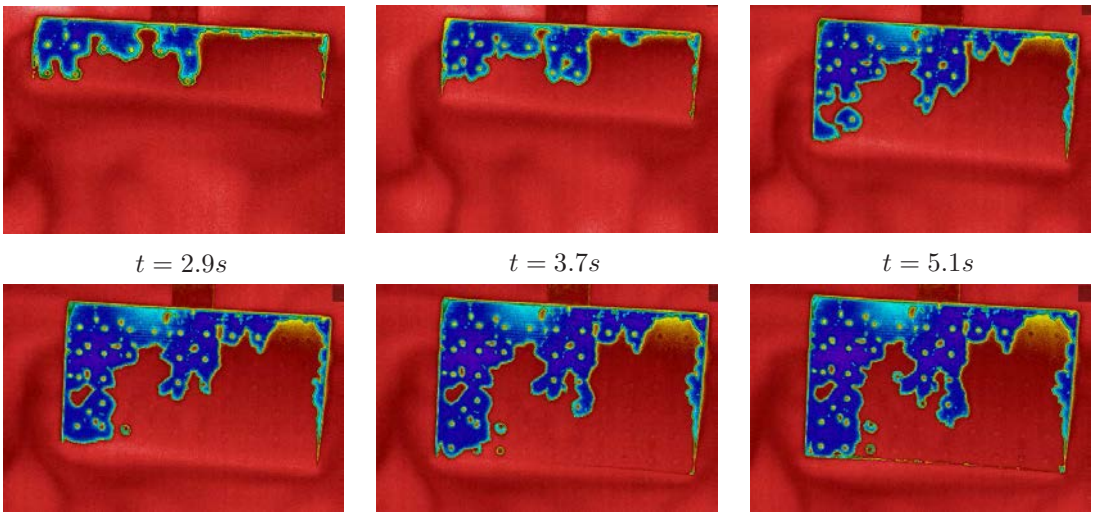

Figure 6.2 – Progressive roughening of a receding contact line on a regular array of defects. Experiments performed and images kindly provided by E. S. Bogya and Á. Kukovecz. In the experiment, a square array of defects was placed on a flat surface. The size of a defect is 1 mm and the distance between defects is 5 mm. The surface was tilted by 30° compared to horizontal and lifted out of water at a constant velocity of 10 cm/min. Images were taken by a thermal camera for better contrast. Upon lifting, a thin layer of liquid is left behind. During contraction, the contact line is pinned on the defects resulting in roughening and eventual tearing up of the layer.

Along with the development of the polymer industry, contraction of polymer films started to gain interest [145, 192, 197]. Dewetting turned out to be a useful investigative tool for determining various rheological and interfacial properties of thin polymer films due to the fact that molecular properties are reflected in the macroscopic shape of the solid-liquid-gas triple interface [146].

In other cases, liquids are used as carriers for certain substances (nanoparticles, for example), thus dewetting eventually accompanied by drying on rough surfaces of such solutions, results in deposition of the dissolved substance on the substrate. In fact, this deposition process can only be controlled through controlling the dynamics of the carrier liquid film, and, in particular, the evolution of the morphology of the triple line. In a recent study, DNA molecules were deposited in a highly ordered array by dissolving them in a solvent and letting the solvent dewet a micropillar-structured surface [104].

The dynamics of wetting on flat solid and liquid surfaces is quite well understood [197, 66], however, despite its applicability, only a few experiments were performed on inhomogeneous, either patterned or disordered surfaces [43, 132, 42, 56, 44, 45] (see, for example, Figure 6.1), while the dynamics of a receeding contact line remains almost unexplored. Figure 6.2 shows snapshots of such an experiment, where the roughening

of a receding contact line on a surface with an array of defects is observable. In spite of the apparent simplicity of the phenomenon, there are no simple, easily manageable models for describing it. Although in the lubrication approximation the Navier-Stokes (or, in the highly viscous regime the Stokes) equation reduces to two dimensions [129], the numerical modeling of layers with large planar extent is still computationally time consuming and cumbersome due to the discontinuities on the liquid-solid and liquid-gas interfaces. These discontinuities are tackled within the framework of phase-field models [87], it remains unclear however, how substrate inhomogeneities would be introduced in such models. It is also also unsettled how the actual dynamics of the layer is influenced by the chosen particular form of the phase interface.

The continuous emergence of newer and newer schemes in the topic suggests that the demand for a convenient approach for modeling thin liquid layers' dynamics is still unsatisfied [87, 163, 152, 55, 19, 103]. Based on the revolutionary paper of J. F. Joanny and P. G. de Gennes on the perturbed contact line shape [88, 68], a series of depinning type models were constructed which aimed to describe interface dynamics in presence of disorder [134, 191, 159, 189]. These models are not restricted to dewetting phenomena, as they apply to fracture front propagation or even magnetic domain wall motion. In the framework of these models, small deformations of the interface and a linear restoring force acting on the contact line resulting from a perturbative approach are considered. They are thus inherently linear, and the only source of nonlinearity is the disorder of the landscape they propagate in. Although they have had a great success in the sampling of the depinning transition and determination of various critical exponents [173, 92, 93], they have the drawback that they neither allow for large deformations, nor for local backward movement of the line. Consequently, they are unable to account for the tearing up of the dewetting film, which, in fact, is a common phenomenon.

Our purpose here is precisely to address the question of large deformations and the eventual tearing of the film with an efficient and easily manageable model for the contact line motion. Our method works best for viscous, flat and extended droplets with small wetting angle. It is shown that in this regime, in contrast to the perturbative treatment [88], the line is soft and ductile, meaning that a localized perturbation of the line induces only short range forces. Considering a viscous regime, the line's equation of evolution becomes an overdamped one. In the following sections, we will describe this method in detail. We will show how to handle substrate inhomogeneities, and an application is presented. Our results have been published in [186].

6.2 Basic concepts

Energy of the contact line

Let the upper surface of the contracting fluid layer be described by $z = z(x, y, t)$. Our approach is restricted to the description of large, flat layers in the highly viscous regime, the same assumption that is made when deriving the lubricant equations [129], i.e. $|\nabla z| \ll 1$. One further assumption we make is that the relative change in the height of the droplet is

small, therefore its height is almost constant in time, $\partial z/\partial t \to 0$. Under these considerations, the layer's free energy has two terms. The first component is the joint contribution of the well-known liquid-solid and liquid-gas (air) surface tensions. If the layer is flat, its upper and lower surface areas are approximately equal, S. Denoting by γ_{XY} the appropriate surface tension coefficients, the surface energy writes as:

$$U_{surface} = \gamma_{SL} S + \gamma_{LG} S = \gamma S \tag{6.1}$$

The second contribution to the total free energy of the layer is the line energy which occurs due to the unbalanced forces acting on the layer boundaries on the molecules from the liquid-substrate-air triple interface. This is a curve with finite thickness, thus this energy is comparable to the surface energy and it is proportional to the length of the triple interface, l

$$U_{line} = \alpha l, \tag{6.2}$$

where α is the line tension coefficient. Neither the interpretation of α, nor its measurement is straightforward. In fact, there is still less consensus regarding its magnitude: values ranging from $10^{-11}N$ to $10^{-6}N$ were measured or computed in various experiments and simulations [140, 21, 53, 54, 168, 5]. The major difficulty arises from the fact that dewetting is often accompanied by a precursor layer with a much smaller thickness than the rest of the layer. In our case, in term (6.2) a contribution resulting from the layer's side surface has to be also considered. This yields an extra surface energy that is also proportional with l, consequently, we believe that an effective α has to be used instead. Therefore in calculations larger values than the presented range should be used. In the case of a real two dimensional flow (for instance, flow in a Hele-Shaw cell [42, 132]), the line tension is well defined and it is clearly a result from the finite side surface of the layer between the plates. For complete wetting, i.e. zero wetting angle, $\alpha = \pi\gamma_{LG}h/2$, where h is the distance between the plates of the Hele-Shaw cell [132]. Alternatively, if a quantitative upscaling of the elastic type of energy introduced in [88] was possible (properly removing the third dimension from the model), it could provide the correct expression for the line tension for sufficiently flat droplets, bounded by one solid surface only. Such an expression however is not available, hence it remains an open question.

The total free energy of the system is the sum of these two contributions: $U = U_{surface} + U_{line}$.

Our approach is based on the fact that both the surface and the line energies are functionals of the shape of the triple interface, which is a one-dimensional curve. When inertial effects do not play an important role (the highly viscous, low Reynolds number regime), the total energy of the system is uniquely defined by the shape of the contact line, it is therefore enough to track solely its dynamics.

Dynamics of a circular hole

In order to illustrate that the dynamics is defined by the motion of the contact line, we consider a simple example: the dynamics of a circular hole. Due to the symmetry of the problem, an analytically study is possible. From energy terms (6.1) and (6.2) the forces

acting on the edge of the hole can be derived, which, due to symmetry considerations act in the radial direction

$$F_{surface} = -\frac{\partial U_{surface}}{\partial R} = -\frac{\partial}{\partial R}(-\gamma\pi R^2) = 2\pi\gamma R, \tag{6.3}$$

where R is the radius of the hole. Similarly, the force resulting from the line tension:

$$F_{line} = -\frac{\partial U_{line}}{\partial R} = -\frac{\partial}{\partial R}(\alpha 2\pi R) = -2\pi\alpha \tag{6.4}$$

Assuming an overdamped motion of the edge of the hole (the triple interface), the following equation of motion yields for its radius:

$$(F_{line} + F_{surface})m = \frac{dR}{dt} \tag{6.5}$$

In the above expression, m is the mobility of the three-phase line and is inversely proportional to its length, i.e. the longer the line, the more sluggish it is: $m = m_0 l_0/(2\pi R)$, where m_0 is the mobility of a line segment of length l_0. The equation of motion for the contact line is thus:

$$\left(\gamma - \frac{\alpha}{R}\right) m_0\ l_0 = \frac{dR}{dt} \tag{6.6}$$

It can be seen that the equilibrium radius of the hole is $R_0 = \alpha/\gamma$ which is an intrinsic length scale of the system. For large radii ($R/R_0 \gg 1$) the line energy can be neglected and the velocity of the contact line is constant:

$$\frac{dR}{dt} = \gamma m_0\ l_0 \tag{6.7}$$

Note that when R is large, $R(t) \propto t$, which is in complete agreement with previous results, for instance [197].

Mobility of the contact line

So far the mobility of the triple interface has been introduced as a phenomenological parameter which, in turn, defines the time-scale of the problem. Considering the case when no slippage of the interface occurs (the flow of the interface is a Poiseuille flow), in previous studies similar results to eq. (6.7) have been derived for the radial velocity of the triple interface for a drying patch nucleated into a liquid film [197, 143, 27, 144]:

$$\frac{dR}{dt} = \frac{\theta_e^3}{12\sqrt{2}\ln(\theta_e l/b)\mu}\gamma \tag{6.8}$$

where θ_e is the equilibrium contact angle, l is the rim width, b is the extrapolation length (the distance from the rim at which the velocity extrapolates to zero) and μ is the viscosity. Comparing eq. (6.7) to eq. (6.8) one can identify the mobility given now

in terms of independently measurable quantities that are now properties of the contact line:

$$m_0\ l_0 = \frac{\theta_e^3}{12\sqrt{2}\ln(\theta_e l/b)\mu} \tag{6.9}$$

In case of a curve-like interface with parametric equation $\vec{r} = \vec{r}(u)$ (where u is some arbitrary parameter), the equation of motion writes as

$$\dot{\vec{r}}(u) = m[\vec{r}(u)]\ \cdot \vec{F}[\vec{r}(u)], \tag{6.10}$$

hence the mobility and the force in this case are both functionals of the shape of the interface.

6.3 The simulation method

Discretization of the contact line: characteristic points

In order to model the dynamics of contact lines of arbitrary shape, numerical methods are necessary. As a first step, the contact line is discretized into *representative points*. After the contour is discretized, the points are connected through directed line segments (vectors). Each of the points "tracks" its previous and upcoming neighbors and, by convention, the vectors are directed so that the liquid always lies on their left hand side. Following the direction of the vectors connecting the points, a directed chain is established. We denote by S_i the index of the ensuing point corresponding to point i and by W_i the point preceding i (Fig.6.3). In terms of the representative points' coordinates,

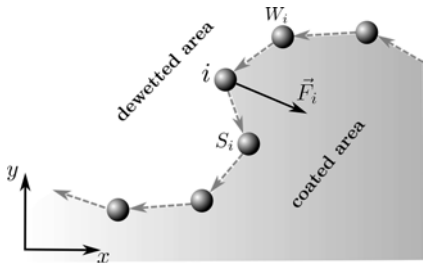

Figure 6.3 – Discretization of the contact line. The contact line is considered as a chain of representative points with directional connections and nearest neighbor interactions.

the line and surface tension energies write as:

$$U_{line} = \alpha \sum_i \sqrt{(x_i - x_{S_i})^2 + (y_i - y_{S_i})^2} \tag{6.11}$$

$$U_{surface} = \gamma \frac{1}{2} \sum_i x_i y_{S_i} - x_{S_i} y_i \tag{6.12}$$

Nearest neighbor interactions

Once the energies are obtained, the forces acting on the representative points are computed as $\vec{F}_i = -\nabla_i U$. In our two-dimensional approximation, the two components of this force are

$$\begin{aligned} F_{ix} &= -\frac{\partial U}{\partial x_i} = \qquad (6.13) \\ &= -\alpha \left[\frac{x_i - x_{W_i}}{d_{i,W_i}} + \frac{x_i - x_{S_i}}{d_{i,S_i}} \right] + \gamma(y_{S_i} - y_{W_i}) \\ F_{iy} &= -\frac{\partial U}{\partial y_i} = \qquad (6.14) \\ &= -\alpha \left[\frac{y_i - y_{W_i}}{d_{i,W_i}} + \frac{y_i - y_{S_i}}{d_{i,S_i}} \right] - \gamma(x_{S_i} - x_{W_i}), \end{aligned}$$

where $d_{k,l}$ is the distance between points k and l. It can be readily seen that each point interacts with its nearest neighbors only. We emphasize that the localized nature of the forces is a direct consequence of our primary hypothesis, i.e. the droplet is flat and its height profile does not change significantly during the movement of the contact line. Either at lower scales, where the fine structure of the contact line becomes relevant or in the case of non-flat droplets the Green function of the contact line (its response to a localized perturbation) is of long-range nature. As mentioned in the introduction, a perturbative treatment for small deformations of the contact line is described in Ref. [88], while the propagation of such lines in random media resulting in depinning transition and a consequent advancing accompanied by avalanches are extensively studied in Ref. [191] and [189]. For the present case, we stick to the lubricant approximation, thus proceed with eq. (6.13).

Dynamics of the interface

The system composed of interacting representative points is very similar to an interacting particle system, therefore a simulation method resembling the classical molecular dynamics method is suitable for investigating their dynamics. The overdamped equation of motion for the points is:

$$\dot{\vec{r}}_i = m_i \vec{F}_i \qquad (6.15)$$

The mobility m_i associated to point i is inversely proportional to the length element of the respective point on the triple interface:

$$m_i = m_0 \frac{2d_{max}}{d_{i,S_i} + d_{i,W_i}}, \qquad (6.16)$$

where we remind that d_{i,S_i} is the distance between point i and its upcoming neighbor, while d_{i,W_i} is the distance between point i and its previous neighbor. During their dynamics, the representative points will approach or move away from each other. In

order to preserve numerical accuracy, their density on the triple line should be kept constant. Imposing a constant density however, is incompatible with the movement of the individual points, therefore, an optimal fluctuation around an average value is necessary. This issue is solved by inserting a new point between two neighboring points whenever they move farther than a predefined distance d_{max}. In case they come closer than another predefined distance d_{min}, one of the points is removed. As a rule of thumb, we consider $d_{min} = 0.8\ d_{max}/2$, which ensures that no insertion is necessary right after a removal. With this choice, m_0 is then the mobility of one line segment. Note that continuous indexing of neighboring points is not possible due to the repeated insertions and removals.

Whenever two segments intersect, the points are reconnected such that the line breaks up, hence allowing for tearing the layer. The used reconnection mechanism is sketched on Figure 6.4.

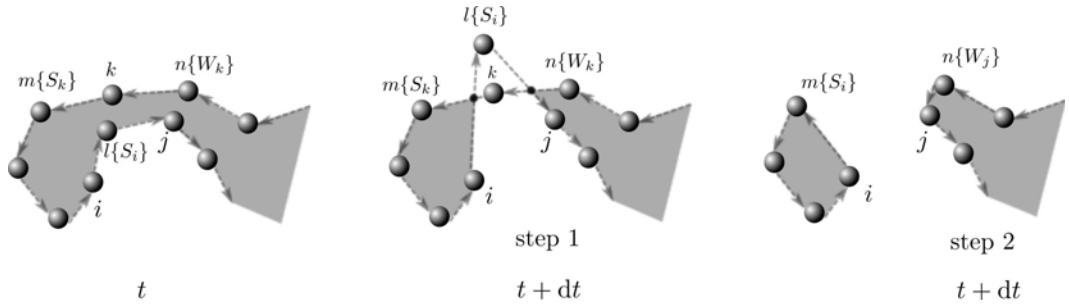

Figure 6.4 – The reconnection mechanism for the tearing of the layer. The label values in parenthesis indicates the succeeding order in the oriented chain. Please note that step 1 and step 2 are made in the same time moment.

Pressure

The model introduced so far applies for extended, flat layers. Due to the surface tension, a circular droplet shrinks up until it disappears because there is no force that would eventually stop it. We propose therefore an extremely simplified way to introduce pressure in the system, with the consideration that the height of the layer is the same everywhere, h. A new force is thus introduced which is always perpendicular to the rim, points towards outside and has the same magnitude for each of the points. Since this force correspond to the hydrostatic pressure, its value is proportional to the actual height of the liquid film:

$$F_{pressure} = Ch \tag{6.17}$$

where C is a positive constant and is related to the density of the liquid.
The height of the layer is derived from the mass of the droplet, from now on therefore each droplet's mass has to be conserved. Besides, we have to keep track of the individual loops, the points belonging to certain loops and when droplets are split, the mass is

distributed among them proportionally to their actual area. The height of droplet k is obtained by:

$$h_k = C_1 \frac{M_k}{A_k(x_p, y_p, ...)} \tag{6.18}$$

where A_k is the (time dependent) area and M_k the mass of loop k. The area is obtained as:

$$A_k = \frac{1}{2} \sum_i x_i y_{S_i} - x_{S_i} y_i \tag{6.19}$$

where the summation refers to all points belonging to loop k.
Through the height thus a global coupling of the points is established. The force resulting from the pressure is weighted in a similar manner as the mobility with the curve element the given point represents:

$$F_{i\ pressure} = C_2 \frac{M_k}{A_k} (d_{i,S_i} + d_{i,W_i}) \tag{6.20}$$

It is assured that this force always points towards outside by checking the concavity of the rim at the given point and changing the direction of the force if necessary. The direction of the previous forces was automatically assured by their x and y components, but in the case of the hydrostatic pressure this has to be adjusted manually.
An immediate consequence of the pressure is that there will be an equilibrium position in the case of the droplets as well. A circular droplet does not shrink and disappear any more, but approaches its stable equilibrium state assimptotically. Since we have no real comparison related to the accuracy of such a rough approximation, the force resulting from pressure will only be used for qualitative purposes.

6.4 Inhomogeneities

The substrate the liquid droplets or thin films move on is usually inhomogeneous: both the roughness and chemical heterogeneities of the underlying surface modify the contact line dynamics and lead to the ripped-edged shapes. Similarly to previous descriptions, one may introduce inhomogeneities of the substrate in terms of pinning points. Here we provide two possibilities to introduce such pinning dots: in the first method, dots are extended patches and the surface and line tension coefficients modify when the contact line arrives above the dot. This method along with the pressure described in the previous section gives qualitative results regarding the roughened shape of the contact line. In the second method we are interested in the statistical quantities describing the roughening. In this case, pinning dots are considered point-like and are generated on the run. We do not consider any pressure force in this second case.

6.4.1 Extended inhomogeneities

Inhomogeneities (defects) of the substrate can be relatively easily built into our model using some pinning dots spread over the substrate. If any of the representative points

arrives above such a pinning surface, both the surface and the line tension coefficients change since the layer's interaction with the surface on these dots is different. The main advantage of this treatment is that the defects are introduced in a simple, yet motivated manner into the model.
For the sake of simplicity, the shape of these pinning dots is taken to be circular, because this way it is easier to check whether any of the representative points is above a given dot or not. The size and place of the dots as well as the line and surface tension on them might be chosen randomly, according to a given distribution that is specific to a given substrate. Usually both the line and surface tension coefficients are smaller on the dots than on the bare surface otherwise an acceleration of the receding rim occurs instead of its blocking.
In order to keep the transition of α and γ from the pinning dots to the surface continuous, a (possibly) linear increase of these coefficients can be considered from the center of the pinning dot to their edge, where they reach their bare surface value. As a first convention, when more pinning dots are superimposed, the lowest value for α and γ are chosen. The equilibrium position on such a surface is presented on Figure 6.5. For illustrative purposes, Figure 6.6 shows the equilibrium positions on a surface with a regular array of inhomogeneities.

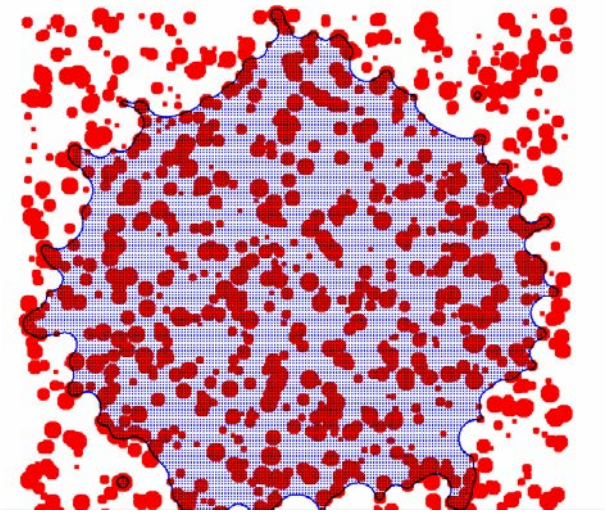

Figure 6.5 – Equilibrium position of the liquid film on an inhomogeneous surface. Pinning dots are marked as red dots. Splitted drops are also observable. Equilibrium in this case can be reached due to the forces resulting from pressure.

6.4.2 Point-like inhomogeneities

While the above method of handling the surface inhomogeneities is appealing, it has two major drawbacks. First, inhomogeneities have to be pre-generated and at each time step

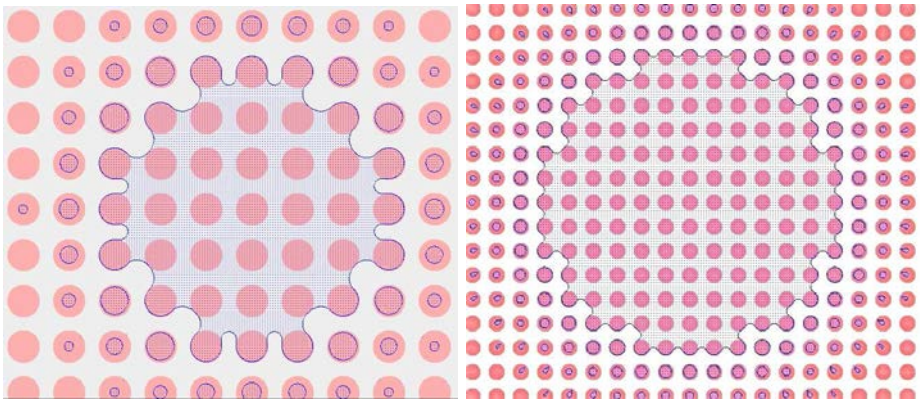

Figure 6.6 – Equilibrium position of the liquid film on a surfaces with a regular array of inhomogeneities. Left: large pinning dots, right: small pinning dots. Note again the tearing up of the layer on some of the dots.

each point has to be checked whether it reached a pinning surface. This is computationally expensive. Second, it involves many additional parameters: size distribution of dots, distribution of α and γ on the dots, density of dots, etc. Adjusting these parameters is useful in particular applications, but they may hide the generic behavior behind the contact line roughening. In this section, we introduce an alternative method which handles the pinning dots as point-like. A threshold force is associated to each dot that has to be crossed by the contact line. With the method developed here, pinning dots are generated on the run, yet they represent quenched disorder. We do not consider pressure here and this is the method we are going to use to investigate the contact line roughening.

Whenever the contact line hits a pinning point, it is blocked as long as the force acting on it does not reach a given threshold. Eq. 6.10 then modifies to:

$$\dot{\vec{r}}(\theta) = m[\vec{r}(\theta)] \cdot \left(\vec{F}[\vec{r}(\theta)] + \vec{F}_{pin}[\vec{r}(\theta)] \right) \tag{6.21}$$

where $\vec{F}_{pin}$ is the pinning force resulting from inhomogeneities:

$$\vec{F}_{pin}(\vec{r}) = \begin{cases} -\eta(\vec{r}) \frac{\vec{F}(\vec{r})}{|\vec{F}(\vec{r})|} & \text{if } \mid \vec{F}(\vec{r}) \mid > \eta(\vec{r}) \\ -\vec{F}(\vec{r}) & \text{if } \mid \vec{F}(\vec{r}) \mid \leq \eta(\vec{r}) \end{cases} \tag{6.22}$$

Note that the above formulation simply tells that the characteristic point trapped on a pinning dot only can pass if the force acting on the point from its neighbors is strong enough to exceed a threshold value η. Here $\eta(\vec{r})$ characterizes the pinning strength at site with position at $\vec{r}$. In case of point-like inhomogeneities, localized at spatial coordinates $\vec{r}_k$

$$\eta(\vec{r}) = \begin{cases} \eta_k & \text{if } \vec{r} = \vec{r}_k \\ 0 & \vec{r} \neq \vec{r}_k, \end{cases} \tag{6.23}$$

where η_k are the thresholds of the pinning points. In the followings, spatially uniformly distributed and uncorrelated inhomogeneities are considered. For simplicity reasons, the η_k threshold values are considered also uniformly and uncorrelatedly distributed on the $[0, \eta_0)$ interval.

The concentration of the point-like inhomogeneities is

$$c = \lim_{S\to\infty} \frac{1}{S} \int_S \sum_k \delta(\vec{r} - \vec{r}_k) d\vec{r}, \tag{6.24}$$

while their average distance is given by $L_0 = 1/\sqrt{c}$.

Note that the disorder is quenched, which means that in principle their positions would have to be generated and fixed right from the beginning of the simulation. The line segments have to be tested at any instant of the simulation, whether they cross any of the pinning points, a procedure which is extremely time consuming. In order to avoid this, a simplified procedure is used to generate pinning points on the run, yet preserving their statistical properties.

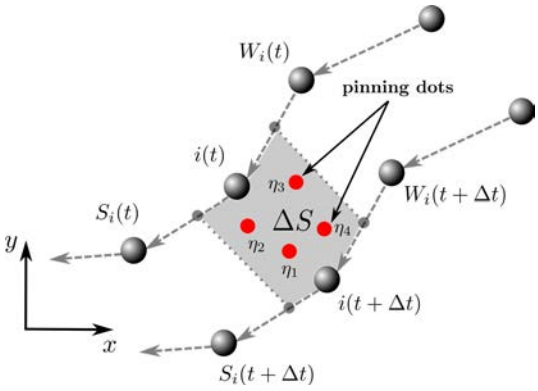

Figure 6.7 – Handling the substrate inhomogeneities. In this example, the line segment corresponding to point i crosses 4 pinning centers, each with its own threshold. The effective threshold experienced by point i is the largest one out of those 4. The pinning points are considered point-like, with no planar extension.

If the line segment belonging to point i sweeps a small area ΔS within a time interval Δt (Fig. 6.7), the probability of finding exactly n pinning points within that area has a Poisson distribution:

$$P(n) = \frac{1}{n!}(c\Delta S)^n \exp(-c\Delta S) \tag{6.25}$$

Since the pinning is related to thresholds, whenever the line segment crosses n pinning points, with thresholds $\{\eta_1, \eta_2, ..., \eta_n\}$, it will experience an effective threshold which is the maximum of all the thresholds of the points within ΔS:

$$\eta_{eff} = \max\{\eta_1, \eta_2, ..., \eta_n\} \tag{6.26}$$

Bearing in mind that η_k is uniformly distributed on the $[0, \eta_0)$ interval, the probability distribution of the maximum is given by:

$$P(\eta_{eff}|n) = n\ \eta_{eff}^{n-1}\ \eta_0^{n-2} \quad \text{where } \eta_{eff} < \eta_0 \tag{6.27}$$

At every time step, for each site, the number of pinning points is drawn according to the (6.25) distribution, while the thresholds are generated according to the (6.27) distribution.

6.5 Soft line in quenched disorder

Overview of the system

As application to the previously discussed method, we will study the dynamics and topology of a moving dewetting line on a substrate with uniformly distributed quenched disorders. Disorders act as pinning centers, and we consider them point-like with the statistical properties described in the previous section. The initial state of the interface is a straight line along the x axis ($y(t = 0) = 0$), and the liquid is considered to be under this line in the $y < 0$ semiplane. Periodic boundary conditions are imposed along the x axis, hence while the liquid contracts, the contact line moves towards the negative y direction. After a transient period, the line reaches a dynamic equilibrium state, in which its statistical properties are stationary.

$R_0 = \alpha/\gamma$ is chosen as the unit length of the simulation. All the lengths are then expressed in terms of dimensionless coordinates $\widetilde{\vec{r}} = \vec{r}/R_0$. Let us introduce $R_1 = \eta_0/\gamma$, which would correspond to a flat line element subjected to a capillary force that would move it over a pinning dot with threshold η_0. Its dimensionless form is $\widetilde{R}_1 = R_1/R_0$. The dimensionless time is $\widetilde{t} = \gamma m_0 t$. The equation of motion (6.21) can then be rewritten in terms of these dimensionless quantities which leaves us with two parameters only: the length scale $\widetilde{R}_1$ defined by the amplitude of the inhomogeneity thresholds and the length scale $\widetilde{L}_0 = L_0/R_0$ defined by their concentration. Consequently, the dynamics of the line is a result of the competition between these two length scales.

Simulations were carried out for a system length along the x direction $\widetilde{L}_x = 160$, representative points distance $\widetilde{d}_{max} = 0.2$ and a time step $\Delta\widetilde{t} = 10^{-3}$. As mentioned previously, tearing up of the layer is possible, however, the resulting droplets (droplets left behind as a result of tearing) are disregarded as they have no more influence on the dynamics of the main line. Wherever it was meaningful, an ensemble average over 10 ensembles (independent runs) was considered.

A depinning-like transition

We present now the results obtained for the dynamics of the model system described in the previous section. First, we study qualitatively the dynamics of the interface. Fig. 6.8 shows the time evolution of the contact line for various parameters $\widetilde{R}_1$ and $\widetilde{L}_0$. As the line's average velocity decreases, i.e. as it approaches the depinning transition,

its length and roughness increases. One will observe that the contact line reaches a statistically stable conformation, and its shapes are in good qualitative agreement with the experiments carried out by Clotet et al.[42] and Paterson et al. [131, 132] in a Hele-Shaw cell, although both experiments were carried out for wetting on disordered substrates, i.e. the opposite dynamics of the contact line.

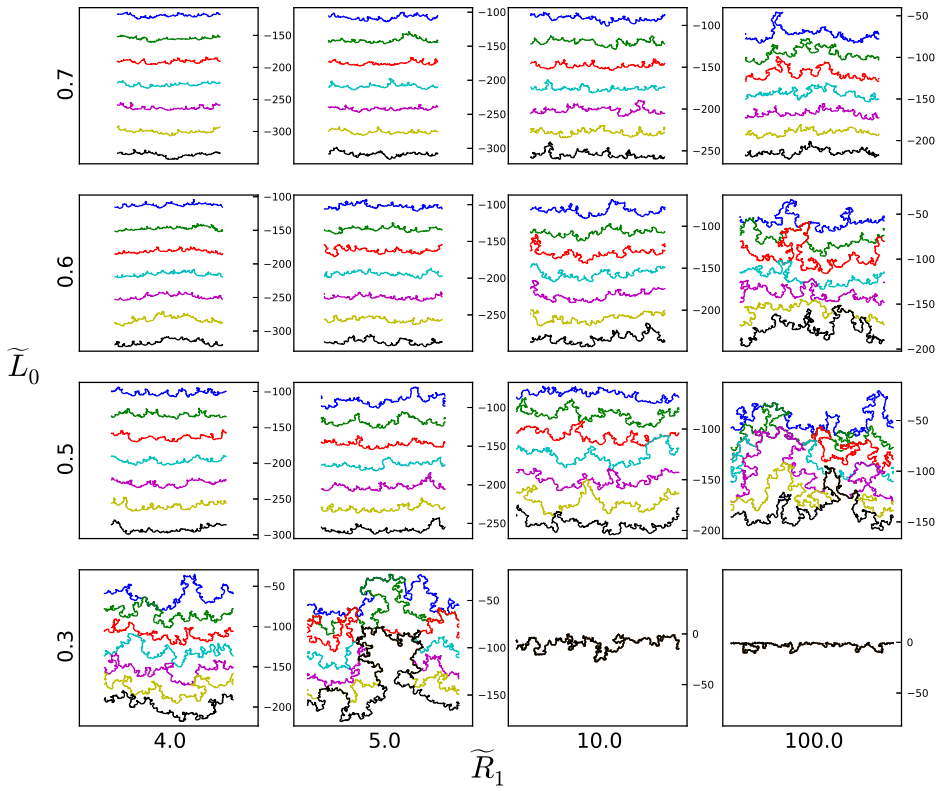

Figure 6.8 – Contact line morphology for equally spaced time moments (plots in the $x-y$ plane). Evolution of the interface is from top to bottom (from the blue line to the black one). The inset graphs from left to right correspond to increasing $\widetilde{R}_1$ values (indicated in the horizontal direction), while from bottom to top we consider increasing $\widetilde{L}_0$ values (indicated in the vertical direction). The roughness and velocity fluctuations increase, long range correlation and large deformation develops as the system approaches the depinning transition. In the two bottom-right cases, after sweeping a finite distance, the line is pinned. In order to better visualize every position of the line within the desired interval, different scales on the y axis have been used. The scale in the x direction is always 200 units

In the dynamic equilibrium (stationary regime of the moving interface), the mean velocity of the interface along the y direction presents a nontrivial, phase-transition like behavior as a function of $\widetilde{L}_0$. There is a critical concentration, below which the line is depinned (Fig. 6.9) which is similar to the *depinning transition*.

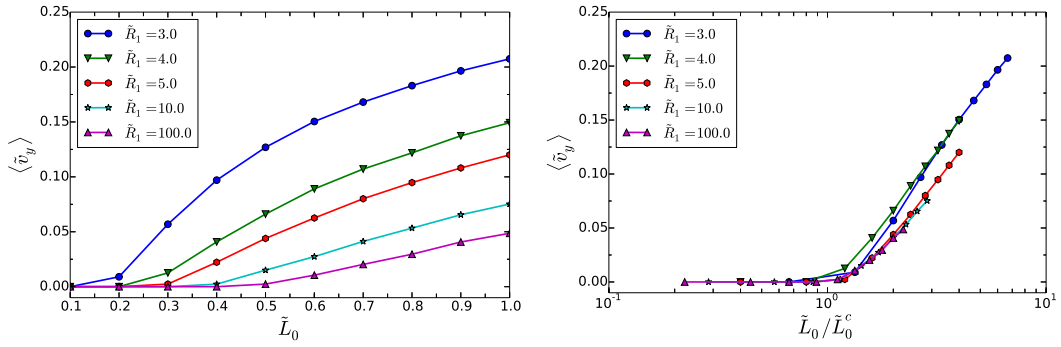

Figure 6.9 – Left: mean velocity of the interface along the y axis, in the stationary regime, as a function of $\widetilde{L}_0$ for different $\widetilde{R}_1$ parameters. Right: the mean velocity as a function of $\widetilde{L}_0/\widetilde{L}_0^c$. A reasonable collapse is obtained.

This critical concentration (or, the associated length $\widetilde{L}_0^c$) depends on the pinning strength. From Fig. 6.9 we also learn that $\widetilde{L}_0^c$ increases with $\widetilde{R}_1$ and converges to $\widetilde{L}_0^c = 1/2 \pm 0.1$ as $\widetilde{R}_1 \to \infty$. This value is significantly lower than $\widetilde{L}_0^c = 2$, which would be the critical length for a regular array of defects with infinite strength that would prevent tearing. Collective trapping of parts of the contact line thus is possible if the distance between the neighboring defects is less than 2. The existence of such a threshold, lower than $\widetilde{L}_0^c = 2$ has been shown experimentally [131], however, since the experiment was carried out in gravity, its value is related to the capillary length. In our case, the obtained lower limit is merely a consequence of the competition between the line and surface tensions and the value $\widetilde{L}_0^c = 1/2$ is thus a consequence of the underlying disorder. It is related to the percolation of the contact line between the localized defects. As it is expected for a critical behavior, the mean velocity curves have a reasonable collapse if they are plotted as a function of $\widetilde{L}_0/\widetilde{L}_0^c$. Figure 6.9 shows the results in such sense.

Phase diagram of the transition

Although the number of the simulated data points was rather limited for this purpose, we made an attempt to find the $\widetilde{L}_0^c = \widetilde{L}_0^c(\widetilde{R}_1)$ dependence. We considered the mesh illustrated on Fig. 6.10 in the $\widetilde{R}_1 - \widetilde{L}_0$ plane to detect the occurrence of the depinning transition. Figure 6.10 shows that $\widetilde{L}_0^c = 1/2 - \widetilde{R}_1^{-1}$ is a reasonable fit for describing the boundary between the two phases in the mapped region. Interestingly, this fit suggests that for $\widetilde{R}_1 < 2$ a total pinning is not possible.

For the high inhomogeneity and low threshold regime ($\widetilde{L}_0 \ll 1$, $\widetilde{R}_1 \ll 1$), one would

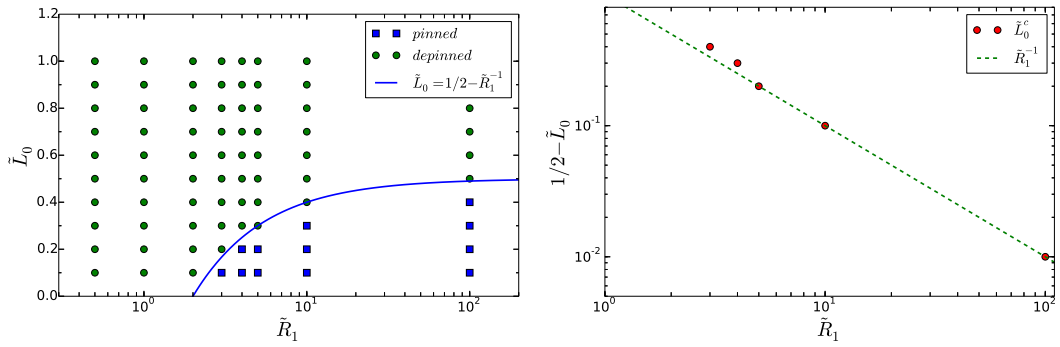

Figure 6.10 – Left: phase diagram of the contact line in the $(\widetilde{R}_1, \widetilde{L}_0)$ parameter space. Symbols indicate parameter values at which simulations were performed. Blue squares indicate the obtained pinning phase, green dots the depinning phase. Right: derived from the separation points shows that the two phases are delimited by the curve $\widetilde{L}_0^c = 1/2 - \widetilde{R}_1^{-1}$, the dashed line indicating a slope -1.

expect the possibility of a classical depinning transition, with small deformations of the contact line. Interestingly however, we could not observe such a transition, even for extremely low values of $\widetilde{L}_0$ and $\widetilde{R}_1$. In their experiments, Duprat et al. [56] investigated the depinning of a wetting contact line from an individual defect. They reported that depending on the pinning strength the contact line either jumped off the defect or completely wetted it, and advanced by tearing up and leaving an air hole behind. For individual or localized group of inhomogeneities we observed the same behavior, however, it turned out to be impossible to recover a collective depinning transition without the tearing up of the film. This is probably the result of the high ductility of the contact line. The classical depinning transition occurs due to the competition between disorder and long range elastic restoring forces [90], while in our case, we lack the long range part, therefore, we encounter a new transition, which is mainly governed by large deformations and tearing up of the layer. In the experiments of Paterson and Fermigier [131], the authors distinguish between strong and weak pinning as a function of the spatial distribution of the inhomogeneities. In the strong pinning case, defects were spread randomly and uniformly over the whole surface, while in the weak pinning case, they were spread by positioning randomly only one defect in each unit cell of a larger square lattice, hence obtaining a more homogeneous pattern. For the same defect concentration, the second case results in smaller average distance $\widetilde{L}_0$ between the defects. The observation that in the strong pinning case (small $\widetilde{L}_0$) the contact line breaks up, and in the weak pinning case (large $\widetilde{L}_0$) it advances with a rather smooth shape, is compatible with our simulation results, even though we tuned $\widetilde{L}_0$ by changing the defect concentration rather than changing their distribution or correlation.

Large deformations and backward movement

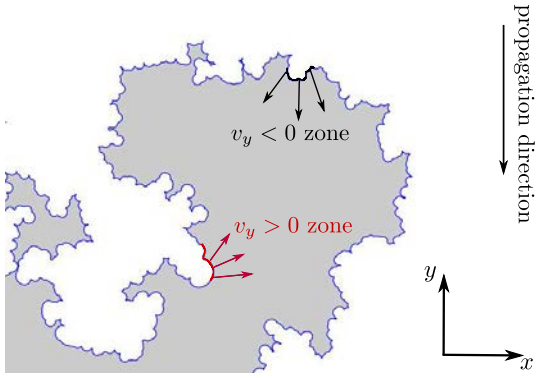

Figure 6.11 – An example from computer simulations where local backward movement of the interface occur. The liquid layer sketched in gray contracts by moving in the bottom direction (negative direction of the y axis). Due to the highly deformed shape of the interface, there will be parts of the interface where the velocity vector of the interface will have a positively oriented y component.

Another major difference compared to classical depinning models is that in our system local backward movements of the interface may appear, and, indeed, approaching the transition, positive velocities of the representative points occur, which plays an important role in the roughening mechanism (see the scenario presented in Figure 6.11). This backward motion does not imply however, that the interface will sweep over the same substrate area twice. This scenario will never happen, and in such sense our method for generating the pinning points is consistent. The local backward motion has to be understood in the context that the withdrawing liquid layer has a complex shape, and the contraction is realized in a complicated manner, as it is sketched on Figure 6.11. The contraction of some peninsula-like formations can lead to such backward oriented motion of the interface.

Figure 6.12 shows how the distribution of the velocity components in the y direction changes as we approach the transition point. Far from the transition point we experience an almost bimodal distribution (one peak corresponding to the unpinned part, while the other one, at zero, to the pinned part), while close to it we obtain an almost zero-averaged symmetric distribution. Clearly, it is due to the slight asymmetry that the contact line moves forward on average.

Morphology at the transition

In order to quantify the morphology of the contact line around the transition, we performed a classical rasterization analysis. The length of the contact line L was measured by taking into account only every Δ^{th} representative point, and the scaling of L with respect to Δ was investigated. This means that for $\Delta = 1$, L is computed by adding up

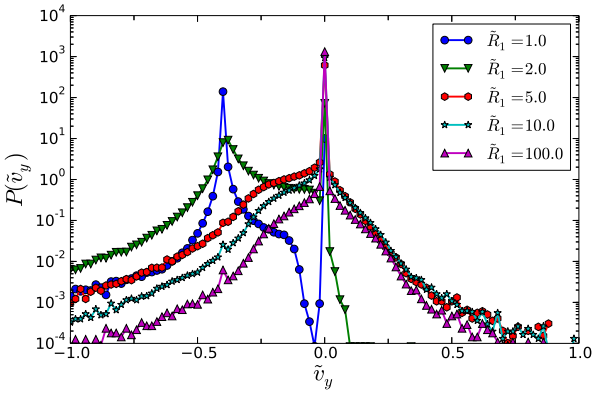

Figure 6.12 – Distribution of the y component of velocities along the contact line for $\widetilde{L}_0 = 0.5$. Note that when we approach the depinning transition ($\widetilde{R}_1 \to 10^2$) a considerable local backward movement ($v_y > 0$) of the interface occurs. Also, far from the transition ($\widetilde{R}_1 \ll 10^2$), the pinned part of the line is quite well separated from the moving part.

the distance between each nearest neighboring point, for $\Delta = 2$ by summing the distance between each second neighbor points and so on, hence the length of the curve is approximated at different precisions. Figure 6.13 shows that as the system approaches the depinning transition, the scaling converges to a power law, $L(\Delta) \propto \Delta^{-1/4}$. This suggests a fractal-like structure and a scale-free morphology with a diverging total length as Δ decreases. This is again a direct consequence of the undergoing phase transition.

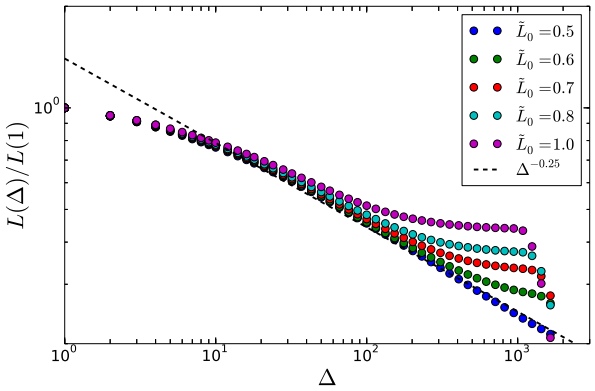

Figure 6.13 – Development of the scale-free morphology as the system approaches the critical state. The normalized length $L(\Delta)$ of the contact line as a function of Δ (see the text for the definitions). Results for $\widetilde{R}_1 = 10^2$ and different values of $\widetilde{L}_0$. The dashed line is a guide for the eye, and has a slope -0.25. A natural upper cutoff arises due to the finite system size, and a lower cutoff from the discretization.

Since Δ can be used to parametrize the contact line $(x(\Delta), y(\Delta))$, further information concerning its shape can be extracted by investigating the structure factor $S_y(k_\Delta)$ defined as the power spectrum of $y(\Delta)$: $S_y(k_\Delta) = |\hat{y}(\Delta)|^2$ where $\hat{y}(\Delta)$ is the Fourier transform of $y(\Delta)$. Figure 6.14 shows the convergence of $S_y(k_\Delta)$ to a power law in the vicinity of the transition point: $S_y(k_\Delta) \propto k_\Delta^{-2}$. This suggests again the scale-free, fractal-like shape for the interface. As expected, the main difference between the various curves $S_y(k_\Delta)$ arises from the low frequency, hence large wavelength values, showing that long range correlation develops close to the transition point.

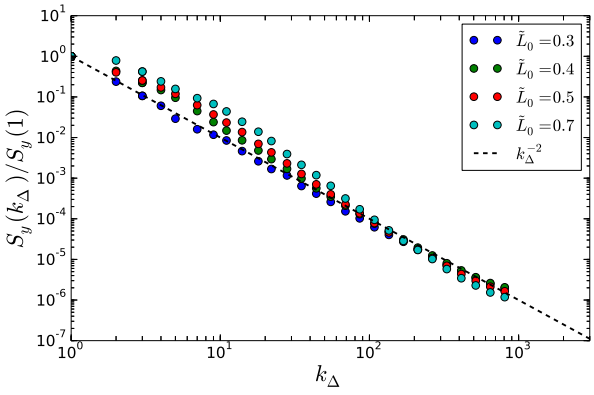

Figure 6.14 – Development of the scale-free morphology as the system approaches the critical state. The structure factor $S_y(k_\Delta)$ as a function of Δ (see the text for definitions). Results for $\widetilde{R}_1 = 5.0$ and different values of $\widetilde{L}_0$. The dashed line has a slope -2.0 and the range $1 \leq \Delta < 2048$ was used for the Fourier transform.

The average position of the contact line was also followed as a function of time. Results for a fixed $\widetilde{R}_1 = 10^2$ value and a wide range of $\widetilde{L}_0$ values are plotted on Figure 6.15. When approaching the critical point, fluctuations increase and the sudden jumps in the average position become more and more dominating. These jumps are the result of either the slip of the contact line over individual defects or the tearing up of the layer. Analogously to jumps in the magnetization (Barkhausen noise), these jumps are termed avalanches, since the average position of the line is governed by fast slips. Close to the transition, the sizes of the jumps exhibit a power-law distribution with an exponent -2 (Figure 6.15). Our results along this line are however modest (the scaling is on an interval less than two orders of magnitude), due to the lack of statistics for the large avalanche sizes. It is important to note however that experimental data presented in Ref [121] clearly shows values around -2, giving thus some confidence to the results of our model.

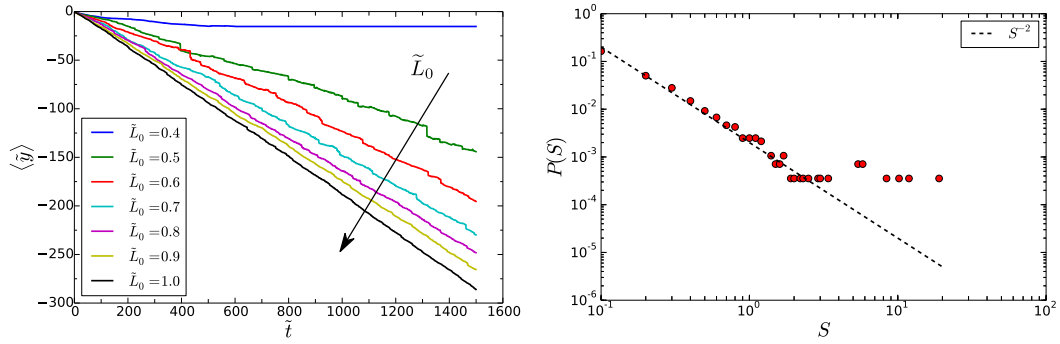

Figure 6.15 – Left: average position of the contact line as a function of time, for $\widetilde{R}_1 = 10^2$ and $\widetilde{L}_0 = \{0.4, 0.5, 0.6, 0.7, 0.8, 0.9, 1.0\}$. The arrow indicates increasing values of $\widetilde{L}_0$. Note how fluctuations increase as approaching the transition point and the dynamics becomes intermittent. Right: the avalanche size distribution for $\widetilde{R}_1 = 10^2$ and $\widetilde{L}_0 = 0.5$, while the solid line has a slope: -2.0.

6.6 Conclusions

A novel and efficient off-lattice simulation method, resembling the classical molecular dynamics, has been introduced for investigating the dynamics of thin and viscous liquid layers, dewetting on inhomogeneous surfaces. By using this simulation method the existence of an unusual depinning-like transition was revealed. This transition is governed by large deformations of the interface and the breaking up of the layer. The two-dimensional parameter space of the investigated system was explored, and the obtained results were discussed in view of available experimental observations. We learned that the contact line's dynamics is a result of an interplay between the capillary forces and the substrate disorder, however, with the appropriately introduced adimensional form, both relevant parameters are related to the inhomogeneities. In such an approach, the universal properties of the contact line can be viewed as a result of the competition between the inhomogeneities strength and their density. The difference between the dynamics of a receding and an advancing contact line (dewetting vs. wetting), other than the contact angle hysteresis, remains an open question and could be investigated in the future by rigorously introducing pressure in our model.

Conclusions and perspectives

Throughout this thesis, we studied two disordered systems from the depinning point of view. The complex phenomenology in these systems stems from the competition between disorder and the elastic interactions between regions in the system.

In the first part, we examined the generic plastic properties of amorphous systems via a simple mesoscopic model. We showed that the threshold dynamics is a natural consequence of the multistability arising from the competition between elasticity and the underlying disorder and local thresholds are related to the heights, whereas plastic slip amplitudes are related to the widths of the disordered potential wells. Accordingly, we considered two extreme cases of the disorder (distributed barriers or distributed positions of wells), and we found that generic properties are unaffected by the particular form of the disorder. This has yet to be confirmed by intermediate cases, namely by gathering the precise distributions of thresholds and slip amplitudes from molecular dynamics, however, based on our results, we do not expect considerable change in the universal properties.

While the yielding of amorphous materials is, in many aspects, similar to the depinning transition, we found that plastic yielding is not depinning. Consequently, mean field approaches are insufficient to fully describe the yielding transition. Amorphous plasticity shows additional phenomenology compared to depinning such as localization and diffusive fluctuations. We have shown that the existence of soft modes in the anisotropic elastic interactions at play in amorphous plasticity are at the origin of these extra features. Soft modes allow for the constant increase of fluctuations and thus the ultimate failure of the material. We found that, in amorphous plasticity, the soft modes of the elastic interaction kernel are nothing but percolating shear bands. In this context, soft modes explain not only the diffusing fluctuations but the localization behavior as well. Moreover, we provided a new framework to describe amorphous plasticity as the interaction between loosely coupled shear bands. The weak interaction between shear bands results from the inhomogeneity of the plastic strain along the band.

However weak this coupling may be, it still matters on the long run. A simple independently diffusing shear band model for instance is unable to predict the finite size scaling of the diffusion coefficient on the long run. A detailed investigation of the statistical properties of the mechanical noise induced by the inhomogeneous plastic deformation along the shear bands could help to elucidate the role of this coupling in the long term dynamics. In the meantime, localization on short times follows slip lines as predicted by

scaling and observed in molecular dynamics. However, a more thorough analysis of the spatial correlation of the plastic activity induced by the individual avalanches is necessary to firmly confirm that avalanches indeed follow slip line patterns.

Diverging fluctuations and the associated shear banding in amorphous materials ultimately lead to failure. Understanding the shear band formation mechanism is therefore the first step in developing materials with enhanced mechanical characteristics. The next step in the process is to control the nucleation of shear bands. We found that shear band nucleation is affected by adding hard inclusions to the amorphous matrix. We have shown that the reinforcement of amorphous materials by hard inclusions shows finite size effects and a linear mixing law gives an upper bound to the flow stress. Furthermore, we found that reinforcement is related to the percolation of shear bands in between the hard inclusions. Although we carried out simulations with soft inclusions as well, the reinforcing mechanism there is less clear. This is a work under progress and not discussed here, however, we expect soft sites to contribute in suppressing permanent shear band formation.

The mesomodels we used are meant to capture the generic phenomenology of amorphous plasticity. In this spirit, they are oversimplified caricatures of real world amorphous systems and the effect of these simplifications has yet to be clarified. For instance, we were using scalar models with the strong hypothesis that the plastic slips follow the symmetry of the external loading. Stresses and strains however are tensorial quantities, and a tensorial model is necessary to support this hypothesis. Another, related simplification is that we did not account for densification. This assumption probably applies to dense amorphous systems such as metallic glasses. On the other hand, even a pure shear plastic deformation of an Eshelby inclusion induces a pressure component in the stress field, and the consequences may be nontrivial.

In the second part of the thesis we considered another depinning-like system. We developed a novel approach to model the dynamics of thin liquid layers on inhomogeneous surfaces. In our simplified picture we considered the layer as flat, and followed the motion of the contact line only. We found that in this approximation, interactions are short ranged, hence the line is soft. The roughening of the line is governed by the competition of these short range interactions and the disorder of the surface. We revealed the existence of a critical concentration of inhomogeneities below which the line stops within finite time, and above this concentration it moves indefinitely. Around the threshold concentration the line shows critical-like properties such as fractal-like structure and long spatial correlations. This is a peculiar transition: although depinning-like in the sense that it results from the competition of short range interactions and the pinning forces of the disorder, it is associated to the large deformations and tearing up of the layer. Large deformations and tearing up are not accounted for in standard depinning models, we therefore hope that our method may open a new perspective in the study of jerky interface motion.

Publications

Publications related to the thesis

- B. Tyukodi, C. Lemarchand, J. Hansen, D. Vandembroucq, "Finite size effects in a model for plasticity of amorphous composites", Physical Review E, 93, 023004 (2016)
- B. Tyukodi, S. Patinet, D. Vandembroucq, S. Roux, "From depinning transition to plastic yielding of amorphous media: a soft modes perspective" (2015, submitted)
- B. Tyukodi, Y. Bréchet, Z. Néda, "Kinetic roughening of a soft dewetting line under quenched disorder - a numerical study", Physical Review E 90, 052404 (2014)

Conferences

- B. Tyukodi, W. Zhu, D. Vandembroucq, C. Maloney, "Diffusion and localization in elasto-plastic models of amorphous plasticity", Materials Research Society fall meeting (2015, Boston, talk)
- B. Tyukodi, Y. Bréchet, Z. Néda, "Kinetic roughening of a soft dewetting line - a novel computer simulation method ", Physics Conference TIM14 (2014, Timişoara, co-author of plenary talk)
- B. Tyukodi, C. Lemarchand, D. Vandembroucq, "Plasticity of strongly heterogeneous materials", Condensed Matter in Paris (2012, Paris, poster)

Other publications

- B. Bresson, C. Brun, X. Buet, Y. Chen, M. Ciccotti, J. Gateau, G. Jasion, M. Petrovich, F. Poletti, D. J. Richardson, R. Sandoghchi, G. Tessier, B. Tyukodi, D. Vandembroucq, "The long memory of glass surfaces" (2016, in preparation)
- Sz. Boda, Z. Néda, B. Tyukodi, A. Tunyagi, "The rhythm of coupled metronomes", The European Physical Journal B 86, 263 (2013)
- B. Tyukodi, I. A. Chioar, Z. Néda "A kinetic Monte Carlo study for stripe-like magnetic domains in ferrimagnetic thin films", Central European Journal of Physics 11, 487 (2013)

- B. Tyukodi, Zs. Sárközi, Z. Néda, A. Tunyagi, E. Györke, "Boltzmann constant from a snifter", European Journal of Physics 33, 455 (2012)
- Z. Néda, B. Tyukodi, Á-E. Kacsó "Foundations of classical statistical mechanics" (textbook, 2014, in Hungarian, ISBN 978-973-114-187-9)

Bibliography

[1] Al-Rub, R. K. A. (2009). Modeling the Particle Size and Interfacial Hardening Effects in Metal Matrix Composites with Dispersed Particles at Decreasing Microstructural Length Scales. *International Journal for Multiscale Computational Engineering*, 7(4):1–22.

[2] Al-Rub, R. K. A., Darabi, M. K., You, T., Masad, E. A., and Little, D. N. (2011). A Unified Continuum Damage Mechanics Model for Predicting the Mechanical Response of Asphalt Mixtures and Pavements. *International Journal of Roads and Airports*, 1(1):68–84.

[3] Al-Rub, R. K. A., You, T., Masad, E. A., and Little, D. N. (2011). Mesomechanical modeling of the thermo-viscoelastic, thermo-viscoplastic, and thermo-viscodamage response of asphalt concrete. *International Journal of Advances in Engineering Sciences and Applied Mathematics*, 3(1-4):14–33.

[4] Albe, K., Ritter, Y., and Sopu, D. (2013). Enhancing the plasticity of metallic glasses: Shear band formation, nanocomposites and nanoglasses investigated by molecular dynamics simulations. *Mechanics of Materials*, 67:94–103.

[5] Amirfazli, A. and Neumann, A. W. (2004). Status of the three-phase line tension. *Advances in Colloid and Interface Science*, 110(3):121–141.

[6] Amon, A., Nguyen, V. B., Bruand, A., Crassous, J., and Clément, E. (2012). Hot Spots in an Athermal System. *Physical Review Letters*, 108(13):135502.

[7] Antonaglia, J., Wright, W. J., Gu, X., Byer, R. R., Hufnagel, T. C., LeBlanc, M., Uhl, J. T., and Dahmen, K. A. (2014). Bulk Metallic Glasses Deform via Slip Avalanches. *Physical Review Letters*, 112(15):155501.

[8] Argon, A. S. (1979). Plastic deformation in metallic glasses. *Acta Metallurgica*, 27:47 – 58.

[9] Argon, A. S. and Kuo, H. Y. (1979). Plastic Flow in a Disordered Bubble Raft (an Analog of a Metallic Glass). *Materials Science and Engineering*, 39(1):101–109.

[10] Ashwin, J., Gendelman, O., Procaccia, I., and Shor, C. (2013). Yield-strain and shear-band direction in amorphous solids under two-dimensional uniaxial loading. *Physical Review E*, 88(2):022310.

[11] Bak, P. (1999). *How Nature Works*. New York.

[12] Bak, P., Chen, K., and Creutz, M. (1989). Self-organized criticality in the 'Game of Life'. *Nature*, 342:780–782.

[13] Bak, P. and Sneppen, K. (1993). Punctuated Equilibrium and Criticality in a Simple Model of Evolution. *Physical Review Letters*, 71(24):4083–4086.

[14] Bak, P., Tang, C., and Wiesenfeld, K. (1987). Self-Organized Criticality: An Explanation of the 1/f Noise. *Physical Review Letters*, 59(4):381–384.

[15] Barabási, A. L. (2003). *Linked*.

[16] Baret, J. C., Vandembroucq, D., and Roux, S. (2002). Extremal Model for Amorphous Media Plasticity. *Physical Review Letters*, 89(19):195506.

[17] Barrat, J. L. and Lemaître, A. (2011). Heterogeneities in amorphous systems under shear. *HAL*.

[18] Baumberger, T. and Caroli, C. (2005). Solid Friction from stick-slip to pinning and aging. *Advances in Physics*, 55(3):279–348.

[19] Beltrame, P. and Thiele, U. (2010). Time Integration and Steady-State Continuation for 2d Lubrication Equations. *SIAM Journal for Applied Dynamical Systems*, 9(2):484–518.

[20] Bhargava, R. D. and Kapoor, O. P. (1965). Two-dimensional rectancular inclusion. 32(1):46–55.

[21] Binder, K., Block, B., Das, S. K., Virnau, P., and Winter, D. (2011). Monte Carlo Methods for Estimating Interfacial Free Energies and Line Tensions. *Journal of Statistical Physics*, 144(3):690–729.

[22] Blondeau, C. (2011). *La cryptanalyse differentielle et ses generalisations*. PhD thesis.

[23] Blondeau, C., Gérard, B., and Tillich, J. P. (2011). Accurate estimates of the data complexity and success probability for various cryptanalyses. *Designs, Codes, and Cryptography*, 59(1-3):3–34.

[24] Bocquet, L., Colin, A., and Ajdari, A. (2009). Kinetic theory of plastic flow in soft glassy materials. *Physical Review Letters*, 103(3):1–4.

[25] Bonn, D., Eggers, J., Indekeu, J., Meunier, J., and Rolley, E. (2009). Wetting and spreading. *Reviews of Modern Physics*, 81(2):739–805.

[26] Bormashenko, E., Musin, A., Whyman, G., Barkay, Z., and Zinigrad, M. (2015). On universality of scaling law describing roughness of triple line. *The European Physical Journal E*, 38(1):2.

[27] Brochard-Wyart, F., de Gennes, P. G., Herver, H., and Redon, C. (1994). Wetting and Slippage of Polymer Melts on Semi-ideal Surfaces. *Langmuir*, 10(5):1566–1572.

[28] Budrikis, Z. and Zapperi, S. (2013). Avalanche localization and crossover scaling in amorphous plasticity. *Physical Review E*, 88(6):062403.

[29] Bulatov, V. V. and Argon, A. S. (1994). A stochastic model for continuum elastoplastic behavior: I. Numerical approach and strain localization. *Modelling and Simulation in Materials Science and Engineering*, 2:167 – 184.

[30] Bulatov, V. V. and Argon, A. S. (1994). A stochastic model for continuum elastoplastic behavior: II. A study of the glass transition and structural relaxation. *Modelling and Simulation in Materials Science and Engineering*, 2:185–202.

[31] Bulatov, V. V. and Argon, A. S. (1994). A stochastic model for continuum elastoplastic behavior: III. Plasticity in ordered versus disordered solids. *Modelling and Simulation in Materials Science and Engineering*, 2:203–222.

[32] Burgers, J. M. (1939). Physics -Some considerations on the fields of stress connected with dislocations in a regular crystal lattice I. *Proceedings of the koninklijke nederlandse akademie van wetenschappen*, 42:335–389.

[33] Cai, W., Bulatob, V. V., Chang, J., Li, J., and Yip, S. (2003). Periodic image effects in dislocation modelling. *Philosophical Magazine*, 83(5):539–567.

[34] Caroli, C. and Nozières, P. (1998). Hysteresis and elastic interactions of microasperities in dry friction. *European Physical Journal B*, 4:233–246.

[35] Castaneda, P. P. and Debotton, G. (1992). On the Homogenized Zield Strength of Two-Phase Composites. *Proc. R. Soc. Lond. A*, 438:419–431.

[36] Charleux, L., Gravier, S., Verdier, M., Fivel, M., and Blandin, J. J. (2007). Indentation plasticity of amorphous and partially crystallized metallic glasses. *Journal of Materials Research*, 22(2):525–532.

[37] Chen, J. S. and Lin, K. Y. (2005). Mechanism and behavior of bitumen strength reinforcement using fibers. *Journal of Materials Science*, 40(1):87–95.

[38] Chen, J. S. and Peng, C. H. (1998). Analyses of Tensile Failure Properties of Asphalt-Mineral Filler Mastics. *Journal of Materials in Civil Engineering*, 10:256–262.

[39] Chen, M. (2011). A brief overview of bulk metallic glasses. *NPG Asia Materials*, 3:82–90.

[40] Chen, Y. Z. (2014). Closed form solution and numerical analysis for Eshelbyâs elliptic inclusion in plane elasticity. *Applied Mathematics and Mechanics*, 35(7):863–874.

[41] Clauset, A., Shalizi, C. R., and Newman, M. E. J. (2009). Power-Law Distributions in Empirical Data. *SIAM Review*, 51(4):661–703.

[42] Clotet, X., Planet, R., and Ortín, J. (2012). Capillary rise in Hele-Shaw models of disordered media. *Journal of Colloid and Interface Science*, 377(1):387–395.

[43] Cubaud, T. and Fermigier, M. (2001). Faceted drops on heterogeneous surfaces. *EPL (Europhysics Letters)*, 55(2):239–245.

[44] Cubaud, T. and Fermigier, M. (2004). Advancing contact lines on chemically patterned surfaces. *Journal of Colloid and Interface Science*, 269(1):171–177.

[45] Cubaud, T., Fermigier, M., and Jenffer, P. (2001). Spreading of Large Drops on Patterned Surfaces. *Oil & Gas Science and Technology*, 56(1):23–31.

[46] Dahmen, K. A., Ben-Zion, Y., and Uhl, J. T. (2009). Micromechanical Model for Deformation in Solids with Universal Predictions for Stress-Strain Curves and Slip Avalanches. *Physical Review Letters*, 102(17):175501.

[47] Dahmen, K. A., Ben-Zion, Y., and Uhl, J. T. (2011). A simple analytic theory for the statistics of avalanches in sheared granular materials. *Nature Physics*, 7(7):554–557.

[48] Dasgupta, R., Hentschel, H. G. E., and Procaccia, I. (2012). Microscopic Mechanism of Shear Bands in Amorphous Solids. *Physical Review Letters*, 109(25):255502.

[49] Dasgupta, R., Mishra, P., Procaccia, I., and Samwer, K. (2013). Micro-alloying and the toughness of glasses: Modeling with pinned particles. *Applied Physics Letters*, 102(19):191904.

[50] Debotton, G. (1995). The effective yield strength of fiber-reinforced composites. *International Journal of Solids and Structures*, 32(12):1743 – 1757.

[51] Dimiduk, D. M., Woodward, C., LeSar, R., and Uchic, M. D. (2006). Scale-Free Intermittent Flow in Crystal Plasticity. *Science*, 312(5777):1188–1190.

[52] Ding, J., Patinet, S., Falk, M. L., Cheng, Y., and Ma, E. (2014). Soft spots and their structural signature in a metallic glass. *Proceedings of the National Academy of Sciences*, 111(39):14052–14056.

[53] Drelich, J. (1996). The significance and magnitude of the line tension in three-phase (solid-liquid-fluid) systems. *Colloids and Surfaces A: Physicochemcal Engineering Aspects*, 116:43–54.

[54] Drelich, J., Miller, J. D., Kumar, A., and Whitesides, G. M. (1994). Wetting characteristics of liquid drops at heterogeneous surfaces. *Colloids Surfaces A- Physicochemical and Engineering Aspects*, 93:1–13.

[55] Du, P., Khenner, M., and Wong, H. (2010). A tangent-plane marker-particle method for the computation of three-dimensional solid surfaces evolving by surface diffusion on a substrate. *Journal of Computational Physics*, 229(3):813–827.

[56] Duprat, J. F., Goulaouic, F., Jenffer, P., and Fermigier, M. (1992). Two-phase flow in an imperfect Hele-Shaw cell: influence of wettability defects on interface dynamics. *Compt. Rend. Acad. Sci. Paris*, 314(879).

[57] Eshelby, J. D. (1957). The Determination of the Elastic Field of an Ellipsoidal Inclusion, and Related Problems. *Proceedings of the Royal Society A: Mathematical, Physical and Engineering Sciences*, 241(1226):376–396.

[58] Eyring, H. (1934). The activated complex in chemical reactions. *The Journal of Chemical Physics*, 3(2):107–115.

[59] Falk, M. L. and Langer, J. S. (1998). Dynamics of viscoplastic deformation in amorphous solids. *Physical Review E*, 57(6):7192–7205.

[60] Falk, M. L. and Maloney, C. E. (2010). Simulating the mechanical response of amorphous solids using atomistic methods. *European Physical Journal B*, 75(4):405–413.

[61] Ferry, M., Laws, K. J., White, C., Miskovic, D. M., Shamlaye, K. F., Xu, W., and Biletska, O. (2013). Recent developments in ductile bulk metallic glass composites. *MRS Communications*, 3(1):1–12.

[62] Fiocco, D., Foffi, G., and Sastry, S. (2014). Encoding of Memory in Sheared Amorphous Solids. *Physical Review Letters*, 112(2):025702.

[63] Fisher, D. S. (1998). Collective transport in random media: from superconductors to earthquakes. *Physics Reports*, 301:113–150.

[64] Fleck, N. A. and Willis, J. R. (2004). Bounds and estimates for the effect of strain gradients upon the effective plastic properties of an isotropic two-phase composite. *Journal of the Mechanics and Physics of Solids*, 52:1855–1888.

[65] Gao, H. and Rice, J. R. (1989). A First-Order Perturbation Analysis of Crack Trapping by Arrays of Obstacles. *Journal of Applied Mechanics*, 56(4):828.

[66] Gau, H., Herminghaus, S., Lenz, P., and Lipowsky, R. (1999). Liquid Morphologies on Structured Surfaces: From Microchannels to Microchips. *Science*, 283:46–49.

[67] Gendelman, O., Joy, A., Mishra, P., Procaccia, I., and Samwer, K. (2014). On the effect of microalloying on the mechanical properties of metallic glasses. *Acta Materialia*, 63:209–215.

[68] Gennes, P. G. (1985). Wetting: Statics and dynamics. *Reviews of Modern Physics*, 57(3):827–863.

[69] Ghosh, P., Ghosh, S., Mitra, J., and Bera, N. (2015). Finite size effect on classical ideal gas revisited. *European Journal of Physics*, 36(5):055046.

[70] Golestanian, R. (2004). Moving contact lines on heterogeneous substrates. *Philosophical Transactions of the Royal Society A- Mathematical, Physical, and Engineering Sciences*, 362(1821):1613–23.

[71] Gong, S. X. and Meguid, S. A. (1993). Interacting circular inhomogeneities in plane elastostatics. *Acta Mechanica*, 99:49–60.

[72] Hardin, T. J. and Homer, E. R. (2015). Microstructural factors of strain delocalization in model metallic glass matrix composites. *Acta Materialia*, 83:203–215.

[73] Hébraud, P. and Lequeux, F. (1998). Mode-Coupling Theory for the Pasty Rheology of Soft Glassy Materials. *Phys. Rev. Lett.*, 81(14):2934–2937.

[74] Hentschel, H. G. E., Jaiswal, P. K., Procaccia, I., and Sastry, S. (2015). Stochastic approach to plasticity and yield in amorphous solids. *Physical Review E - Statistical, Nonlinear, and Soft Matter Physics*, 92(6):062302.

[75] Hofmann, D. C., Suh, J. Y., Wiest, A., Duan, G., Lind, M. L., Demetriou, M. D., and Johnson, W. L. (2008). Designing metallic glass matrix composites with high toughness and tensile ductility. *Nature*, 451:1085–1089.

[76] Holly, F. J. (1973). Formation and Rupture of the Tear Film. *Experimental Eye Research*, 15(5):515–525.

[77] Homer, E. R. (2010). *Modeling the Mechanical Behavior of Amorphous Metals by Shear Transformation Zone Dynamics*. PhD thesis.

[78] Homer, E. R., Rodney, D., and Schuh, C. A. (2010). Kinetic Monte Carlo study of activated states and correlated shear-transformation-zone activity during the deformation of an amorphous metal. *Physical Review B*, 81(6):064204.

[79] Homer, E. R. and Schuh, C. A. (2009). Mesoscale modeling of amorphous metals by shear transformation zone dynamics. *Acta Materialia*, 57(9):2823–2833.

[80] Iguain, J. L., Bustingorry, S., Kolton, A. B., and Cugliandolo, L. F. (2009). Growing correlations and aging of an elastic line in a random potential. *Physical Review B - Condensed Matter and Materials Physics*, 80(9):094201.

[81] Ingleton, A. W. (1955). The rank of circulant matrices. *Journal of the London Mathematical Society*, 4:445–460.

[82] Inoue, A., Wada, T., and Louzguine-Luzgin, D. V. (2007). Improved mechanical properties of bulk glassy alloys containing spherical pores. *Materials Science and Engineering A*, 471(1-2):144–150.

[83] Jagla, E. A. (2015). Avalanche-size distributions in mean-field plastic yielding models. *Physical Review E - Statistical, Nonlinear, and Soft Matter Physics*, 92(4):042135.

[84] Jagla, E. A., Landes, F. P., and Rosso, A. (2014). Viscoelastic Effects in Avalanche Dynamics: A Key to Earthquake Statistics. *Physical Review Letters*, 112(17):174301.

[85] Jaswon, M. A., Bhargava, R. D., and Oldroyd, J. G. (2008). Two-dimensional elastic inclusion problems. *Mathematical Proceedings of the Cambridge Philosophical Society*, 57(03):669–680.

[86] Jensen, K. E., Weitz, D. A., and Spaepen, F. (2014). Local shear transformations in deformed and quiescent hard-sphere colloidal glasses. *Physical Review E*, 90(4):042305.

[87] Jiang, W., Bao, W., Thompson, C. V., and Srolovitz, D. J. (2012). Phase field approach for simulating solid-state dewetting problems. *Acta Materialia*, 60(15):5578–5592.

[88] Joanny, J. F. and de Gennes, P. G. (1984). A model for contact angle hysteresis. *The Journal of Chemical Physics*, 81(1):552.

[89] Joanny, J. F. and de Gennes, P. G. (1986). Upward creep of a wetting fluid: a scaling analysis. *Journal de Physique*, 47(1):121–127.

[90] Kardar, M. (1998). Nonequilibrium dynamics of interfaces and lines. *Physics Reports*, 301:85–112.

[91] Kermouche, G., Barthel, E., Vandembroucq, D., and Dubujet, P. (2008). Mechanical modelling of indentation-induced densification in amorphous silica. *Acta Materialia*, 56(13):3222–3228.

[92] Krishnamurthy, S., Tanguy, A., Abry, P., and Roux, S. (2000). A stochastic description of extremal dynamics. *EPL (Europhysics Letters)*, 51(1):1–7.

[93] Krishnamurthy, S., Tanguy, A., and Roux, S. (2000). Dynamic exponent in extremal models of pinning. *The European Physical Journal B*, 15:149–153.

[94] Krisponeit, J. O., Pitikaris, S., Avila, K. E., Küchemann, S., Krüger, A., and Samwer, K. (2014). Crossover from random three-dimensional avalanches to correlated nano shear bands in metallic glasses. *Nature communications*, 5(3616):1–5.

[95] Kuykendall, W. P. and Cai, W. (2013). Conditional convergence in two-dimensional dislocation dynamics. *Modelling and Simulation in Materials Science and Engineering*, 21(5):055003.

[96] Lacroix, R., Kermouche, G., Teisseire, J., and Barthel, E. (2012). Plastic deformation and residual stresses in amorphous silica pillars under uniaxial loading. *Acta Materialia*, 60:5555–5566.

[97] Le Bouil, A., Amon, A., McNamara, S., and Crassous, J. (2014). Emergence of Cooperativity in Plasticity of Soft Glassy Materials. *Physical Review Letters*, 112(24):246001.

[98] Le Bouil, A., Amon, A., Sangleboeuf, J. C., Orain, H., Bésuelle, P., Viggiani, G., Chasle, P., and Crassous, J. (2014). A biaxial apparatus for the study of heterogeneous and intermittent strains in granular materials. *Granular Matter*, 16(1):1–8.

[99] Lees, A. W. and Edwards, S. F. (1972). The computer study of transport processes under extreme conditions. *Journal of Physics C: Solid State Physics*, 5(15):1921–1928.

[100] Lemaître, A. (2014). Structural Relaxation is a Scale-Free Process. *Physical Review Letters*, 113(24):245702.

[101] Lemaître, A. and Caroli, C. (2007). Plastic response of a two-dimensional amorphous solid to quasistatic shear: Transverse particle diffusion and phenomenology of dissipative events. *Physical Review E - Statistical, Nonlinear, and Soft Matter Physics*, 76(3):036104.

[102] Lewandowski, J. J. and Greer, A. L. (2006). Temperature Rise at Shear Bands in Metallic Glasses. *Nature Materials*, 5(1):15–18.

[103] Liao, Q., Shi, Y., Fan, Y., Zhu, X., and Wang, H. (2009). Numerical simulations of the equilibrium shape of liquid droplets on gradient surfaces. *Applied Thermal Engineering*, 29(2-3):372–379.

[104] Lin, C. H., Guan, J., Chau, S. W., Chen, S. C., and Lee, L. J. (2010). Patterning nanowire and micro-/nanoparticle array on micropillar-structured surface: Experiment and modeling. *Biomicrofluidics*, 4(3):034103.

[105] Lin, J., Gueudré, T., Rosso, A., and Wyart, M. (2015). Criticality in the Approach to Failure in Amorphous Solids. *Physical Review Letters*, 115(16):168001.

[106] Lin, J., Lerner, E., Rosso, A., and Wyart, M. (2014). Scaling description of the yielding transition in soft amorphous solids at zero temperature. *Proceedings of the National Academy of Sciences of the United States of America*, 111(40):14382–14387.

[107] Lin, J., Saade, A., Lerner, E., Rosso, A., and Wyart, M. (2014). On the density of shear transformations in amorphous solids. *EPL (Europhysics Letters)*, 105(2):26003.

[108] Lin, J. and Wyart, M. (2016). Mean-field description of plastic flow in amorphous solids. *Physical review X*, 6(1):011005.

[109] Louzguine-Luzgin, D. V., Louzguina-Luzgina, L. V., and Churyumov, A. Y. (2013). Mechanical Properties and Deformation Behavior of Bulk Metallic Glasses. *Metals*, 3(1):1–22.

[110] Maas, R., Klaumunzer, D., and Loffler, J. F. (2011). Propagation dynamics of individual shear bands during inhomogeneous flow in a Zr-based bulk metallic glass. *Acta Materialia*, 59(8):3205–3213.

[111] Maloney, C. and Lemaître, A. (2004). Subextensive Scaling in the Athermal, Quasistatic Limit of Amorphous Matter in Plastic Shear Flow. *Physical Review Letters*, 93(1):016001–1.

[112] Maloney, C. and Lemaître, A. (2004). Universal Breakdown of Elasticity at the Onset of Material Failure. *Physical Review Letters*, 93(19):195501.

[113] Maloney, C. E. (2006). Correlations in the elastic response of dense random packings. *Physical Review Letters*, 97(3):035503.

[114] Maloney, C. E. and Lemaître, A. (2006). Amorphous systems in athermal, quasistatic shear. *Physical Review E*, 74(1):016118.

[115] Maloney, C. E. and Robbins, M. O. (2008). Evolution of displacements and strains in sheared amorphous solids. *Journal of Physics: Condensed Matter*, 20(24):244128.

[116] Maloney, C. E. and Robbins, M. O. (2009). Anisotropic Power Law Strain Correlations in Sheared Amorphous 2D Solids. *Physical Review Letters*, 102(22):225502.

[117] Manning, M. L., Langer, J. S., and Carlson, J. M. (2007). Strain localization in a shear transformation zone model for amorphous solids. *Physical Review E - Statistical, Nonlinear, and Soft Matter Physics*, 76(5):056106.

[118] Martens, K., Bocquet, L., and Barrat, J. L. (2011). Connecting Diffusion and Dynamical Heterogeneities in Actively Deformed Amorphous Systems. *Physical Review Letters*, 106(15):156001.

[119] Martens, K., Bocquet, L., and Barrat, J. L. (2012). Spontaneous formation of permanent shear bands in a mesoscopic model of flowing disordered matter. *Soft Matter*, 8:4197.

[120] Martin, P. and Brochard-Wyart, F. (1998). Dewetting at Soft Interfaces. *Physical Review Letters*, 80(15):3296–3299.

[121] Moulinet, S., Guthmann, C., and Rolley, E. (2002). Roughness and dynamics of a contact line of a viscous fluid on a disordered substrate. *The European Physical Journal E, Soft Matter*, 8(4):437–443.

[122] Muskhelishvili, I. N. (1977). *Some basic problems of the mathematical theory of elasticity*. Springer.

[123] Narayan, O. (2000). Anomalous scaling in depinning transitions. *Physical Review E*, 62(6):7563.

[124] Narayan, O. and Fisher, D. S. (1993). Threshold critical dynamics of driven interfaces in random media. *Physical Review B*, 48(10):7030–7042.

[125] Nicolas, A. (2014). *Écoulements de solides amorphes: modélisation élastoplastique et théorie de couplage de modes*. PhD thesis.

[126] Nicolas, A. and Barrat, J. L. (2013). A mesoscopic model for the rheology of soft amorphous solids, with application to microchannel flows. *Faraday Discussions*, 167:567–600.

[127] Nicolas, A., Martens, K., and Barrat, J. L. (2014). Rheology of athermal amorphous solids: Revisiting simplified scenarios and the concept of mechanical noise temperature. *EPL (Europhysics Letters)*, 107:44003.

[128] Nicolas, A., Martens, K., Bocquet, L., and Barrat, J. L. (2014). Universal and non-universal features in coarse-grained models of flow in disordered solids. *Soft Matter*, 10(26):4648–4661.

[129] Oron, A., Davis, H. S., and Bankoff, S. G. (1997). Long-scale evolution of thin liquid films. *Reviews of Modern Physics*, 69(3):931–980.

[130] Papanikolaou, S. (2016). Shearing a glass and the role of pinning delay in models of interface depinning. *Physical Review E*, 93(3):032610.

[131] Paterson, A. and Fermigier, M. (1997). Wetting of heterogeneous surfaces: Influence of defect interactions. *Physics of Fluids*, 9(8):2210.

[132] Paterson, A., Fermigier, M., Jenffer, P., and Limat, L. (1995). Wetting on heterogeneous surfaces: Experiments in an imperfect Heie-Shaw cell. *Physical Review E*, 51(2):1291.

[133] Patinet, S., Vandembroucq, D., and Falk, M. L. (2016). Connecting local yield stresses with plastic activity in amorphous solids. *Preprint*.

[134] Patinet, S., Vandembroucq, D., and Roux, S. (2013). Quantitative Prediction of Effective Toughness at Random Heterogeneous Interfaces. *Physical Review Letters*, 110(16):165507.

[135] Persson, B. N. J., Tartaglino, U., Albohr, O., and Tosatti, E. (2005). Rubber friction on wet and dry road surfaces: The sealing effect. *Physical Review B - Condensed Matter and Materials Physics*, 71(3):035428.

[136] Persson, B. N. J., Volokitin, A. I., and Tosatti, E. (2003). Role of the external pressure on the dewetting of soft interfaces. *European Physical Journal E*, 11(4):409–413.

[137] Picard, G., Ajdari, A., Bocquet, L., and Lequeux, F. (2002). Simple model for heterogeneous flows of yield stress fluids. *Physical Review E - Statistical, Nonlinear, and Soft Matter Physics*, 66(5):051501.

[138] Picard, G., Ajdari, A., Lequeux, F., and Bocquet, L. (2004). Elastic consequences of a single plastic event: A step towards the microscopic modeling of the flow of yield stress fluids. *The European Physical Journal E, Soft Matter*, 15:371–381.

[139] Picard, G., Ajdari, A., Lequeux, F., and Bocquet, L. (2005). Slow flows of yield stress fluids: Complex spatiotemporal behavior within a simple elastoplastic model. *Physical Review E*, 71(1):010501.

[140] Popescu, M. N., Oshanin, G., Dietrich, S., and Cazabat, A. M. (2012). Precursor films in wetting phenomena. *Journal of Physics: Condensed Matter*, 24:243102.

[141] Prandtl, L. (1928). A Conceptual Model to the Kinetic Theory of Solid Bodies. *Zeitschrift für Angewandte*, 8(3):85–106.

[142] Puglisi, G. and Truskinovsky, L. (2005). Thermodynamics of rate-independent plasticity. *Journal of the Mechanics and Physics of Solids*, 53(3):655–679.

[143] Redon, C., Brochard-Wyart, F., and Rondelez, F. (1991). Dynamics of dewetting. *Phys. Rev. Lett.*, 66(6):715–718.

[144] Redon, C., Brzoska, J. B., and Brochard-Wyart, F. (1994). Dewetting and Slippage of Microscopic Polymer Films. *Macromolecules*, 27(2):468–471.

[145] Reiter, G. (1992). Dewetting of Thin Polymer Films. *Physical Review Letters*, 68(1):75–78.

[146] Reiter, G., Al Akhrass, S., Hamieh, M., Damman, P., Gabriele, S., Vilmin, T., and Raphael, E. (2009). Dewetting as an investigative tool for studying properties of thin polymer films. *European Physical Journal: Special Topics*, 166(1):165–172.

[147] Rodney, D., Tanguy, A., and Vandembroucq, D. (2011). Modeling the mechanics of amorphous solids at different length scale and time scale. *Modelling and Simulation in Materials Science and Engineering*, 19:083001.

[148] Roux, S. and Vandembroucq, D. (2011). Transition de dépiégeage: une approche par renormalisation. *20ème Congrès Français de Mécanique*.

[149] Roux, S., Vandembroucq, D., and Hild, F. (2003). Effective toughness of heterogeneous brittle materials. *European Journal of Mechanics, A/Solids*, 22:743–749.

[150] Salerno, K. M., Maloney, C. E., and Robbins, M. O. (2012). Avalanches in Strained Amorphous Solids: Does Inertia Destroy Critical Behavior? *Physical Review Letters*, 109(10):105703.

[151] Salerno, K. M. and Robbins, M. O. (2013). Effect of inertia on sheared disordered solids: Critical scaling of avalanches in two and three dimensions. *Physical Review E-Statistical, Nonlinear, and Soft Matter Physics*, 88(6):062206.

[152] Savva, N., Kalliadasis, S., and Pavliotis, G. A. (2010). Two-Dimensional Droplet Spreading Over Random Topographical Substrates. *Physical Review Letters*, 104(8):084501.

[153] Schall, P., Weitz, D. A., and Spaepen, F. (2007). Structural rearrangements that govern flow in colloidal glasses. *Science (AAAS)*, 318:1895–1899.

[154] Schuh, C. A., Hufnagel, T. C., and Ramamurty, U. (2007). Mechanical behavior of amorphous alloys. *Acta Materialia*, 55:4067–4109.

[155] Schuh, C. A. and Lund, A. C. (2003). Atomistic basis for the plastic yield criterion of metallic glass. *Nature materials*, 2:449–452.

[156] Sethna, J. P., Dahmen, K. A., and Myers, C. R. (2001). Crackling noise. *Nature*, 410(6825):242–250.

[157] Sharma, A. and Ruckenstein, E. (1985). Mechanism of Tear Film Rupture and Formation of Dry Spots on Cornea. *Journal of Colloid And Interface Science*, 106(1):12–27.

[158] Shi, Y. and Falk, M. L. (2006). Atomic-scale simulations of strain localization in three-dimensional model amorphous solids. *Physical Review B - Condensed Matter and Materials Physics*, 73(21).

[159] Skoe, R., Vandembroucq, D., and Roux, S. (2002). Front propagation in random media: from extremal to activated dynamics. *International Journal of Modern Physics C*, 13(6):751–757.

[160] Sneppen, K. (1992). Self-organized pinning and interface growth in a random medium. *Physical Review Letters*, 69(24):3539–3542.

[161] Sollich, P., Lequeux, F., Hébraud, P., and Cates, M. E. (1997). Rheology of Soft Glassy Materials. *Physical Review Letters*, 78(10):2020.

[162] Spaepen, F. (1976). A microscopic mechanism for steady state inhomogeneous flow in metallic glasses. *Technical report*, 7.

[163] Sprittles, J. E. and Shikhmurzaev, Y. D. (2013). Finite element simulation of dynamic wetting flows as an interface formation process. *Journal of Computational Physics*, 233(1):34–65.

[164] Su, C. and Anand, L. (2006). Plane strain indentation of a Zr-based metallic glass: Experiments and numerical simulation. *Acta Materialia*, 54(1):179–189.

[165] Sun, B. A. and Wang, W. H. (2011). Fractal nature of multiple shear bands in severely deformed metallic glass. *Applied Physics Letters*, 98(20):201902.

[166] Sun, B. A., Yu, H. B., Jiao, W., Bai, H. Y., Zhao, D. Q., and Wang, W. H. (2010). Plasticity of Ductile Metallic Glasses: A Self-Organized Critical State. *Physical Review Letters*, 105(3):035501.

[167] Suquet, P. and Lahellec, N. (2014). Elasto-plasticity of heterogeneous materials at different scales. *Procedia IUTAM*, 10:247–262.

[168] Tadmor, R. (2008). Line energy, line tension and drop size. *Surface Science*, 602:L108–L111.

[169] Talamali, M. (2011). *Plasticite des materiaux amorphes: etude et developpement d'un modele statistique*. PhD thesis.

[170] Talamali, M., Petaja, V., Vandembroucq, D., and Roux, S. (2008). Path-independent integrals to identify localized plastic events in two dimensions. *Physical Review E*, 78(1):016109.

[171] Talamali, M., Petaja, V., Vandembroucq, D., and Roux, S. (2011). Avalanches, precursors, and finite-size fluctuations in a mesoscopic model of amorphous plasticity. *Physical Review E*, 84(1):016115.

[172] Talamali, M., Petaja, V., Vandembroucq, D., and Roux, S. (2012). Strain localization and anisotropic correlations in a mesoscopic model of amorphous plasticity. *Comptes Rendus Mecanique*, 340(4-5):275–288.

[173] Tanguy, A., Gounelle, M., and Roux, S. (1998). From individual to collective pinning: Effect of long-range elastic interactions. *Physical Review E*, 58(2):1577–1590.

[174] Tanguy, A., Leonforte, F., and Barrat, J. L. (2006). Plastic response of a 2D Lennard-Jones amorphous solid: Detailed analysis of the local rearrangements at very slow strain rate. *The European Physical Journal E, Soft Matter*, 20(3):355–364.

[175] Tanguy, A. and Roux, S. (1997). Memory effects in friction over correlated surfaces. *Physical Review E - Statistical Physics, Plasmas, Fluids, and Related Interdisciplinary Topics*, 55(3):2166–2173.

[176] Tannoudji, C. C., Diu, B., and Laloe, F. (1991). *Quantum mechanics*. Wiley, Paris, 1 edition.

[177] Taylor, E. W. (1949). Plastic Deformation of Optical Glass. *Nature*, 163(4139):323.

[178] Thrope, M. and Jasiuk, I. (1992). New Results in Theory of Elasticity for Two-Dimensional Composites. *Mathemical and Physical Sciences*, 438(1904):531–544.

[179] Török, J., Krishnamurthy, S., Kertész, J., and Roux, S. (2000). Self-Organization, Localization of Shear Bands, and Aging in Loose Granular Materials. *Physical review letters*, 84(17):3851–3854.

[180] Torquato, S. (2002). *Random heterogeneous materials. Microstructure and macroscopic properties*. Springer, New York.

[181] Toukmaji, A. Y. and Board, J. A. (1996). Ewald summation techniques in perspective: a survey. *Computer Physics Communications*, 95(2-3):73–92.

[182] Tsamados, M. (2009). *Mechanical response of glassy materials*. PhD thesis.

[183] Tsamados, M., Tanguy, A., Goldenberg, C., and Barrat, J. L. (2009). Local elasticity map and plasticity in a model Lennard-Jones glass. *Physical Review E*, 80(2):026112.

[184] Turcsanyi, B., Pukanszky, B., and Tudos, F. (1988). Composition dependence of tensile yield stress in filled polymers. *Journal of Materials Science Letters*, 7:160–162.

[185] Turgeman, S. and Guessab, B. (2011). Lower bound of effective yield strength domain for random heterogeneous materials. *Mechanics Research Communications*, 38:181–185.

[186] Tyukodi, B., Bréchet, Y., and Néda, Z. (2014). Kinetic roughening of a soft dewetting line under quenched disorder: A numerical study. *Physical Review E*, 90(5):052404.

[187] Tyukodi, B., Lemarchand, C. A., Hansen, J. S., and Vandembroucq, D. (2016). Finite-size effects in a model for plasticity of amorphous composites. *Physical Review E*, 93(2):023004.

[188] Tyukodi, B., Patinet, S., Roux, S., and Vandembroucq, D. (2015). From depinning transition to plastic yielding of amorphous media: A soft modes perspective. *arXiv: 1502.07694v1.*

[189] Vandembroucq, D. and Roux, S. (2004). Large-scale numerical simulations of ultrametric long-range depinning. *Physical Review E*, 70(2):026103.

[190] Vandembroucq, D. and Roux, S. (2011). Mechanical noise dependent aging and shear banding behavior of a mesoscopic model of amorphous plasticity. *Physical Review B*, 84(13):134210.

[191] Vandembroucq, D., Skoe, R., and Roux, S. (2004). Universal depinning force fluctuations of an elastic line: Application to finite temperature behavior. *Physical Review E*, 70(5):051101.

[192] Vilmin, T. and Raphael, E. (2006). Dewetting of thin polymer films. *European Physical Journal E*, 21:161–174.

[193] Weinberger, C. and Cai, W. (2004). Eshelby's Inclusion I. Lecture notes. pages 1–12.

[194] Weinberger, C., Cai, W., and Barnett, D. (2005). Lecture Notes - Elasticity of Microscopic Structures. pages 5–118.

[195] Weiss, J., Girard, L., Gimbert, F., Amitrano, D., and Vandembroucq, D. (2014). (Finite) statistical size effects on compressive strength. *Proceedings of the National Academy of Sciences of the United States of America*, 111(17):6231–6236.

[196] Wikipedia (2015). Stone mastic asphalt. *en.wikipedia.org/wiki/Stone_ mastic_ asphalt.*

[197] Xue, L. and Han, Y. (2012). Inhibition of dewetting of thin polymer films. *Progress in Materials Science*, 57:947–979.

[198] You, T., Al-Rub, R. K. A., Darabi, M. K., Masad, E. A., and Little, D. N. (2012). Three-dimensional microstructural modeling of asphalt concrete using a unified viscoelastic-viscoplastic-viscodamage model. *Construction and Building Materials*, 28(1):531–548.

[199] Zhang, Q. S., Zhang, W., Xie, G. Q., Louzguine-Luzgin, D. V., and Inoue, a. (2010). Stable flowing of localized shear bands in soft bulk metallic glasses. *Acta Materialia*, 58(3):904–909.

[200] Zhang, Y. and Greer, A. L. (2006). Thickness of shear bands in metallic glasses. *Applied Physics Letters*, 89(7):071907.